

Numerical Modelling of Metal Soap Formation in Historical Oil Paintings

Citation for published version (APA):

Eumelen, G. J. A. M. (2022). *Numerical Modelling of Metal Soap Formation in Historical Oil Paintings*. [Phd Thesis 1 (Research TU/e / Graduation TU/e), Built Environment]. Eindhoven University of Technology.

Document status and date:

Published: 08/09/2022

Document Version:

Publisher's PDF, also known as Version of Record (includes final page, issue and volume numbers)

Please check the document version of this publication:

- A submitted manuscript is the version of the article upon submission and before peer-review. There can be important differences between the submitted version and the official published version of record. People interested in the research are advised to contact the author for the final version of the publication, or visit the DOI to the publisher's website.
- The final author version and the galley proof are versions of the publication after peer review.
- The final published version features the final layout of the paper including the volume, issue and page numbers.

[Link to publication](#)

General rights

Copyright and moral rights for the publications made accessible in the public portal are retained by the authors and/or other copyright owners and it is a condition of accessing publications that users recognise and abide by the legal requirements associated with these rights.

- Users may download and print one copy of any publication from the public portal for the purpose of private study or research.
- You may not further distribute the material or use it for any profit-making activity or commercial gain
- You may freely distribute the URL identifying the publication in the public portal.

If the publication is distributed under the terms of Article 25fa of the Dutch Copyright Act, indicated by the "Taverne" license above, please follow below link for the End User Agreement:

www.tue.nl/taverne

Take down policy

If you believe that this document breaches copyright please contact us at:

openaccess@tue.nl

providing details and we will investigate your claim.

Numerical modelling of metal soap formation in historical oil paintings

PROEFSCHIFT

ter verkrijging van de graad van doctor aan de Technische Universiteit Eindhoven, op gezag van de rector magnificus prof.dr.ir. F.P.T. Baaijens, voor een commissie aangewezen door het College voor Promoties, in het openbaar te verdedigen op donderdag 08 september 2022 om 16:00 uur

door

Gerardus Johannes Anna Maria Eumelen

geboren te Nijmegen

Dit proefschrift is goedgekeurd door de promotoren en de samenstelling van de promotiecommissie is als volgt:

voorzitter: prof.dr.ir. P.J.V. van Wesemael
promotor: prof.dr.ir. A.S.J. Suiker
copromotor: dr.ir. E. Bosco
leden: prof.dr. N.A. Fleck (University of Cambridge)
prof.dr. L. Fuster-López (Universitat Politècnica de València)
prof.dr. P.D. Iedema (Universiteit van Amsterdam)
dr. M. Łukomski (The Getty Conservation Institute)
dr.ir. R.H.J. Peerlings

Het onderzoek of ontwerp dat in dit proefschrift wordt beschreven is uitgevoerd in overeenstemming met de TU/e Gedragscode Wetenschapsbeoefening.

Numerical modelling of metal soap formation in historical oil paintings

A catalogue record is available from the Eindhoven University of Technology Library
ISBN: 978-90-386-5541-3
Bouwstenen: 333

Cover design by Bas Eumelen
Printed by Dereumaux, 's-Hertogenbosch

Copyright © G.J.A.M. Eumelen, 2022
All rights reserved. No parts of this document may be reproduced, distributed, modified, stored, or transmitted, in any form or by any means, without the prior written permission of the author.

Acknowledgements

When I started with my bachelor education in 2010 I never expected that I would continue studying to get my Master's degree, let alone that I would do a PhD. Yet here we are, 12 years later, and before you lies my dissertation. These last few years have been some of the most interesting ones in my professional life; not only because of the topic I was working on, or the people I met along the way, but also because I found beauty in activities I greatly disliked¹ – and sometimes still do. None of this would have been possible without the help and support from many people, some of whom I, hereby, would like to thank by name.

First and foremost I would like to thank both my promotor Akke Suiker and copromotor Emanuela Bosco. I cannot describe how thankful I am for the opportunity that you gave me. Without both of you it would not have been possible for me to complete this dissertation. Your continuous enthusiasm and passion for research and applied mechanics is one of the things that made me want to do a PhD in the first place, and it has helped me to get through some of the more difficult periods of the entire process. The support you provided to me and the patience you had while I was experiencing difficulties in my work have been of tremendous help. Therefore, once again. Thank you!

I would also like to thank some of the other people that have been invaluable in the development of this dissertation. Specifically, I would like to thank Joen Hermans, Piet Iedema, Katrien Keune, and Annelies van Loon for sharing their experience and knowledge regarding the chemistry of metal soap formation and its manifestation in historical oil paintings. The discussions and meetings I had with you really helped me grasp the chemical processes much faster and better than when I would have to study it by myself. I am also very grateful for the helpful discussions provided by Naoki Fujisawa and Michał Łukomski on the indentation of embedded materials. Finally, I would like to thank Norman Fleck. Even though we only had a limited number of interactions, they were always very informative for me and they have helped me to improve my scientific communication skills.

Besides the people that directly contributed to the development of this dissertation, there are also numerous people that indirectly helped me. I would like to start by thanking my colleagues at the 9th floor. You all provided a very relaxed and accessible environment, which always made it a pleasure to come to work. I would further like to thank Frits Rooyackers and Irene Scheperboer more personally. Irene, I enjoyed the time we spent in the “trenches” together – you a bit more literal than I. You were always high-spirited, which would brighten my day, and I could discuss anything with you no matter how small. Furthermore, the lunch walks and the celebratory drinks we had were always appreciated. Frits, you made my time at the university so much more enjoyable. Thank

¹I think hated would suit better here, but this is such a strong word.

you for introducing me to all kinds of new music, and, equally important, for the daily coffee breaks. The discussions we had over coffee regarding our projects helped me solve more than one problem. With respect to the coffee breaks I would also like to thank the employees of the Structures Laboratory Eindhoven. Even though I did not do any experiments, you allowed me to join your coffee breaks once the university had to close due to the CoViD-19 pandemic, for which I am very grateful.

Tot slot wil ik graag nog mijn familie en vrienden bedanken voor de steun die ze mij hebben gegeven tijdens het hele proces. Mam, Bas en Karla, bedankt voor jullie steun en voor het begrip dat jullie hebben opgebracht om mij dit avontuur te laten ondernemen; ik kan me voorstellen dat het niet altijd even makkelijk was. Pap en Ellen, Eline, Jesse, bedankt voor alle steun die jullie mij de afgelopen jaren hebben gegeven. Mark, Chris, heel erg bedankt voor de eindeloze game avonden die we hebben gehad; dit heeft me meer dan eens geholpen om goed af te kunnen schakelen.

Summary

Numerical modelling of metal soap formation in historical oil paintings

The formation of metal soap is a common degradation mechanism affecting historical oil paintings in museum collections worldwide. Metal soap formation is governed by a series of complex chemical reactions between saturated fatty acid molecules that are released from the oil binder and metal ions originating from the pigments. Metal soap forms initially in an amorphous state, and may ultimately develop into crystalline metal soap aggregates. These aggregates can reach relatively large sizes that disfigure the paint surface and protrude through it, resulting in paint loss. Furthermore, the formation of metal soap may promote other degradation mechanisms, such as craquelure and delamination.

Current research into metal soap formation principally focuses on the identification and analysis of metal soap extracted from oil paintings, or on the chemical processes involved in the formation of metal soap. The mechanical behaviour of oil paintings due to metal soap formation, however, has received little attention and is therefore poorly understood.

The objective of this dissertation is to gain in-depth insight into the chemo-mechanical behaviour of historical oil paintings due to metal soap formation. The research described here covers two main topics: *i*) the development of a chemo-mechanical damage model that describes metal soap formation inside an oil painting, specifically focusing on the formation of lead soap protrusions; and *ii*) the development of an analytical model that can be used to extract the material properties of embedded (paint) materials from indentation tests. The main conclusions of this thesis are summarised below.

The chemo-mechanical response of historical oil paintings due to metal soap formation is studied by means of a chemo-mechanical damage model. This model consists of a diffusion-reaction model that is sequentially coupled to a mechanical model. The spatial growth of the metal soap crystal introduces stresses, which is accounted for in the mechanical model through a chemically-induced growth strain. This can ultimately lead to the nucleation and propagation of cracks. This behaviour is simulated by using a cohesive zone approach. The mechanical cohesive interface elements are equipped with a traction-separation law, while for the diffusive interface elements a flux-concentration relationship is defined that depends on the mechanical damage. The applicability of this model is demonstrated through different sets of numerical simulations. For the initial simulations, a simplified reaction process is assumed, which neglects the formation of amorphous metal soap, i.e. it assumes that the reaction between saturated fatty acids and metal ions directly forms crystalline metal soap.

Further, to improve the model accuracy, particularly regarding the predicted time scale of the process, the chemical model formulation is extended to describe the formation of amorphous metal soap. The extended model has been applied to analyse different numer-

ical examples that are representative of typical metal soap-related degradation processes observed in historical oil paintings. These simulations show that the growth process of crystalline metal soap, the deformation of the paint surface, and the consequent cracking and delamination patterns are predicted in a realistic fashion.

The second part of this thesis focuses on the accurate calibration of mechanical properties of paint samples obtained from nanoindentation tests. Nanoindentation testing is an experimental technique that enables accurate measurements of the material properties at small length scales. This technique is particularly appropriate to analyse historical oil paint, as small scale samples that are extracted from original oil paintings can be tested. However, these samples are embedded in a supporting resin with different material properties, which can affect the measured properties if the indentation size is relatively large. To efficiently calibrate the elastic and plastic properties of the embedded paint sample, an analytical model is developed. This model exploits the analytical solutions for the elastic and elasto-plastic indentation of a homogeneous material and adapts these by replacing the homogeneous stiffness modulus with an effective stiffness modulus. The accuracy of the model is determined by comparing its results to results obtained from dedicated finite element simulations. These analyses show that for a wide range of materials the model accurately describes the elastic and elasto-plastic indentation response of the embedded material. Furthermore, it is shown that the plastic response of the material is essentially set by the yield strength of the embedded material. Finally, the practical applicability of the model is demonstrated by accurately calibrating the elastic stiffness from indentation tests on an embedded paint sample, as reported in the literature.

Samenvatting

Numeriek modelleren van metaalzeepvorming in historische olieverfschilderijen

Metaalzeepvorming is een veel voorkomend degradatiemechanisme dat optreedt in historische olieverfschilderijen in museumcollecties over de hele wereld. Metaalzeep vormt ten gevolge van een reeks complexe chemische reacties tussen verzadigde vetzuurmoleculen die uit de oliebinder komen en metaalionen die oorspronkelijk uit de pigmenten komen. Metaalzeep vormt initieel in een amorfe staat, en kan zich uiteindelijk ontwikkelen tot metaalzeepkristallen. Deze kristallen kunnen relatief grote afmetingen bereiken waardoor het verfloppervlak vervormt. Daarbij kunnen de kristallen ook door de verf heen breken, wat resulteert in het verlies van verf. De vorming van metaalzeep kan ook andere degradatiemechanismen versnellen, zoals craquelé en delaminatie.

Op dit moment is onderzoek in metaalzeepvorming voornamelijk gefocust op de identificatie en analyse van metaalzeep uit olieverfschilderijen, of op de chemische processen die betrokken zijn bij de vorming van metaalzeep. Het mechanisch gedrag van olieverfschilderijen door metaalzeepvorming heeft echter vrij weinig aandacht gekregen en wordt daardoor slecht begrepen.

De algemene doelstelling van dit proefschrift is om inzicht te krijgen in het chemisch-mechanisch gedrag van historische olieverfschilderijen ten gevolge van metaalzeepvorming. Het onderzoek wat hierin beschreven staat is onderverdeeld in twee onderwerpen: *i*) de ontwikkeling van een chemisch-mechanisch schademodel dat de vorming van metaalzeep in olieverfschilderijen beschrijft, waarbij specifiek gefocust is op de vorming van loodzeepprotrusies; en *ii*) de ontwikkeling van een analytisch model dat kan worden gebruikt voor het bepalen van materiaaleigenschappen van ingebedde (verf) materialen, beproefd door middel van indentatietesten. De belangrijkste conclusies van dit proefschrift zijn hieronder samengevat.

Het chemisch-mechanisch gedrag van historische olieverfschilderijen ten gevolge van metaalzeepvorming wordt bestudeerd door middel van een chemisch-mechanisch schademodel. Dit model bestaat uit een diffusie-reactie model dat incrementeel-sequentieel gekoppeld is aan een mechanisch model. Het groeien van het metaalzeepkristal introduceert spanningen, die worden meegenomen in het mechanisch model door middel van een chemische groeirek. Dit kan uiteindelijk leiden tot het ontstaan van scheuren en het groter worden daarvan. Het scheurgedrag wordt gesimuleerd door het gebruik van een cohesief zone-model. Het mechanische gedrag van de cohesieve interface elementen wordt beschreven door middel van een tractie-separatie wet, terwijl voor de diffusieve cohesieve interface elementen een flux-concentratie relatie is gedefinieerd, die afhankelijk is van de mechanische schade. De toepassingsmogelijkheden van dit model worden gedemonstreerd door middel van verschillende series van numerieke simulaties. Voor de

initiële simulaties wordt een versimpeld reactieproces verondersteld waarbij de vorming van het amorfe metaalzeep wordt genegeerd. Met andere woorden, er wordt aangenomen dat de reactie tussen verzadigde vetzuren en metaalionen direct resulteert in metaalzeepkristallen.

Om de nauwkeurigheid van het model te verbeteren, vooral met betrekking tot de voorspelde tijdschaal van het proces, is vervolgens de chemische modelformulering uitgebreid zodat deze ook de vorming van het amorfe metaalzeep bevat. Het uitgebreide model is toegepast voor de analyse van verschillende numerieke voorbeelden die representatief zijn voor typische metaalzeep gerelateerde degradatieprocessen die worden waargenomen in olieverfschilderijen. Deze simulaties laten zien dat het groeiproces van de metaalzeepkristallen, de vervorming van het verfoppervlak, en het ontstaan van de scheur- en delaminatiepatronen op een realistische manier worden voorspeld.

Het tweede deel van dit proefschrift focust op het nauwkeurig vaststellen van de mechanische eigenschappen van verfmonsters, beproefd door middel van nano-indentatietesten. De nano-indentatietest is een experimentele techniek die kan worden gebruikt om materiaaleigenschappen op een kleine lengteschaal vast te stellen. Deze techniek is zeer bruikbaar voor het analyseren van historische olieverfschilderijen, omdat zeer kleine proefstukken verkregen uit de originele olieverfschilderijen kunnen worden getest. Deze proefstukken worden ingebed in een hars met afwijkende materiaaleigenschappen, wat, bij relatief grote indentaties, invloed kan hebben op de gemeten materiaaleigenschappen. Voor het efficiënt kalibreren van de elastische en plastische eigenschappen van een ingebed verfmonster is een analytisch model ontwikkeld. Dit model maakt gebruik van de analytische oplossingen voor de elastische en elastisch-plastische indentatie van een homogeen materiaal, waarbij de homogene stijfheidsmodulus wordt vervangen door een effectieve stijfheidsmodulus. De nauwkeurigheid van dit model is vastgesteld door resultaten van dit model te vergelijken met resultaten die zijn verkregen door middel van gedetailleerde eindige-elementensimulaties. Deze analyses laten zien dat voor een grote groep materialen het elastisch en elastisch-plastisch indentatiegedrag nauwkeurig wordt beschreven door het model. Daarbij wordt ook gedemonstreerd dat het plastisch indentatiegedrag in principe wordt bepaald door de vloeisterkte van het ingebedde materiaal. Tot slot is de praktische toepasbaarheid van het model gedemonstreerd door de elastische stijfheid van een ingebed verfmonster nauwkeurig vast te stellen, waarvoor resultaten van indentatietesten zijn gebruikt die zijn gerapporteerd in de literatuur.

Table of contents

Acknowledgements	i
Summary	iii
Samenvatting	v
1 Introduction	3
1.1 Oil paint	3
1.2 Metal soap	4
1.3 Objectives and scope	6
1.4 Outline	7
2 A computational model for chemo-mechanical degradation of historical oil paintings due to metal soap formation	11
2.1 Introduction	12
2.2 Chemical process of metal soap formation	14
2.3 Chemo-mechanical model	15
2.3.1 Modelling assumptions	15
2.3.2 Diffusion-reaction model	17
2.3.3 Mechanical model	18
2.3.4 Crack nucleation and propagation	20
2.4 Numerical simulations	23
2.4.1 Multi-physics coupling	23
2.4.2 Material parameters	24
2.4.3 Geometry, initial conditions, and boundary conditions	26
2.5 Numerical results	28
2.5.1 Reference model	29
2.5.2 Parameter variation study	33
2.6 Conclusions and discussion	38
3 Influence of nucleus geometry and location and fatty acid concentration on metal soap induced damage in paint layers	43
3.1 Introduction	44
3.2 Chemo-mechanical model	44
3.2.1 Modelling assumptions	45
3.2.2 Modelling strategy	46
3.3 Numerical simulations	47

3.3.1	Material parameters	47
3.3.2	Geometry and initial and boundary conditions	48
3.4	Results and discussion	50
3.4.1	Influence of nucleus geometry	50
3.4.2	Influence of fatty acid concentration profile	52
3.4.3	Influence of the metal soap distribution	54
3.5	Conclusions	56
4	A chemo-mechanical model to predict degradation in oil paintings by amorphous and crystalline metal soaps	61
4.1	Introduction	62
4.2	Model description	66
4.2.1	Chemical model	66
4.2.2	Mechanical model	69
4.2.3	Numerical solution procedure	72
4.3	Parameter calibration for the diffusion-reaction model	73
4.3.1	Review of the experiment	73
4.3.2	Reference model and calibration procedure	73
4.3.3	Result of calibration procedure	75
4.4	Numerical example 1: Single-layer paint system	75
4.4.1	Definition of the problem	76
4.4.2	Results	80
4.5	Numerical example 2: Multi-layer paint system	83
4.5.1	Definition of the problem	83
4.5.2	Results	86
4.6	Conclusions	88
5	Analytical model for elasto-plastic indentation of a hemispherical surface inclusion	93
5.1	Introduction	94
5.2	Review of indentation models for homogeneous materials	95
5.2.1	Indentation of an elastic solid	95
5.2.2	Elastic unloading of an elasto-plastic solid	97
5.2.3	Indentation of an elastic, ideally plastic solid	98
5.3	Closed-form expression for the effective elastic modulus of a bi-material	101
5.3.1	Elastic displacement field	102
5.3.2	Effective elastic modulus of an embedded spherical shell	103
5.4	Indentation of embedded hemispherical particles	104
5.4.1	Indentation of an elastic hemispherical particle embedded in an elastic half space	104
5.4.2	Indentation of an elastic, ideally plastic hemispherical particle embedded in an elastic half space	110
5.5	Case study: use of analytical model to interpret indentation test on embedded paint sample	112
5.6	Conclusions	115

6 Conclusions and recommendations	119
6.1 Conclusions	119
6.1.1 Chemo-mechanical behaviour of historic oil paintings	119
6.1.2 Mechanical properties of embedded historical oil paints	120
6.2 Recommendations	121
Appendices	125
A Three-dimensional finite element model versus analytical model for a paint indentation problem	125
Bibliography	129
Curriculum Vitae	143
Publication List	145

Introduction

Chapter 1

Introduction

Oil paintings consist of different layers of oil paint that are generally adhering to a wooden or canvas substrate. The thickness of the individual paint layers can vary drastically depending on the painting technique and historical period; for example, pictorial layers have thicknesses that are usually of the order of micrometres [144, 148], whereas ground layers and impastos (especially in modern paintings) can have thicknesses of up to a few millimetres [103]. The characteristics of both the paint material and the substrate do not only determine the appearance of the painting, but also influence various chemical and physical processes that ultimately affect the (structural) integrity of an oil painting [109, 112]. One of these processes is the formation of metal soaps.

Metal soaps form from chemical reactions between metal ions and saturated fatty acids, which are released by the pigments and the oil binder, respectively. The reaction between metal ions and saturated fatty acids results in the formation of metal soap, which is initially considered to be in an amorphous state. As the concentration of amorphous metal soap reaches a critical threshold value, it can crystallise. Crystalline metal soap formation has been linked to various forms of mechanical damage that are observed in paintings, such as crack formation and delamination. Unravelling the relation between the formation of metal soap and the mechanical behaviour of oil paintings can assist conservation decisions to preserve these paintings for future generations. The research presented in this dissertation is precisely aimed at improving the fundamental understanding of the chemo-mechanical degradation of oil paintings due to metal soap formation.

1.1 Oil paint

Oil paint consists of a drying oil, e.g. linseed oil or poppy seed oil, in which pigment particles are suspended. From a chemical point of view, these drying oils are triglycerides, which are three fatty acid molecules bound to glycerol molecules. In a drying oil, more than 50% of the fatty acids are (poly)unsaturated, i.e. they are characterised by one or more C=C bonds [11, 15]. Due to the (poly)unsaturation of the fatty acid molecules, drying oils form a densely cross-linked polymer film when they are exposed to light and oxygen, i.e. the fatty acids react with each other via autoxidation reactions [9, 11, 14, 165]. In addition to these unsaturated fatty acids, drying oils also contain substantially lower concentrations of saturated fatty acids. These saturated fatty acids do not contain any C=C bonds and can, therefore, be unbound from the polymer network. As the paint ages, the bonds between the glycerol molecule and the fatty acid molecules can be broken by

means of hydrolysis reactions. The saturated fatty acid molecules thus become suspended in the paint film as free fatty acids [70]. The presence of these free fatty acids can result in the formation of metal soap, which can contribute to the mechanical instability of the painting, as will be discussed in Section 1.2.

While the drying oil acts as a binder, the pigments give colour to the paint. Pigments are fine powdered (in)organic materials that can have a natural or an artificial origin [141]. The type of pigment that is used determines the material behaviour. Specifically, if the pigment particles are able to react with the binder, a durable, strong, and stiff paint film forms, as, for example, observed for most lead and zinc containing pigments [50, 111, 112]. Conversely, if inert pigments (e.g. earth pigments) are used, a very weak and fragile paint film forms that may even require the addition of driers (usually metal salts containing, for example, lead, zinc or manganese) to form a solid paint film [50, 111, 112].

In the case of a durable paint film, carboxyl groups (COOH) attached to the fatty acid molecules react with the metal ions that originate from the pigment particles or driers [9, 112]. These carboxyl groups are formed during various stages of the drying and ageing of the paint. Initially, the autoxidation reactions result in the formation of carboxyl groups. Additionally, as the paint continues to age, carboxyl groups are formed when ester bonds are broken due to hydrolysis reactions [9], e.g. the bonds between the glycerol and fatty acid molecules. If the carboxyl group belongs to an unsaturated fatty acid molecule, the metal ions become complexed with the polymer network, forming an ionomer [8, 10, 70, 71]. However, if the carboxyl group is part of a saturated fatty acid molecule, metal soap will form [8, 10, 70, 71], as will be discussed in the following section.

1.2 Metal soap

The formation of metal soap is the result of a series of complex reaction steps, which are still topic of scientific debate in the chemistry community. Metal soap forms from a chemical reaction between metal ions and saturated fatty acids. The metal soap is hypothesised to initially be in an amorphous state. However, as the concentration of amorphous metal soap reaches a critical threshold, the metal soap can start to crystallise [8, 10, 70, 71]. The formation of amorphous metal soap is expected to be a reversible process, as the metal ions can equivalently react with the carboxyl group (COOH) of either free saturated fatty acids or unsaturated fatty acids from the polymer network [8, 10, 70, 71].

In principle, metal soap can form from different kinds of metal ions; however, the formation of lead or zinc soap appears to be more favourable than other types of metal soap [30, 83, 120]. Lead and zinc soaps are often observed in reality. This is due to the fact that until the nineteenth century lead white was the only white pigment used for paintings (in Europe), after which it was replaced by zinc white in modern paintings [141]. Metal soap formation may thus pose a large threat to oil paintings worldwide, as confirmed by a survey [123] and subsequent studies, e.g. [155]. A selection of paintings from the Mauritshuis, The Hague, in which metal soap was detected, can be seen in Figure 1.1. Due to the large scale of this problem and the possible complications that metal soap formation has on the appearance and structural integrity of oil paintings, metal soap formation is one of the most significant topics in painting conservation research since its discovery in the late 1990s–early 2000s [30, 120].



(a) Johannes Vermeer, *View of Delft*, ca. 1660–1661, Oil on canvas, 96.5 cm × 115.7 cm, Mauritshuis, The Hague, The Netherlands.



(b) Rembrandt van Rijn, *The anatomy lesson of dr. Nicolaes Tulp*, 1632, Oil on canvas, 216.5 cm × 169.5 cm, Mauritshuis, The Hague, The Netherlands.



(c) Aert van der Neer, *River landscape*, 1650, Oil on panel, 63 cm × 44.8 cm, Mauritshuis, The Hague, The Netherlands.

Figure 1.1: Selection of paintings of the Mauritshuis, The Hague, in which metal soap formation was detected [122–124, 166, 167]. Detail photos courtesy of: (a) A. van Loon, and (b, c) P. Noble [120].

The research into this topic has mainly focused on identifying and analysing metal soaps in historical oil paintings by means of various optical and analytical techniques [23, 70, 89, 122, 137, 163], and on the chemical aspects of metal soap formation, such as the reaction kinetics and crystallisation processes [8, 10, 28, 67, 69–72, 74, 130]. These studies have also indicated the influence of metal soap formation on various types of degradation mechanisms [29, 62, 75, 87, 105, 121–124, 140, 167]. For example, metal soap can appear as (relatively) large crystalline aggregates inside a paint layer. These crystals disfigure the paint surface and can even protrude through multiple layers, resulting in paint loss [29, 75, 87, 121]. The formation of these metal soap protrusions was also observed in the paintings shown in Figures 1.1(a) and (b), as can be seen from the magnifications in the insets [120, 166, 167]. Further, metal soap may crystallise as a separate layer inside the painting. This layer can then influence the adhesion of the adjacent paint layers, resulting in their delamination [62, 105, 140]. If the metal soap does not crystallise and remains trapped in an amorphous state, this may cause transparency of the paint, whereby the underlying paint layers or support become visible, as observed for the painting shown in Figure 1.1(c), see the inset for more detail [120]. The specific type of metal soap-induced degradation depends on various factors, for example, the type of metal ions (e.g. lead or zinc), the paint and painting composition, and the climate conditions [9, 10, 74, 83, 90, 120].

Even though metal soap formation is a topic of current and broad research, the understanding of the coupled chemo-mechanical influence in historic oil paintings remains very limited. The work presented in this dissertation provides the first steps into improving this understanding by systematically studying the growth of crystalline metal soap and the corresponding mechanical response of the paint through advanced numerical simulations.

1.3 Objectives and scope

The objective of this dissertation is to improve the understanding of the chemo-mechanical degradation of historical oil paintings due to metal soap formation. The research presented here is divided into two main topics, as outlined below.

The first topic focuses on the numerical modelling of the formation of crystalline metal soap inside paint layers. To this aim, a chemo-mechanical damage model has been developed. The developed framework consists of a diffusion-reaction model that is sequentially coupled to a mechanical model. The coupling between the two models is achieved by defining a chemically-induced growth strain, which quantifies the effect of the growth of the metal soap crystal on the stress field. As a result, cracks might form in the paint layer. A discrete crack model is used to describe the nucleation and propagation of the cracks. Further, cracking might hamper the diffusion of the saturated fatty acid in the paint layer. This is modelled by locally reducing the diffusion coefficient as a function of mechanical damage.


Initially, a simplified reaction process is assumed for the diffusion-reaction model, whereby the intermediate state of amorphous metal soap is neglected, i.e. it is assumed that the reaction between saturated fatty acid and metal ions directly forms crystalline metal soap. This preliminary model is used to study the chemo-mechanical degradation process as a function of the different material properties of the paint and the metal soap, the chemical and mechanical boundary conditions, and geometrical features of the problem. The model is proven to qualitatively capture the process of metal soap formation; however, the predicted time scale is significantly shorter than in reality. To improve the accuracy of the predictions, the chemical model formulation is subsequently extended to include the formation of amorphous metal soap.

The numerical simulations presented in the first part of this dissertation use mechanical material properties that are estimated from uniaxial tensile tests reported in the literature. These tensile tests, however, were performed on relatively young paints, and at a (much) larger length scale than that characterising the modelled domains. In order to quantitatively improve the model predictions, material properties extracted from real paint samples should be used, for example obtained through nanoindentation testing [47, 48, 103]. Therefore, the second part of this dissertation focuses the development of an analytical model that can be used to efficiently calibrate the elastic and plastic properties of embedded materials from nanoindentation tests. Nanoindentation tests are ideally suited to determine the material properties of historical oil paintings, as only micrometre sized samples are available for testing. However, if the (relative) indentations are large, the measured response may be significantly influenced by the embedding resin [47, 48, 103]. The presented model makes use of an analytical expression for an effective stiffness modulus representative of the embedded sample. The validity of the model is assessed by comparing its results to results obtained from dedicated numerical simulations and experimental tests presented in the literature [48].

1.4 Outline

The topics discussed in the previous section are treated separately in different chapters of this dissertation. The development of the preliminary chemo-mechanical damage model along with a parameter variation study is treated in Chapter 2. In Chapter 3, the preliminary model is used to analyse the effect of different metal soap nucleus shapes, different fatty acid concentration profiles, and the effect of metal soap distribution on the predicted chemo-mechanical damage. In Chapter 4, the chemo-mechanical damage model is subsequently extended by including the formation of amorphous metal soap. Chapter 5 presents the analytical model to predict the indentation response of bi-materials and compares the model predictions to results from numerical simulations and experimental measurements. Finally, the main conclusions and recommendations of this work are summarised in Chapter 6.

Chapters 2 to 5 are based on journal and conference papers. Specifically, Chapter 2 is based on [37], Chapter 3 is based on [38, 39], Chapters 4 is submitted as [40], and Chapter 5 is based on [41]. Consequently, the chapters are presented such that they can be read separately, i.e. a chapter starts with a general introduction, followed by the content, and the main conclusions.



**A computational model for
chemo-mechanical degradation of
historical oil paintings due to metal soap
formation**

Chapter 2

A computational model for chemo-mechanical degradation of historical oil paintings due to metal soap formation

A large percentage of oil paintings in museum collections suffers from chemo-mechanical degradation phenomena that are primarily due to metal soap formation. Metal soaps result from the chemical reaction between metal ions present in the pigments and saturated fatty acids released by the oil paint. They appear as large protrusions that disfigure the surface texture, possibly triggering mechanical damage and flaking of the painting. Despite that these phenomena have been widely observed *in situ*, the interaction between chemical and mechanical degradation processes is far from being understood. This chapter¹ proposes a chemo-mechanical model to predict metal soap formation and the resulting chemo-mechanical damage in historical oil paintings. The chemical process is described by means of a diffusion-reaction model, whereby the spatial growth of the metal soap crystal takes place in a small reaction zone at the boundary of the crystal. Metal soap crystallisation and growth, driven by the diffusion of saturated fatty acids and metal ions, result in a chemically-induced volumetric growth strain. This introduces stresses in the paint, ultimately promoting crack nucleation and propagation. The fracture process is simulated with a cohesive zone approach, using interface elements equipped with a traction-separation law. The mass flux-concentration relation at the interfaces is consistently specified as a function of the mechanical damage. A set of numerical simulations illustrates the capability of the model to predict metal soap crystallisation and growth and the fracture induced in the paint. The study finally illustrates the influence of various chemical and mechanical parameters (i.e. the size of the metal soap nucleus, the mismatch in elastic stiffness parameters between the metal soap and paint materials, the fracture length scale of the paint material, the chemical growth strain and the reaction rate) on the chemo-mechanical degradation of the paint layer.

¹This chapter is based on:

[37] G.J.A.M. Eumelen, E. Bosco, A.S.J. Suiker, A. van Loon, and P.D. Iedema. *Journal of the Mechanics and Physics of Solids*, 132:103683, 2019.

2.1 Introduction

The prediction of material degradation and failure is a challenging task in computational mechanics, particularly when these phenomena are governed by the coupled influence of multiple physical processes. Appropriate numerical strategies are required to capture the complexity of the material response in multi-physics fracture processes, which is relevant for a variety of problems, ranging from industrial engineering applications (including e.g. the chemo-mechanical damage of cementitious materials [81] or the chemo-mechanical fracture of Li-ion batteries [117]), to, surprisingly, cultural heritage objects.

This study is particularly motivated by the degradation of historical oil paintings resulting from the formation of metal soaps. Oil paintings typically consist of one or more oil paint layers and ground layers on a canvas or wooden panel support. The oil paint is usually composed of metal-based pigment particles bound together by a drying oil. Metal soaps can form from a chemical reaction between metal ions released by the pigments or driers and saturated fatty acids, which are degradation products of the oil binder [72]. According to the reaction scheme hypothesised in [8], the initial reaction is thought to be reversible, and leads to the formation of metal soaps in an amorphous state. Metal soaps can subsequently crystallise into insoluble aggregates or form new mineral phases by interaction with atmospheric compounds (e.g. CO_2 , SO_2) via an irreversible reaction, appearing as opalescent hazes on the paint surface or large protrusions deforming the paint layers, often visible with the naked eye [167]. A clear example of metal soap aggregates protruding through several paint layers and reaching the top paint surface can be observed in the painting *View of Delft* (ca. 1660–1661) by Johannes Vermeer (Mauritshuis, The Hague), see Figure 2.1. The formation of metal soaps may also cause an increased transparency of the upper paint layers, thereby revealing colours from underlying paint layers [167]. Metal soaps are not only detrimental to the visual appearance of artworks, but their nucleation and growth can also introduce mechanical strains in the paint system, which may lead to cracking, flaking and delamination of paint layers [105, 130]. It has been estimated that about 70% of the oil paintings displayed in museum collections worldwide, ranging from sixteenth century paintings to paintings from the present time, suffers to some extent from metal soap formation [16, 155]. The development of a comprehensive modelling approach of the degradation of historical oil paintings, which includes the relevant chemical and mechanical processes and their mutual interactions, is of utmost importance in order to better understand the deterioration of artworks, and hence to ensure timely and effective conservation interventions.

Metal soap protrusions in artworks have been identified and analysed by means of images of paint surfaces and paint cross-sections [31, 87], micro-spectroscopic images and chemical analyses [16, 73, 93]. Nonetheless, many details of the underlying mechanisms related to their formation and development are not yet well understood. State-of-the-art research focuses on different chemical aspects, such as the kinetics of the chemical reactions [20, 28, 104], the composition of metal soaps [68, 70] and their crystallisation process [72]. Additional works investigate the influence of environmental conditions and external factors on metal soap formation. In this regard, it has been shown that climate conditions, such as moisture and temperature levels [90], and past conservation treatments done on the painting [13], may accelerate metal soap related degradation phenomena. Finally, the interplay between mechanical and chemical mechanisms promotes the overall degradation of the system: metal soaps may lead to paint cracking and flaking [30]; conversely, the presence of cracks influences the diffusion of chemical species,

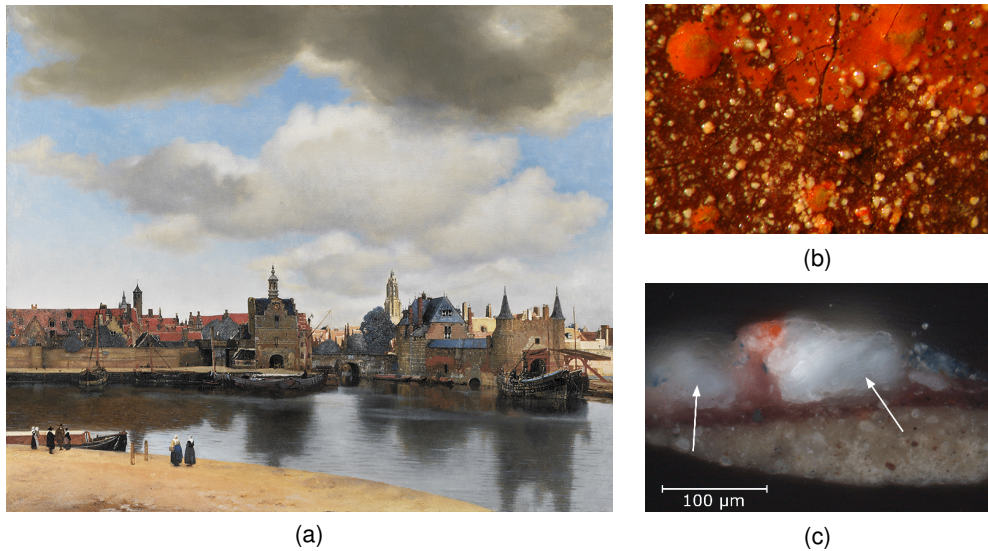


Figure 2.1: (a) Johannes Vermeer, *View of Delft*, ca. 1660–1661, Oil on canvas, 96.5 cm × 115.7 cm, Mauritshuis, The Hague, The Netherlands. (b) Micro-detail of the red-tiled roofs showing whitish globules of lead soaps protruding through the paint surface. (c) A paint cross-section is taken at the left edge of the painting where the green (now blue) bush is painted of the red-tiled roof, showing the formation of large metal soap protrusions in the dark-red paint layer that have erupted through the blue-green surface paint layer, image taken under normal light illumination [166, 167].

which makes the chemo-mechanical degradation of paintings a two-way coupled problem. Despite the vast amount of work on the chemical aspects of the process, predictive models that are able to quantify the extent of chemo-mechanical damage in oil paintings as a function of metal soap formation are currently not available.

This chapter proposes a computational multi-physics approach to model the degradation of historical oil paintings, as induced by metal soap formation and growth. Using a finite element framework, the chemical processes are translated into a diffusion-reaction model, along the lines of [78, 79]. The diffusion-reaction model is formulated in terms of the concentration of saturated fatty acids, which are assumed to be the reference diffusing species. The reaction (sink) term allows to describe the crystallisation and growth processes. For simplicity, in this chapter the intermediate state of amorphous metal soap is neglected, and only the irreversible part of the chemical reaction is simulated. The diffusion-reaction model is coupled with a mechanical model by defining a chemically-induced growth strain, which quantifies the effect of metal soap growth on the stress field generated in the paint system. Additionally, the change in mechanical properties associated to the formation of crystalline metal soap is computed by using a rule of mixtures with respect to the volume fractions of the chemical species. The spatial growth of the metal soap crystal takes place in a small reaction zone at the boundary of the crystal, which is determined using a scanning algorithm that identifies the uncrystallised material points present within a small radial distance of the crystallised material points located nearest to the boundary of the crystal. In addition, to allow for the formation of discrete

cracks in the paint layer at arbitrary locations and under arbitrary directions, cohesive interface elements are placed between all continuum elements discretising the paint layer geometry, in correspondence with the approach originally proposed in [171]. The nucleation and propagation of cracks is prescribed in accordance with the interface damage model proposed in [25], which has proven to be accurate, efficient and numerically robust for various problems characterised by complex fracture events [26, 27, 46, 102]. Furthermore, as part of the coupling between the mechanical and chemical processes, across the crack faces the constitutive relation between the flux of the saturated fatty acid and its concentration is prescribed to be a function of the damage generated in the crack. The numerical update procedure of the two-way coupled chemical and mechanical processes is performed by using a staggered approach. Note that numerical frameworks accounting for complicated multi-physics interactions have been the subject of several recent publications [4, 42, 52, 116, 139, 143, 169]; yet, studies focusing on the coupling of multi-physics behaviour with discrete crack formation are limited, which offers room to the present chapter for discussing modelling aspects that may be considered as advanced from both a physical and a numerical point of view.

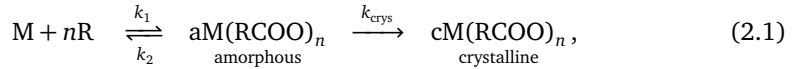
The chapter is organised as follows. The chemical process of metal soap formation is discussed in Section 2.2. Section 2.3 describes the diffusion-reaction model, the mechanical model and the simulation of crack nucleation and propagation. The multi-physics coupling scheme, the geometry, and the material parameters used in the simulations are provided in Section 2.4. In Section 2.5, the results of a reference simulation are discussed. Subsequently, a variation study considering the effect of various material parameters on metal soap degradation is presented. The main conclusions of the study are summarised in Section 2.6, followed by a discussion of future work.

2.2 Chemical process of metal soap formation

Oil paints consist of a drying oil binding medium (typically linseed oil) containing pigment particles, which are often metal salts. The approximate thickness of an individual paint layer varies between 5–150 μm [148], while pigment particles are characterised by an average diameter within the range of 1–25 μm [80]. From a chemical point of view, linseed oil is a triglyceride, composed of three fatty acid molecules bound to a glycerol backbone via an ester bond. While most of the fatty acids chains in a drying oil are unsaturated (i.e. containing one or more C=C bonds), saturated fatty acids (palmitic and stearic acid) represent approximately 5–15% of the total fatty acid content. During oil paint drying, the unsaturated fatty acid chains in the oil binder polymerise, resulting in a densely cross-linked polymer network. On a larger time scale, the ester bond between the fatty acid chains and the glycerol backbone can be broken by hydrolysis reactions, leading to the release of saturated fatty acids as a degradation product. Lead or zinc are present in the common pigments lead white and zinc white, and in several other pigments [80, 88]. Lead and zinc ions that are released from the pigments tend to become complexed with the carboxyl groups (COOH) of the polymer network, forming an ionomer [70, 164]. Either during paint drying or in fully polymerised networks, free saturated fatty acids may react with the metal ions from the ionomer, forming complexes of amorphous metal soaps. Their general chemical formula is $\text{M}(\text{RCOO})_n$, in which M is a metal ion, R is a fatty acid chain and n is the charge number of the metal ion. The formation of amorphous metal soaps is expected to be a reversible process, if it is assumed that the bond between metal ions and the carboxylic acid groups is essentially the same whether they are part of

the ionomer or of a fatty acid [68]. The amorphous metal soaps subsequently crystallise by means of an irreversible chemical reaction into larger aggregates. Crystallisation can only occur when the local concentration of amorphous metal soap becomes sufficiently high. The process is thought to be driven by the alignment of alkyl chains² of the fatty acids into an ordered lattice.

Crystallisation is commonly assumed to proceed by a nucleation process followed by growth of the nuclei. This happens through a diffusion-reaction process that is governed by the diffusion of free saturated fatty acids and metal ions through the paint. The irreversible crystallisation depletes these from the surface of the crystal, creating a concentration gradient that drives further diffusion and therefore the progression of crystallisation [62, 72]. The reactions governing metal soap formation can be summarised as [67]



in which $M + nR$ denotes a metal ion M bound to n fatty acid chains R that are part of the polymer network, $M(\text{RCOO})_n$ is the metal soap complex, k_+ , k_- and k_{crys} are the rate constants for each reaction, and prefixes a and c refer to the amorphous or crystalline state of metal soap. For lead and zinc, $n = 2$. Note that the reaction rates may be affected by conservation treatments (i.e. the presence of solvents [13]) and environmental conditions, in terms of moisture and temperature levels [90], thereby accelerating metal soap formation and growth.

Metal soap crystals may grow in protrusions of diameters up to 500 μm [87]. The growth of these aggregates, which may penetrate through several paint layers, generates mechanical strain (and thus stress) in the system. This may ultimately initiate fracture and delamination, causing flaking of the paint [16]. A schematic representation of the process of metal soap formation described above, and the consequent onset of chemo-mechanical damage, is given in Figure 2.2.

2.3 Chemo-mechanical model

2.3.1 Modelling assumptions

Metal soap formation and crystallisation, as described in Section 2.2, is governed by a complex sequence of chemical processes. In order to simplify the modelling, in this chapter some hypotheses are made. First, it is assumed that the initial state of the domain is represented by an ionomer with a certain concentration of free saturated fatty acids – Figure 2.2(c) –, i.e. the hydrolysis reactions leading to the release of free saturated fatty acids by the oil binder and the formation of the ionomer are not explicitly modelled. Moreover, despite that the oil paint is a multi-phase material consisting of the ionomer with embedded pigment particles, it is here considered as a homogeneous continuum. Accordingly, the individual constituents are not explicitly modelled and the response of the paint is defined in terms of effective chemical and mechanical properties, which implicitly account for the heterogeneous substructure. The free saturated fatty acids and the metal ions, which are characterised by a smaller length scale, enter the model through their concentrations. Next, it is assumed that the metal soap growth process departs from pre-existing crystal nuclei of a small specified size and that the reaction between fatty acids and metal ions takes place in a moving transition region at the interface between

²Hydrocarbon chains missing one hydrogen atom

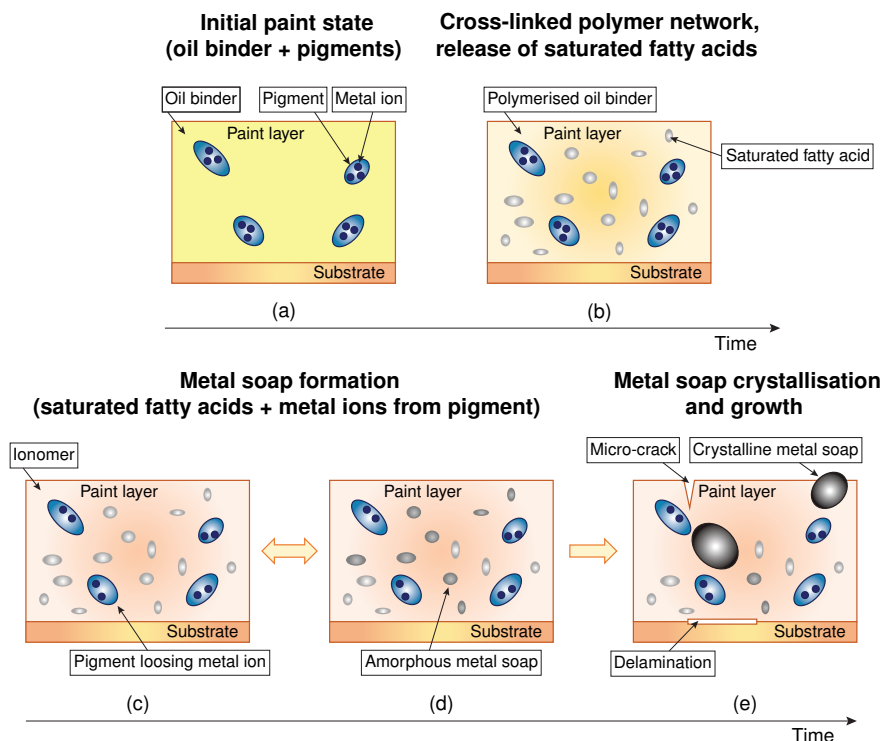
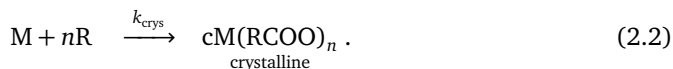


Figure 2.2: Scheme of the processes governing metal soap formation and the onset of chemo-mechanical damage, with the arrows between two process states indicating the reversibility (two arrow heads) and irreversibility (one arrow head) of the process. (a) Initial state: oil binder with embedded pigment particles. (b) The oil binder polymerises into a cross-linked polymer network and releases saturated fatty acids as a degradation product of hydrolysis reactions; (c) Metal ions are released from the pigment particles and become complexed with the polymer network forming an ionomer; (d) Metal ions from the ionomer and saturated fatty acids react, forming amorphous metal soap; (e) Amorphous metal soap crystallises and grows, potentially leading to micro-cracking, delamination and protrusion of metal soap particles through the surface of the paint layer.

these nuclei and the paint. Additionally, once the reaction occurs, for simplicity it is presumed that the corresponding local paint material is entirely transformed into metal soap. In the chemistry community it is a point of debate up to which extent this hypothesis is representative, which will be investigated in more detail in future studies. Further, only the irreversible part of the diffusion-reaction process is modelled, neglecting the intermediate state of amorphous metal soap. It is therefore assumed that once the free saturated fatty acids react with the metal ions, they immediately form crystalline metal soap. This is expected to lead to a faster metal soap formation, but not to influence the final amount of crystallised material to a large extent. The reaction sequence presented in expression (2.1) thus simplifies to:



Relation (2.2) represents a second-order reaction that depends on the amount of fatty acids R and metal ions M , whereby the rate of this reaction is a function of the relative abundance of these species. In the present model, a simplification is made on the stoichiometry of the reaction (2.2), for which equimolar amounts of reacting species are assumed. This implies that the entire amount of fatty acids and metal ions present in the domain is consumed by the reaction. Moreover, despite that in ionomers both the free saturated fatty acids and the metal ions can diffuse [156], metal ion diffusion is not taken into account, as this process indeed is slow compared to fatty acid diffusion. Hence, the free saturated fatty acids are selected as the reference diffusing species, with respect to which the diffusion-reaction model is formulated, whereas the metal ion distribution through the paint medium is considered as uniform. It is noted that the chemistry community currently is investigating up to which extent metal ion diffusion, despite characterised by a relatively low velocity, influences the concentration profiles of the chemical species [8]. This aspect is left out of consideration in this chapter, and may be incorporated in future research. Furthermore, the stress field (typically in terms of the hydrostatic pressure) may have an influence on the kinetic conditions of a chemical reaction, as for instance occurs in the process of Li-ions diffusion in the active particles of Li-ion batteries [117]. In specific, the Arrhenius equation allows for incorporating the effect of pressure on the activation energy for the chemical reaction. Nonetheless, the range of pressures commonly required for generating a significant influence on the activation energy is not reached in the process of metal soap crystallisation. Therefore, it is a valid assumption to ignore the effect of pressure on the kinetics of the chemical process. Finally, the dependence of the reaction kinetics on moisture, temperature, and other external environmental factors is also neglected.

2.3.2 Diffusion-reaction model

In order to describe the growth of the metal soap crystal, in each material point two different volume fractions are distinguished. When denoting the volume fraction of the paint as ϕ_p , with the subscript “p” referring to “paint”, and the volume fraction of the crystalline metal soap as ϕ_s , with the subscript “s” referring to “soap”, and considering that both volume fractions take values between 0 and 1, they should satisfy the constraint equation $\phi_p + \phi_s = 1$. For notational convenience, in the sequel these volume fractions are denoted as $\phi_s = \phi$ and $\phi_p = (1 - \phi)$. In view of the hypotheses made, the formation of metal soaps in the paint system can be described by a diffusion-reaction equation in terms of free saturated fatty acids

$$\frac{\partial c}{\partial t} - \nabla \cdot (D \nabla c) = -S, \quad (2.3)$$

where c is the available concentration of free saturated fatty acids, D is the fatty acid diffusion coefficient and S is a sink term. The symbol ∇ indicates the gradient operator. The sink term S should incorporate the fact that the free saturated fatty acids do not further react once the reaction with metal ions into crystallised metal soap has occurred. Consistently, the sink term is taken to be proportional to the rate of crystallised metal soap formation $\partial \phi / \partial t$ via a constant \mathcal{M} , which represents the molarity of saturated fatty acids in a crystallised metal soap molecule [79],

$$S = \mathcal{M} \frac{\partial \phi}{\partial t}. \quad (2.4)$$

The rate of metal soap formation $\partial\phi/\partial t$ can be assumed to be proportional to the product of the concentration of available free saturated fatty acids and the volume fraction of the paint in which crystallisation has not (yet) occurred. This volume fraction provides a measure of the amount of metal ions that are still available for a reaction. Accordingly, the rate of crystallised metal soap formation can be expressed as

$$\frac{\partial\phi}{\partial t} = \mathcal{R}(1 - \phi)c, \quad (2.5)$$

where \mathcal{R} is a constant of proportionality specifying the reaction rate, which is associated to the rate constant k_{crys} defined in relation (2.2). Note that relation (2.5) expresses the rate at which the metal ions and fatty acids concentrations decrease due to the second-order reaction (2.2), under the assumption of equimolar reactants. Combining finally relations (2.3), (2.4), and (2.5) yields the coupled system of equations

$$\begin{cases} \frac{\partial c}{\partial t} - \nabla \cdot (D\nabla c) = -\mathcal{M}\frac{\partial\phi}{\partial t}, \\ \frac{\partial\phi}{\partial t} = \mathcal{R}(1 - \phi)c. \end{cases} \quad (2.6)$$

The solution of the system of equations (2.6), to be completed with appropriate initial and boundary conditions, describes the evolution of the concentration of the free saturated fatty acids c and the volume fraction of crystallised metal soap ϕ in the painting. Note that, according to these equations, metal soap growth can occur in the domain at any location in which free saturated fatty acids are present, as long as $\phi \neq 1$. However, as discussed in Section 2.2, a set of nuclei is defined *a priori*, i.e. small areas where fully crystallised metal soap is already present ($\phi = 1$) and around which further metal soap crystallisation and growth are allowed. This essentially entails the definition of a reaction zone of finite thickness around the nuclei. The reaction zone is a transition region, in which both free saturated fatty acid and crystallised metal soaps are present ($0 < \phi < 1$) and where the diffusion-reaction process is governed by Equation (2.6). The thickness of the reaction zone is set via a scanning algorithm (schematically illustrated in Figure 2.3), which identifies the uncrystallised material (integration) points present within a small, prescribed radial distance of the crystallised material points located nearest to the current boundary of the crystal. In the remainder of the domain, where $\phi = 0$ or $\phi = 1$, it is assumed that only diffusion takes place, i.e. the evolution of saturated fatty acid concentration is described by Equation (2.3), whereby the reaction term S is set to zero.

2.3.3 Mechanical model

In accordance with the diffusion-reaction process described in Section 2.3.2, in the paint system two material phases can be distinguished – the paint and the fully crystallised metal soap – that are separated by a narrow interfacial transition zone in which the chemical reaction occurs. For an arbitrary material point in the domain ($0 \leq \phi \leq 1$, with ϕ being the volume fraction of the crystallised metal soap), the total strain tensor $\boldsymbol{\varepsilon}$ can be written as the sum of the elastic strain tensor $\boldsymbol{\varepsilon}^e$ and a growth strain tensor $\boldsymbol{\varepsilon}^g$:

$$\boldsymbol{\varepsilon} = \boldsymbol{\varepsilon}^e + \boldsymbol{\varepsilon}^g. \quad (2.7)$$

The growth strain tensor $\boldsymbol{\varepsilon}^g$ represents the effect of the volumetric expansion of the material due to metal soap formation [16], and is here defined as

$$\boldsymbol{\varepsilon}^g = \phi \boldsymbol{\varepsilon}^g \mathbf{I}, \quad (2.8)$$

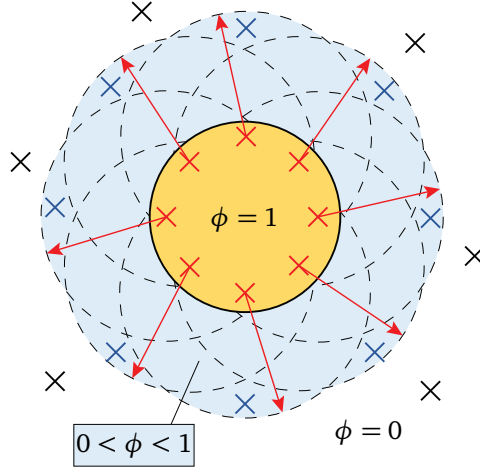


Figure 2.3: Principle of the scanning algorithm used for constructing the reaction zone (in which $0 < \phi < 1$). This is done by identifying the material points (blue crosses in the light blue region) that fall within a prescribed radial distance (indicated by the red arrows) from the fully crystallised material points ($\phi = 1$) at the boundary of the metal soap crystal (red crosses in the yellow region). The black crosses in the white region denote yet unreacted material points ($\phi = 0$).

with ε^g the growth strain associated to the formation of crystalline metal soap and I the second-order identity tensor. For the material points in the paint phase ($\phi = 0$), the growth strain given by Equation (2.8) is equal to zero, by which the total strain given by Equation (2.7) reduces to the elastic strain, i.e.

$$\varepsilon_p = \varepsilon_p^e. \quad (2.9)$$

Conversely, for the material points in the fully crystallised metal soap phase ($\phi = 1$), the growth strain obtains its maximum value, which, with Equations (2.7) and (2.8), leads to:

$$\varepsilon_s = \varepsilon_s^e + \varepsilon_s^g, \quad \text{with} \quad \varepsilon_s^g = \varepsilon^g I. \quad (2.10)$$

Finally, for the material points in the interfacial reaction zone, where the paint and the metal soap phases are present at the same time ($0 < \phi < 1$), the total strain ε_{rz} , with the subscript “rz” referring to “reaction zone”, is taken identical for both phases, i.e. Voigt’s assumption is used. In accordance with Equations (2.7) and (2.8), the strain ε_{rz} is given by:

$$\varepsilon_{rz} = \varepsilon_{rz}^e + \varepsilon_{rz}^g, \quad \text{with} \quad \varepsilon_{rz}^g = \phi \varepsilon^g I. \quad (2.11)$$

In correspondence with the above representation, an assumption on the constitutive response of the paint and metal soap materials needs to be made. The mechanical behaviour of oil paint films is governed by the interaction between the oil binder material and the embedded pigments. Depending on the nature of the pigments, a large variability in the mechanical response has been observed, reflected by stress-strain diagrams ranging from

elastic to visco-elasto-plastic [50]. Moreover, no information is available on the mechanical stress-strain behaviour of crystalline metal soaps. Hence, as a working assumption an isotropic linear elastic model is assumed for the “bulk response” of both the crystalline metal soap and the paint, i.e.

$$\boldsymbol{\sigma}_s = {}^4\mathbf{C}_s : \boldsymbol{\varepsilon}^e \quad \text{and} \quad \boldsymbol{\sigma}_p = {}^4\mathbf{C}_p : \boldsymbol{\varepsilon}^e, \quad (2.12)$$

with $\boldsymbol{\sigma}_s$ and $\boldsymbol{\sigma}_p$ representing the stresses in the crystalline metal soap and the paint material, respectively. The fourth-order tensors ${}^4\mathbf{C}_s$ and ${}^4\mathbf{C}_p$ reflect the corresponding isotropic linear elastic stiffness tensors, which are characterised by the values of the elastic modulus and the Poisson’s ratio of the materials. Note that Equations (2.7) and (2.12) provide a coupling between the chemical process of metal soap formation and the associated stress state. Consistent with Voigt’s assumption given by Equation (2.11), the effective Cauchy stress $\boldsymbol{\sigma}_{rz}$ in the reaction zone is calculated in accordance with a rule of mixtures, as the volume average of the stresses of the individual constituents:

$$\boldsymbol{\sigma}_{rz} = \phi \boldsymbol{\sigma}_s + (1 - \phi) \boldsymbol{\sigma}_p, \quad \text{with} \quad 0 < \phi < 1. \quad (2.13)$$

Finally, in any point of the domain ($0 \leq \phi \leq 1$), in the absence of body forces the response of the material is governed by the mechanical equilibrium condition

$$\nabla \cdot \boldsymbol{\sigma} = \mathbf{0}, \quad (2.14)$$

to be completed with the constitutive specifications (2.12) and (2.13) and the appropriate boundary conditions.

2.3.4 Crack nucleation and propagation

Equations (2.6) and (2.14) govern the processes of metal soap formation and mechanical equilibrium of the paint system. According to Equation (2.7), the growth of the metal soap crystal introduces mechanical strain in the domain, which may trigger the formation of cracks. With the aid of the finite element method (FEM), the nucleation and propagation of discrete cracks is simulated using the interface damage model presented in [25], which has proven to provide accurate and numerically robust results in various applications, see e.g. [26, 27, 46, 102]. As demonstrated in these references, this interface damage model can be used to describe cracking processes in bulk materials as well as along bi-material interfaces. A unique feature of this interface damage model is that the formulation of the mode-mixity is consistently derived from an energy criterion commonly applied in linear elastic fracture mechanics. In addition, the kinetic law describing the evolution of the damage process is taken as rate-dependent, which helps to avoid numerical convergence problems induced by crack bifurcations. In order to allow for the formation of arbitrary, complex cracking patterns in the paint layer configuration, interface elements equipped with the interface damage model are placed between all continuum elements modelling the “bulk response” of the paint material and the crystallised metal soap, in accordance with the approach originally proposed in [171]. The main advantages of this approach are that: *i*) the nucleation and growth of cracks are fully determined by the interaction between existing cracks and the corresponding stress distribution in the surrounding bulk material, and *ii*) branching and coalescence of cracks emerge as a natural outcome of the simulation, without the need for additional selection criteria. A disadvantage of the method is that the chosen spatial discretisation of the actual boundary value problem may have an influence on the location and direction of

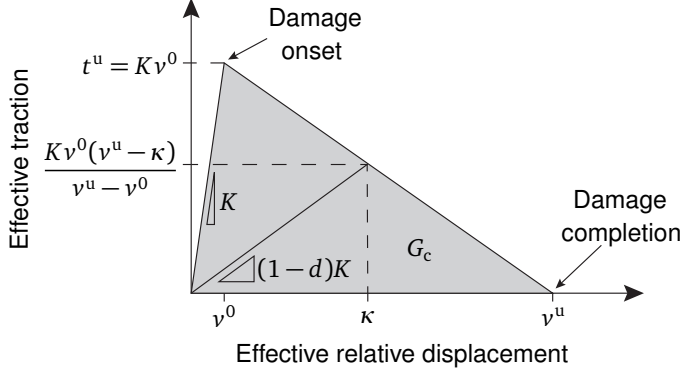


Figure 2.4: Traction-separation law taken from [25].

the cracking path. However, as demonstrated in the mesh refinement study performed in [26], this effect can be kept small by choosing a sufficiently fine finite element mesh, whereby it should be noted that the mesh fineness is bounded by a maximum in order to limit artificial response contributions related to the use of an elastic interfacial stiffness in the traction-separation law. For completeness, the main features of the interface damage model presented in [25] are reviewed below.

In a two-dimensional domain, the constitutive relation between the traction $\mathbf{t} = (t_1, t_2)$ and the displacement jump $\mathbf{v} = (v_1, v_2)$ at an interface, with subscripts 1 and 2 indicating the normal and shear components, respectively, can be written as

$$t_i = (1-d)K\delta_{ij}v_j - dK\delta_{ij}\delta_{1j}\langle -v_1 \rangle \quad \text{with } i, j \in \{1, 2\}, \quad (2.15)$$

where K represents the elastic interfacial stiffness and δ_{ij} is the Kronecker delta symbol. The values of the damage parameter d are bounded as $0 \leq d \leq 1$, where $d = 0$ represents an undamaged material point, while $d = 1$ reflects a fully damaged material point. The second term in the right-hand side of Equation (2.15) prevents penetration of two opposite crack faces in the normal direction of the interface; in specific, the Macauley brackets $\langle \cdot \rangle$, defined as $\langle x \rangle = \frac{1}{2}(x + |x|)$, guarantee that for a negative normal displacement jump v_1 the crack faces are considered to be in contact, and thus interact elastically.

During a loading process, the damage in an interfacial material point evolves with deformation, $d = \hat{d}(\kappa)$, where κ is a deformation history variable that monotonically increases (since damage is an irreversible process). The specific form of $\hat{d}(\kappa)$ can be derived from the shape of the softening curve of the traction-separation law. In the present study, a linear softening law is adopted, see Figure 2.4, where the onset of damage relates to $\kappa = v^0$ (in accordance with $d = 0$) and the completion of damage is reflected by $\kappa = v^u$ (in correspondence with $d = 1$), where v^0 and v^u are equivalent crack face displacements at which damage is initiated and completed, respectively. Figure 2.4 illustrates that for a specific value of κ the effective traction equals $Kv^0(v^u - \kappa)/(v^u - v^0)$, or, alternatively, in terms of the damage parameter d , is given by $(1-d)K\kappa$. From equating these two expressions, the damage parameter follows as

$$d = \hat{d}(\kappa) = \frac{v^u(\kappa - v^0)}{\kappa(v^u - v^0)}. \quad (2.16)$$

The damage parameter is assumed to evolve in accordance with a rate-dependent description, in analogy to the formulation of the plastic strain rate used in the well-known viscoplastic model of Perzyna [61, 134]:

$$\dot{d} = \begin{cases} \frac{\hat{F}(\lambda, \kappa)}{\eta} & \text{for } \lambda \geq \kappa \quad \text{and} \quad v^0 \leq \kappa \leq v^u \\ 0 & \text{for } 0 \leq \lambda \quad \text{or} \quad \kappa = v^u \end{cases}. \quad (2.17)$$

Here, $\hat{F}(\lambda, \kappa)$ is the damage loading function, which depends on the history variable κ and on a deformation measure λ , calculated as the Euclidean norm of the vector of relative crack face displacements, i.e. $\lambda = \|\mathbf{v}\| = \sqrt{v_1^2 + v_2^2}$. Additionally, η is a relaxation parameter with dimension of time. The damage loading function can be expressed as

$$\hat{F}(\lambda, \kappa) = \hat{f}(\lambda) - \hat{d}(\kappa) = \frac{v^u(\lambda - v^0)}{\lambda(v^u - v^0)} - \frac{v^u(\kappa - v^0)}{\kappa(v^u - v^0)}, \quad (2.18)$$

where the final expression in the right-hand side is obtained by inserting Equation (2.16) for $\hat{d}(\kappa)$, and choosing the form of $\hat{f}(\lambda)$ similar to that for $\hat{d}(\kappa)$. From Equation (2.17), it can be observed that in the limit of the relaxation parameter going to zero, $\eta \rightarrow 0$, the rate-independent loading function, $\hat{F}(\lambda, \kappa) = 0$, is recovered, which, as Equation (2.18) shows, corresponds to $\lambda = \kappa$. Note that Equation (2.17)₁ determines the rate of damage when the effective deformation λ exceeds the history variable κ . Equation (2.17)₂ sets the rate of damage to zero in case the threshold value for damage nucleation has not (yet) been reached, in case of unloading, or when damage has completed.

Finally, considering that cracks may develop under arbitrary mode-mixity, the equivalent relative crack face displacements v^0 and v^u must be made dependent on the ratio between the relative normal and the shear interface displacements. This is accounted for by introducing a mode-mixity parameter β [25, 157]:

$$\beta = \frac{|v_2|}{|v_2| + \langle v_1 \rangle}. \quad (2.19)$$

Note that in the above expression pure mode I fracture corresponds to $v_2 = 0$ and thus $\beta = 0$, while pure mode II fracture relates to $v_1 = 0$ and thus $\beta = 1$. Accordingly, mixed-mode fracture is bounded by $0 < \beta < 1$. Adopting a well-known energy-based failure criterion from linear elastic fracture mechanics, which relates the energy release rates G_I and G_{II} to the fracture toughnesses $G_{I,c}$ and $G_{II,c}$ under pure mode I and mode II loading conditions as

$$\frac{G_I}{G_{I,c}} + \frac{G_{II}}{G_{II,c}} = 1, \quad (2.20)$$

the specific expressions for the functions $v^0 = \hat{v}^0(\beta)$ and $v^u = \hat{v}^u(\beta)$ become [25]

$$v^0 = \hat{v}^0(\beta) = v_1^0 v_2^0 \sqrt{\frac{1 + 2\beta^2 - 2\beta}{(\beta v_1^0)^2 + ((1 - \beta)v_2^0)^2}} \quad (2.21)$$

$$v^u = \hat{v}^u(\beta) = \frac{2(1 + 2\beta^2 - 2\beta)}{K v^0} \left[\left(\frac{(1 - \beta)^2}{G_{I,c}} \right) + \left(\frac{\beta^2}{G_{II,c}} \right) \right]^{-1}. \quad (2.22)$$

Here, $v_1^0 = t_1^u/K$ and $v_2^0 = t_2^u/K$ are the displacements at which damage initiates under pure mode I and pure mode II loading conditions, respectively, with t_1^u and t_2^u the ultimate normal and shear tractions. For more details on the above model and its numerical implementation, the reader is referred to [25].

Equations (2.15)–(2.22) thus describe crack development in the paint medium, triggered by metal soap formation. Conversely, the appearance of cracks hampers the diffusion of free saturated fatty acids across crack surfaces, which makes the chemo-mechanical degradation of paintings a two-way coupled problem. In order to account for the latter effect, the concentration of the free fatty acid across a discrete crack is assumed to be discontinuous and the flux is assumed to be continuous, in analogy with the adiabatic cracking assumption typically made in the modelling of thermo-mechanical problems [1, 58]. Hence, the jump in fatty acid concentration across a crack is denoted as $[[c]]$, while the corresponding mass flux across the crack reads $q = \mathbf{q} \cdot \mathbf{n}$, with \mathbf{q} the mass flux vector and \mathbf{n} the unit vector normal to the crack faces. With these quantities, the constitutive relation between the fatty acid flux and the jump in concentration across a crack is given by

$$q = \mathcal{D}_c [[c]], \quad (2.23)$$

where the parameter \mathcal{D}_c is the diffusion coefficient at the crack. It is assumed that \mathcal{D}_c evolves from the diffusion coefficient \mathcal{D} of the intact paint material as a function of the damage d , in a similar fashion as the interfacial stiffness in the traction-separation law, Equation (2.15), i.e.

$$\mathcal{D}_c = (1 - d)\mathcal{D}, \quad (2.24)$$

with the evolution of the damage parameter thus prescribed by relations (2.16)–(2.17).

2.4 Numerical simulations

2.4.1 Multi-physics coupling

The above-described two-way coupling effects between the mechanical and chemical fields are accounted for using the staggered approach summarised in Table 2.1. In this approach the chemical and mechanical fields are analysed sequentially, with the couplings being established via temporal extrapolation. It has been confirmed that, by choosing a sufficiently small time increment, the error introduced in the temporal extrapolation becomes rather small, such that it has a negligible effect on the numerical result. In accordance with an incremental-iterative time-marching scheme, at each time step the diffusion-reaction analysis defined by the system of equations (2.6) is performed first, whereby the flux of free saturated fatty acid across cracks is determined through Equations (2.23) and (2.24), based on the damage parameter d at the previous time increment. This provides the values of the concentration c of free saturated fatty acid and the volume fraction ϕ of the crystallised metal soap in the modelled paint configuration. The formation of crystallised metal soap (for $0 < \phi \leq 1$) leads to the development of the growth strain in accordance with expression (2.8), which, together with the updated volume fraction of the crystallised metal soap, are transferred to the mechanical analysis. The growth strain and metal soap volume fraction lead to the updated stress field in correspondence with Equations (2.8) to (2.13). As a next step, the equilibrium equations (2.14) are solved in an iterative fashion in order to account for cracking, which occurs if at a specific location within the domain the fracture criterion defined by Equations (2.16) and (2.17) is met. Accordingly, the damage parameter is updated and provided as input

1. Diffusion-reaction model.

1.1 Initialise diffusion-reaction simulation.

1.1.A If time increment $i = 0$. Apply initial conditions for the diffusion-reaction model.

1.1.B If time increment $i \geq 1$. Apply boundary conditions for the diffusion-reaction model.

1.2 Solve system of equations (2.6). The flux of free saturated fatty acid across cracks is determined through Equations (2.23) and (2.24), based on the damage parameter d at the previous time increment. Obtain the values of concentration c of free fatty acids and volume fraction ϕ of crystalline metal soap.

1.3 Transfer the value of the volume fraction ϕ of crystalline metal soap to the mechanical analysis.

2. Mechanical model.

2.1 Apply boundary conditions for the mechanical model.

2.2 Calculate the growth strain ε^g from relation (2.8) and the stress field in the reaction zone from Equation (2.13), as a function of the volume fraction ϕ of crystallised metal soap.

2.3 Solve equilibrium equations (2.14) accounting for possible cracking within the paint domain, using relations (2.16)–(2.17) defining the fracture criterion. Obtain the displacement field u and the damage parameter d .

2.4 Transfer the damage parameter d to the diffusion-reaction analysis.

2.5 Return to 1.1.B.

Table 2.1: Schematic representation of the staggered approach used in the incremental-iterative update procedure.

for the diffusion-reaction analysis in the next time increment. Subsequently, the sequential solution procedure above is repeated for this new time increment.

With the aid of the commercial finite element program ABAQUS Standard³, the paint layer configuration is discretised with continuum elements, whose behaviour is defined by the set of relations (2.3)–(2.14). The constitutive response of the interface elements placed between these continuum elements is governed by the discrete, mixed-mode fracture law (2.15) and by the flux-concentration relation (2.23), which are incorporated in the FEM framework by means of user-defined material routines.

2.4.2 Material parameters

The material parameters adopted for the diffusion-reaction model and the mechanical model are listed in Tables 2.2 and 2.3, respectively. Most of these material properties were taken from the literature. The parameters for which experimental data are not available are estimated by means of engineering judgement, and are subsequently varied over a range that presumably should cover the behaviour of the real paint material. Accordingly, a reference simulation based on the initial set of parameters is discussed in Section 2.5.1,

³Dassault Systems Simulia Corp, Providence, RI, U.S.A.

and the influence of parameter variations on the numerical results is presented in Section 2.5.2.

Note that the modelling approach is general and is able to capture the formation of metal soaps for different types of saturated fatty acids (e.g. palmitic or stearic) and metal pigments (e.g. lead or zinc). The formation of crystalline lead soaps is generally a faster process than that of zinc soaps [68, 72]. The latter process requires a larger structural reordering to form a crystal, and therefore often remains trapped in an amorphous state. As a consequence, zinc soaps form relatively small crystalline aggregates of an average diameter of 10 μm [72]. Conversely, lead soaps develop into isolated particles of large size, with diameters ranging between 50 and 500 μm (with common ranges of 100–200 μm) [87], which obviously have a stronger effect on the structural integrity of the paint medium. For this reason, reference is made here to lead-based pigment particles, which, in combination with a stearic acid ($\text{C}_{18}\text{H}_{35}\text{O}_2$), are expected to form a large lead stearate protrusion, $\text{Pb}(\text{C}_{18}\text{H}_{35}\text{O}_2)_2$. In the numerical examples, this process is analysed by considering a single metal soap crystal embedded halfway the thickness of a paint layer, see Section 2.4.3.

The molarity \mathcal{M} is obtained as the ratio between the volumetric weight of lead stearate and the molecular weight of the stearic acid confined into lead stearate. The volumetric weight of lead stearate and the molecular weight of stearic acid are 1400 kg/m^3 and 0.2835 kg/mol , respectively [98]. Considering that lead stearate contains two stearic acid chains, this yields a molarity $\mathcal{M} = 2470 \text{ mol}/\text{m}^3$. The diffusion coefficient of stearic acid in the paint is taken as $\mathcal{D} = 3.6 \cdot 10^{-11} \text{ m}^2/\text{s}$ and the reaction rate is $\mathcal{R} = 4.2 \cdot 10^{-1} \text{ m}^3/(\text{mol s})$ [67]. As a working assumption, the stearic acid is allowed to diffuse in the metal soap crystal, whereby the diffusion coefficient is taken the same as in the surrounding paint matrix. The validity of this hypothesis currently is an open research question in the chemistry community.

Parameter	Value	Unit
Molarity \mathcal{M}	2470	mol/m^3
Diffusion coefficient \mathcal{D}	$3.6 \cdot 10^{-11}$	m^2/s
Reaction rate \mathcal{R}	$4.2 \cdot 10^{-1}$	$\text{m}^3/(\text{mol s})$

Table 2.2: Material parameters for the diffusion-reaction model.

As explained, the coupling between the chemical and the mechanical processes partly takes place through the development of a growth strain associated to metal soap formation. Experimental values of this parameter are not presented in the literature; hence, a reference value for the growth strain is chosen as $\varepsilon^g = 0.1$. The elastic modulus and Poisson's ratio of the paint, used in expression (2.12), are taken as $E_p = 115 \text{ MPa}$ and $\nu_p = 0.3$, respectively [50]. No experimental information on the elastic properties of the crystallised metal soap is currently available in the literature. As a working assumption, in the reference simulation the elastic properties of the metal soap crystal E_s are assumed to be equal to that of the binder material, i.e. $E_s = 115 \text{ MPa}$ and $\nu_s = 0.3$. The fracture properties of the paint and crystallised metal soap are estimated from the stress-strain diagrams reported in [50], leading to an ultimate tensile strength of $t_1^u = 2.2 \text{ MPa}$ and a fracture toughness of $G_{1,c} = 0.418 \text{ N}/\text{mm}$. The fracture processes within the paint layer may be expected to be dominated by mode I cracking; hence, the fracture properties in mode II only have a minor influence on the computational results, and for simplicity are

taken equal to those in mode I ($t_1^u = t_2^u = t^u$, $G_{I,c} = G_{II,c} = G_c$). Note from Figure 2.4 that the ultimate separation v^u of the crack can be determined from the strength and toughness properties as $v^u = 2G_c/t^u$. The elastic stiffness of the interface elements is chosen relatively high, $K = 10^6 \text{ N/mm}^3$, to ensure that the elastic response of the paint configuration is virtually determined by the elastic response of the adjacent continuum elements. Finally, the relaxation parameter describing the evolution of damage via expression (2.17) is chosen as $\eta = 2 \cdot 10^{-3} \text{ s}$. It has been confirmed that this value is sufficiently small for the fracture response to closely approach the rate-independent fracture limit.

Parameter	Value	Unit
Continuum model		
Growth strain ε^g	0.1	–
Elastic modulus paint medium E_p	115	MPa
Poisson's ratio paint medium ν_p	0.3	–
Elastic modulus crystallised metal soap E_s	115	MPa
Poisson's ratio crystallised metal soap ν_s	0.3	–
Interface damage model		
Fracture strength $t^u (= t_1^u = t_2^u)$	2.2	MPa
Fracture toughness $G_c (= G_{I,c} = G_{II,c})$	0.418	N/mm
Interface elastic stiffness K	10^6	N/mm ³
Relaxation parameter η	$2 \cdot 10^{-3}$	s

Table 2.3: Material parameters for the mechanical model.

2.4.3 Geometry, initial conditions, and boundary conditions

In the FEM simulations the paint layer is modelled as a rectangular domain of size $l \times 2l$, with the thickness as $l = 15 \text{ }\mu\text{m}$, see Figure 2.5. The thickness is chosen to be in the range of typical paint layer sizes applied in historical paintings [148]. At the centre of the paint layer, a single, small nucleus of crystallised metal soap is assumed to be initially present, around which further metal soap crystallisation may develop as a result of a diffusion-reaction process between metal ions and free fatty acid. The shape of the nucleus is taken as circular, with an initial radius $r_0 = l/10 = 1.5 \text{ }\mu\text{m}$. Due to symmetry of the problem, only half of the domain is modelled. The domain is discretised using 6420 continuum elements. For the mechanical analysis 6-node plane-stress isoparametric elements with a 3-point Gauss quadrature are used, while for the diffusion-reaction analysis 3-node isoparametric elements with a 3-point Gauss quadrature are adopted. It should be noted that the in-plane chemo-mechanical response computed under plane-stress conditions translates to that under plane-strain conditions when taking common values for the representative stiffness moduli E_i^* and ν_i^* of the paint ($i = p$) and metal soap ($i = s$), and for the chemical growth strain, ε^{g*} , in accordance with the definitions

$$E_i^* = E_i, \quad \nu_i^* = \nu_i, \quad \varepsilon^{g*} = \varepsilon^g, \quad \text{for plane-stress conditions,} \quad (2.25)$$

and

$$E_i^* = \frac{E_i}{1 - \nu_i^2}, \quad \nu_i^* = \frac{\nu_i}{1 - \nu_i}, \quad \varepsilon^{g*} = (1 + \nu_s)\varepsilon^g, \quad \text{for plane-strain conditions.} \quad (2.26)$$

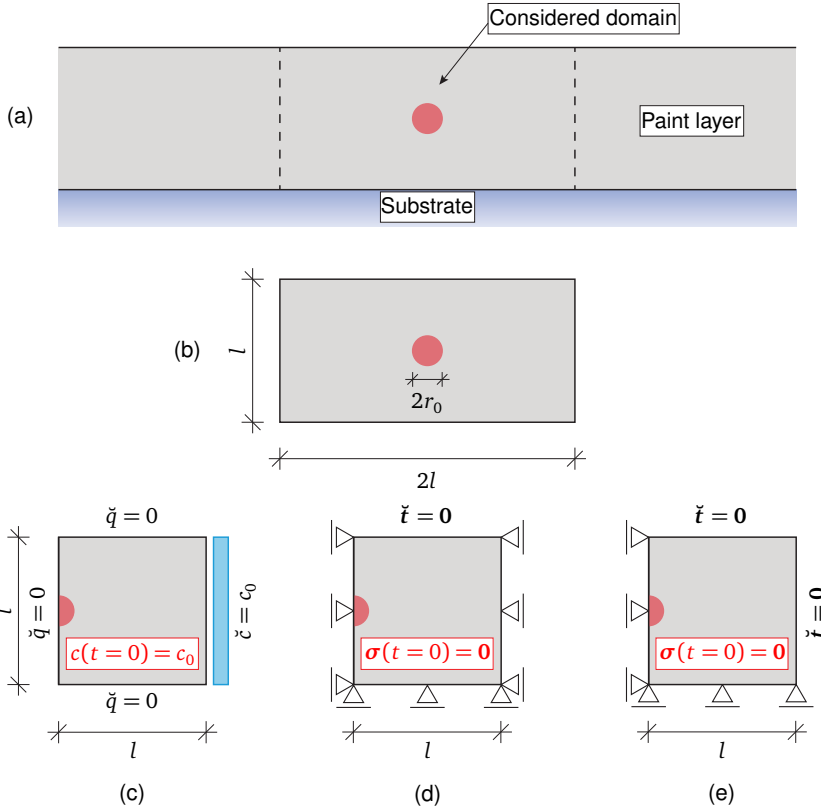


Figure 2.5: (a) Paint system. (b) Section of the paint layer with thickness l and length $2l$, containing a small crystalline metal soap nucleus of radius $r_0 = l/10$. Due to symmetry, only half of the paint section is modelled. (c) Initial and boundary conditions in the diffusion-reaction analysis. (d)–(e) Initial and boundary conditions in the mechanical analysis, considering both (d) zero horizontal displacement at the right boundary (*constrained* boundary), and (e) a traction-free boundary condition at the right boundary (*unconstrained* boundary).

Furthermore, the interface elements describing the fracture process are placed between all continuum elements by using a dedicated Python script that shrinks all the original continuum elements by 1%, detects the opposing element edges, and places the interface elements in between. This procedure provides the finite element mesh with a total of 9531 interface elements. For the mechanical analysis 6-node interface elements with a 3-point Lobatto quadrature are employed, and for the diffusion-reaction analysis 4-node elements with a 2-point Gauss quadrature are applied. The former element formulation was not available in the commercial version of ABAQUS Standard, and therefore was incorporated by means of a user-defined element routine, following the numerical implementation presented in [145]. An initial comparison study not presented here indicated that the use of 6-node interface elements for the mechanical analysis was necessary to avoid the appearance of checker-board patterns in the stress field described by the adjacent continuum elements. It has been further confirmed that the finite element discretisation used in the simulations is sufficiently fine to have a negligible influence on the

discrete fracture patterns generated.

For the diffusion-reaction analysis, the following initial and boundary conditions are used. The initial concentration of the free saturated fatty acids c_0 is taken to be uniform throughout the entire domain. Assuming the presence of stearic acid and lead based pigments, the value of c_0 is estimated by dividing the volumetric weight of the fatty acid in the oil binder by its molecular weight. The volumetric weight of fatty acid is calculated by multiplying the volumetric percentage of linseed oil in a lead white paint (=55.6%, see [50]) with its volumetric weight (= 930 kg/m³, see [2]), and subsequently with the weight percentage of stearic acid in linseed oil (5%). Using the fact that the molecular weight of the stearic acid is 0.2835 kg/mol [2], its concentration becomes $c_0 = 91 \text{ mol/m}^3$. This value for the initial concentration is further prescribed at the right boundary of the domain ($\tilde{c} = c_0$). At the left boundary of the domain a zero-flux boundary condition ($\tilde{q} = 0$) is adopted, which accounts for the symmetry of the problem. This boundary condition is also used at the lower boundary of the domain, thereby reflecting that the diffusion of fatty acid remains constrained to the paint layer and does not penetrate the (canvas or wooden) substrate. At the upper boundary of the domain a zero-flux boundary condition applies. The small radial distance used for defining a reaction zone from the integration points nearest to the boundary of the crystalline metal soap is set equal to 0.2 μm . Note that the size of the reaction zone is 7.5 times smaller than the initial radius $r_0 = 1.5 \mu\text{m}$ of the metal soap nucleus, and further is 75 times smaller than the thickness $l = 15 \mu\text{m}$ of the paint layer; hence, it has a negligible influence on the computational results.

In the mechanical analysis, the paint is initially considered to be stress-free. The vertical displacement at the lower boundary of the domain is prescribed to be zero, thereby mimicking the constraining effect of the paint substrate. At the upper boundary of the domain the normal and tangential tractions are set to zero ($\tilde{\mathbf{t}} = \mathbf{0}$). The horizontal displacement at the left boundary is prescribed to be zero to account for the symmetry of the problem. At the right boundary two types of boundary conditions are successively considered, namely *i*) a constrained horizontal displacement and *ii*) traction-free boundary conditions. These two boundary conditions will be referred to as the *constrained* and *unconstrained* horizontal boundary displacements, and act as upper and lower limits for the (arbitrary) horizontal constraining effects generated in *in situ* paint layers. Note that in the unconstrained case the paint layer can freely glide along the boundary with the substrate, thus reflecting a frictionless contact condition. The influence of these boundary conditions on the chemo-mechanical response will be explored in detail in Section 2.5.1.

2.5 Numerical results

For generality, it is convenient to present the numerical results in terms of dimensionless parameters. To this aim, the dimensionless time variable $\bar{t} = tD/l^2$ is introduced for analysing the evolution of the chemical and mechanical processes. Since cracking in the paint material is dominated by mode I, the maximal opening of the most prominent crack in the simulated domain is quantified in terms of its normal component v_1 , which in its dimensionless form becomes $\bar{v}_1 = v_1/l$, with l being the thickness of the paint layer. Further, r is the average radius of the formed metal soap crystal, which in its dimensionless form becomes $\bar{r} = r/l$. In addition, following [46, 132, 151, 158], the fracture process

can be characterised by introducing a fracture length scale:

$$l_f = \frac{G_c E_p}{(t^u)^2}. \quad (2.27)$$

This fracture length scale may be interpreted as a measure for the cohesive zone at the crack tip, although in general it is not equal to it. The fracture length scale is normalised by dividing it by the thickness of the paint layer, $\bar{l}_f = l_f/l$, which allows for considering the relative importance of toughness and strength on the fracture response at the scale of observation l . In specific, in the limit of the strength at the crack tip going to infinity, $t^u \rightarrow \infty$, the normalised fracture length scale becomes $\bar{l}_f \rightarrow 0$, and fracture is controlled by toughness. Conversely, in the limit of the toughness going to infinity, $G_c \rightarrow \infty$, the normalised fracture length scale becomes $\bar{l}_f \rightarrow \infty$, and fracture is controlled by strength. In the intermediate range, both toughness and strength have an influence on the fracture process. In the parameter variation study performed in Section 2.5.2, the time evolutions of the crack opening \bar{v}_1 and the radius of the metal soap \bar{r} will be investigated as a function of six dimensionless parameters, which are the normalised initial radius of the metal soap crystal, r_0/l , the stiffness mismatch between the metal soap and paint materials, E_s/E_p , the normalised fracture length scale, \bar{l}_f , the growth strain, ε^g , the dimensionless reaction rate, $\bar{\mathcal{R}} = \mathcal{R}/(Dl)$, and the difference in the Poisson's ratios of the paint material, ν_p , and the metal soap, ν_s . Other dimensionless parameters are kept fixed, which are the dimensionless molarity, $\bar{\mathcal{M}} = \mathcal{M}l^3$, the dimensionless fracture strength, $\bar{t}^u = t^u/E_p$, and the dimensionless concentration initially present within the paint system and, throughout the process, applied at the right boundary, $\bar{c}_0 = c_0l^3$.

2.5.1 Reference model

The reference model is based on the geometry discussed in Section 2.4.3 and on the material properties given in Tables 2.2 and 2.3. Accordingly, the dimensionless parameters introduced above become: $r_0/l = 0.1$, $E_s/E_p = 1$, $\nu_s = \nu_p = 0.3$, $\bar{l}_f = 6.62 \cdot 10^2$, $\varepsilon^g = 0.1$ and $\bar{\mathcal{R}} = 7.8 \cdot 10^{14}$. Further, $\bar{\mathcal{M}} = 8.33 \cdot 10^{-12}$, $\bar{t}^u = 0.019$ and $\bar{c}_0 = 3.07 \cdot 10^{-13}$ (mol).

The deformed configuration of the paint layer (plotted on true scale) is shown in Figure 2.6 for different values of the dimensionless time \bar{t} , illustrating the progressive growth of the metal soap crystal and the induced fracturing of the paint. The left and right columns of Figure 2.6 refer to domains with constrained – as in Figure 2.5(d) – and unconstrained – as in Figure 2.5(e) – horizontal displacements at the right boundary, respectively. The contour plot variable indicates the volume fraction ϕ of crystallised metal soap. The red and blue colours denote fully crystallised metal soap ($\phi = 1$) and the original paint material ($\phi = 0$), respectively. The small reaction zone, with $0 < \phi < 1$, defines the transition between the crystalline metal soap and the paint material. As the metal soap crystal grows, close to the surface the paint layer experiences a significant upward deformation in order to accommodate for the volumetric growth of the metal soap crystal, see Figure 2.6(d). This behaviour is qualitatively similar to that obtained from experimental cross-sectional observations on metal soap formation, as, for example, shown in Figure 2.1(c).

Figures 2.7(a) and (b) illustrate the growth of the metal soap crystal along the horizontal line A–A' and along the vertical line B–B', respectively. The growth is measured

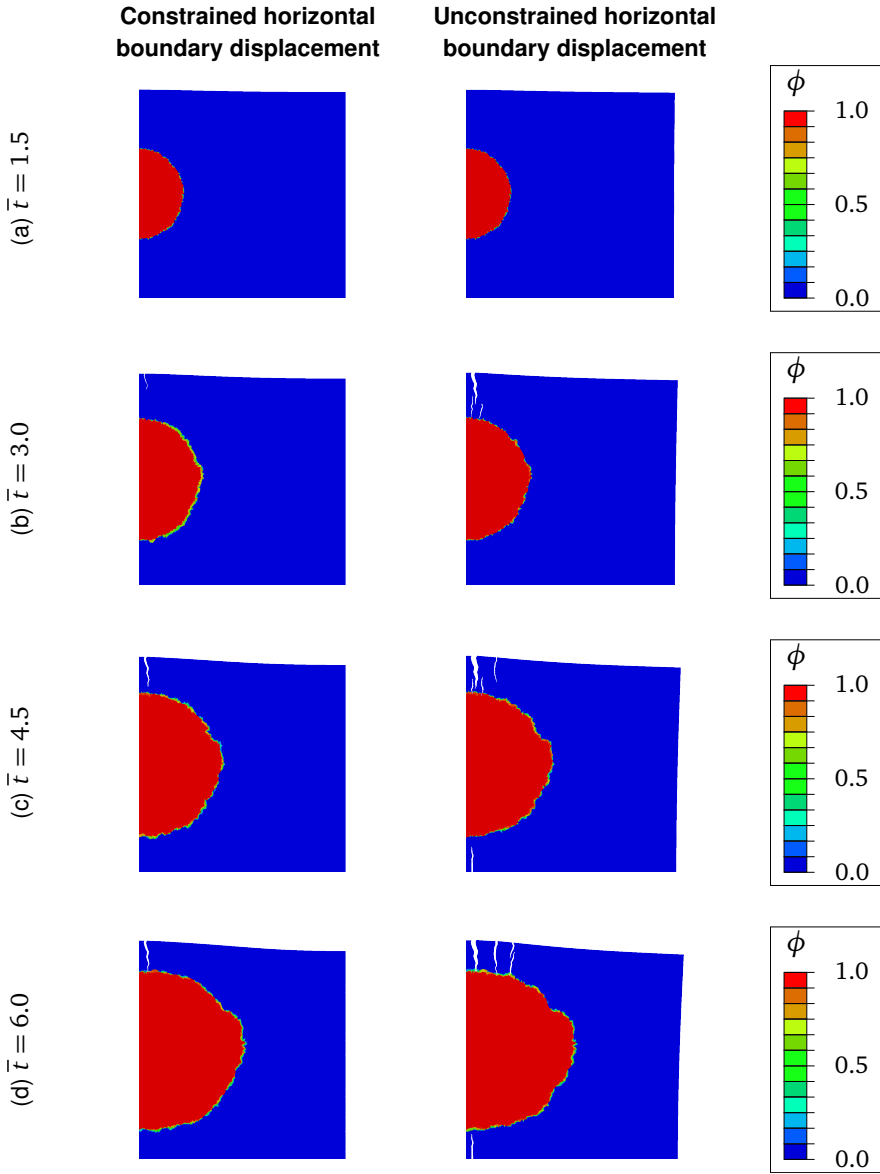


Figure 2.6: Time evolution of the paint configuration (with the deformation plotted at true scale) illustrating the growth of the metal soap crystal and the fracture induced in the paint material. The contour plot variable ϕ refers to the volume fraction of crystallised metal soap. The results for the *constrained* and *unconstrained* horizontal displacements at the right boundary (see also Figures 2.5(d) and (e)) are displayed in the left and right columns, respectively.

by using the normalised radii $\bar{r}_x = r_x/l$ and $\bar{r}_y = r_y/l$ in the horizontal and vertical directions, respectively. The time evolution of the average radius $\bar{r} = (\bar{r}_x + \bar{r}_y)/2$ of the crystal is presented in Figure 2.7(c). It can be observed that the growth characteristics of the crystal are insensitive to the level of constraint applied at the right boundary. Further, due to the prescribed concentration \bar{c}_0 at the right vertical boundary, the fatty acids easily reach the reaction zone along line A–A', thereby allowing the crystal to grow relatively fast and steadily in the horizontal direction, see Figure 2.7(a). Due to this spatial effect, the amount of fatty acids available for the chemical reaction along line B–B' is less, so that the growth rate of the metal soap crystal in the vertical direction is lower, and eventually decreases to a relatively small value when the crystal size becomes large, see Figure 2.7(b). It can be confirmed from Figure 2.6(d), that the difference in growth characteristics along the horizontal and vertical directions cause the metal soap crystal to develop in an approximately elliptical shape. The decrease towards a rather low growth rate in the vertical direction further will result in the crystal reaching the surface of the paint layer only after a very long time. Note finally the small, staircase-type increments in the response in Figures 2.7(a)–(c). These may be ascribed to the scanning algorithm used for the spatial identification of the reaction zone; in specific, the staircase increments correspond to the time required to form a fully crystallised metal soap within the reaction zone, a process that keeps the reaction zone temporarily fixed in space before it is advanced to its new location. Hence, the staircase-type increments can be expected to vanish in the limit of an infinitely small reaction zone, thereby turning the chemo-mechanical response into an ideally smooth curve.

Observe further from Figure 2.6 that for both boundary conditions depicted in Figures 2.5(d) and (e), a mode I-dominated crack develops right above the crystalline metal soap. The time evolution of the normalised mode I opening $\bar{v}_1 = v_1/l$, of this predominant crack – evaluated at the upper surface of the paint layer, which is where the crack mouth opening is maximal – is shown in Figure 2.7(d). Crack initiation occurs once the fracture strength of the material is reached, and its subsequent growth is influenced by the amount of horizontal constraint applied at the right boundary; in specific, for an unconstrained horizontal boundary displacement the maximum crack mouth opening is about 2.5 times larger than for a constrained horizontal boundary displacement. Although during cracking the amount of fatty acid diffusion across a crack reduces, see Equations (2.23) and (2.24), the growth of the crystal is nevertheless similar under unconstrained and constrained horizontal boundary displacements, see Figure 2.7(c), and thus appears to be hardly influenced by the difference in cracking. This is, since the amount of cracking in the paint domain is limited, and further does not really interfere with the path of fatty acid diffusion towards the metal soap crystal, as resulting from the prescribed concentration at the right boundary of the paint domain. Once a failure crack is about to penetrate the approaching metal soap crystal, the crack faces near the crack tip start to close as a result of a compressive stress developing in the metal soap crystal under restrained volumetric growth. This mechanism is more evident in the case of the unconstrained right boundary, as illustrated by the reduction in normalised crack length of the predominant failure crack from $l_c/l = 0.165$ at $\bar{t} = 3$ (Figure 2.6(b)) to $l_c/l = 0.150$ at $\bar{t} = 6$ (Figure 2.6(d)), where l_c is the crack length and l is the height of the paint layer. Crack closure under restrained volumetric expansion caused by phase transformations has also been reported for other materials, see e.g. [82, 114]. As illustrated in Figure 2.7(d), for the constrained and unconstrained models crack closure occurs for $\bar{t} > 5.3$ and $\bar{t} > 4.1$, respectively. The rate of crack closure of the dominant failure crack is somewhat larger for the unconstrained

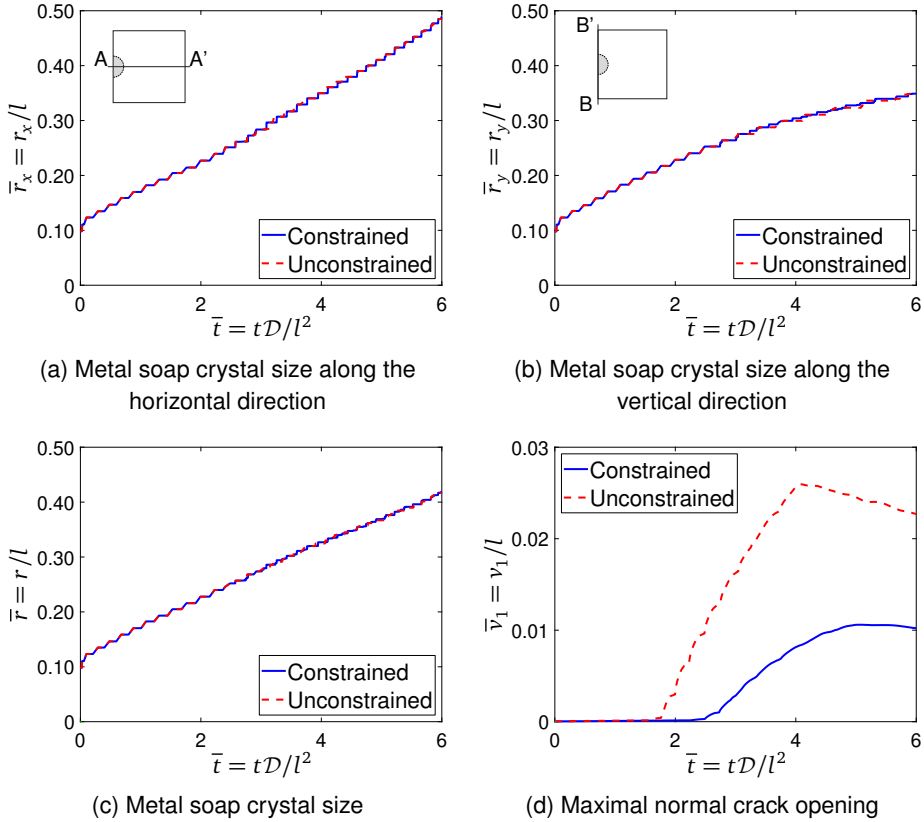


Figure 2.7: Time evolution of (a) the metal soap crystal size \bar{r}_x along the horizontal line A–A', (b) the metal soap crystal size \bar{r}_y along the vertical line B–B', and (c) the average metal soap crystal size $\bar{r} = (\bar{r}_x + \bar{r}_y)/2$, and (d) the maximum normal crack opening \bar{v}_1 of the most prominent crack for *constrained* and *unconstrained* horizontal displacements at the right boundary of the computational domain, see also Figures 2.5(d) and (e).

model, as a result of the gradual formation of adjacent, secondary cracks that induce an additional relaxation of the local tensile stress, see Figures 2.6(c) and (d). These secondary cracks may eventually coalesce with the dominant crack, promoting flaking of the paint material, see also [105, 130].

The stress development under restrained volumetric expansion can be considered in more detail by constructing a contour plot of the dimensionless hydrostatic stress, defined as $\bar{\sigma}_h = 1/3 \text{tr}(\boldsymbol{\sigma})(E_p G_c/l)^{-1/2}$, at time $\bar{t} = 6$ for constrained and unconstrained horizontal boundary displacements, see Figures 2.8(a) and (b). It may be confirmed that at the location of the predominant crack (right above the metal soap crystal) the hydrostatic stress indeed is close to zero. The metal soap crystal is in a state of compression, with the hydrostatic compressive stress clearly being substantially larger when the right boundary is horizontally constrained. On average, the paint matrix is subjected to tension, whereby the stress magnitude quantifies the restraining influence on the metal soap crystal, i.e. the average hydrostatic tensile stress is lower when the horizontal boundary displacement is constrained.

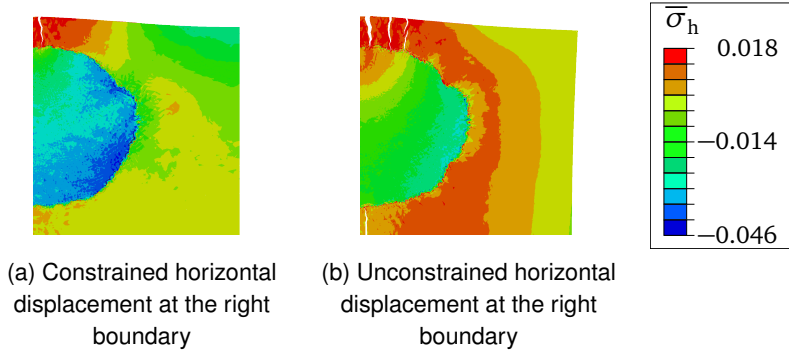


Figure 2.8: Dimensionless hydrostatic stress $\bar{\sigma}_h = 1/3 \text{tr}(\boldsymbol{\sigma})(E_p G_c/l)^{-1/2}$ depicted in the deformed configuration at $\bar{t} = 6$ for a (a) horizontally *constrained* right boundary and a (b) horizontally *unconstrained* right boundary of the computational domain, see also Figures 2.5(d) and (e).

The evolution of the dimensionless concentration \bar{c} of free saturated fatty acids is illustrated in Figure 2.9 for the domain with constrained horizontal displacements at the right boundary. The concentration is evaluated along the horizontal line A–A', for time instants \bar{t} at the early stage of the chemo-mechanical process. The time window considered in Figure 2.9 is relatively small, since it refers to a temporarily fixed location of the reaction zone corresponding to the region $0.110 < \bar{x} < 0.123$, as designated in the figure by the dashed vertical lines. At $\bar{t} = 0.0012$, the reaction zone entirely consists of uncrystallised paint material ($\phi = 0$), whereby the concentration varies smoothly from the prescribed value $\bar{c} = c_0 l^3$ at the right boundary to the approximately uniform concentration inside the crystal, see the blue solid line. Under the formation of additional metal soap, the fatty acid concentration in the reaction zone drops, as governed by the sink term in Equation (2.4). This local drop in concentration increases the concentration gradient, which drives further diffusion from the region surrounding the reaction zone, as illustrated by the concentration profiles at $\bar{t} = 0.0025$ (red dashed line) and $\bar{t} = 0.0053$ (magenta dotted line). At $\bar{t} = 0.0203$ (green dash-dotted line) the reaction has completed and the reaction zone has become fully crystallised ($\phi = 1$). In accordance with relations (2.4) and (2.5), the sink term has reduced to zero, and the concentration of fatty acids becomes essentially governed by diffusion. At this point, the new location of the reaction front is identified by the scanning algorithm illustrated in Figure 2.3, after which the process above is repeated.

2.5.2 Parameter variation study

The influence of specific process parameters on metal soap development and crack formation is investigated through a parameter variation study, whereby the horizontal displacements at the right boundary of the computational domain are *constrained*, see also Figure 2.5(d). In these simulations, the values of the dimensionless strength \bar{t}^u , the dimensionless molarity \bar{M} , and the dimensionless concentration \bar{c}_0 are kept constant, and given the same values as in the reference model discussed in Section 2.5.1. The dimensionless parameters r_0/l , E_s/E_p , \bar{l}_f , ε^g and \bar{R} are varied successively, and the computational results are compared against those obtained for the reference model.

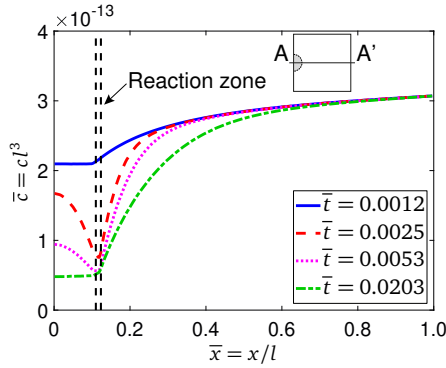


Figure 2.9: Time evolution of the dimensionless concentration \bar{c} along the horizontal line A–A', for the reference case with a horizontally constrained right boundary. The selected time instants \bar{t} are taken at the early stage of the chemo-mechanical process.

Finally, an additional variation study, in which the Poisson's ratio of the metal soap crystal takes the values $\nu_s = [0.2, 0.3, 0.4]$ and the value of the Poisson's ratio of the paint material is kept at the reference value of $\nu_p = 0.3$, illustrated that the effect of the Poisson's ratio of the metal soap on the chemo-mechanical response of the paint system is negligible.

Size of the metal soap nucleus

The effect of the size of the metal soap nucleus on its growth is investigated by considering three different values for the (dimensionless) initial radius of the nucleus, namely $r_0/l = [0.05, 0.1, 0.25]$. Note that $r_0/l = 0.1$ corresponds to the reference geometry discussed in Section 2.5.1. Figures 2.10(a) and (b) show the time evolutions of the average radius \bar{r} of the metal soap crystal and the maximal normal crack opening \bar{v}_1 of the most prominent crack in the paint medium, respectively. It can be observed that the initial growth rate of the crystal is larger when the nucleus size is smaller. However, after a certain amount of growth the growth rate reduces to a constant, steady-state value, which appears to be independent of the size of the initial nucleus. In addition, Figure 2.10(b) shows that for a larger metal soap nucleus the fracture process in the paint layer starts earlier, whereby for the largest nucleus, $r_0/l = 0.25$, fracture is generated as soon as the chemo-mechanical process initiates. It can be further observed that the rate of crack growth and the corresponding maximum crack opening are almost insensitive to the size of the initial nucleus.

Stiffness mismatch

The influence of the mismatch in the stiffnesses of the metal soap crystal and the paint material E_s/E_p on metal soap growth and crack formation is illustrated in Figures 2.11(a) and (b), respectively. By varying the stiffness E_s of the metal soap, three different values for the stiffness mismatch are considered, namely $E_s/E_p = [0.1, 1, 10]$, whereby $E_s/E_p = 1$ corresponds to the reference model presented in Section 2.5.1. Clearly, the value of the stiffness mismatch only mildly influences the growth characteristics of the metal soap crystal. The effect of the stiffness mismatch on the amount of crack opening, however, is relatively strong, whereby a larger relative stiffness of the metal soap leads to a larger

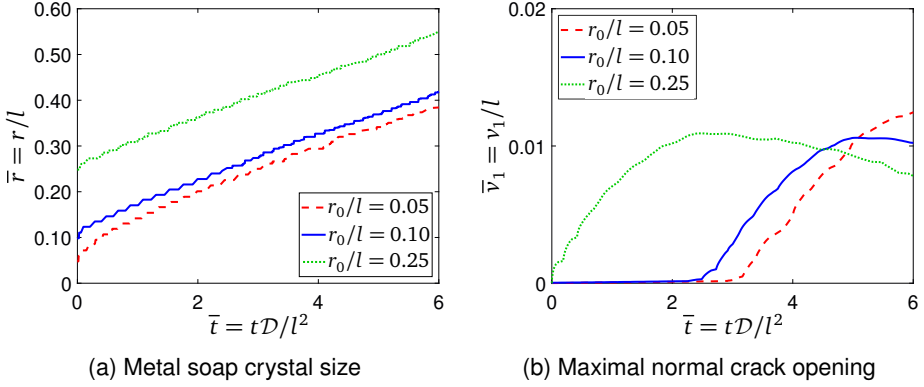


Figure 2.10: Influence of the size of the nucleus r_0/l of the metal soap crystal on the time evolution of (a) the metal soap crystal size \bar{r} (with \bar{r} being the average radius of the crystal) and (b) the maximal normal crack opening \bar{v}_1 of the most prominent crack. The horizontal displacements at the right boundary of the computational domain are *constrained*, see also Figure 2.5(d).

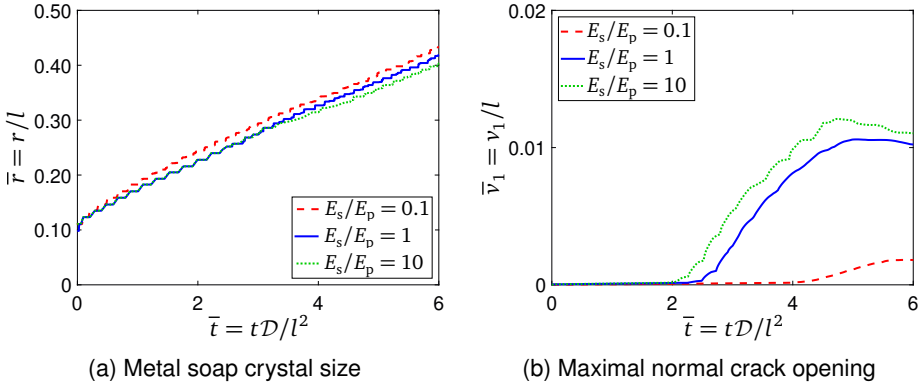


Figure 2.11: Influence of the stiffness mismatch E_s/E_p on the time evolution of (a) the metal soap crystal size \bar{r} (with \bar{r} being the average radius of the crystal) and (b) the maximal normal crack opening \bar{v}_1 of the most prominent crack. The horizontal displacements at the right boundary of the computational domain are *constrained*, see also Figure 2.5(d).

maximal crack opening. Note also that for $E_s/E_p = [1, 10]$, the onset of cracking starts at approximately the same time, whereas for the lower stiffness mismatch $E_s/E_p = 0.1$, it occurs considerably later.

Fracture length scale

The influence of the normalised fracture length scale \bar{l}_f on metal soap growth and crack formation is shown in Figures 2.12(a) and (b), respectively. The value of the normalised fracture length scale adopted in the reference model equals $\bar{l}_f = l_f/l = 6.62 \cdot 10^2$, and thus is much larger than unity, $\bar{l}_f \gg 1$. Accordingly, the fracture process at the present scale of observation l is relatively ductile, whereby the cracks observed in the paint layer system are controlled by strength rather than by toughness. The effect of the normalised

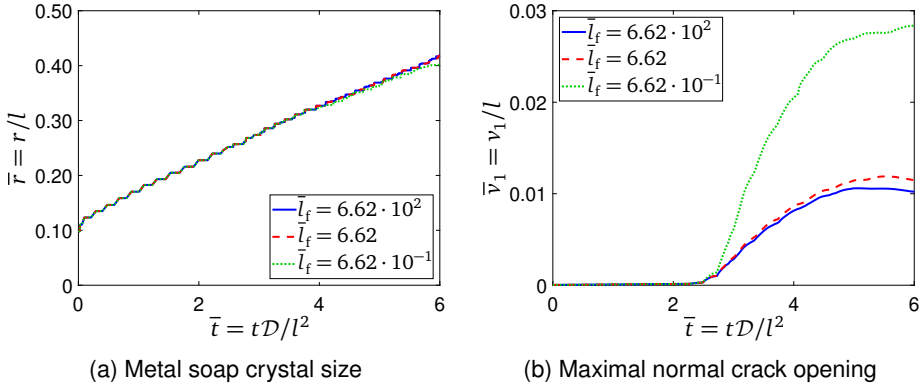


Figure 2.12: Influence of the normalised fracture length scale \bar{l}_f on the time evolution of (a) the metal soap crystal size \bar{r} (with \bar{r} being the average radius of the crystal) and (b) the maximal normal crack opening \bar{v}_1 of the most prominent crack. The horizontal displacements at the right boundary of the computational domain are *constrained*, see also Figure 2.5(d).

fracture length scale on the paint system response is investigated by successively lowering the toughness value used in the reference model by a factor of 10^2 and 10^3 , in correspondence with the values $\bar{l}_f = [6.62 \cdot 10^{-1}, 6.62, 6.62 \cdot 10^2]$. Figure 2.12(a) shows a negligible influence of the fracture length scale on the growth of the relative size of the metal soap crystal \bar{r} . Conversely, Figure 2.12(b) illustrates that the crack mouth opening \bar{v}_1 of the most prominent crack typically increases for a decreasing value of the fracture length scale. The influence, however, is limited when decreasing the length scale from $\bar{l}_f = 6.62 \cdot 10^2$ (blue solid line) to 6.62 (red dashed line), indicating that fracture in this range is mainly controlled by strength. On the contrary, for $\bar{l}_f = 6.62 \cdot 10^{-1}$ (green dotted line) the fracture process turns out to become relatively brittle and significantly governed by toughness, in correspondence with a substantially larger opening of the prominent failure crack than for the other two cases.

Chemical growth strain

The influence of the chemical growth strain on metal soap growth and crack formation is analysed by selecting three different values, namely $\varepsilon^g = [0.075, 0.1, 0.125]$. Note that $\varepsilon^g = 0.1$ corresponds to the reference case presented in Section 2.5.1. Figures 2.13(a) and (b) show the time evolutions of the average radius \bar{r} of the metal soap crystal and the maximal normal crack opening \bar{v}_1 of the most prominent crack, respectively. The effect of the growth strain on the growth characteristics of the crystal turns out to be negligible. The influence of the chemical growth strain on the amount of crack formation, however, is relatively strong; for a larger growth strain the stresses in the paint layer become higher, causing cracking to start earlier and to develop at a higher rate. Note, however, that the time at which the crack reaches its maximum opening and starts to close seems to be unaffected by the magnitude of the growth strain.

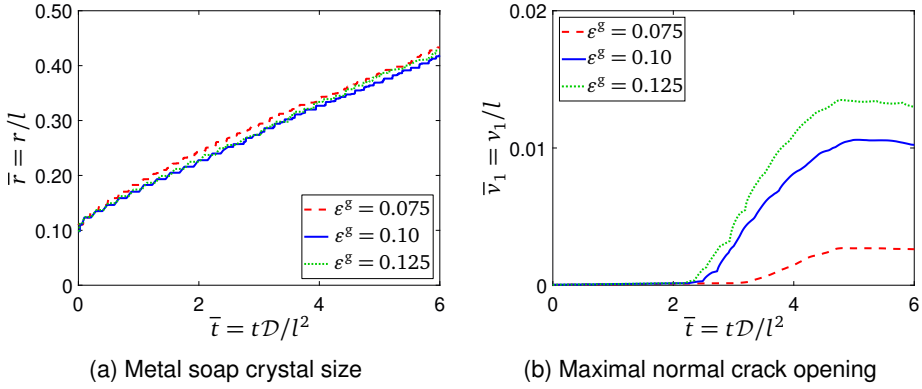


Figure 2.13: Influence of the chemical growth strain ε^g on the time evolution of (a) the metal soap crystal size \bar{r} (with \bar{r} being the average radius of the crystal) and (b) the maximal normal crack opening \bar{v}_1 of the most prominent crack. The horizontal displacements at the right boundary of the computational domain are *constrained*, see also Figure 2.5(d).

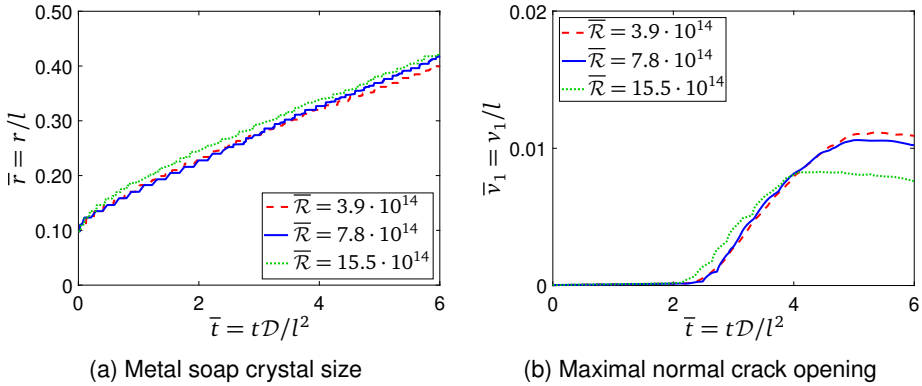


Figure 2.14: Influence of the chemical reaction rate $\bar{\mathcal{R}}$ on the time evolution of (a) the metal soap crystal size \bar{r} (with \bar{r} being the average radius of the crystal) and (b) the maximal normal crack opening \bar{v}_1 of the most prominent crack. The horizontal displacements at the right boundary of the computational domain are *constrained*, see also Figure 2.5(d).

Chemical reaction rate


The effect of the dimensionless chemical reaction rate $\bar{\mathcal{R}}$ on metal soap formation and crack evolution is examined by selecting three different values: $\bar{\mathcal{R}} = [3.9 \cdot 10^{14}, 7.8 \cdot 10^{14}, 15.5 \cdot 10^{14}]$, whereby the reference simulation corresponds to $\bar{\mathcal{R}} = 7.8 \cdot 10^{14}$. The time evolution of the average radius of the metal soap depicted in Figure 2.14(a) shows that a higher reaction rate mildly increases the growth rate of the crystalline metal soap. From Figure 2.14(b) it can be observed that the maximum crack opening is smaller for a higher reaction rate. Essentially, for a higher reaction rate at a specific time instant the metal soap occupies a larger volume, which effectively leads to more compressive stress in the domain and thus to less cracking of the paint material.

2.6 Conclusions and discussion

This chapter proposes a chemo-mechanical model to simulate metal soap formation in historical oil paintings and the induced chemo-mechanical degradation by crack formation, metal soap growth and upward paint surface deflection. The simulation framework combines a diffusion-reaction model with a mechanical model. The growth of a metal soap generates elastic strains – and therefore stresses – in the paint layer, possibly leading to crack formation. Crack nucleation and propagation are modelled using a cohesive zone approach, which combines a traction-separation law with a flux-concentration relationship in order to describe the onset and evolution of discrete chemo-mechanical cracking. The coupled model has been implemented numerically within a finite element framework, using a staggered approach. Numerical analyses of a single metal soap nucleus in a paint layer illustrate that the proposed methodology allows to realistically simulate the growth of a metal soap crystal and the associated crack formation. The upward surface deflection generated when the metal soap crystal approaches the free surface of the paint layer is in qualitative agreement with cross-sectional observations on real paintings. The level of constraint generated by the boundary conditions in the horizontal direction of the paint layer does not influence the growth rate of the crystal, but appears to have a significant influence on the amount of fracture developing in the paint layer. A parameter variation study has indicated that the amount of chemo-mechanical fracture is significantly influenced by the stiffness mismatch between the paint material and the metal soap, the fracture length scale, the chemical growth strain of the metal soap, and the reaction rate. For a relatively high value of the fracture length scale the fracture process at the scale of observation considered is relatively ductile and essentially stress-driven. Lowering the value of the fracture length scale makes the fracture process more brittle and determined by toughness, leading to a larger opening of the most prominent failure crack. The size of the initial nucleus of the metal soap crystal only determines the moment at which the fracture process starts, but does not have an influence on the amount of cracking. Further, the growth characteristics of the crystal appear to be (almost) insensitive to the above-mentioned parameter variations.

The modelling strategy and numerical analyses presented in the current chapter provide a first step towards gaining more insight into the coupled chemo-mechanical degradation mechanisms of historical oil paintings. The next step in this research should aim at further refining the model predictions in a quantitative sense, which requires *i*) the input from more detailed measurements on the material parameters of the individual constituents (metal soap, paint material), as for example can be done via nanoindentation tests [47], and *ii*) the accurate measurement and verification of the *time* and *length scales* characterising the deterioration mechanisms in a paint system. These characteristic time and length scales are determined by many aspects, such as the material parameters characterising the kinetics of the diffusion-reaction and cracking processes, the sizes, locations and mutual distances of crystalline metal soap nuclei, the initial concentration profile of the fatty acid, the actual geometry of the paint layer, the boundary conditions applied, etc. It is further emphasised that the kinetics of metal soap formation are currently incorporated by modelling only the irreversible part of the chemical reaction, and leaving the reversible part out of consideration. Preliminary estimates that do take the reversible part into account nevertheless indicate that this contribution may have a significant influence on the characteristic time scale of crystalline metal soap formation. This aspect, together with the other aspects mentioned above, will be investigated in more detail in

future work. Also, for an adequate calibration and verification of characteristic time and length scales, the design and performance of additional experiments are necessary, which measure the temporal and spatial development of both metal soap formation and crack growth, and accurately determine the diffusion paths of the fatty acid. Finally, in order to limit metal soap formation and crack growth in paint systems, it is worth investigating the efficiency of particular conservation interventions (e.g. the use of specific solvents) and conservation procedures (e.g. controlling indoor climate conditions).



**Influence of nucleus geometry and
location and fatty acid concentration on
metal soap induced damage in paint
layers**

Chapter 3

Influence of fatty acid concentration and nucleus shape and location on metal soap induced damage in paint layers

Metal soap formation is one of the most wide-spread degradation mechanisms observed in historical oil paintings, affecting works of art from museum collections worldwide. Metal soaps develop from a chemical reaction between metal ions present in the pigments and saturated fatty acids, which are released by the oil binder. The presence of large metal soap crystals inside paint layers or at the paint surface can be detrimental for the visual appearance of artworks. Moreover, metal soaps can possibly trigger mechanical damage, ultimately resulting in flaking of the paint. This chapter¹ departs from the computational model presented in Chapter 2 and [37] to predict chemo-mechanical degradation in historical oil paintings. The model describes metal soap formation and growth, which are phenomena that are driven by the diffusion of saturated fatty acids and develop from a crystalline nucleus of small size. This results into a chemically-induced strain in the paint, which may promote crack nucleation and propagation. The proposed model is used in this chapter to investigate the effects of *i*) the initial nucleus geometry, *ii*) the saturated fatty acid concentration, and *iii*) the locations of the metal soap nuclei, on the generated chemo-mechanical damage. Numerical simulations show that the first two factors have a marginal influence on the growth rate of the metal soap crystal, but have a significant effect on the extent of fracture induced in the paint. Finally, the locations of the metal soap nuclei in the paint layer strongly affect both the onset of cracking and the growth rate of the metal soap crystals.

¹This chapter is based on:

[38] G.J.A.M. Eumelen, E. Bosco, A.S.J. Suiker, J.J. Hermans, A. van Loon, K. Keune, and P.D. Iedema. *SN Applied Sciences*, 2:1310, 2020.

[39] G.J.A.M. Eumelen, E. Bosco, A.S.J. Suiker, J.J. Hermans, A. van Loon, P.D. Iedema, and K. Keune. *Transcending Boundaries: Integrated Approaches to Conservation*. ICOM-CC 19th Triennial Conference, 2021.

3.1 Introduction

This chapter is motivated by the degradation of historical oil paintings associated with metal soap formation and growth. Oil paintings generally consist of multiple layers of paint, composed of metal-based pigment particles embedded in an oil binding medium, which are supported by a canvas or wooden substrate. Metal soaps form as a result of the chemical reaction between metal ions released from pigments or driers and saturated fatty acids extricated from the drying oil [72]. The initial reaction leading to metal soap formation is hypothesised to be reversible and to result into metal soaps in an amorphous state. Metal soaps can subsequently crystallise into insoluble aggregates by means of an irreversible reaction [8], thereby progressively growing into crystals of large size that deform pictorial layers and protrude through the paint surface. This growth process generates so-called chemically-induced strains in the paint system, ultimately causing damage and flaking of the paint [105, 130, 167]. Figure 3.1 shows a clear example of a metal soap crystal originating in the ground layer and breaking through several layers of paint until it reached the top of the paint surface, as observed in the *Portrait of Marten Soolmans* (1634) by Rembrandt van Rijn (Rijksmuseum, Amsterdam) [125].

Eumelen et al. [37] have recently presented a computational multi-physics model to predict the chemo-mechanical degradation of historical oil paintings as a result of metal soap formation and growth, see also Chapter 2. The methodology allows to describe the growth of a metal soap crystal and shows the associated crack formation, revealing that the amount of chemo-mechanical damage is significantly affected by the stiffness mismatch between the paint material and the metal soap, the fracture strength and toughness, the chemically-induced strain, and the reaction rate. Three additional factors that may play a relevant role in determining the metal soap-induced fracture response of a painting are the geometrical characteristics of the metal soap nucleus around which the growth of a crystal initiates, the concentration of saturated fatty acids, which represents the “driving force” of the chemical reaction, and the spatial distribution of metal soap nuclei. In this chapter, the model proposed in Chapter 2 is used to investigate the effect of *i)* the initial nucleus geometry, *ii)* the saturated fatty acid concentration, and *iii)* the locations of metal soap nuclei, on the degradation process of a paint layer.

This chapter is organised as follows. A review of the chemo-mechanical model proposed in Chapter 2 is presented in Section 3.2. Section 3.3 describes the geometries and material parameters used in the numerical simulations, and the results are discussed in Section 3.4. Conclusions are finally presented in Section 3.5.

3.2 Chemo-mechanical model

The computational model proposed in Chapter 2, is based on the coupling between a diffusion-reaction model and a mechanical model. The framework allows to simulate the spatial growth of a metal soap crystal, and computes the corresponding stress and strain fields generated inside a paint layer. The diffusion-reaction model and mechanical model are solved in an incremental-iterative fashion, using a staggered update scheme. Accordingly, at each time increment the diffusion-reaction model is solved first, whereby the results are transferred to the mechanical model. The mechanical model is then solved iteratively in order to account for the appearance of cracks. The results from the mechanical model are subsequently used to solve for the next time increment of the diffusion-reaction model, after which the incremental process described above is repeated, see Table 3.1. In

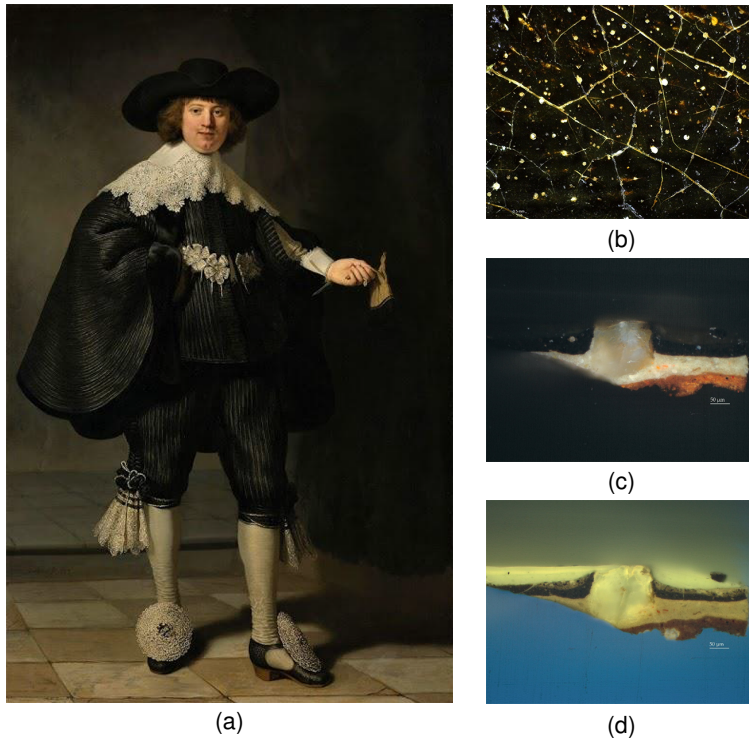


Figure 3.1: (a) Rembrandt van Rijn, Portrait of Marten Soolmans, 1634, Oil on canvas, 207.5 cm \times 132 cm, Rijksmuseum, Amsterdam, The Netherlands. After treatment. (b) Micro-detail of the painting (before treatment) showing tiny whitish globules of lead soaps protruding through the black paint surface. (c)–(d) A paint cross-section is taken at the top left of the painting, showing a large metal soap protrusion (diameter circa 150 μm). The light microscopic images of the metal soap aggregate are taken under (c) normal light illumination (bright field) and (d) ultraviolet illumination (365 nm). See [125]. Photos: copyright Rijksmuseum.

order to keep computational times manageable, representative configurations are simplified to two-dimensional plane-stress models. The three-dimensional simulation of paint configurations remains a topic for future research. For clarity, the adopted assumptions and modelling strategy are reviewed below.

3.2.1 Modelling assumptions

The complex chemical processes resulting in metal soap formation are modelled in accordance with a series of assumptions. First, the paint is idealised as a homogeneous domain with a specific initial concentration of saturated fatty acids. Pigment particles are not explicitly modelled; their properties are incorporated in the effective behaviour of the paint material. Next, the metal soap growth process is assumed to depart from a pre-existing crystalline nucleus of a (small) specified size. The spatial growth of the metal soap crystal occurs by defining a moving reaction zone at the interface between the crystal and the paint material. Additionally, only the irreversible part of the chemical process leading to metal soap formation is modelled, i.e. the intermediate, amorphous state of the metal soap is neglected. This implies that crystalline metal soap immediately forms upon the

1. Diffusion-reaction model.

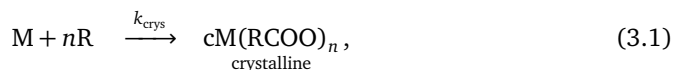
- 1.1 Perform the diffusion-reaction simulation by applying the initial (only at the first time increment) and boundary conditions.
- 1.2 Solve the diffusion-reaction equation together with the kinetic relation for metal soap development. Obtain the values of the concentration of saturated fatty acids and the volume fraction of crystalline metal soap.
- 1.3 Transfer the value of the volume fraction of crystalline metal soap to the mechanical analysis.

2. Mechanical model.

- 2.1 Apply the boundary conditions for the mechanical model.
- 2.2 Calculate the growth strain as a function of the volume fraction of crystallised metal soap.
- 2.3 Solve the equilibrium equations iteratively by accounting for possible cracking within the paint domain. Obtain the displacement field and the local damage parameters.
- 2.4 Transfer the values of the damage parameters to the diffusion-reaction analysis.
- 2.5 Return to 1.1 for performing the next time increment.

Table 3.1: Staggered approach used in the incremental-iterative solution procedure.

reaction between metal ions and saturated fatty acids. Based on this assumption, the reaction scheme for the formation of crystalline metal soap can be written as [37] (see also Chapter 2):



where $M + nR$ designates a metal ion M reacting with n fatty acid chains R , as a result of which crystalline metal soap $cM(\text{RCOO})_n$ forms. The crystallisation rate is denoted as k_{crys} . For the preservation of museum collections, the indoor climate fluctuations, characterised by temperature and relative humidity variations, are typically kept within relatively strict bounds [7, 12]. As a first modelling step, the dependency of the metal soap reaction rate on these factors is therefore neglected in the present analyses. However, environmental conditions can generally influence both the mechanical properties [110] and the chemical characteristics [90, 118] of paint layers, and may affect the choice of conservation treatments [96]. The sensitivity of metal soap formation to temperature and relative humidity variations still needs to be better quantified in experiments in order to adequately account for this effect in the modelling of chemo-mechanical degradation of paint systems. Hence, this is a topic for future study.

3.2.2 Modelling strategy

The reaction scheme described above is translated into a diffusion-reaction model along the lines of [79]. The diffusion-reaction equation is expressed in terms of the concentration of free saturated fatty acids. The reaction kinetics are incorporated in a sink

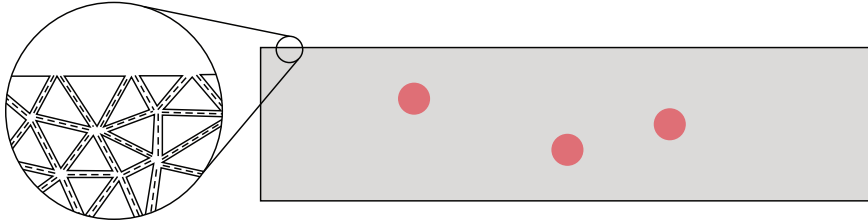


Figure 3.2: Model of a paint layer containing multiple metal soap nuclei (red circles). The geometry is discretised with continuum elements and cohesive interface elements placed in between them, indicated in the inset by the triangles and dashed lines, respectively.

term, with its value being proportional to the rate of crystalline metal soap formation. In a second equation, the time evolution of the crystalline metal soap is specified as a function of the concentration of saturated fatty acids available for the reaction and the volume fraction of the paint material in which metal soap has not yet formed, see Chapter 2, for more details.

The spatial growth of a metal soap crystal, which occurs in a small reaction zone at the boundary of the crystal, induces a strain field (and a corresponding stress field) in the paint system. This coupling between the chemical and mechanical fields is quantified by defining a chemically-induced growth strain, which is taken proportional to the volume fraction of crystalline metal soap. Moreover, changes in the mechanical properties associated to crystalline metal soap formation are determined by using a rule of mixtures, in which the effective stiffness is calculated as the volume average of the properties of the chemical phases present in the specific material point. Mechanical equilibrium equations finally complete the chemo-mechanical modelling of the paint system.

The chemical and mechanical models are solved with the aid of the finite element method (FEM). Accordingly, the paint geometry is discretised into plane-stress continuum elements that simulate the two-dimensional bulk responses of the metal soap and paint materials. In accordance with the approach originally proposed in [171], cohesive interface elements are placed in between all continuum elements modelling the paint configuration, see Figure 3.2, thereby allowing to describe the nucleation and propagation of relatively complex, discrete cracking patterns. The mesh density used in the FEM simulations is similar to that of the simulations presented in Chapter 2, whereby it has been confirmed that the spatial discretisation is sufficiently fine for obtaining converged numerical results. The constitutive behaviour of a crack is simulated with the interface damage model proposed in [25]. The appearance of cracks locally hampers the diffusion of saturated fatty acids; this effect is accounted for by making the flux-concentration relation of the fatty acid at the crack surfaces a function of the generated mechanical damage, see Chapter 2, for more details.

3.3 Numerical simulations

3.3.1 Material parameters

Most of the material parameters adopted in the numerical simulations were taken from different sources in the literature [50, 67, 98] and refer to lead-based pigment particles in combination with a stearic acid, forming lead stearate. The parameters for which

experimental data are not available have been estimated by means of engineering judgement. The specific parameter values are summarised in Table 3.2, see Chapter 2, for more details on the assumptions taken for the parameter selection.

Parameter	Value	Unit	Reference
Diffusion-reaction model			
Molarity	2470	mol/m ³	[98]
Diffusion coefficient	$3.6 \cdot 10^{-11}$	m ² /s	[67]
Reaction rate	$4.2 \cdot 10^{-1}$	m ³ /(mol s)	[67]
Mechanical model			
<i>Continuum elements</i>			
Growth strain	0.1	–	
Elastic modulus paint material	115	MPa	[50]
Poisson's ratio paint material	0.3	–	
Elastic modulus crystallised metal soap	115	MPa	
Poisson's ratio crystallised metal soap	0.3	–	
<i>Interface elements</i>			
Fracture strength	2.2	MPa	[50]
Fracture toughness	0.418	N/mm	[50]

Table 3.2: Material parameters used in the numerical simulations, adopted from Chapter 2 and references therein. The parameters for which experimental data are not available have been estimated by means of engineering judgement, see Chapter 2 for more details.

3.3.2 Geometry and initial and boundary conditions

The first paint layer geometry analysed in this chapter departs from the reference configuration studied in Chapter 2, which consists of a rectangular domain of width $2l$ and thickness l , with $l = 15 \mu\text{m}$. The thickness of the paint layer is chosen to be representative of paint layers in historical paintings [148]. A small nucleus of crystallised metal soap is considered to be initially present, with its location chosen at the centre of the paint layer. Because of symmetry only half of the paint configuration has been modelled, as illustrated in Figure 3.3(a). The second paint layer geometry considered consists of a rectangular domain with a width of $4l$ and a thickness of l , where l is again taken as $l = 15 \mu\text{m}$. In this domain, three metal soap nuclei are assumed to be initially present, as illustrated in Figure 3.4. The shape of the nuclei is circular, with an initial radius $r_0 = l/10 = 1.5 \mu\text{m}$. The effect of the initial nucleus size on the chemo-mechanical degradation process has been investigated in Chapter 2, which has demonstrated that it governs the specific moment in time at which the fracture process initiates, but that it does not affect the crack growth rate and the corresponding maximum crack opening.

For the diffusion-reaction analysis, the initial condition is formulated by assuming a uniform fatty acid concentration $c_0 = 91 \text{ mol/m}^3$ [37] (see also Chapter 2) throughout the entire domain. For the geometry of Figure 3.3(a), at the right domain boundary a uniform saturated fatty acid concentration profile $\check{c} = c_0 = 91 \text{ mol/m}^3$ is imposed. Further, to account for symmetry, a zero-flux boundary condition is prescribed at the left boundary. For the domain depicted in Figure 3.4, at the left and right domain boundaries a uniform saturated fatty acid concentration profile $\check{c} = c_0 = 91 \text{ mol/m}^3$ is imposed. For

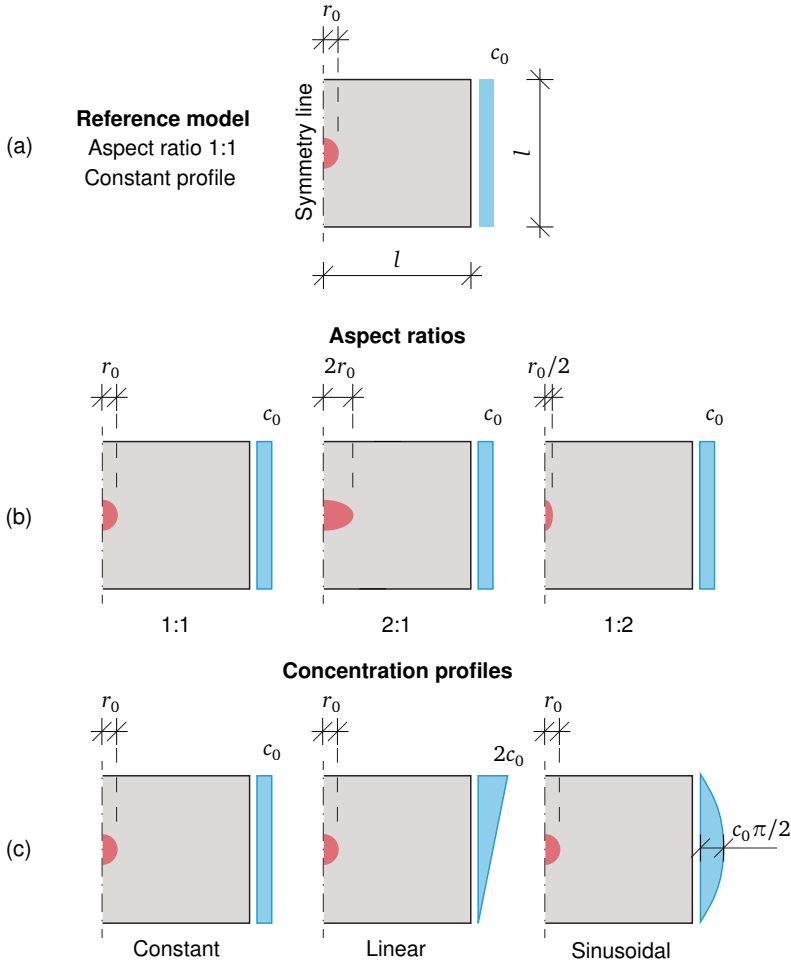


Figure 3.3: (a) Reference model used in the numerical analyses. (b)–(c) Input for the models for the parameter variation study, exploring the effect of (b) the aspect ratio of the initial metal soap nucleus and (c) the saturated fatty acid concentration profile at the right domain boundary.

both geometries, the top and bottom boundaries are characterised by a zero-flux boundary condition.

For the mechanical analysis, it is assumed that the paint layer is initially stress-free. Further, the horizontal displacement is constrained at the left and right domain boundaries. The bottom domain boundary is constrained in the vertical direction, in order to mimic the support provided by the substrate.

Departing from the reference model the influence on metal soap development and crack formation by the geometry of the metal soap nucleus and the fatty acid concentration profile applied at the right domain boundary is investigated through a parameter variation study. The effect of the geometrical characteristics of the metal soap nucleus is explored by considering elliptical nuclei of width-to-height aspect ratios 2:1 and 1:2, whereby the height of the ellipse is kept the same for all three cases, see Figure 3.3(b).

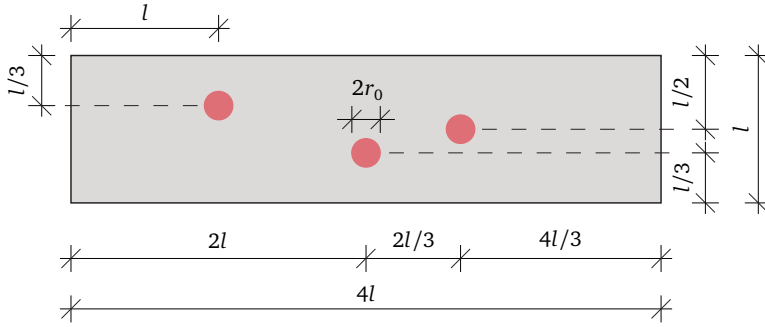


Figure 3.4: Input for the model to explore the effect of multiple metal soap crystals.

The assumed nucleus geometries are considered to be representative of metal soap aggregates observed *in situ*. The influence of the fatty acid concentration profile is investigated by considering two concentration profiles at the right domain boundary, namely a linear profile $\check{c}(y) = 2c_0y/l$ and a sinusoidal profile $\check{c}(y) = (c_0\pi/2)\sin(\pi y/l)$, see Figure 3.3(c). Note that all three profiles are characterised by the same average concentration value c_0 .

3.4 Results and discussion

3.4.1 Influence of nucleus geometry

The effect of the nucleus geometry on metal soap formation is investigated by considering a set of nuclei characterised by different width-to-height aspect ratios, as illustrated in Figure 3.3(b), whereby the case of a circular nucleus corresponds to the reference simulation presented in Chapter 2.

Figure 3.5 shows the progressive growth of the metal soap crystal and the resulting fracturing of the paint, for a nucleus with a width-to-height aspect ratio 1:1 (left column), 2:1 (centre column), and 1:2 (right column). The evolution of the process is described in terms of a dimensionless time parameter, defined as $\bar{t} = tD/l^2$, with t the real time, D the diffusion coefficient and l the thickness of the simulated domain. The contour plot variable indicates the volume fraction ϕ of crystallised metal soap. The fully crystallised material is represented by the red colour ($\phi = 1$), while the original paint material corresponds to the blue colour ($\phi = 0$). Notice further the narrow transition zone at the interface between the metal soap crystal and the paint in which the chemical reaction occurs, with $0 < \phi < 1$. It can be clearly seen that the growth of the metal soap crystal eventually causes a significant deformation of the paint surface. This effect is also observed in cross-sections of metal soap crystals taken from real artworks, as for instance shown in Figure 3.1.

Figure 3.6(a) illustrates the time evolution of the average radius $r = (r_x + r_y)/2$ of the metal soap crystal, as expressed in its dimensionless form $\bar{r} = r/l$. From the similarity in the slopes of the three curves it is concluded that the initial nucleus geometry has a minor influence on the growth rate of the crystal.

Figure 3.6(b) presents the time evolution of the maximal normal opening \bar{v}_1 of the predominant crack in the paint system, which appears right above the metal soap crystal as a result of the stress generated by crystal growth reaching the tensile strength of the

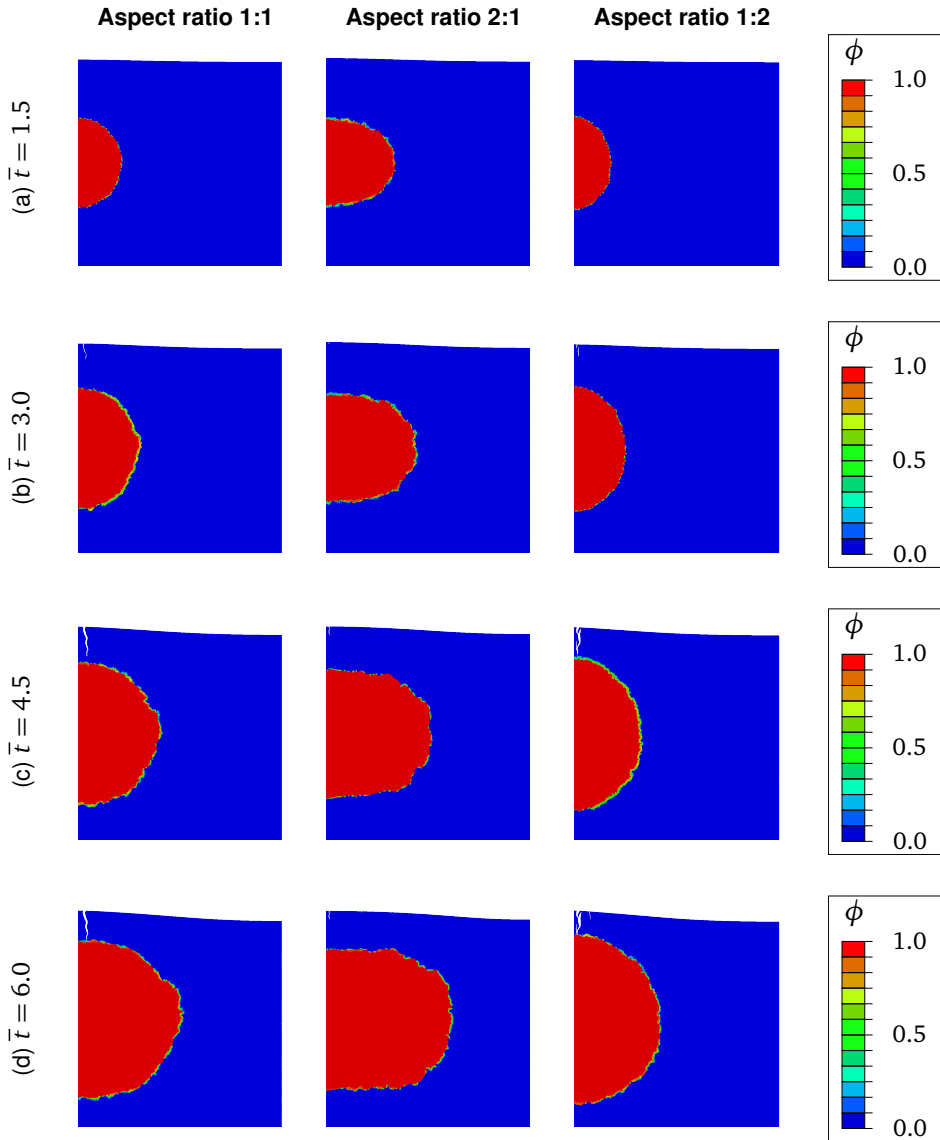


Figure 3.5: Time evolution of the paint configuration (with the deformation plotted at true scale) illustrating the growth of the metal soap crystal and the fracture and surface deflection of the paint material. The contour plot variable ϕ refers to the volume fraction of crystallised metal soap. The results refer to a metal soap nucleus of initial aspect ratio 1:1 (left column), 2:1 (centre column), and 1:2 (right column).

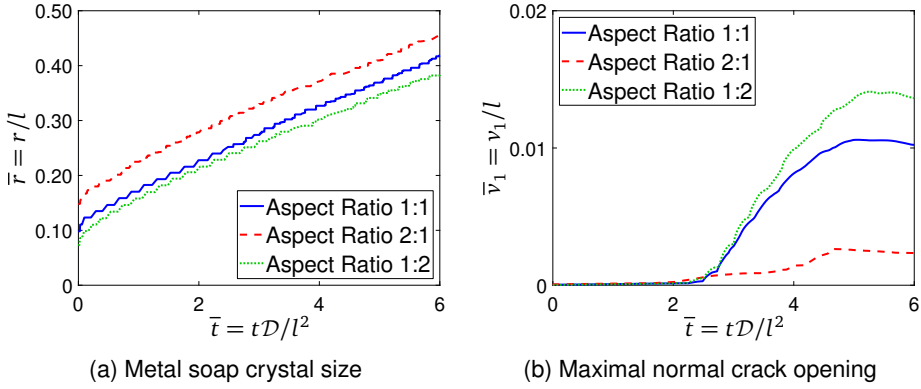


Figure 3.6: Influence of the initial nucleus aspect ratio on the time evolution of (a) the metal soap crystal size \bar{r} (with \bar{r} being the average radius of the crystal) and (b) the maximal normal crack opening \bar{v}_1 of the predominant crack.

paint material, see Figure 3.5. The normal crack opening is presented in its dimensionless form, $\bar{v}_1 = v_1/l$. While the onset of damage occurs approximately at the same time for the three nucleus geometries considered, the crack opening clearly increases for a decreasing width-to-height aspect ratio of the nucleus. This is, because a metal soap aggregate developing an elliptical shape characterised by a large width (aspect ratio 2:1) introduces a relatively low tensile stress in the upper part of the domain. Correspondingly, for a nucleus aspect ratio of 2:1 the crack turns out to be almost not visible, see Figure 3.5. When a crack is about to penetrate the approaching metal soap crystal, the crack faces at the crack tip close. Crack closure is due to the volumetric expansion of the metal soap crystal. This locally induces compressive stresses around the crack tip, in the zone adjacent to the crystal boundary, leading to crack closure. This mechanism can be clearly observed for the case of a nucleus with an aspect ratio 1:2, illustrating that the normalised crack length of the predominant crack reduces from $l_c/l = 0.133$ at $\bar{t} = 4.5$ – see Figure 3.5(c) – to $l_c/l = 0.119$ at $\bar{t} = 6$ – see Figure 3.5(d).

3.4.2 Influence of fatty acid concentration profile

The influence of the saturated fatty acid concentration prescribed at the right domain boundary on the amount of developed chemo-mechanical damage is investigated by considering three different concentration profiles, which are uniform, linear, and sinusoidal, as illustrated in Figure 3.3(c). The uniform concentration profile corresponds to the reference simulation presented in Chapter 2. The deformed configuration of the paint layer is shown in Figure 3.7 at different values of the dimensionless time \bar{t} . Similar to what is observed in Figure 3.5, the metal soap crystal gradually grows, deforming the top surface of the paint and generating a vertical crack in the top part of the sample. For the uniform and sinusoidal fatty acid profiles the shape of the metal soap crystal develops in a smooth, almost circular fashion. Conversely, for a linear fatty acid profile the metal soap aggregate gradually grows into a more irregular shape.

The time evolutions of the normalised average crystal radius \bar{r} and the normalised maximum crack opening \bar{v}_1 are shown in Figures 3.8(a) and (b), respectively. The imposed concentration profile appears to have essentially no influence on the growth rate and average size of the crystal. The influence on the crack opening, however, is quite

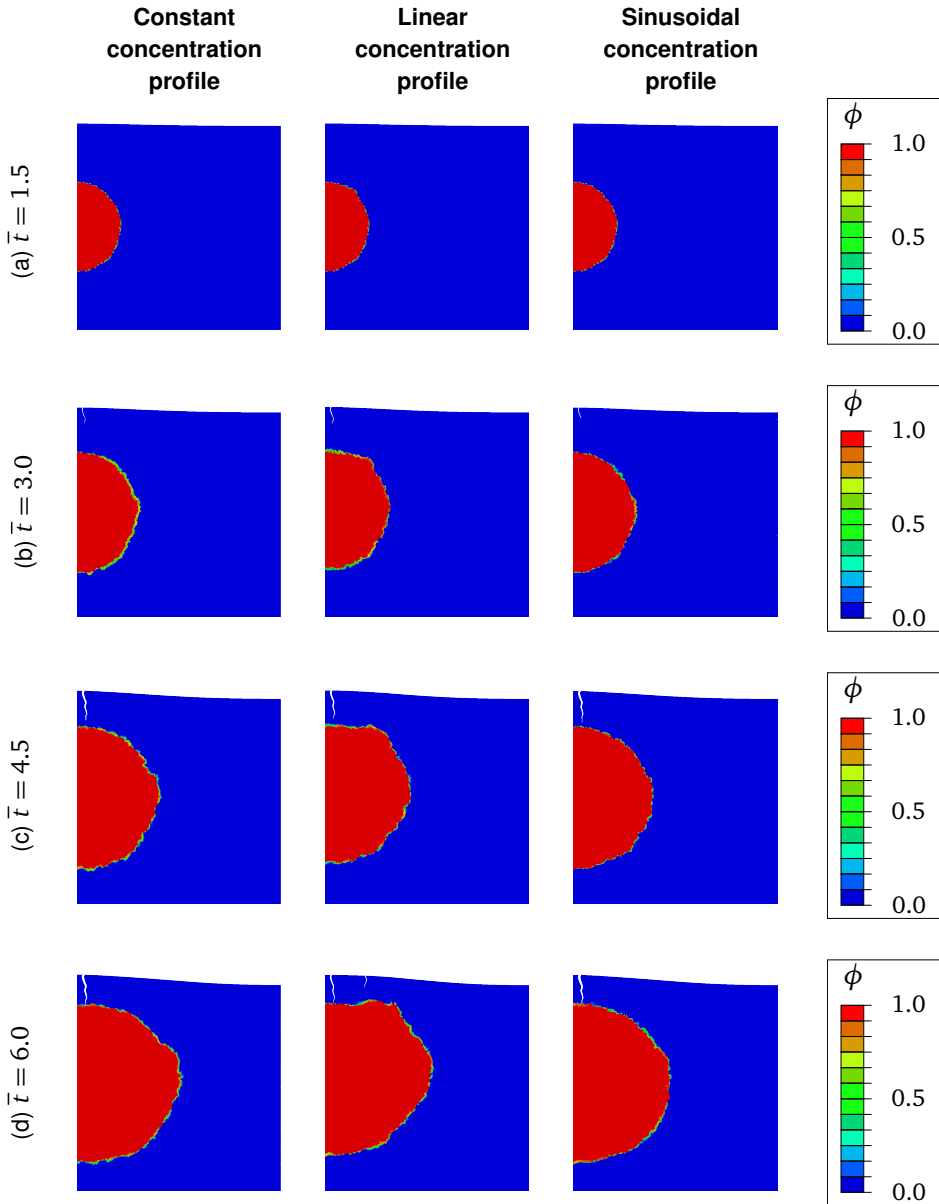


Figure 3.7: Time evolution of the paint configuration (with the deformation plotted at true scale) illustrating the growth of the metal soap crystal and the fracture and surface deflection of the paint material. The contour plot variable ϕ refers to the volume fraction of crystallised metal soap. The results for the constant, linear, and sinusoidal fatty acid concentration profiles at the right domain boundary are displayed in the left, central and right columns, respectively.

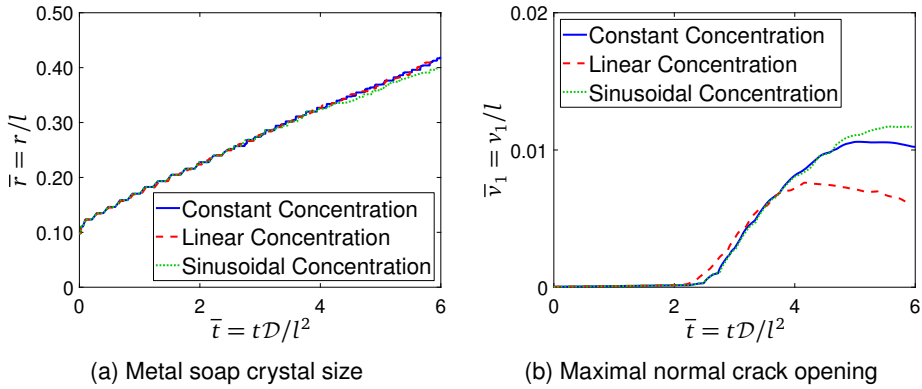


Figure 3.8: Influence of the prescribed saturated fatty acid concentration on the time evolution of (a) the metal soap crystal size \bar{r} (with \bar{r} being the average radius of the crystal) and (b) the maximal normal crack opening \bar{v}_1 of the most predominant crack.

significant. This can be ascribed to the growth characteristics of the metal soap aggregate along the *horizontal direction* (as dominant in the case of an aspect ratio 2:1). A larger crystal size in the horizontal direction (as observed for the linear concentration profile) generates a more uniform stress distribution, and therefore a lower stress in the top part of the paint, which leads to less crack development. The sinusoidal and constant concentration profiles, which are characterised by crystals of comparable shape, lead to a similar crack response until $\bar{t} = 4.5$, after which the crack starts to close for the constant concentration profile while it slightly advances for the sinusoidal concentration profile.

3.4.3 Influence of the metal soap distribution

The progressive growth of the metal soap crystals and the consequent deformation and fracturing of the paint layer are shown in Figure 3.9 for different values of the dimensionless time \bar{t} . Similar to the results of the previous geometry, the growth of the metal soap crystals deforms the top surface, thereby inducing crack formation. It can be observed that the two outer crystals grow predominantly in the direction of the vertical domain boundaries, and less towards the centre of the geometry. These two crystals also develop a mild elliptical shape, whereas the middle crystal remains circular.

Figure 3.10(a) shows the evolution of the dimensionless, average, metal soap crystal radius, \bar{r} . From this graph, it can be seen that the growth rates of the three crystals are initially comparable. However, since the initially uniform concentration of saturated fatty acids gradually becomes non-uniform, by decreasing to zero across the middle part of the configuration, see Figure 3.11, the growth rate of the crystals becomes dependent on their location. Thus, the two outer crystals are closer to the source of saturated fatty acid provided through the boundary conditions, which allows for a relatively fast growth of these crystals, such that they reach a substantially larger size than the middle crystal. Although not shown here, at a later stage the three crystals may eventually merge to form a large metal soap aggregate. Note finally that the growth rate of the metal soap crystals appears to reach a steady state relatively early in the process (at $\bar{t} = 0.8$), i.e. the growth rates of the three crystals remain constant upon a further increase in time.

Above the left metal soap crystal, four micro-cracks develop. Figure 3.10(b) shows the evolution of the maximal normalised crack openings \bar{v}_1 , evaluated at the top surface.

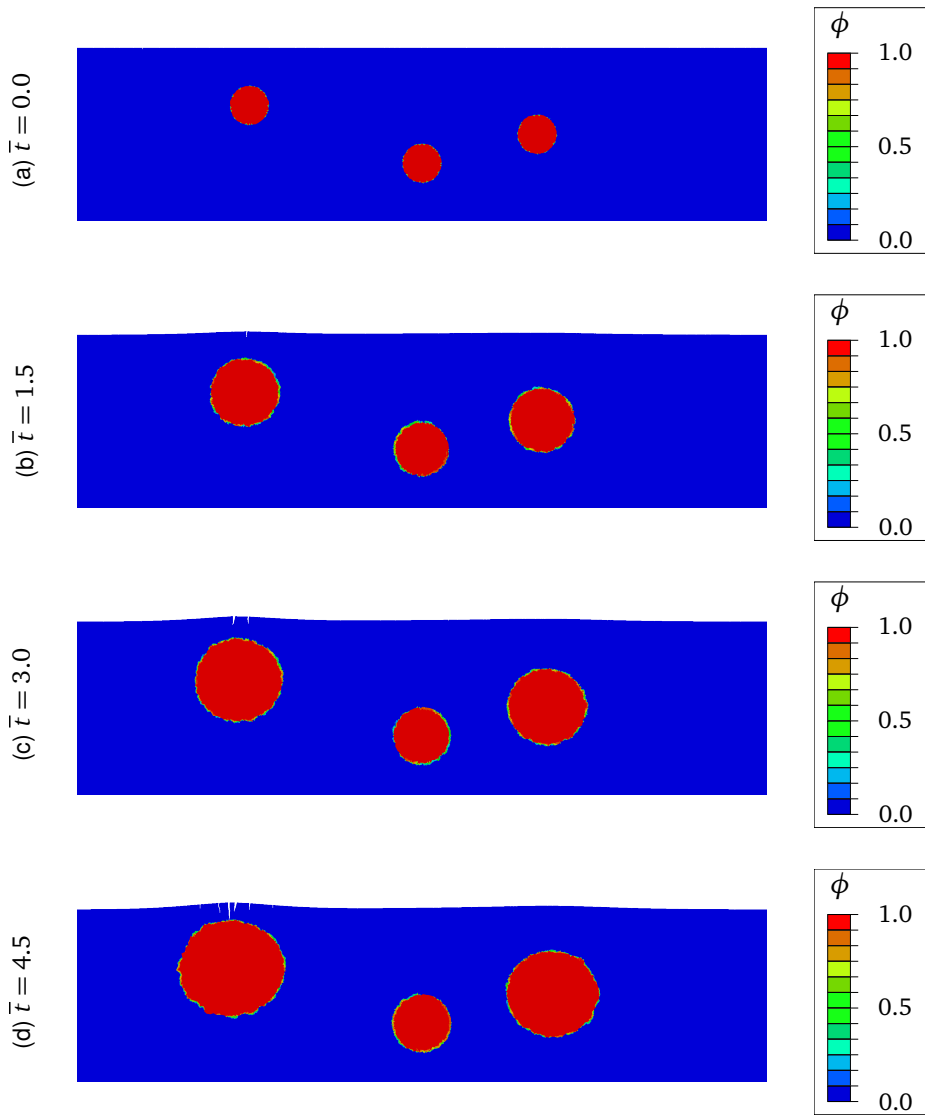


Figure 3.9: Time evolution of the paint layer configuration (deformation plotted at true scale), showing the growth of the metal soap crystals and the formation of micro-cracks above the left crystal. The contour plot shows the volume fraction (ϕ) of crystallised metal soap, with the red colour indicating fully crystallised material and the blue colour indicating the original paint material.

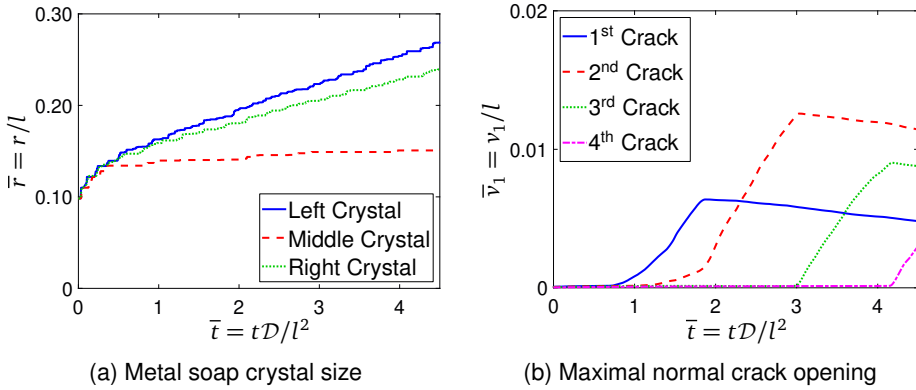


Figure 3.10: Time evolution of (a) the normalised average size of the three crystals and (b) the normalised crack opening of the four micro-cracks that develop above the left crystal.

These cracks nucleate when the local tensile strength of the paint material is reached. The first crack develops immediately above the centre of the left crystal, as illustrated in Figure 3.9(b). Three additional cracks successively form in the direct neighbourhood of the first crack, causing a mild relaxation of the local tensile stresses near the paint surface. This leads to crack closure, as indicated in Figure 3.9(b) by the branches related to a decreasing crack opening.

The temporal evolution of the concentration distribution in Figure 3.11 shows that with increasing time the initially uniform concentration becomes non-uniform, by decreasing to zero across the middle part of the paint layer. This indicates that fatty acids in this region are rapidly consumed for the purpose of metal soap growth. When $\bar{t} > 1.5$, the concentration distribution has approximately reached a steady state, whereby fatty acids remain locally present only through the concentration values imposed at the vertical domain boundaries. This allows the two outer metal soap crystals to continue to grow over time, whereas the size of the inner crystal remains constant, see also Figures 3.9 and 3.10(a).

3.5 Conclusions

Departing from a recent computational model on chemo-mechanical paint degradation by metal soap formation as presented in Chapter 2, this chapter investigates the effect on chemo-mechanical damage by: *i*) the geometrical features of the metal soap nucleus, *ii*) the profile of the saturated fatty acid concentration imposed on the paint sample, and *iii*) the metal soap nuclei distribution in a paint sample. Numerical simulations are performed on systems representing a paint layer containing either a single metal soap nucleus, or multiple nuclei, thereby mimicking the growth of the metal soap crystal and the induced crack formation. From the numerical analyses, it has been observed that both the fatty acid concentration profile and the aspect ratio of the metal soap nucleus have a significant influence on the amount of crack formation in the paint layer. On the contrary, the growth rate and the average radius of the metal soap crystal appear to be virtually insensitive to the concentration profile and nucleus geometry. Further, the locations of the metal soap nuclei within the domain may significantly influence their growth rate. Additionally, the presence of multiple crystals can cause asymmetrical growth of a crystal

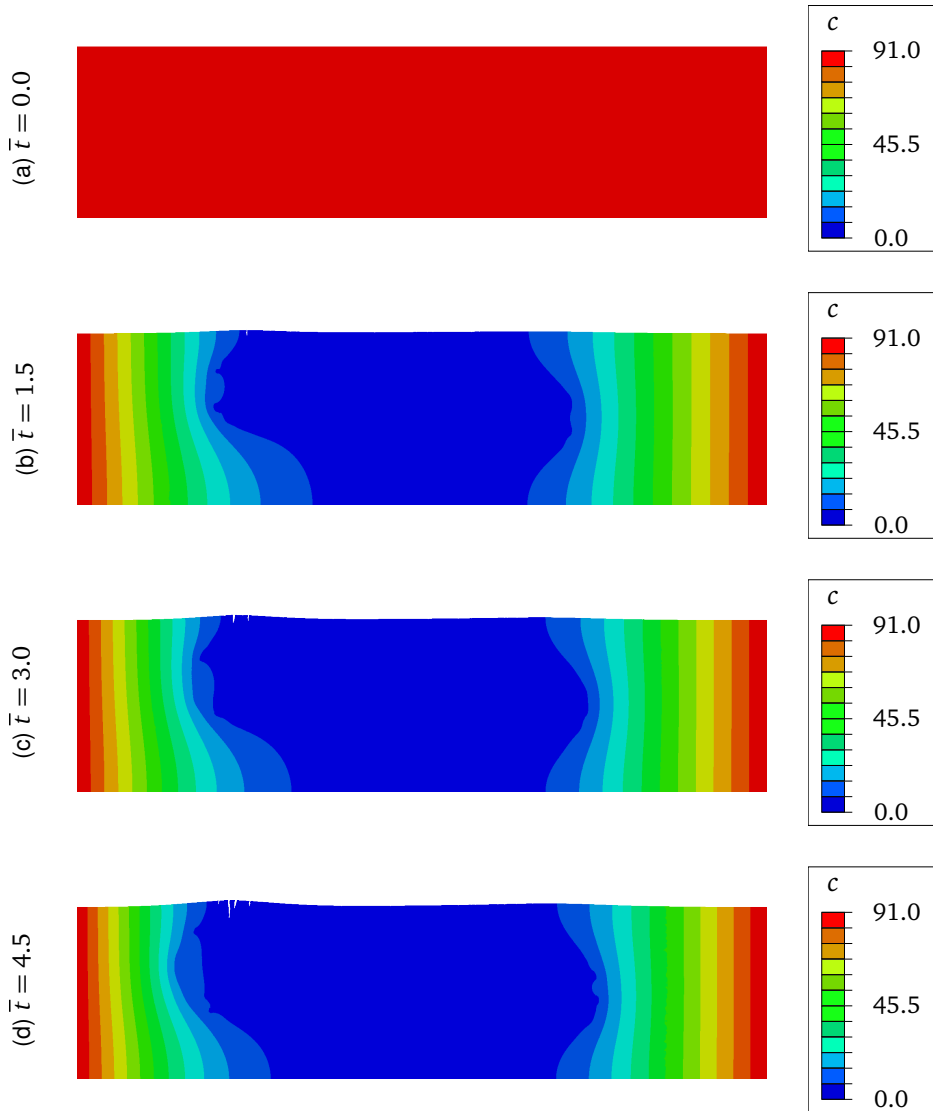
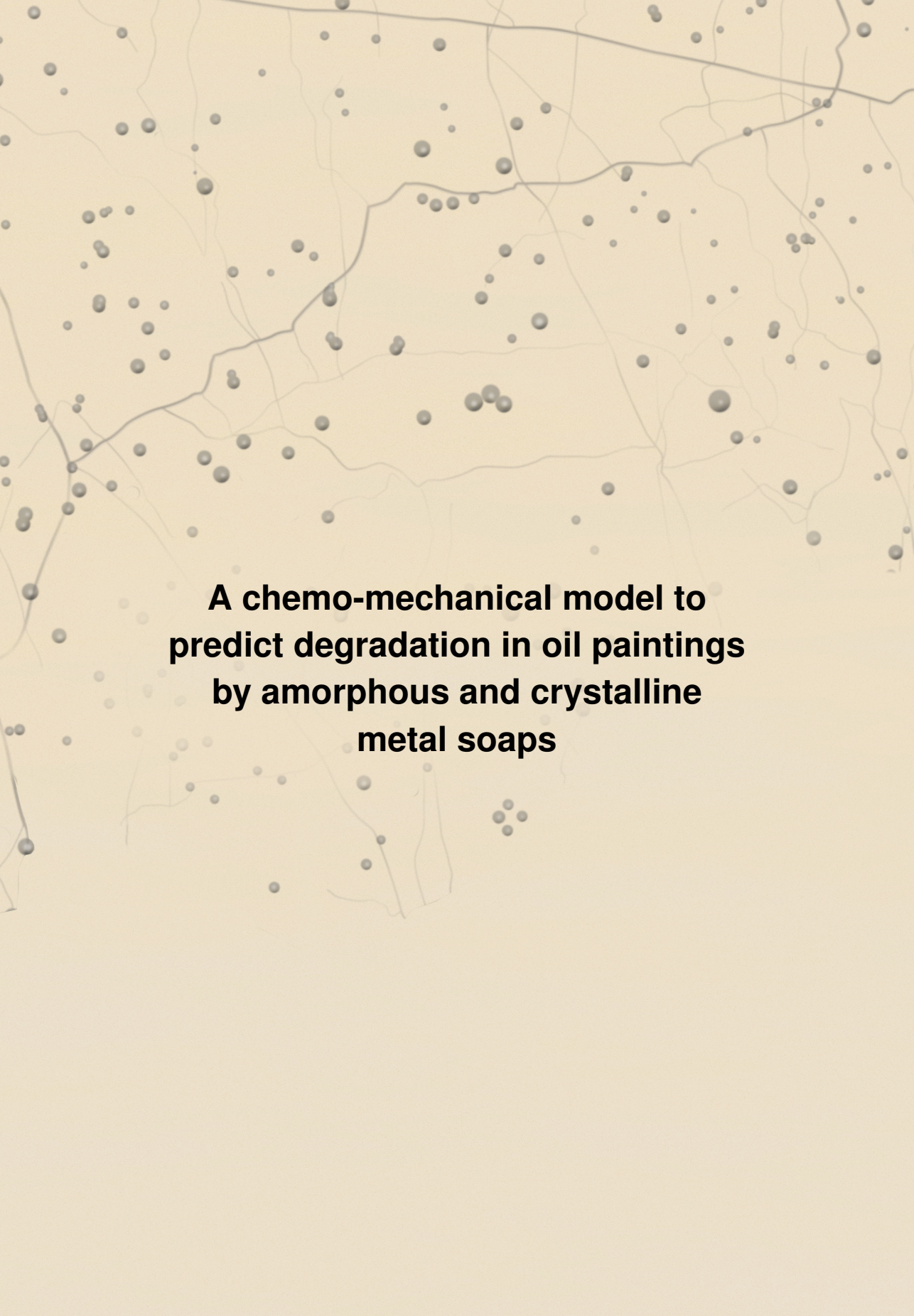


Figure 3.11: Time evolution of the distribution of saturated fatty acids in the paint layer. The contour plot shows the concentration of saturated fatty acid (c), in mol/m^3 .

from its original nucleus. Both phenomena can be ascribed to the heterogeneous spatial development of the fatty acid concentration profile over time.

In order to limit crack growth, it is worth investigating how particular conservation interventions (e.g. the use of specific solvents) and conservation procedures (e.g. controlling the indoor climate conditions) may influence the saturated fatty acid concentration profile and the rate of the chemical reaction. Another topic for future research is the accurate determination of material parameters of historical paints from dedicated, small-scale experiments, such as nanoindentation tests [41, 47, 48, 103], which will support an accurate validation of the modelling results. Finally, the present model will be extended to incorporate the reversible part of the chemical reaction that relates to the formation of amorphous metal soap, which is expected to provide a more realistic representation of the time scale at which metal soap growth occurs.

The background of the slide features a light beige or cream-colored surface. Scattered across this surface are numerous small, semi-transparent grey circles of varying sizes. These circles are interconnected by a network of thin, light grey lines that form a complex, web-like pattern. The overall appearance is reminiscent of a microscopic view of a material or a network diagram.

**A chemo-mechanical model to
predict degradation in oil paintings
by amorphous and crystalline
metal soaps**

Chapter 4

A chemo-mechanical model to predict degradation in oil paintings by amorphous and crystalline metal soaps

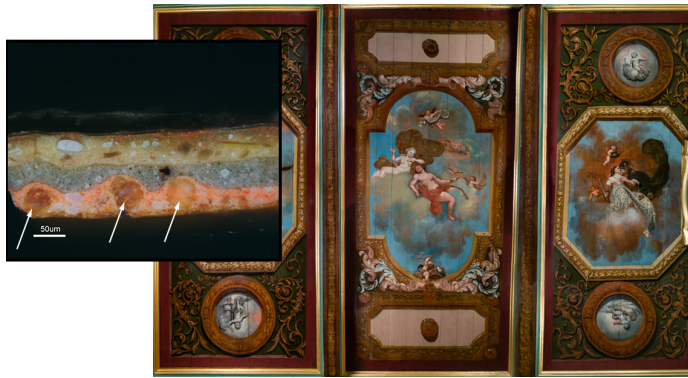
Metal soap formation is recognised as a critical degradation mechanism in historical oil paintings, which threatens the preservation of museum collections worldwide. Metal soaps form via a complex sequence of chemical reactions between metal ions released by the pigments and saturated fatty acids originating from the drying oil. The latest advances in chemistry research suggest that metal ions and saturated fatty acids may initially react by means of a reversible reaction, which leads to the formation of metal soaps in an amorphous state. Metal soaps may subsequently crystallise via an irreversible reaction into large aggregates that deform the paint layers, potentially triggering delamination, cracking, and ultimately flaking of the paint. This chapter¹ proposes a chemo-mechanical model to predict metal soap formation and the consequent mechanical damage in historical oil paintings. The chemical process is described in terms of a set of diffusion-reaction equations, which account for *both* the reversible reaction between free saturated fatty acids and metal ions forming amorphous metal soap, and the subsequent irreversible reaction to crystalline metal soap. The chemical model is two-way coupled with a mechanical model that effectively describes the cracking processes caused by metal soap formation and growth. The coupling is generated from the mechanical model by accounting for the development of a chemically-induced growth strain in the crystalline metal soap. In addition, the presence of cracks locally hampers the diffusion of chemical species, which is taken into account in the chemical model through a dependency of the diffusion parameter at the crack faces on the amount of generated mechanical damage. The spatial development of the crystalline metal soap phase is simulated by using a tailor-made scanning algorithm that identifies the reaction zone in which metal soap formation takes place. The proposed model is calibrated on experimental data presented in the literature. The model is subsequently applied to analyse two numerical examples that are representative of typical metal soap-related degradation processes observed in historical oil paintings, revealing that the growth process of crystalline metal soap, the deformation of the paint surface, and the consequent cracking and delamination patterns are predicted in a realistic fashion.

¹This chapter is based on:

[40] G.J.A.M. Eumelen, E. Bosco, A.S.J. Suiker, and J.J. Hermans. *Submitted*.

4.1 Introduction

The process of metal soap formation and growth has been identified by cultural heritage conservators as one of the most crucial degradation mechanisms for the appearance, integrity and longevity of historic oil paintings [30, 120]. Metal soaps typically appear as opalescent aggregates that deform the pictorial layers, possibly protruding through the paint surface [29, 75, 87, 121]. Metal soaps may additionally lead to an increased transparency of the paint, thereby revealing the colour of the underlying paint layers [121]. Metal soaps do not only influence the visual appearance of oil paintings, but may also promote cracking, delamination and ultimately flaking of the paint [62, 105, 140]. Two striking examples of metal soap-induced degradation phenomena can be observed in Figure 4.1. Figure 4.1(a) illustrates a ceiling painting located in the Room of Trustees of the Burgerweeshuis in Zierikzee, The Netherlands, in which multiple metal soap crystals have formed inside the orange-red bottom paint film, causing a substantial deformation of the above pictorial layers. Figure 4.1(b) represents *View of Delft* by Johannes Vermeer (Mauritshuis, The Hague, The Netherlands), in which a distinguishable, large metal soap aggregate has protruded through several paint layers and has reached the paint surface. Metal soap formation and growth are governed by a complex sequence of chemical reactions, as schematically depicted in Figure 4.2. Oil paintings consist of layers of a drying oil binding medium (typically linseed oil), which contain pigment particles and adhere to a substrate made of prepared canvas or wood. From a chemical point of view, drying oils are triglycerides, composed of three fatty acid molecules bound to a glycerol backbone via an ester bond. Fatty acids are carboxylic acids, i.e. organic compounds of carbon, oxygen and hydrogen, with long hydrocarbon chains [95]. Most of the fatty acids chains in a drying oil are *unsaturated*, containing one or more C=C bonds. However, *saturated* fatty acids, such as palmitic and stearic acids, are also present in the oil binder, representing approximately 5–15% of the total fatty acid content. During paint drying, the unsaturated fatty acid chains in the oil binder react by means of autoxidation reactions to form a densely cross-linked polymer network [9, 14, 165]. Moreover, on a larger time scale, due to the presence of water molecules in the paint film, the ester bonds between the fatty acid chains and the glycerol backbone can be broken by means of hydrolysis reactions [9, 13, 161, 162]. This leads to the release of free saturated fatty acids as a reaction product [36]. The process of metal soap formation is especially relevant in the case of lead- or zinc-based pigments, which are present, for instance, in the common lead white and zinc white paints [88]. Lead and zinc ions that are released from the pigments may become complexed with the carboxyl groups (COOH) of the polymer network, forming an ionomer [8, 10, 70, 71], see Figure 4.2(a). The free saturated fatty acids present in the system may further react with the metal ions from the ionomer, forming complexes of amorphous metal soaps, see Figure 4.2(b). The formation of amorphous metal soaps is expected to be a reversible process, for which the metal ions can be bound either to the carboxylic acid groups of the ionomer or to those of the free saturated fatty acids [70]. If the local concentration of amorphous metal soap becomes sufficiently high, it can subsequently crystallise by means of an irreversible chemical reaction and coalesce into larger metal soap aggregates, reaching diameters varying between 50 and 500 μm [121], see Figure 4.2(c).



(a) Ceiling painting with allegorical representations, 1680, Room of Trustees, Burgerweeshuis, Zierikzee, The Netherlands (Photo: Wim Ruigoord).



(b) Johannes Vermeer, *View of Delft*, ca. 1660–1661, Oil on canvas, Mauritshuis, The Hague, The Netherlands.

Figure 4.1: Examples of metal soap-induced degradation mechanisms. (a) The detail shows a dark-field image of a sample cross-section taken from the red sky of Justitia and Mars in a Warm Embrace, right painting. In the bottom orange-red paint layer, which contains lead white and red lead, three lead soap protrusions have formed. An interface undulation can be observed in this cross-section, whereby the crystals in the bottom layer start to penetrate the layers above [152]. (b) The detail shows a bright-field image of a paint cross-section taken at the left edge of the painting, where the green (now blue) bush is painted over the red-tiled roof, showing the formation of large metal soap protrusions in the dark-red paint layer that have erupted through the blue-green surface paint layer [166, 167].

Figure 4.3 shows the internal material structure of a metal (zinc) soap nucleus at the nano-scale. The image, which has been taken from [73], has been obtained by using transmission electron microscopy, and clearly illustrates that the crystalline metal soap dendrites (indicated in red) that have developed inside the nucleus are surrounded by paint material (indicated in blue) based on a linseed oil polymer. In other words, the metal soap nuclei, and also the larger aggregates developing from these nuclei, are not fully occupied by crystalline metal soap, but also contain paint material, as confirmed from other

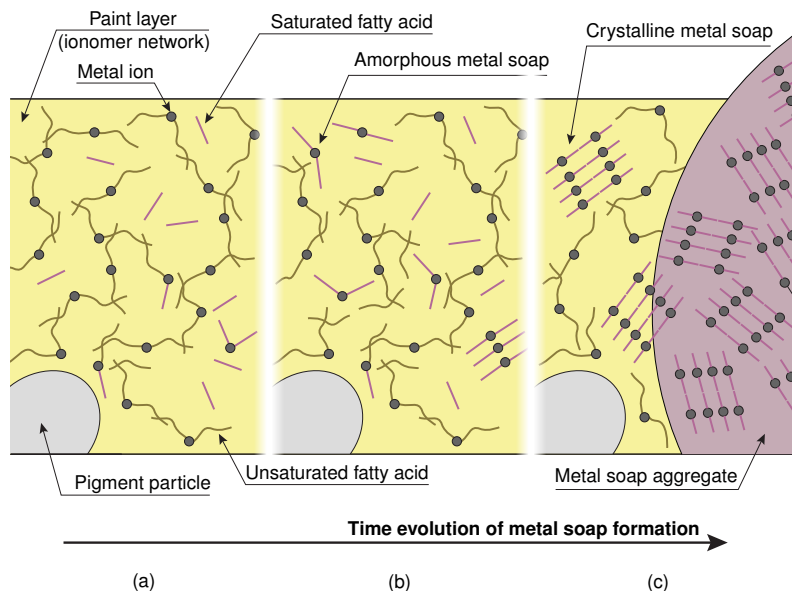


Figure 4.2: Schematic representation of the processes governing metal soap formation. (a) During the drying process of the paint film, the oil binder polymerises into a densely cross-linked polymer network by means of autoxidation reactions and releases free saturated fatty acids as a degradation product. Metal ions, which are released from the pigment particles, become complexed with the polymer network, thereby forming an ionomer. (b) Metal ions from the ionomer react by means of a *reversible reaction* with the free saturated fatty acid molecules to form amorphous metal soap. (c) Amorphous metal soap crystallises by means of an *irreversible reaction* and grows in large metal soap aggregates.

experimental studies [63, 129]. For simplicity reasons, however, in the present chapter the metal soap nuclei and aggregates will be designated as “metal soap crystals”, and in the model formulation are effectively treated as homogeneous and isotropic. The latter assumption is reasonable, as the model refers to the length scale associated to the thickness of a paint layer, i.e. the micro-scale, which is considerably larger than the nano-scale considered in Figure 4.3. Nevertheless, in the numerical simulations the initial concentration of metal ions will be determined by considering that the aggregates are not fully occupied by crystalline metal soap, which essentially means that only a certain fraction of the metal ions present in the initial paint material is available for metal soap formation.

The process of metal soap formation has been primarily investigated in the literature from a chemical perspective, by focusing on the *in situ* identification of metal soap in historic paintings [23, 89, 122, 137, 163], or by exploring the kinetics of the chemical reaction [28, 83, 104] and the composition of metal soap aggregates [72]. On the contrary, only a few studies are available that investigate the consequences of metal soap formation on the mechanical response of paint films. In [161], it has been reported that metal soap formation can contribute to an increase of oil paint stiffness and brittleness. Moreover, the presence of metal soap aggregates has been associated to micro-cracks and delamination phenomena [62, 105, 130, 140], which are triggered by the mechanical strain (and thus

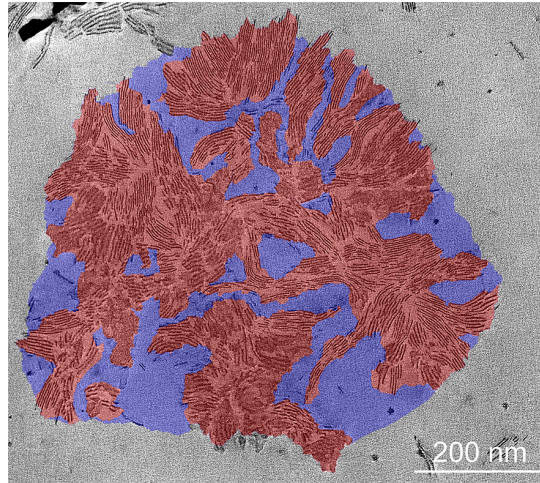


Figure 4.3: Transmission electron microscope (TEM) bright field image of a metal soap nucleus, which contains crystalline zinc soap dendrites (indicated in red) that are surrounded by paint material (indicated in blue) based on a linseed oil polymer. The picture (without the colours) is taken from [73].

stress) generated in the painting system under metal soap growth. Recently, a computational chemo-mechanical model has been proposed that predicts damage development in paint layers as a result of metal soap formation and growth [37] (see also Chapter 2). The model departs from a simplified chemical description in which the intermediate state of amorphous metal soap is neglected and *only* the irreversible crystallisation process is modelled. Accordingly, the diffusion reaction model is formulated solely in terms of the concentration of saturated fatty acid and the volume fraction of crystalline metal soap formed. The chemo-mechanical model is implemented within a finite element framework, whereby the chemical and mechanical fields are solved in an incremental-iterative fashion, using a staggered solution scheme.

Departing from the formulation presented in Chapter 2, in the present chapter the chemo-mechanical model for metal soap formation is substantially enhanced by accounting for *both* the reversible reaction between free saturated fatty acids and metal ions forming amorphous metal soap, and the irreversible reaction governing the process of metal soap crystallisation. Along similar lines as the one-dimensional formulation proposed in [67], these chemical processes are described via a set of (diffusion-)reaction equations in terms of the concentrations of free saturated fatty acids, metal ions, amorphous metal soap and crystalline metal soap. Although, in principle, both the free saturated fatty acids and the metal ions can diffuse in the ionomer [156], metal ion diffusion is ignored here, as this process typically is very slow compared to fatty acid diffusion. As a consequence, the free saturated fatty acids are considered as the sole diffusing species, for which a diffusion-reaction equation is formulated, whereas the time evolution of the concentrations of the metal ions and the amorphous and crystalline metal soaps are governed by reaction equations. Along the lines of Chapter 2, the coupling between the diffusion-reaction model and the mechanical analysis is obtained by defining a chemically-induced growth strain, which quantifies the effect of the expansion of the growing metal soap

crystal on the stress field generated in the painting. Additionally, the local change in the mechanical properties associated to the formation of crystalline metal soap is computed by a basic phase transformation model, whereby the effective stiffness is obtained as the volume average of the properties of the material phases present in the specific material point. Mechanical equilibrium equations finally complete the definition of the mechanical problem. The paint geometry is discretised into plane-strain continuum elements that represent the two-dimensional bulk responses of the metal soap and paint materials. Further, in order to describe the onset and propagation of discrete cracks at arbitrary locations in the paint domain, cohesive interface elements are placed between all continuum elements modelling the paint configuration, in correspondence with the approach originally proposed in [171]. The constitutive behaviour of a crack is defined in accordance with the interface damage model proposed in [25]. The presence of cracks locally hampers the diffusion of the free saturated fatty acids, which is accounted for by specifying the constitutive relation between the flux and the concentration of free saturated fatty acids across a crack as a function of the mechanical damage. Consequently, the chemo-mechanical model is two-way coupled.

The enhanced chemo-mechanical model proposed in this chapter is applied to analyse two different boundary value problems, which are representative of typical metal soap-related degradation mechanisms observed in historical paintings. The first boundary value problem focuses on the interplay between the growth process and coalescence of *multiple metal soap crystals* and the crack patterns generated in a *single-layer paint system*. The second boundary value problem refers to a *multi-layer paint system* composed of an upper pictorial layer and a supporting ground layer, and focuses on the competition between surface cracking in the upper layer and delamination at the interface between the two layers, as induced by the formation and growth of a *single metal soap crystal* in the ground layer.

This chapter is organised as follows. Section 4.2 describes the chemo-mechanical modelling framework, including the diffusion-reaction equations, the mechanical model and the coupling terms between the two physical processes. In Section 4.3, the chemical properties that serve as input for the diffusion-reaction model are calibrated based on the experimental results presented in [67]. Section 4.4 treats the definition of the geometry, material properties, initial and boundary conditions, and the numerical results of the *single-layer paint model*. In Section 4.5, the geometrical details, input parameters, initial and boundary conditions, and simulation results of the *multi-layer paint model* are discussed. Finally, the main conclusions of the work are summarised in Section 4.6.

4.2 Model description

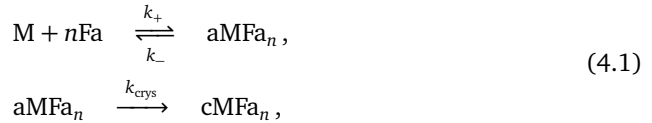
The chemo-mechanical model describing the degradation of oil paintings by metal soap formation consists of a chemical model and a mechanical model, which are successively described in Sections 4.2.1 and 4.2.2. The numerical solution procedure that is used to solve the coupled chemical and mechanical models is reviewed in Section 4.2.3.

4.2.1 Chemical model

Departing from the formulation presented in Chapter 2, in the present chapter the chemo-mechanical model for metal soap formation is substantially enhanced by accounting for *both* the reversible reaction forming amorphous metal soap, and the irreversible reaction leading to metal soap crystallisation. The proposed model is based on the following assumptions. First, the initial state of the domain is assumed to be represented by

an ionomer characterised by given concentrations of free saturated fatty acids and metal ions. Accordingly, the autoxidation reactions leading to the formation of the ionomer and the reactions associated to the release of free saturated fatty acids by the oil binder and the metal ions from the pigments are not explicitly modelled. Moreover, despite that the paint is a heterogeneous material, composed of the ionomer with embedded pigment particles, it is here treated as an equivalent, homogeneous continuum, characterised by effective chemical and mechanical properties. The paint and the fully crystallised metal soap are the two physical material phases that together form the paint system. Conversely, the free saturated fatty acids, the metal ions, and the amorphous metal soaps only enter the model through their concentrations. It is assumed that metal soap crystallisation develops from pre-existing crystal nuclei, which are small regions in which fully crystallised metal soap is present, see Figure 4.3. The chemical reactions leading to metal soap formation are enforced to occur in a (moving) transition region named the “reaction zone”, which is located at the interface between the metal soap crystal and the adjacent paint material.

The chemical process leading to the formation of crystalline metal soap can be expressed by means of two successive chemical reactions [67]:



in which $M + nFa$ denotes a metal ion M reacting with n free saturated fatty acid molecules Fa . The term MFa_n indicates the metal soap complex, for which prefixes “a” and “c” refer to the amorphous and crystalline states of the metal soap compound, respectively. Further, k_+ and k_- are the rate constants for the formation and dissolution of amorphous metal soap, respectively, while k_{crys} is the rate constant of the irreversible crystallisation reaction. In the present chapter lead-based pigments will be considered, for which $n = 2$. The chemical reactions described by Equation (4.1) can be converted to a system of diffusion-reaction equations, expressed in terms of the individual species that are involved in the chemical process, i.e. saturated fatty acids, metal ions, and amorphous and crystalline metal soaps. However, the diffusion process of saturated fatty acids is characterised by a significantly smaller characteristic time scale than that of the metal ions [8] and of the amorphous or crystalline metal soap compounds. Hence, metal ion diffusion and amorphous metal soap diffusion are ignored, and the free saturated fatty acids are selected as the sole diffusing species.

Based on the above assumptions, the chemical process is defined by the following system of coupled (diffusion-)reaction equations [67]:

$$\begin{cases} \frac{\partial [M]}{\partial t} = -Q_{aMFa_2}, \\ \frac{\partial [aMFa_2]}{\partial t} = Q_{aMFa_2} - Q_{cMFa_2}, \\ \frac{\partial [cMFa_2]}{\partial t} = Q_{cMFa_2}, \\ \frac{\partial [Fa]}{\partial t} - \nabla \cdot (D \nabla [Fa]) = -2Q_{aMFa_2}. \end{cases} \quad (4.2)$$

Here $[i]$, with $[i] \geq 0$, represents the available concentration of the chemical species i , with $i = Fa, M, aMFa_2$, and $cMFa_2$. Further, t represents time, and $\nabla \cdot$ denotes the

divergence operator, with ∇ being the gradient operator. Finally, \mathcal{D} indicates the diffusion coefficient.

Refer first to Equations (4.2)₁–(4.2)₃ that describe the development of the concentration of the species $i = M, \text{aMFa}_2$, and cMFa_2 that react but do not diffuse. The minus sign in front of some of the reaction terms Q_i indicates that, if the value of Q_i is positive, the corresponding species i is consumed during the specific chemical reaction. Define now \mathcal{R}_i^+ as the reaction rate of the reactants, which characterises the “forward reaction”, and \mathcal{R}_i^- as the reaction rate of the reaction products, characterising the “backward reaction”. Following [131], the reaction terms Q_{aMFa_2} and Q_{cMFa_2} can be expressed as

$$\begin{aligned} Q_{\text{aMFa}_2} &= \mathcal{R}_{\text{aMFa}_2}^+ - \mathcal{R}_{\text{aMFa}_2}^-, \\ Q_{\text{cMFa}_2} &= \mathcal{R}_{\text{cMFa}_2}^+. \end{aligned} \quad (4.3)$$

Note that Equation (4.1)₂ describes an irreversible chemical reaction. Therefore, in Equation (4.3), the reaction term Q_{cMFa_2} is prescribed to be non-negative, $Q_{\text{cMFa}_2} \geq 0$. The specific expressions for the forward and backward reaction rates in Equation (4.3) can be formulated in terms of the concentrations of the involved species, raised to a power equal to their stoichiometric coefficient [131, 178]. Considering the chemical reactions, Equation (4.1), and recalling again that $n = 2$, leads to

$$\begin{aligned} \mathcal{R}_{\text{aMFa}_2}^+ &= k_+[M][\text{Fa}]^2, \\ \mathcal{R}_{\text{aMFa}_2}^- &= k_-[\text{aMFa}_2], \\ \mathcal{R}_{\text{cMFa}_2}^+ &= k_{\text{crys}}[\text{aMFa}_2]. \end{aligned} \quad (4.4)$$

Inserting Equation (4.4) into Equation (4.3) finally specifies the reaction terms Q_{aMFa_2} and Q_{cMFa_2} as

$$\begin{aligned} Q_{\text{aMFa}_2} &= k_+[M][\text{Fa}]^2 - k_-[\text{aMFa}_2], \\ Q_{\text{cMFa}_2} &= k_{\text{crys}}[\text{aMFa}_2], \end{aligned} \quad (4.5)$$

which need to be substituted in the system of (diffusion-)reaction equations, Equation (4.2).

Consider now Equation (4.2)₄ that describes the diffusion and reaction process of the free saturated fatty acids [Fa]. The reaction term Q_{aMFa_2} present in the right-hand side of the equation is defined by Expression (4.5)₁, and introduces a coupling with the reaction equations, Equations (4.2)₁–(4.2)₃, of the non-diffusing species. Note further that the factor of 2 appearing in front of the reaction term Q_{aMFa_2} in Equation (4.2)₄ accounts for the conservation of mass and equals the stoichiometric coefficient $n = 2$ of fatty acids [Fa] in the corresponding chemical reaction, Equation (4.1)₁. Further, in accordance with the experimental observations presented in [67], the diffusion coefficient \mathcal{D} is assumed to vary between the diffusion coefficients of the two physical material phases, i.e. the paint without any metal soap and the fully crystallised metal soap. This variation is quantified by the local volume fraction of the crystalline metal soap ϕ as

$$\mathcal{D} = \phi \mathcal{D}_s + (1 - \phi)^b \mathcal{D}_p \quad \text{with} \quad 0 \leq \phi \leq 1, \quad (4.6)$$

where \mathcal{D}_p and \mathcal{D}_s are the diffusion coefficients for fatty acid diffusion in the paint and in the crystalline metal soap, with the subscripts “p” and “s” referring to “paint” and “soap”, respectively. Further, the exponent $b \geq 1$ is a constant that determines the rate at which the diffusion coefficient decreases as a function of the volume fraction ϕ of

crystalline metal soap formed. The value of ϕ is determined by the ratio between the current concentration $[cM\text{Fa}_2]$ and the maximum concentration $[cM\text{Fa}_2]_{\max}$ of crystalline metal soap, i.e.

$$\phi = \frac{[cM\text{Fa}_2]}{[cM\text{Fa}_2]_{\max}}. \quad (4.7)$$

The maximum concentration of crystalline metal soap $[cM\text{Fa}_2]_{\max}$ is dictated by the initial concentration of metal ions $[M](t=0) = [M]_0$, which, in accordance with the reaction equations given by Equation (4.1), drives the formation of amorphous and crystalline metal soaps. Based on the reaction equations, Equation (4.1), and considering that metal ions and metal soaps do not diffuse, from the conservation of mass the maximum concentration of crystalline metal soap can be computed as $[cM\text{Fa}_2]_{\max} = [M]_0$.

Equation (4.2), to be completed with appropriate initial and boundary conditions, describes the concentration development of the metal ions, amorphous and crystalline metal soaps, and free saturated fatty acids in the painting. According to this equation, metal soap formation can in principle occur at any location in the domain where free saturated fatty acids are present, provided that $\phi \neq 1$. As discussed above, the metal soap growth process is assumed to depart from a crystalline nucleus of a small, specified size, for which $\phi = 1$. The chemical reactions are allowed to occur only in a small transition region located in between the metal soap crystal and the adjacent paint material, termed the *reaction zone*. Within this reaction zone, the volume fraction of crystalline metal soap is characterised by $0 < \phi < 1$, and the evolution of all chemical species is governed by the full system of (diffusion-)reaction equations, Equation (4.2). The reaction zone is defined via a scanning algorithm that identifies the uncrystallised material points present within a small, prescribed radial distance from the crystallised material points located closest to the current boundary of the metal soap crystal, see Chapter 2 for more background information on the scanning algorithm. In the remaining domain, where either $\phi = 0$ (paint) or $\phi = 1$ (crystalline metal soap), the reaction term $Q_{cM\text{Fa}_2}$ is set to 0 and the diffusion coefficient is specified, respectively, as D_p (paint) or D_s (crystalline metal soap).

4.2.2 Mechanical model

Continuum model

The mechanical model applied in this chapter is based on the formulation presented in Chapter 2, as reviewed below. In any material point of the domain, the total strain tensor $\boldsymbol{\varepsilon}$ is defined as the sum of the elastic strain tensor $\boldsymbol{\varepsilon}^e$ and a growth strain tensor $\boldsymbol{\varepsilon}^g$:

$$\boldsymbol{\varepsilon} = \boldsymbol{\varepsilon}^e + \boldsymbol{\varepsilon}^g. \quad (4.8)$$

The growth strain tensor $\boldsymbol{\varepsilon}^g$ describes the volumetric expansion of the metal soap during the crystallisation process [16, 87, 121] and is taken to be proportional to the volume fraction ϕ of crystalline metal soap [37] (see also Chapter 2):

$$\boldsymbol{\varepsilon}^g = \phi \boldsymbol{\varepsilon}^g \mathbf{I} \quad \text{with} \quad 0 \leq \phi \leq 1, \quad (4.9)$$

where ϕ is defined in accordance with Equation (4.7), $\boldsymbol{\varepsilon}^g$ is the growth strain associated to the formation of crystalline metal soap, and \mathbf{I} is the second-order identity tensor. The formation and growth of crystalline metal soap thus induces stresses and strains in the paint layer, thereby generating a coupling between the chemical and mechanical fields.

For material points in the paint phase ($\phi = 0$), the growth strain is equal to zero, and the total strain reduces to the elastic strain:

$$\boldsymbol{\varepsilon}_p = \boldsymbol{\varepsilon}_p^e. \quad (4.10)$$

Conversely, in material points located in the fully crystallised metal soap phase ($\phi = 1$), the growth strain reaches its maximum value $\boldsymbol{\varepsilon}_s^g = \varepsilon^g \mathbf{I}$, whereby the total strain is expressed by

$$\boldsymbol{\varepsilon}_s = \boldsymbol{\varepsilon}_s^e + \boldsymbol{\varepsilon}_s^g. \quad (4.11)$$

Finally, for material points in the reaction zone, where the paint and the metal soap phases are jointly present ($0 < \phi < 1$), Equation (4.8) specifies into:

$$\boldsymbol{\varepsilon}_{rz} = \boldsymbol{\varepsilon}_{rz}^e + \boldsymbol{\varepsilon}_{rz}^g \quad \text{with} \quad \boldsymbol{\varepsilon}_{rz}^g = \phi \varepsilon^g \mathbf{I}, \quad (4.12)$$

where the subscript rz refers to “reaction zone”.

Departing from the above description, a constitutive assumption needs to be made for the two material phases considered, i.e. the paint and the crystalline metal soap. In general, the mechanical properties of oil paints depend on the type of pigment particles, drying oils and pigment to binder volume ratio, as well as the age of the paint and the specific environmental conditions, see [50, 51, 55, 111, 112]. In the present chapter, the “bulk behaviour” of the paint and the crystalline metal soap, for simplicity, is considered to be isotropic linear elastic, in accordance with the expressions

$$\boldsymbol{\sigma}_p = {}^4C_p : \boldsymbol{\varepsilon}_p^e \quad \text{and} \quad \boldsymbol{\sigma}_s = {}^4C_s : \boldsymbol{\varepsilon}_s^e, \quad (4.13)$$

where 4C_s and 4C_p are the fourth-order elastic stiffness tensors of the paint and crystalline metal soap, respectively, and $\boldsymbol{\sigma}_p$ and $\boldsymbol{\sigma}_s$ are the corresponding stress tensors. Further, the symbol “:” denotes a double tensorial contraction. In order to describe the transformation from the paint material to the crystalline metal soap material, a basic phase transformation model is constructed as follows: Consider a material point located in the interfacial reaction zone, in which both the paint and the metal soap phases are present ($0 < \phi < 1$). Here, the total strain is assumed to be the same for both phases, $\boldsymbol{\varepsilon}_{rz} = \boldsymbol{\varepsilon}_s = \boldsymbol{\varepsilon}_p$, i.e. Voigt’s assumption is adopted, as a result of which the effective Cauchy stress tensor $\boldsymbol{\sigma}_{rz}$ follows from the weighted volume average of the stresses in the individual constituents [37, 78]:

$$\boldsymbol{\sigma}_{rz} = \phi \boldsymbol{\sigma}_s + (1 - \phi) \boldsymbol{\sigma}_p \quad \text{with} \quad 0 < \phi < 1. \quad (4.14)$$

With the above constitutive models for the paint, crystalline metal soap, and their mixture in the reaction zone, Equations (4.13) and (4.14), in the absence of body forces the material response in any point of the domain is governed by the mechanical equilibrium equation

$$\nabla \cdot \boldsymbol{\sigma} = \mathbf{0}. \quad (4.15)$$

Equation (4.15) is completed by the appropriate boundary conditions.

Interface damage model

The stress field generated in a paint layer as a result of metal soap formation may trigger the onset and propagation of cracks. The discrete cracking behaviour of the paint is simulated by surrounding the continuum elements in the finite element model with interface elements equipped with a mixed-mode interface damage model. This modelling

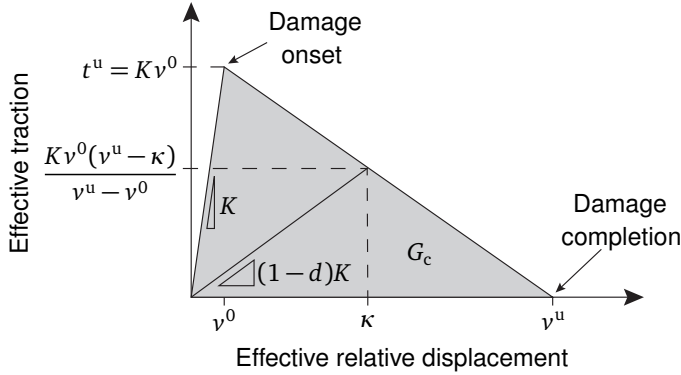


Figure 4.4: Traction-separation law of the interface damage model, taken from [25].

strategy was originally proposed in [171], and allows for the robust simulation of crack patterns at arbitrary locations and in arbitrary directions. It naturally includes the effects of crack bifurcation, crack branching and crack coalescence, as previously demonstrated for applications related to historical paints [37–39] (see also Chapters 2 and 3), wood [101, 102, 146], polymers [154], fibrous composites [26, 27, 54] and cementitious materials [147]. The interface elements are characterised by the interface damage model proposed in [25]. The fracture process in a material point initiates when the effective interfacial traction attains the value of the ultimate fracture strength of the material t^u , which corresponds to a relative crack face separation v^0 , as shown in Figure 4.4. The fracture process is defined by a linear softening branch, for which the tensile strength progressively decays as a function of a damage parameter d that can vary between 0 (no damage) and 1 (damage completion). The elastic interfacial stiffness K consequently decreases by a factor $1 - d$. The evolution of the fracture process is monitored by a damage history variable κ . The fracture process is completed when the interfacial material point has lost its strength ($d = 1$), which occurs when the relative ultimate crack face separation v^u is reached. The toughness G_c is obtained as the area under the traction-separation law, with $G_c = t^u v^u / 2$. A damage loading function is defined that governs the loading and unloading conditions during fracture. The evolution of the fracture process is described by a rate-dependent kinetic law. The adopted model additionally accounts for the mode-mixity of the fracture process, by considering a combination of the crack face separations in the normal and tangential directions of the crack. This enables to distinguish between the contributions of mode I (tension) and mode II (shear) cracking. For more details on the interface damage model and its numerical implementation, the reader is referred to [25].

The presence of cracks in the domain has consequences for the chemo-diffusive response of the system, since, across the crack surfaces, the diffusion of the free saturated fatty acids is reduced. In order to account for this coupling effect, following [37, 101], in the diffusion-reaction model the concentration of the free saturated fatty acids across a discrete crack is assumed to be discontinuous while the flux is taken as continuous. Denoting the concentration jump of free saturated fatty acids across a crack as $[[\text{Fa}]]$, the corresponding flux is $J_{\text{Fa}} = \mathbf{j}_{\text{Fa}} \cdot \mathbf{n}$, where \mathbf{j}_{Fa} is the mass flux vector of the fatty acid species Fa, and \mathbf{n} is the unit vector normal to the crack faces. The flux-concentration relation is

given by

$$J_{\text{Fa}} = \mathcal{D}_c \llbracket \text{Fa} \rrbracket, \quad (4.16)$$

where \mathcal{D}_c is the crack-reduced diffusion coefficient of the paint material, which is assumed to evolve as a function of the damage parameter d as

$$\mathcal{D}_c = (1 - d)\mathcal{D}_p. \quad (4.17)$$

4.2.3 Numerical solution procedure

The coupled chemo-mechanical analysis is performed with the aid of the commercial finite element package ABAQUS standard², employing tailored user-subroutines for incorporating *i*) the scanning algorithm described in Section 4.2.1 that is used for identifying and updating the interfacial reaction zone, *ii*) the phase transformation model applied in the reaction zone, Equation (4.14), *iii*) the interface damage model employed for modelling discrete cracking, as outlined in Section 4.2.2, and *iv*) the crack-reduced diffusion effect following from Equations (4.16) and (4.17). The chemical and mechanical field variables are solved for each time increment using a staggered, incremental-iterative update procedure, with the couplings between the chemical and mechanical fields established via a temporal extrapolation. The time increment is chosen relatively small, such that the error introduced by the time discretisation has a negligible influence on the numerical result. Each time increment starts with solving the coupled set of (diffusion-)reaction equations of the chemical model, as given by Equation (4.2). The reactions between the various chemical species are hereby considered in the actual (updated) interfacial reaction zone between the paint material and the crystalline metal soap, which is constructed by applying the scanning algorithm described in Section 4.2.1. The flux of the free saturated fatty acids across crack surfaces is determined via Equation (4.16), whereby the crack-reduced diffusion coefficient in the paint material is determined from Equation (4.17) using the damage value d computed at the previous time increment. The solution of the coupled diffusion-reaction, Equation (4.2), provides the concentration fields of all chemical species, i.e. the concentrations of the free saturated fatty acids $[\text{Fa}]$, metal ions $[\text{M}]$, amorphous metal soap $[\text{aMFa}_2]$, and crystalline metal soap $[\text{cMFa}_2]$. With this result, the volume fraction of crystalline metal soap ϕ is updated via Equation (4.7). The values of ϕ are next transferred to the mechanical analysis, where they are used for calculating the growth strain tensor $\boldsymbol{\varepsilon}^g$ in accordance with Equation (4.9). Additionally, the stresses in the paint and crystalline metal soap are computed from Equation (4.13), and the stresses inside the interfacial reaction zone are calculated as a function of ϕ via Equation (4.14). With this result, the equilibrium equations (4.15) governing the mechanical problem are solved in an iterative fashion, thereby accounting for the nucleation and propagation of discrete cracks in accordance with the interface damage model outlined in Section 4.2.2. The converged iterative procedure provides the updates of the overall displacement field and the damage parameter d in the integration points. The updated damage parameter d is subsequently transferred to the chemical analysis, after which the incremental-iterative solution procedure above is repeated for the next time increment.

²Dassault Systems Simulia Corp, Providence, RI, U.S.A.

4.3 Parameter calibration for the diffusion-reaction model

The material parameters for the chemical model described by Equations (4.2), (4.5) and (4.6), are calibrated from the experimental measurements reported in [67], which are briefly reviewed in Section 4.3.1. The calibration procedure applied and the parameter values obtained are presented in Sections 4.3.2 and 4.3.3, respectively.

4.3.1 Review of the experiment

The experiments discussed in [67] focused on measuring the time evolution of the concentration of crystalline metal soap forming from a lead-containing ionomer exposed to a fatty acid solution. An ionomer sample was prepared that consisted of a lead sorbate³ mixed with cold-pressed linseed oil. This mixture was spread on a glass plate and cured overnight in an oven. The resulting ionomer film, which was characterised by an average thickness $l_s = 150 \mu\text{m}$, was next placed at the bottom of an attenuated total reflection-Fourier transform infrared (ATR-FTIR) measurement cell. The measurement cell was subsequently filled with a solution of fatty acid (i.e. palmitic acid) and acetone over a height l_{Fa} that ranged between 10 mm and 20 mm, as schematically indicated in Figure 4.5(a). In the designed experimental setup, a one-dimensional diffusion-reaction process is activated, whereby the fatty acid diffuses along the vertical direction in the fatty acid-acetone mixture. Furthermore, the fatty acid, together with acetone, diffuses in the ionomer sample below, whereby it reacts to form metal soap. The process of metal soap formation was monitored by measuring the concentration of crystalline metal soap formed at the bottom of the ionomer sample, using time-dependent ATR-FTIR measurements.

4.3.2 Reference model and calibration procedure

In order to identify the kinetic reaction constants and the diffusion coefficients associated to the diffusion and reaction of saturated fatty acids in the ionomer film, the experimental set-up indicated in Figure 4.5(a) has been idealised to a one-dimensional model. In this model, which is shown in Figure 4.5(b), the height of the saturated fatty acid solution and the thickness of the ionomer sample are represented by two adjacent segments of length l_{Fa} and l_s , respectively. The thickness of the ionomer sample equals $l_s = 150 \mu\text{m}$ [67]. The height of the palmitic acid-acetone solution has been taken equal to the lowest value considered in the experiments, $l_{\text{Fa}} = 10 \text{ mm}$. Note however, that a variation of this value in the range of 10 to 20 mm is expected to have a negligible effect on the experimental result, since the sample thickness l_s is much smaller than the height l_{Fa} of the saturated fatty acid solution, i.e. $l_s/l_{\text{Fa}} \ll 1$. This hypothesis has been confirmed by simulations not presented here.

In the experiment, the saturated fatty acids diffuse through the acetone solution, and further diffuse and react within the ionomer below, see Figure 4.5(b). Accordingly, the one-dimensional diffusion process in the acetone solution can be described via the diffusion equation:

$$\frac{\partial[\text{Fa}]}{\partial t} - D_a \frac{\partial^2[\text{Fa}]}{\partial x^2} = 0, \quad (4.18)$$

where D_a is the diffusion coefficient of the saturated fatty acid in acetone, whereby the subscript “a” refers to the “hosting medium” (i.e. acetone). Further, for the ionomer

³A salt from sorbic acid.

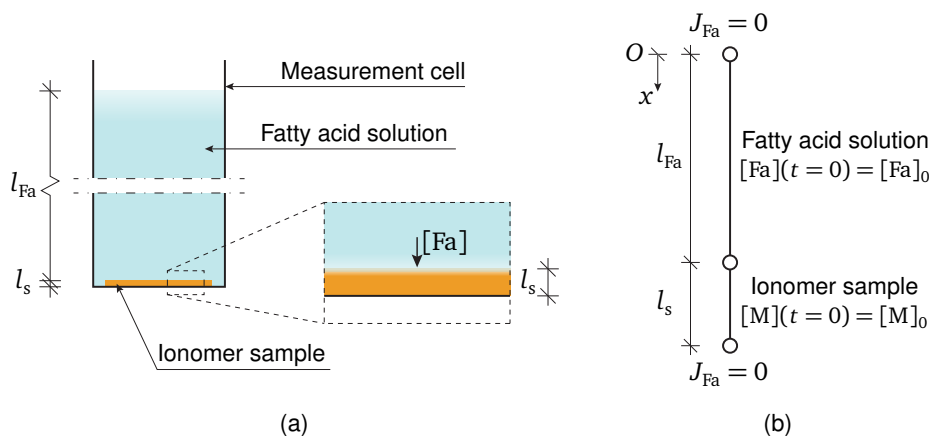


Figure 4.5: (a) Schematic representation of the experiment reported in [67]. The experimental set-up consisted of a lead-based ionomer sample with a thickness l_s located at the bottom of an ATR-FTIR measurement cell, which was filled with a mixture of palmitic acid and acetone over a height l_{Fa} . The concentration of crystalline metal soap forming from the reaction of the palmitic acid with the lead ions from the ionomer was evaluated at the bottom of the ionomer by means of ATR-FTIR measurements. (b) One-dimensional schematisation of the experimental setup presented in [67], with the corresponding initial and boundary conditions.

sample it is assumed that the diffusion-reaction processes leading to metal soap formation are governed by the one-dimensional formulation of the system of chemical equations given by Equation (4.2), complemented with the definitions in Equations (4.5), (4.6), and (4.7).

The boundary value problem described by the geometry presented in Figure 4.5(b) and governed by Equations (4.18) (acetone solution) and (4.2) (ionomer sample) must be completed by initial and boundary conditions. In the measurement cell, the initial concentration of saturated fatty acid is uniform and equal to $[Fa](t=0) = [Fa]_0 = 55 \text{ mol/m}^3$ [67]. In addition, zero-flux boundary conditions $J_{Fa} = 0$ are adopted at the external boundaries $x = 0$ and $x = l_{Fa} + l_s$, which reflect that no saturated fatty acids were added to the palmitic acid-acetone solution after the experiment had started, and that the saturated fatty acids could not diffuse outside the measurement cell. Furthermore, the initial metal ion concentration $[M](t=0) = [M]_0$ is taken as uniform within the ionomer sample and equals $[M]_0 = 160 \text{ mol/m}^3$ [67].

Equations (4.2), (4.5), (4.6), (4.7), and (4.18) have been implemented in the mathematical software program MATLAB, and solved using the standard partial differential equation solver. The computational result has been subjected to a non-linear, least-squares fitting procedure, in order to match the concentration of crystalline metal soap $[cMFA_2]$ measured at the bottom of the sample, $x = l_{Fa} + l_s$, as reported in [67]. For this purpose, the diffusion coefficient of the saturated fatty acid in acetone has been selected as $D_a = 6.1 \cdot 10^{-11} \text{ m}^2/\text{s}$ [67]. Correspondingly, the calibrated parameters are the reaction rates k_+ , k_- and k_{cryst} , the diffusion coefficients D_p and D_s , and the exponent b in Equation (4.6) that governs the transition of the diffusion coefficient in the ionomer from D_p to D_s .

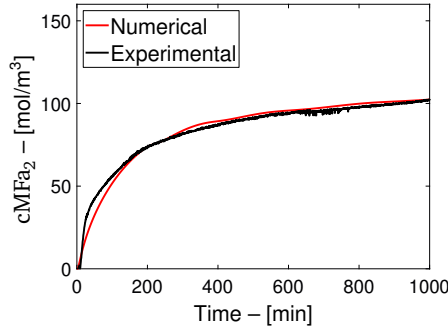


Figure 4.6: Parameter calibration for the diffusion-reaction model. Time evolution (in minutes) of the concentration of crystalline lead soap (mol/m^3), as evaluated at the bottom of an ionomer sample, $x = l_{\text{Fa}} + l_{\text{s}}$. The black line represents the experimental result reported in [67], and the red line reflects the numerical result for the one-dimensional model in Figure 4.5(b) by solving Equation (4.2) for the ionomer sample and Equation (4.18) for the fatty acid-acetone solution.

4.3.3 Result of calibration procedure

Figure 4.6 shows the time evolution of the concentration of crystalline metal soap [cMFa_2], evaluated at the bottom of the ionomer sample, as obtained from the experimental measurement (black line) and the numerical simulation (red line). From the solution of Equations (4.2) and (4.18), combined with the calibration procedure described above, the model parameters have been determined in correspondence with an R^2 -value of 0.9748. Accordingly, the kinetic reaction constants are obtained as $k_+ = 0.491 \cdot 10^{-6} \text{ m}^6 \cdot (\text{mol}^2 \cdot \text{s})^{-1}$, $k_- = 0.169 \text{ s}^{-1}$, and $k_{\text{crys}} = 0.600 \text{ s}^{-1}$. The diffusion coefficients in the paint and in the metal soap are $\mathcal{D}_p = 5.100 \cdot 10^{-11} \text{ m}^2/\text{s}$ and $\mathcal{D}_s = 3.635 \cdot 10^{-16} \text{ m}^2/\text{s}$, respectively, and the exponent defining the transition in the ionomer diffusion coefficient is $b = 2$. The calibrated parameters are summarised in Table 4.1. It is noted that the above calibration procedure somewhat differs from the calibration procedure applied in [67]. For most of the chemical model parameters this difference in the calibration procedure had a minor effect on the actual values obtained, as it should, with the exception being the value of \mathcal{D}_s in Equation (4.6). This difference, however, is consistent with a somewhat lower exponential value of $b = 2$ in Equation (4.6). It may thus be concluded that the calibrated parameters realistically represent the diffusion-reaction behaviour in the experimental system. However, it should be mentioned that the presence of acetone in the experimental system promotes the diffusion of saturated fatty acid in the ionomer film [8], such that the calibrated diffusion parameters of the fatty acid in the ionomer overestimate those in a real historical painting.

4.4 Numerical example 1: Single-layer paint system

In this section a numerical example is analysed that is representative of degradation phenomena in oil paintings associated to the formation of multiple metal soap protrusions, as observed in historical paintings, see Figure 4.1(a). The *single-layer paint system* studied consists of a lead white paint in which *three metal soap crystals* develop. The geometry is equal to that considered in Chapter 3, which was analysed in accordance with the original chemical model introduced in Chapter 2 that neglects the contribution

Parameter	Value	Unit
D_p	$5.100 \cdot 10^{-11}$	m^2/s
D_s	$3.635 \cdot 10^{-16}$	m^2/s
b	2	-
k_+	$0.491 \cdot 10^{-6}$	$\text{m}^6 \cdot (\text{mol}^2 \cdot \text{s})^{-1}$
k_-	0.169	s^{-1}
k_{crys}	0.600	s^{-1}

Table 4.1: Diffusion coefficients and reaction rates calibrated from the experiment reported in [67] in which a palmitic acid diffuses and reacts in a lead-containing ionomer, in accordance with the representation in Figure 4.5.

of the amorphous metal soap in the chemical reaction process. Hence, a comparison between the results obtained with the original model and the current, enhanced model described in Section 4.2.1 allows to reveal the important contribution of the amorphous metal soap on the degradation process. Section 4.4.1 describes the geometry of the paint layer model, the material properties, and the initial and boundary conditions. The results of the numerical simulation are presented in Section 4.4.2.

4.4.1 Definition of the problem

Geometry and FEM discretisation

The single-layer paint system is modelled as a two-dimensional rectangular domain with a thickness $l = 15 \mu\text{m}$ and a width $4l = 60 \mu\text{m}$, in which three metal soap nuclei are present, see Figure 4.7. The shape of the nuclei is taken as circular, with an initial radius equal to one tenth of the layer thickness, $r_0 = l/10 = 1.5 \mu\text{m}$. The finite element discretisation of the geometry is similar to that used in Chapter 3, whereby, after a mesh convergence study, the element size close to the metal soap nuclei was set to $0.2 \mu\text{m}$, and at the corners of the geometry to $0.5 \mu\text{m}$, as required for obtaining mesh-independent numerical results. Accordingly, the computational domain is discretised with 27030 continuum elements. For the diffusion-reaction analysis, 3-node isoparametric elements with a 3-point Gauss quadrature are used, while for the mechanical analysis 6-node plane-strain isoparametric elements with a 3-point Gauss quadrature are employed. The interface elements describing the discrete fracture processes in the FEM geometry are included by using a dedicated Python script, which first reduces the size of all the original continuum elements by 1%, then detects the opposing element edges, and subsequently places interface elements in between the continuum elements, leading to 40345 interface elements in total. For the chemical analysis 4-node interface elements with a 2-point Gauss quadrature are used, and for the mechanical analysis 6-node interface elements with a 3-point Lobatto quadrature are selected. Note that the element formulation for the mechanical interface elements is not available in ABAQUS Standard, and is therefore incorporated by means of a user-defined element routine based to the numerical implementation presented in [145]. Finally, the radial detection distance used in the scanning algorithm for defining the thickness of the interfacial reaction zone from the integration points closest to the boundary of the crystalline metal soap is selected to be $0.2 \mu\text{m}$, which corresponds to the smallest characteristic element size in the FEM model. Hence, the radial detection distance is 7.5 times smaller than the initial radius r_0 of the metal soap nucleus, and 75 times smaller than the thickness l of the paint, and has a negligible influence on the

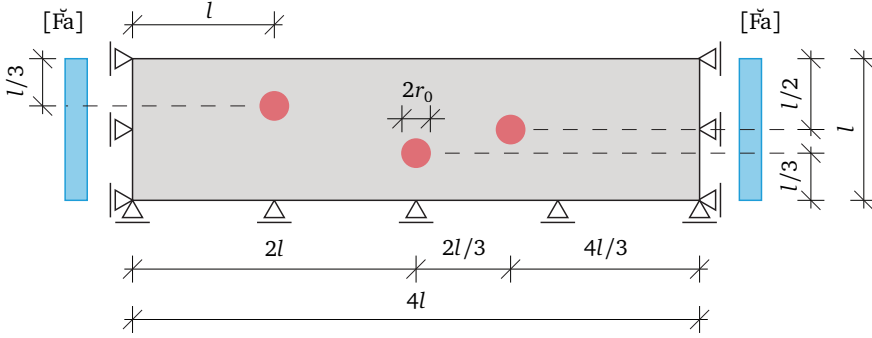


Figure 4.7: Geometry and essential chemical and mechanical boundary conditions of the *single-layer paint system*, as taken from Chapter 3. The grey area represents the paint layer and the three red circles indicate the metal soap nuclei present in the initial paint configuration.

computational results.

Material properties

The paint layer is assumed to be made of lead white paint. For the diffusion-reaction analysis the material properties obtained from the calibration procedure discussed in Section 4.3 have been used, as summarised in Table 4.1. The input parameters for the mechanical analysis are presented in Table 4.2. The Young's modulus of the lead white paint is extracted from the uniaxial stress-strain data presented in [50], leading to $E_p = 115$ MPa, and the Poisson's ratio is set to $\nu_p = 0.3$ [37] (see also Chapter 2). For the crystalline metal soap, no experimental data on the mechanical properties are available in the literature. Nevertheless, in Chapter 2 it was demonstrated that the value of the mismatch between the stiffness of the metal soap crystal and that of the oil binder influences the growth characteristics of the metal soap crystal only marginally. Hence, for simplicity the elastic constants for the metal soap crystal are taken equal to those of the paint material, i.e. $E_p = E_s = 115$ MPa and $\nu_p = \nu_s = 0.3$. The fracture properties of the paint and crystallised metal soap are derived from the stress-strain diagram reported in [50], leading to an ultimate tensile strength $t_1^u = 2.2$ MPa and a mode I fracture toughness $G_{I,c} = 0.418$ N/mm. From the simulation results presented in Chapter 3, it can be observed that the fracture process in the painting is indeed dominated by mode I cracking events. Therefore, the fracture properties in mode II are expected to only have a minor influence on the computational results, and, for simplicity, are taken equal to the properties under mode I conditions, i.e. $t_2^u = t_1^u = 2.2$ MPa and $G_{II,c} = G_{I,c} = 0.418$ N/mm. The elastic stiffness of the interface elements is set to a relatively high value, $K = 10^6$ N/mm³, which, together with the choice of an appropriate mesh fineness, ensures that artificial response contributions related to the use of an elastic interface stiffness K in the traction-separation law are negligible, see [26] for more details. Accordingly, the elastic response of the layer model is correctly determined by the continuum elements through the elastic properties of the paint and the crystalline metal soap.

To the best of the author's knowledge, for the chemical growth strain associated to metal soap formation no experimental value has been reported in the literature. Hence, the value of $\varepsilon^{g*} = 0.1$ pragmatically adopted for the plane-stress analyses presented in Chapters 2 and 3 is adjusted for the current, plane-strain analysis by requiring that the

effective, in-plane chemical growth strain in both 2D models is the same, which, in accordance with Equation (2.26) in Chapter 2, is the case for $\varepsilon^g = (1 + \nu_s)\varepsilon^{g*} = (1 + 0.3) \cdot 0.1 = 0.077$. Note hereby that the choice of representing a 3D paint layer by a 2D plane-stress or plane-strain model is somewhat arbitrary, but, in principle, leads to comparable results for the in-plane chemo-mechanical behaviour of the paint layer.

Parameter	Value	Unit
Continuum elements		
Growth strain ε^g	0.077	-
Elastic modulus E_p, E_s	115	MPa
Poisson's ratio ν_p, ν_s	0.3	-
Interface elements		
Fracture strength t_1^u, t_2^u	2.2	MPa
Fracture toughness $G_{I,c}, G_{II,c}$	0.418	N/mm
Interface elastic stiffness K	10^6	N/mm ³

Table 4.2: Mechanical properties used in the *single-layer paint model* illustrated in Figure 4.7.

Initial and boundary conditions

In the chemical model the initial concentration of saturated fatty acid is assumed to be uniform throughout the domain. The saturated fatty acid concentration has been calculated based on the composition of the lead white paint analysed in [50], which contains stearic acids⁴ and lead-based pigments. The initial fatty acid concentration $[Fa](t = 0) = [Fa]_0$ is taken as *maximal* by assuming that *all* stearic acids from the binder are available for the formation of metal soap, in accordance with dividing the volumetric weight of the fatty acid in the oil binder by its molecular weight. The volumetric weight of the fatty acid is calculated by multiplying the volume fraction of linseed oil in a lead white paint (= 0.556 [50]) by its volumetric weight (= 930 kg/m³ [2]) and by the weight fraction of stearic acid in linseed oil (= 0.05 [2]). By adopting a molecular weight for the stearic acid of 0.2835 kg/mol [3], an initial fatty acid concentration of $[Fa]_0 = 91 \text{ mol/m}^3$ is obtained.

The initial concentration of lead ions $[M](t = 0) = [M]_0$ is determined by assuming that only a specific *fraction* α of the lead ions present in the pigment particles reacts to form crystalline lead soap, see also the discussion below Figure 4.3 in Section 4.1. For this purpose, consider the density of 6700 kg/m³ of the lead white pigment [98] and the density of 1403 kg/m³ of the lead stearate (i.e. lead soap) [107]. The molecular densities of lead white pigment and lead stearate follow from dividing these densities by the corresponding molecular weights, i.e. $\rho_{\text{pigment}} = 6700/0.776 = 8634 \text{ mol/m}^3$ for the lead white pigment and $\rho_s = 1403/0.774 = 1812 \text{ mol/m}^3$ for the lead stearate. From the chemical formula of lead white pigment, $2\text{PbCO}_3 \cdot \text{Pb}(\text{OH})_2$, it can be concluded that one mole of lead white pigment contains three moles of lead ions. Hence, the total molecular density of lead ions in lead white pigment is $\rho_{\text{Pb,pigment}} = 25902 \text{ mol/m}^3$. Consider now a unit volume of original lead white paint material $V_{\text{paint},0} = 1 \text{ m}^3$, which contains a volume

⁴Note that the experiments presented in [67], which in Section 4.3 are used to calibrate the parameters of the chemical model, are based on a palmitic acid solution. However, since the molecular weights of palmitic acid and stearic acid differ by only 10% [3], it is expected that the chemical parameters calibrated in Section 4.3 realistically capture the diffusion-reaction behaviour of stearic acid.

fraction of 0.444 of lead white pigment [50] and a volume fraction of $1 - 0.444 = 0.556$ of binder. The total number of moles of lead ions in the lead white pigment then becomes $N_{\text{Pb,pigm}} = 0.444 \times 25902 = 11500$ mol. After the formation of lead soap, the *new* paint volume V_{paint} is obtained as the sum of the volume of remaining lead ions in the lead white pigment $V_{\text{Pb,pigm}}$, the volume of lead soap V_s , and the volume of the original binder material V_{bin} ($= 0.556 \text{ m}^3$):

$$V_{\text{paint}} = V_{\text{Pb,pigm}} + V_s + V_{\text{bin}}. \quad (4.19)$$

The volume occupied by the lead soap follows from

$$V_s = \frac{\alpha N_{\text{Pb,pigm}}}{\rho_s}, \quad (4.20)$$

where α is the fraction of lead ions available for the reaction into lead soap. The volume of the remaining lead ions in the paint then equals

$$V_{\text{Pb,pigm}} = \frac{(1 - \alpha)N_{\text{Pb,pigm}}}{\rho_{\text{Pb,pigm}}}. \quad (4.21)$$

The new paint volume can be calculated from the volumetric expansion induced by the free chemical growth strain ε^{g*} as

$$\frac{V_{\text{paint}} - V_{\text{paint},0}}{V_{\text{paint},0}} = 1 + 3 \varepsilon^{g*}, \quad (4.22)$$

which, with $\varepsilon^{g*} = 0.1$ [37–39] (see also Chapters 2 and 3) and an original paint volume of $V_{\text{paint},0} = 1 \text{ m}^3$, leads to $V_{\text{paint}} = 1.3 \text{ m}^3$. Combining this result with Equations (4.19) to (4.21), and solving for α , results in $\alpha = 0.051$. Hence, the initial concentration of lead ions in 1 m^3 lead white paint that is available for the reaction into lead soap becomes $[M](t = 0) = [M]_0 = \alpha N_{\text{Pb,pigm}}/1 \text{ m}^3 = 587 \text{ mol/m}^3$.

In the simulations, it is realistic to assume that the initial concentration of lead ions is zero within the crystalline lead soap nuclei. In addition, the initial concentration of amorphous lead soap in the paint material is taken as zero, $[a\text{MFa}_2](t = 0) = [a\text{MFa}_2]_0 = 0 \text{ mol/m}^3$.

The chemical boundary conditions required for the diffusion-reaction analysis need to be prescribed in terms of the *diffusing* species, i.e. the saturated fatty acids. Accordingly, at the left and right domain boundaries the value of the initial concentration $[\check{\text{F}}a] = [\text{Fa}]_0$ is imposed, see Figure 4.7. Furthermore, at the top and bottom boundaries zero-flux boundary conditions are applied, $J_{\text{Fa}} = 0$. At the bottom of the paint layer this boundary condition reflects that the free saturated fatty acids do not penetrate the substrate below.

In the mechanical model the paint layer is initially considered to be stress-free. At the bottom boundary the vertical displacement is constrained, which represents the relatively stiff support provided to the paint by the wooden or canvas substrate. At the left and right boundary of the domain the horizontal displacement is prescribed to be zero. This boundary condition represents the upper limit for the horizontal deformation constraint provided by the paint material outside the computational domain. The top boundary of the domain is stress-free, in correspondence with zero-traction boundary conditions.

4.4.2 Results

For generality, the computational results are presented in terms of dimensionless parameters, with the dimensionless time defined as $\bar{t} = t\mathcal{D}_p/l^2$, where \mathcal{D}_p and l are the diffusion coefficient in the paint material and the thickness of the paint layer, respectively. Since cracking in the paint occurs predominantly under mode I conditions, the local amount of cracking is assessed in terms of the normal (mode I) crack opening v_1 , which in dimensionless form reads $\bar{v}_1 = v_1/l$.

Figure 4.8 depicts the deformed paint layer (with the deformation plotted at true scale) for different values of the dimensionless time \bar{t} , thereby showing the progressive growth of the three metal soap nuclei and the formation of discrete cracks. The contour plot variable indicates the volume fraction ϕ of crystalline metal soap, with the red colour ($\phi = 1$) referring to fully crystallised metal soap and the blue colour ($\phi = 0$) designating the original paint material. The narrow reaction zones defining the transition from the paint material to a metal soap crystal are shown by the range of colours related to $0 < \phi < 1$. The growth of the metal soap crystals and the associated volumetric expansion clearly cause an upward deflection of the upper surface of the paint layer. This is particularly evident at the left crystal, which is able to reach the upper part of the paint layer and then erupts through the outer surface. It can be further seen that the three crystals initially grow at approximately the same rate and develop a circular shape, see Figures 4.8(a), (b), and (c). Note that this shape closely resembles that of the metal soaps visible in the cross-sectional image taken from the ceiling painting in the Room of Trustees, Burgerweeshuis, Zierikzee, see Figure 4.1(a). Nevertheless, at the largest time instant considered, $\bar{t} = 10185$, the central and right crystals have coalesced into a single, elongated metal soap aggregate, see Figure 4.8(d). This elongated shape shows resemblance with that of the metal soap crystals observed in *View of Delft* by Johannes Vermeer, see Figure 4.1(b), although the approximate crystal size of $100\ \mu\text{m}$ observed in this painting is somewhat larger than the maximal crystal size of $25\ \mu\text{m}$ following from the numerical simulation. Trivially, the maximum crystal size is determined by the specific time frame and the paint layer geometry considered in the analysis.

During the process of metal soap growth, discrete cracks are initiated once the stress in the paint material attains the fracture strength. As illustrated in Figure 4.8(c), near the top surface of the paint layer, just above the left metal soap crystal, 6 distinct mode I cracks develop. The time evolution of the dimensionless normal crack opening $\bar{v}_1 = v_1/l$ of the 4 largest mode I cracks is shown in Figure 4.9(a), and is evaluated at the upper surface of the paint layer at which the crack mouth opening is maximal. As shown in Figures 4.8(b) and (c), the first surface crack nucleates close to the vertical symmetry line of the left metal soap crystal, and partly penetrates the crystal. The additional surface cracks develop in the paint material region adjacent to the first surface crack, see Figure 4.8(c), thereby inducing a further relaxation of the tensile stresses at the paint surface. When the left metal soap crystal approaches the tips of these surface cracks, the cracks start to close, due to compressive stresses generated in the crystal by restrained volumetric expansion originating from the chemical growth strain, see Equation (4.9). As illustrated in Figure 4.9(a), the completion of crack closure occurs at approximately the same time instant for all 4 surface cracks. Note further from Figures 4.8(c) and (d) that similar mode I surface cracks develop above the right metal soap crystal, although later in time. In addition, diffusive patterns of micro-cracks are generated in between the three metal soap crystals, which occurs along trajectories directing towards their geometrical centres, see Figures 4.8(b), (c), and (d). As for the surface cracks, crack closure is observed once the metal

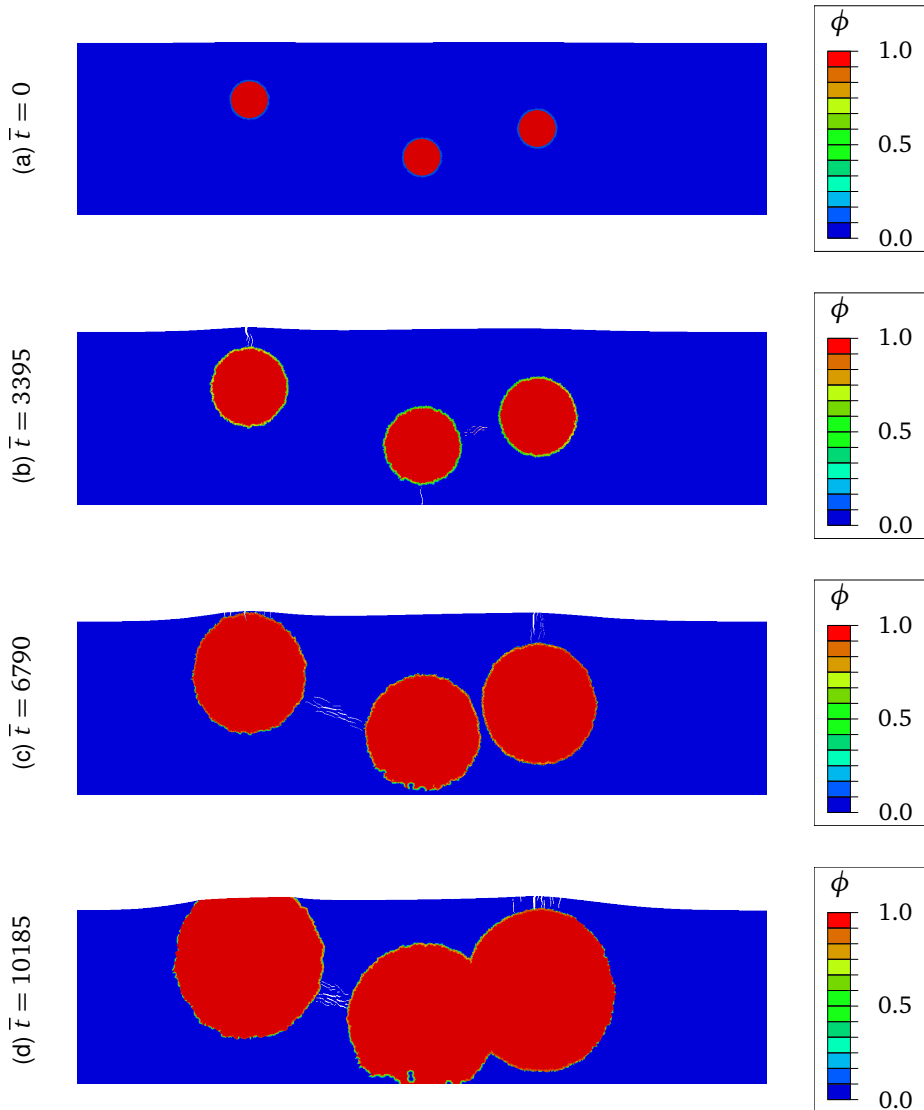


Figure 4.8: *Single-layer paint system:* Time evolution (using the dimensionless time \bar{t}) of the paint configuration (with the deformation plotted at true scale), illustrating the growth of the metal soap crystals and the discrete crack patterns forming in the paint material. The contour plot variable ϕ refers to the volume fraction of crystalline metal soap, with the lower bound $\phi = 0$ designating the paint material (blue colour) and the upper bound $\phi = 1$ indicating the metal soap crystals (red colour).

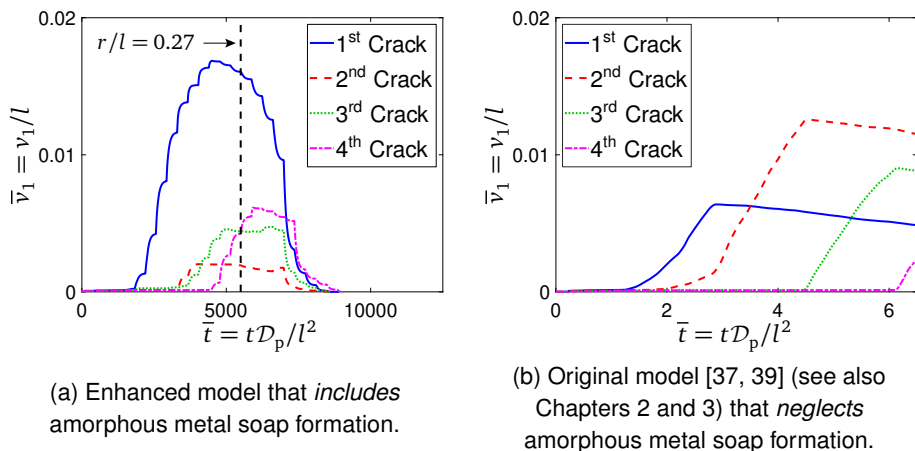


Figure 4.9: *Single-layer paint system:* Time evolution (using the dimensionless time \bar{t}) of the normalised crack opening \bar{v}_1 of 4 dominant mode I surface cracks that develop above the left metal soap crystal, as predicted by (a) the current, enhanced model that *includes* the formation of amorphous metal soap, and (b) the original model presented in Chapters 2 and 3 that *neglects* the formation of amorphous metal soap. The vertical dashed line in Figure 4.9(a) designates the specific time $\bar{t} = 5500$ at which the left metal soap crystal shown in Figure 4.8 reaches a relative size of $\bar{r} = r/l = 0.27$, which corresponds to the final crystal size reached at $\bar{t} = 6.5$ in the simulation considered in Figure 4.9(b).

soap crystals approach these micro-cracks, see Figure 4.8(d).

In order to reveal the specific influence of the enhanced chemical model on the growth processes of the crystalline metal soaps and the discrete cracks, the present numerical results are compared to those in Chapter 3 that are based on the original model proposed in Chapter 2, which, as mentioned, *neglects* the reversible reaction of amorphous metal soaps and only accounts for the formation of irreversible, crystalline metal soap. The numerical simulation presented in Chapter 3 starts from the same initial configuration as that displayed in Figure 4.8(a), and shows that the growth rate and final size and shape of the three metal soap crystals strongly depend on their precise location in the computational domain. Specifically, the two outer metal soap crystals eventually obtain a slightly oval-shaped geometry that is almost two times larger in size than that of the central, circular metal soap crystal, see Figure 3.9 in Chapter 3. This result is rather different from that shown in Figure 4.8, and can be ascribed to the fact that, by ignoring the intermediate amorphous metal soap phase, in the original model the free saturated fatty acid is consumed at a *significantly higher rate*, whereby its spatial distribution, and thus the corresponding development of metal soaps crystals, becomes non-uniform across the paint layer, see Figure 3.11 in Chapter 3. Conversely, the relatively low rate at which the free fatty acid is consumed in the current, enhanced model ensures that its spatial distribution remains uniform when time develops, thus resulting in a virtually homogeneous growth of the three individual metal soap crystals (as long as they do not coalesce).

The fracture response in Figure 4.9(a) is now compared to that in Figure 4.9(b), which illustrates the time evolution of the dimensionless normal crack opening $\bar{v}_1 = v_1/l$ of the 4 main surface cracks as computed by the original model that neglects amorphous metal

soap formation. The 4 surface cracks considered in Figure 4.9(b) are located above the left metal soap crystal, at comparable locations as shown in Figure 4.8 for the enhanced model, and appear to have similar crack widths as those in Figure 4.9(a). The simulation carried out with the original model covers a total time of $\bar{t} = 6.5$, at which the normalised average radius of the left metal soap crystal has reached a value of $\bar{r} = r/l = 0.27$. For a proper comparison with the enhanced model, in Figure 4.9(a) the simulation time corresponding to this crystal size has been indicated by a vertical dashed line. It can be observed that the vertical dashed line is related to a dimensionless time of $\bar{t} = 5500$, which is about a factor of 850 larger than the dimensionless time $\bar{t} = 6.5$ at which the crystal size $\bar{r} = r/l = 0.27$ is reached in the original model. In addition, Figure 4.9(a) illustrates that for the enhanced model the time at which the first surface crack nucleates is approximately 1300 times larger than for the original model in Figure 4.9(b). This again confirms that the addition of the amorphous metal soap phase in the enhanced model substantially delays the formation of crystalline metal soap, and thus the generation of discrete cracks, and shows that the characteristic time scale associated to the chemo-mechanical degradation of the single paint layer is increased by approximately three orders of magnitude. Specifically, from the definition of the dimensionless time $\bar{t} = tD_p/l^2$, it follows that in the enhanced model the metal soap formation process occurs over a time frame of hours to days, while in the original model it takes place over a time frame of seconds to minutes.

Although the characteristic time scale computed by the current, enhanced model is in agreement with that of the experiments reported in [67], see also Figure 4.6, it is still significantly smaller than the time scale of years to decades characterising metal soap degradation processes of historical paintings in museum collections. This difference can be ascribed to the relatively high concentration value used in the definition of the initial and boundary conditions for the saturated fatty acid. As described in Section 4.4.1, the initial and boundary conditions imposed are representative of the *maximum* saturated fatty acid concentration available for the chemical reaction process; in specific, it is assumed that *all* stearic acids from the binder are available for the formation of metal soap. It is further assumed that this maximum concentration is already present in the paint layer from the beginning of the simulation. In real, historical paintings, however, the concentrations of saturated fatty acids and metal ions gradually build up in paint layers as a result of the drying process of the paint, which typically takes place over a period of years to decades [8, 9, 70, 71, 111]. The analysis of the dependency of the characteristic time scale of the chemo-mechanical degradation process on the drying process of paint is considered to be a topic for future research.

4.5 Numerical example 2: Multi-layer paint system

In this section the influence of the formation of a *single metal soap crystal* on cracking and delamination in a *multi-layer paint system* is analysed. The geometry, material properties, and initial and boundary conditions of the multi-layer model are presented in Section 4.5.1, and the results of the numerical simulations are discussed in Section 4.5.2.

4.5.1 Definition of the problem

Geometry and FEM discretisation

The geometry of the multi-layer paint system is characterised by a $2l \times 2l$ square domain whereby $l = 50 \mu\text{m}$, which is composed of a ground layer indicated as *layer 1*, and a pictorial layer indicated as *layer 2*, see Figure 4.10. The ground layer is made of lead

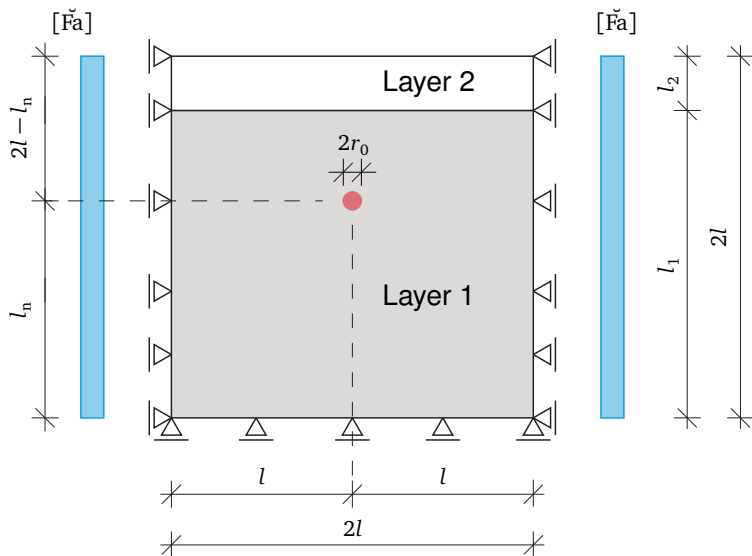


Figure 4.10: Geometry and essential chemical and mechanical boundary conditions for the *multi-layer paint system*. In the ground layer (layer 1, grey colour) metal ions are present, while the the pictorial layer (layer 2, white colour) *no* metal ions are present. The red circle indicates the metal soap nucleus initially present in the ground layer.

white paint and has a thickness $l_1 = 85 \mu\text{m}$, while the pictorial layer consists of cobalt blue paint and has a thickness $l_2 = 15 \mu\text{m}$. The ground layer contains a single, circular metal soap nucleus with an initial radius $r_0 = 1.5 \mu\text{m}$, which is located along the vertical symmetry axis of the domain, at a distance $l_n = 60 \mu\text{m}$ from the bottom of the paint system. The modelled domain is discretised by using 44856 continuum elements and 67185 interface elements. The element types applied in the simulation are the same as those selected for the single-layer model, see Section 4.4.1 for more details. The minimum element size is applied close to the metal soap nuclei and equals $0.2 \mu\text{m}$. The maximum element size taken at the left and right domain boundaries is $5 \mu\text{m}$. The radial detection distance used in the scanning algorithm for defining the thickness of the interfacial reaction zone between the metal soap crystal and the paint material is $0.4 \mu\text{m}$. It has been confirmed that for the chosen mesh density the numerical results converge within a small, specified tolerance.

Material properties

The material properties in the chemical model are presented in Table 4.1, as obtained from the calibration procedure presented in Section 4.3. For simplicity, the diffusion coefficients of the free saturated fatty acids in the ground layer and in the pictorial layer are taken the same.

The material parameters used in the mechanical model are listed in Table 4.3. For the ground layer (layer 1), the elastic modulus is derived from the uniaxial stress-strain response of an 18.75 year old lead white paint [112], leading to $E_p = 130 \text{ MPa}$. For the pictorial layer (layer 2), the elastic modulus is obtained from the stress-strain response of an 18 year old cobalt blue paint presented in [51], resulting in $E_p = 35 \text{ MPa}$. The

Poisson's ratio is taken the same for the two paint layers and equals $\nu_p = 0.3$. Since it is assumed that there are no metal ions present in layer 2, metal soap growth can only occur in layer 1, whereby the elastic properties of the metal soap crystal are taken the same as those of the lead white paint, $E_s = E_p = 130$ MPa and $\nu_s = \nu_p = 0.3$. The ultimate tensile strength of the lead white paint is obtained from the uniaxial stress-strain data presented in [112], resulting in $t_1^u = 4.5$ MPa. The mode I toughness of the lead white paint is derived from the area under the uniaxial stress-displacement response – with the displacement determined as the strain multiplied by the gauge length $l_g = 76$ mm (M. Mecklenburg, personal communication) –, leading to $G_{I,c} = 7.86$ N/mm. Similarly, the ultimate tensile strength and mode I toughness of the cobalt blue paint follow from the experimental data presented in [51], leading to $t_1^u = 0.35$ MPa and $G_{I,c} = 0.033$ N/mm, with the latter value calculated using the applied gauge length of $l_g = 7.5$ mm. For simplicity, for both layers the mode I and mode II fracture properties are taken the same, $t_2^u = t_1^u$ and $G_{II,c} = G_{I,c}$. As for the single-layer paint model analysed in Section 4.4, the growth strain is selected as $\varepsilon^g = 0.077$ and the elastic stiffness in the interface damage model equals $K = 10^6$ N/mm³. Finally, the fracture properties of the delaminating cracks that may develop along the material interface between the ground layer and the pictorial layer are assumed to be equal to the fracture properties of the pictorial layer (layer 2), which is the weaker, more brittle layer.

Parameter	Value	Unit
<i>Lead white ground layer (layer 1)</i>		
Continuum elements		
Growth strain ε^g	0.077	-
Elastic modulus E_p, E_s	130	MPa
Poisson's ratio ν_p, ν_s	0.3	-
Interface elements		
Fracture strength t_1^u, t_2^u	4.5	MPa
Fracture toughness $G_{I,c}, G_{II,c}$	7.86	N/mm
Interface elastic stiffness K	10^6	N/mm ³
<i>Cobalt blue pictorial layer (layer 2)</i>		
Continuum elements		
Elastic modulus E_p	35	MPa
Poisson's ratio ν_p	0.3	-
Interface elements		
Fracture strength t_1^u, t_2^u	0.35	MPa
Fracture toughness $G_{I,c}, G_{II,c}$	0.033	N/mm
Interface elastic stiffness K	10^6	N/mm ³

Table 4.3: Mechanical properties used in the *multi-layer paint model* illustrated in Figure 4.10.

Initial and boundary conditions

The initial conditions and boundary conditions adopted for the multi-layer paint model are comparable to those applied for the single-layer paint model discussed in Section 4.4.1. In the chemical model the initial concentration of free saturated fatty acid is assumed to be uniform throughout the domain and equals $[Fa]_0 = 91$ mol/m³. The initial concentration of lead ions is taken as uniform in the lead white ground layer (layer 1),

and equals $[M]_{0,1} = 587 \text{ mol/m}^3$. As mentioned, *no* lead ions are present in the cobalt blue pictorial layer (layer 2), in correspondence with $[M]_{0,2} = 0$. The initial concentrations of the amorphous and crystalline metal soaps are assumed to be equal to zero, i.e. $[aMFa_2]_0 = [cMFa_2]_0 = 0 \text{ mol/m}^3$. The above value for the initial concentration of free saturated fatty acid $[\check{F}a] = [Fa]_0$ is also imposed at the left and right boundaries of the computational domain. Furthermore, at the top and bottom boundaries of the domain zero-flux boundary conditions are adopted for the saturated fatty acid, $J_{Fa} = 0$.

Similar to the single-layer paint model studied in Section 4.4, in the mechanical model the multi-layer paint system is initially considered to be stress-free. The vertical displacement is prevented at the bottom boundary of the domain, while at the left and right boundaries the horizontal displacement is constrained. Finally, the top boundary is stress-free, in correspondence with zero-traction boundary conditions.

4.5.2 Results

Figure 4.11 shows the progressive growth of the metal soap crystal and the cracks and interfacial delamination generated in the multi-layer paint system, considering 4 different values of the dimensionless time \bar{t} (with the deformation plotted at true scale). The dimensionless time is defined as $\bar{t} = tD_p/l^2$, with $l = 50 \text{ }\mu\text{m}$ taken as half of the total model thickness of the paint system, see also Figure 4.10. The contour plot variable indicates the volume fraction of crystalline metal soap ϕ , with the red colour referring to the fully crystallised metal soap ($\phi = 1$) and the blue colour reflecting the original paint material ($\phi = 0$). In addition, the intact interface between the ground layer (layer 1) and the pictorial layer (layer 2) is designated by the black horizontal lines, and the grey lines in Figures 4.11(c) and (d) indicate two symmetrical, delaminating cracks emerging at the layer interface.

The metal soap crystal develops with a circular shape in the ground layer, see Figures 4.11(a) and (b), and generates a mode I surface crack in the upper, pictorial layer when approaching the interface between the two layers, see Figures 4.11(c) and (d). The volumetric expansion caused by the chemical growth strain induces an upward deflection of the upper, free surface of the paint system. In combination with the mismatch in the material properties of the ground layer and pictorial layer, relatively large shear stresses develop along the layer interface, which result in the nucleation and growth of two symmetrical, mode II delaminating cracks (indicated by the grey lines). It can be seen from Figure 4.11(d) that the delaminating cracks are close to coalescence once the mode I surface crack has grown through the entire thickness of the upper, pictorial layer, thereby forming a T-shape crack with the mode I surface crack. T-shape cracks are regularly observed in historical paintings, and may originate from metal soap formation and/or indoor climate fluctuations, often leading to local paint flaking and paint loss [17, 18].

Figure 4.12(a) presents the time evolution of the normalised normal crack opening $\bar{v}_1 = v_1/l$ of the mode I crack surface crack, as evaluated at the surface of the upper, pictorial layer at which the crack mouth opening is maximal. It can be seen that the crack grows at an approximately constant rate. Contrary to what occurs in the single-layer paint system, see Figure 4.9(a), crack closure does not occur within the time frame considered. This is due to the fact that the compressive stress caused by the constrained volumetric expansion of the metal soap crystal has partially relaxed as a result of the formation of the two mode II delaminating cracks at the layer interface, and that the metal soap crystal is not able to penetrate the upper pictorial layer due to the absence of metal ions in this layer.

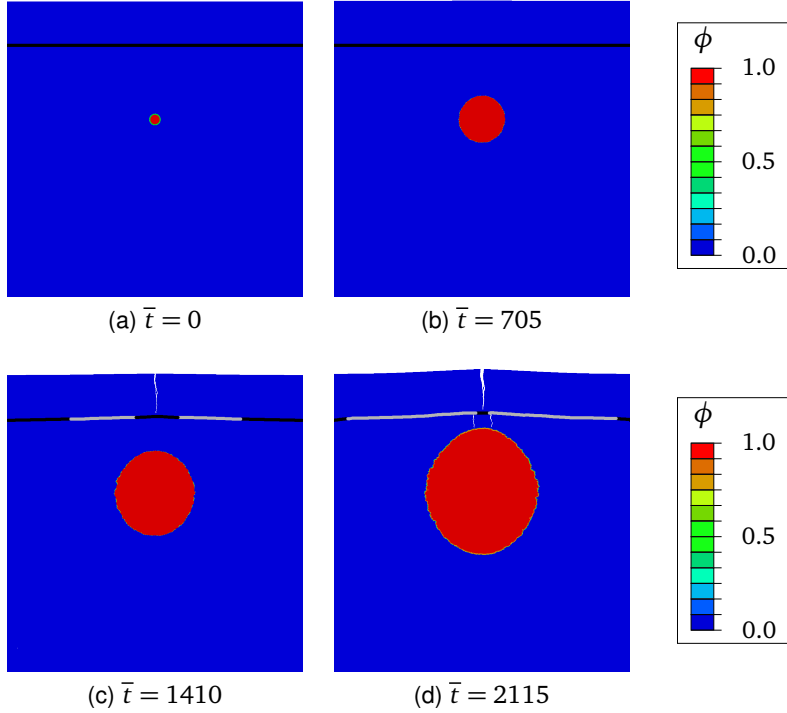


Figure 4.11: *Multi-layer paint system:* Time evolution (using the dimensionless time \bar{t}) of the paint configuration (with the deformation plotted at true scale), illustrating the growth of the metal soap crystal and the discrete cracks and delamination processes forming in the paint material. The contour plot variable ϕ refers to the volume fraction of crystalline metal soap. The black lines indicate the intact interface between the ground and the pictorial layers and the grey lines designate two symmetrical, delaminating cracks at the interface.

Figure 4.12(b) illustrates the time evolution of the two mode II delaminating cracks that develop along the layer interface, expressed in terms of the normalised delamination length, $\bar{l}_d = l_d/l$ with l_d the actual delamination length. Observe that the delaminating cracks grow in a synchronous (symmetrical) fashion at an initially relatively high rate, but that the growth rate decreases substantially when time develops. As illustrated in Figures 4.12(c) and (d), the decrease in growth rate may be caused by the fact that the delaminations get closer to the mode I surface crack with increasing time, thereby reaching a region in which the stress can not grow, such that the driving force for further delamination decreases.

It is finally noted that the small, staircase increments characterising the fracture responses in Figure 4.12 result from the discrete interplay between the local element size and the radial detection distance used in the scanning algorithm for defining the thickness of the interfacial reaction zone. Indeed, in the limit of an infinitesimal element size and an infinitesimal reaction zone, the fracture responses in Figure 4.12 are expected to become ideally smooth.

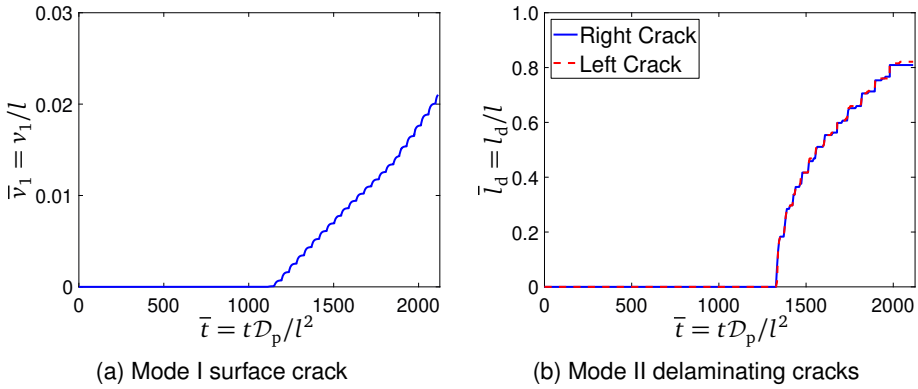


Figure 4.12: *Multi-layer paint system:* Time evolution (using the dimensionless time \bar{t}) of (a) the normalised crack opening \bar{v}_1 of the mode I surface crack, and (b) the normalised delamination length \bar{l}_d of the two mode II delaminating cracks developing along the layer interface.

4.6 Conclusions

This chapter proposes a chemo-mechanical model for the prediction of degradation phenomena in historical oil paintings as induced by metal soap reactions, such as the formation of metal soap aggregates, the deformation of the paint surface, paint cracking, and delamination between paint layers. Departing from the framework presented in Chapter 2, the chemical model has been substantially enhanced to describe *both* the reversible reaction between free saturated fatty acids and metal ions forming amorphous metal soap, and the irreversible reaction into crystalline metal soap. The chemical parameters of the *enhanced chemo-mechanical model* have been calibrated on the experimental results published in [67] that measure the time evolution of the concentration of crystalline metal soap forming from a lead-containing ionomer exposed to a fatty acid solution. Metal soap crystallisation introduces stresses in the paint that promote crack nucleation and propagation; this discrete cracking behaviour of the paint is simulated by surrounding the continuum elements in the finite element model with interface elements equipped with a mixed-mode interface damage model, which allows for the robust simulation of crack patterns at arbitrary locations and in arbitrary directions.

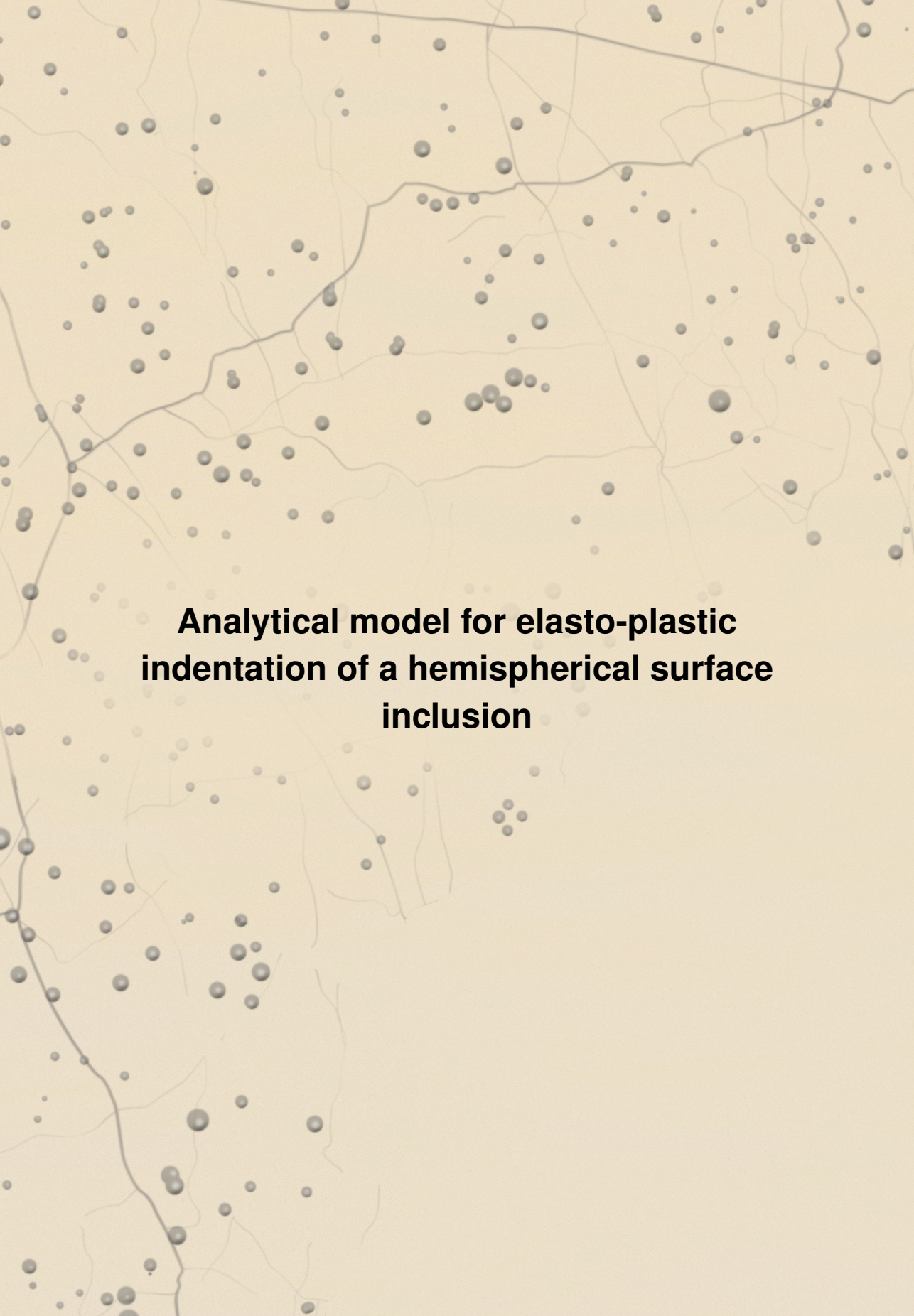
The enhanced chemo-mechanical damage model has been applied for analysing two types of boundary value problems, which capture the essential degradation mechanisms observed in historical oil paintings in museum collections. The first boundary value problem concerns the deformation and fracture response of a *single-layer paint system* under the growth of *multiple metal soap crystals*. The computational results show that the growth of the metal soap crystals and the associated volumetric expansion cause a substantial upward deflection of the top surface of the paint layer and induce multiple cracks at the layer surface and in between the individual metal soap crystals. The growth rate of the three metal soap crystals is independent of their location within the domain, which is due to the homogeneous spatial development of the fatty acid concentration in time. Further, at some stage two different metal soap crystals coalesce into a single, oval-shape metal soap aggregate that is characteristic for metal soaps observed in real, historical paintings.

The modelling results are compared to those presented in Chapter 3 that were computed by the original chemo-mechanical model presented in Chapter 2, which neglects the

intermediate, amorphous metal soap phase and only accounts for the irreversible chemical reaction into crystalline metal soap. From this comparison, it follows that the inclusion of the intermediate, amorphous metal soap phase in the model formulation increases the characteristic time scale associated to the chemo-mechanical degradation process by three orders of magnitude, which is necessary to realistically predict the time-dependency of degradation processes observed in historical paintings in museum collections. Also, local differences are observed in the metal soap growth characteristics and crack profiles predicted by the two models, which are caused by the fact that with the the current, enhanced chemo-mechanical model the saturated fatty acid profile develops homogeneously across the paint layer, while with the original chemo-mechanical model this occurs in a heterogeneous fashion.

The second boundary value problem considers the deformation, cracking and delamination processes in a *multi-layer paint system*, as induced by the growth of a *single metal soap crystal*. The multi-layer paint system is composed of a pictorial layer that is supported by a ground layer containing a metal soap nucleus. The growth of the metal soap nucleus induces a significant upward deformation of the paint surface. In addition, a mode I surface crack develops across the thickness of the upper, pictorial layer, which coalesces with two symmetrical delaminations developing along the layer interface, thereby forming a T-shape crack that ultimately may lead to local paint flaking and paint loss.

The enhanced chemo-mechanical formulation and modelling results presented in this chapter provide a better understanding of the coupled chemo-mechanical degradation behaviour of historical oil paintings due to metal soap formation. Future research will aim at refining the model input parameters by, for example, accurately determining the mechanical parameters of small paint samples taken from historical paintings via nanoindentation testing [41, 47, 48, 144, 153]. Additionally, the effects of conservation treatments [9], indoor climate conditions [90], and paint drying characteristics [111] on the process of metal soap degradation need to be explored in more detail. The interaction between metal soap-induced degradation mechanisms and climate-induced failure of historical paintings [17, 18] is another topic for future study. Such investigations eventually should lead to optimal preventive conservation measures and environmental display/storage conditions required for preserving valuable historical paintings for future generations.



**Analytical model for elasto-plastic
indentation of a hemispherical surface
inclusion**

Chapter 5

Analytical model for elasto-plastic indentation of a hemispherical surface inclusion

An analytical model is developed in this chapter¹ to deduce the elastic and plastic properties of a hemispherical inclusion embedded in the surface of a semi-infinite solid from its indentation response. The model differs from the approaches presented in the literature by starting from the analytical expressions for the elastic and elasto-plastic indentation responses of homogeneous solids, and adapting them by replacing the modulus of the homogeneous solid by an effective modulus for the embedded inclusion. The accuracy of the indentation model is established by comparing the analytical results with detailed finite element simulations for various bi-material configurations of inclusion and substrate. The elastic indentation response is substantially influenced by the elastic modulus of the substrate, whereas the plastic response is dictated by the yield strength of the inclusion. The practical applicability of the indentation model is demonstrated by making use of the measured indentation response of an embedded paint sample, as reported in the literature, to deduce the elastic modulus of the paint.

¹This chapter is based on:

[41] G.J.A.M. Eumelen, A.S.J. Suiker, E. Bosco, and N.A. Fleck. *International Journal of Mechanical Sciences*, 224:107267, 2022.

5.1 Introduction

The indentation test is a widely used experimental technique for measuring material properties, such as elastic modulus [149, 150], yield strength and hardness [64, 85, 113, 170] and fracture toughness [97], over a wide range of length scales. The test entails the measurement of the force to press a shaped indenter tip into the surface of a sample; in principle, it is a simple test to perform but is notoriously difficult to interpret [43, 174]. The application of this technique at the micro- and nano-scales can make it possible to measure the mechanical properties (elastic modulus, strength and toughness) of small-scale material systems, such as thin coatings on a substrate [59, 142], individual crystalline grains of a metallic micro-structure [34, 133, 168], and small particles embedded in a supporting matrix [19, 91], and can allow for the measurement of potential size effects [35, 45, 108, 119, 136]. Due to the local character of an indentation measurement, indentation testing is suitable for determining the properties of a material for which a limited number of (small) samples are available, for example paints that are used in valuable and historical paintings [32, 47, 48, 103, 144, 153].

Paint samples subjected to indentation are typically embedded in a relatively stiff, supporting resin. Several methods have been proposed for obtaining the elastic modulus of embedded samples from experimental indentation data. One method aims at finding the maximum indentation depth such that the measured unloading modulus can be accurately computed without due influence by the embedding material [34, 99, 138, 172]. Nevertheless, it is not always possible to limit the indentation depth to the small value required by this method, and consequently it is necessary to take into account the contribution to macroscopic compliance from the embedding material [19, 22, 48, 49, 84].

Accurate analytical and numerical solutions have been obtained for the elastic indentation of diverse heterogeneous material systems, such as coatings supported by a semi-infinite substrate [6, 53, 173] and bi-materials that contain a vertical material interface [176]. In [5] the elastic indentation of a hemispherical particle embedded at the free surface of a half space was studied, adopting the assumption that the indenter contact area remains relatively small with respect to the particle size. A first-order asymptotic solution of the Boussinesq-type problem was established, and the effect of the mismatch in elastic parameters on the indentation response was shown. However, much less is known about the relationship between Young's modulus and the macroscopic compliance of an embedded surface inclusion under relatively large indentations, as exhibited by indentation tests on embedded paint samples.

In the present chapter, an analytical model is derived to relate the elastic and plastic properties of an embedded hemispherical inclusion to its indentation response. The model differs from the approaches outlined above by starting from the analytical expressions for the elastic and elasto-plastic indentation responses of homogeneous materials, and adapting them by replacing the modulus of the homogeneous solid by an effective modulus for the embedded sample. The effective modulus is derived from the analytical solution for the elastic response of a spherical particle that contains a spherical cavity and is embedded in an infinite medium of different elastic properties. The cavity is subjected to a uniform, internal pressure. The accuracy of the analytical model is established by comparing the analytical indentation results for various bi-material configurations with those from detailed finite element simulations. The practical applicability of the indentation model is demonstrated by determining the elastic modulus of a paint from indentation measurements on an embedded paint sample as reported in the literature [48].

This chapter is organised as follows. In Section 5.2 a review is provided of analytical elastic and elasto-plastic indentation models for homogeneous materials, and the accuracy of the analytical elasto-plastic indentation model is assessed by comparing its response to that obtained from finite element simulations. In Section 5.3 an analytical expression is derived for the effective modulus of a bi-material. In Section 5.4 this analytical expression is combined with the analytical indentation models for homogeneous materials reviewed in Section 5.2 to simulate the indentation response of elastic and elastic, ideally plastic bi-materials. The accuracy of the analytical models is assessed by comparison with detailed finite element simulations. In Section 5.5 the practical applicability of the analytical indentation model is demonstrated by determining the elastic modulus of an embedded paint sample from experimental indentation data. Finally, the main conclusions of the study are presented in Section 5.6.

5.2 Review of indentation models for homogeneous materials

Similarity solutions have been developed for indentation of a half space made from a power-law solid by a headshape of power-law form (such as a paraboloid or cone) [77, 126]. The force F applied to the indenter is related to the indentation depth h and alternatively to the indentation contact radius a by [24, 127, 128, 150, 175]

$$F = C_h h^m \quad \text{and} \quad F = C_a a^n, \quad (5.1)$$

where m , n , C_h , and C_a depend upon the properties of the non-linear solid and upon the geometry of the headshape.

In general, the values of m , n , C_h , and C_a differ for loading and unloading, as unloading is usually associated with an elastic material response [135]². The specific cases of indentation of a linear elastic solid is treated in Sections 5.2.1; elastic unloading of an indented elasto-plastic solid is discussed in Section 5.2.2, and indentation of an elastic, ideally plastic solid is considered in Section 5.2.3.

5.2.1 Indentation of an elastic solid

Consider a homogeneous, elastic solid indented by a frictionless, rigid conical punch. Harding [57] and Sneddon [149, 150] showed that the force-displacement relations given by Equation (5.1) are of the form

$$F = \frac{2 \tan \alpha}{\pi} \frac{E}{1 - \nu^2} h^2 \quad \text{and} \quad F = \frac{\pi}{2 \tan \alpha} \frac{E}{1 - \nu^2} a^2, \quad (5.2)$$

where α is the semi-apex angle of the indenter and E and ν the Young's modulus and Poisson's ratio, respectively. The elastic compliance of the indenter can be accounted for by replacing the plane-strain elastic modulus $E/(1 - \nu^2)$ in the above two expressions by a reduced modulus E_r defined as [85, 127]

$$\frac{1}{E_r} = \frac{1 - \nu^2}{E} + \frac{1 - \nu_{in}^2}{E_{in}}, \quad (5.3)$$

²During elastic unloading of an elasto-plastic material, the indentation depth used in Equation (5.1)₁ refers to the recoverable, elastic part ($h - h_f$), see also Equation (5.11) and Figure 5.2.

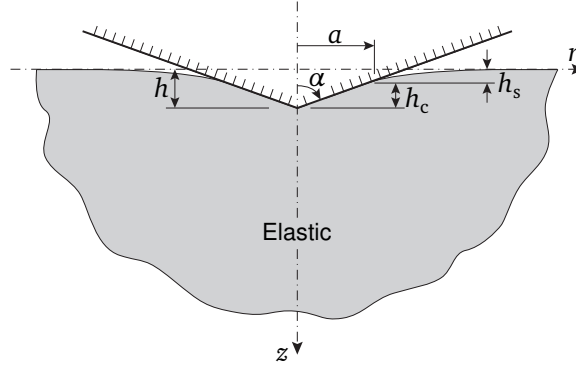


Figure 5.1: Indentation of a homogeneous, elastic material over a depth h , using an indenter with semi-apex angle α . The contact radius, contact depth, and sink-in displacement are given by a , h_c , and h_s , respectively.

where E_{in} and ν_{in} are the Young's modulus and Poisson's ratio of the indenter, respectively. Note from Equation (5.2) that the exponents m and n in Equation (5.1) have the value $m = n = 2$, and C_h and C_a are given by

$$C_h = \frac{2 \tan \alpha}{\pi} \frac{E}{1 - \nu^2} \quad \text{and} \quad C_a = \frac{\pi}{2 \tan \alpha} \frac{E}{1 - \nu^2}. \quad (5.4)$$

The geometrical parameters h and a are related by

$$h = \frac{\pi a}{2 \tan \alpha}. \quad (5.5)$$

As sketched in Figure 5.1, sink-in occurs at the edge of the indenter to a depth h_s , as a result of which the contact depth associated with no sink-in (or pile-up), $h_c = a / \tan \alpha$, is less than the true indentation depth h , such that

$$\frac{h_c}{h} = \frac{2}{\pi}, \quad (5.6)$$

via Equation (5.4). The sink-in displacement h_s follows immediately from the identity

$$h = h_s + h_c, \quad (5.7)$$

as

$$h_s = \frac{(\pi - 2)}{\pi} h. \quad (5.8)$$

The initial value of the unloading contact stiffness $S(h)$ is the derivative of Equation (5.2)₁ with respect to the indentation depth h :

$$S = \frac{\partial F}{\partial h} = \frac{4 \tan \alpha}{\pi} \frac{E}{1 - \nu^2} h. \quad (5.9)$$

Note that, for an elastic indentation, the $F(h)$ curve is reversible and the loading slope equals the unloading slope S . In contrast, for an elasto-plastic indentation the elastic

unloading slope exceeds that of the elasto-plastic loading slope. Upon inserting Equation (5.5) into Equation (5.9) and defining the projected contact area as $A_p = \pi a^2$, the Young's modulus E is related to S via [33, 127, 128]

$$E = \frac{\sqrt{\pi} S(1 - \nu^2)}{2 \sqrt{A_p}}. \quad (5.10)$$

The right-hand side of the above expression needs to be multiplied by a correction factor $1/\zeta$ when the projected contact area A_p is non-circular, with ζ equal to 1.012 and 1.034 for, respectively, square and triangular shape indenters [92].

5.2.2 Elastic unloading of an elasto-plastic solid

Equation (5.10) can be used to determine the Young's modulus from indentation tests on an elasto-plastic solid by following the procedure of Oliver and Pharr [127, 128], summarised as follows. Assume that the indenter is elasto-plastic in nature but unloading is elastic from an indentation depth $h = h_{\max}$ to a residual depth h_f at zero load, see Figure 5.2. Equation (5.1)₁ is used to fit the unloading curve over the recoverable, elastic indentation interval $(h_{\max} - h_f)$ as [127, 128]

$$F = C_h(h - h_f)^m. \quad (5.11)$$

As a result of the residual plastic strain distribution generated during loading, the value of the exponent m can be different from 2 (for conical indentation). The effect depends on the ratio between the Young's modulus E and yield strength σ_y of the material, and thereby depends upon material class, see Table 1 in [135] for specific values measured from indentation tests on different materials. From the calibrated curve Equation (5.11), the unloading contact stiffness S at the indentation depth $h = h_{\max}$ is computed as

$$S = \left. \frac{\partial F}{\partial h} \right|_{h=h_{\max}} = m C_h (h_{\max} - h_f)^{m-1}. \quad (5.12)$$

Oliver and Pharr [128, 135] further assumed that the sink-in displacement h_s is purely elastic; hence, for a conical indenter m equals 2, and h_s is related to the recoverable indentation interval $(h_{\max} - h_f)$ in a manner analogous to Equation (5.8), such that

$$h_s = \frac{(\pi - 2)}{\pi} (h_{\max} - h_f). \quad (5.13)$$

Additionally, by inserting the exponent $m = 2$ for elastic indentation in Equations (5.11) and (5.12), it follows that the initial elastic unloading stiffness S at $h = h_{\max}$ reads

$$S = \frac{2F_{\max}}{(h_{\max} - h_f)}, \quad (5.14)$$

where F_{\max} is the indentation force at the indentation depth h_{\max} , see Figure 5.2. Now combine Equations (5.7), (5.13), and (5.14) to obtain

$$h_c = h_{\max} - h_s = h_{\max} - \xi \frac{F_{\max}}{S}, \quad (5.15)$$

with the unloading contact stiffness S of the elasto-plastic solid given by the general expression, Equation (5.12), and $\xi = 2(\pi - 2)/\pi = 0.73$ for a conical indenter. A slightly

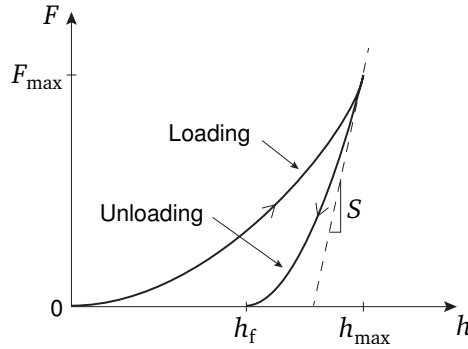


Figure 5.2: Schematic representation of the loading and unloading stages in an indentation experiment. During loading, the load F is increased from zero to a value F_{\max} , whereby the indentation h obtains a value h_{\max} . Under subsequent unloading, the indentation depth decreases towards a residual, plastic indent h_f at zero load. The reversible, elastic indentation experienced during unloading is $(h_{\max} - h_f)$. The elastic contact stiffness at the onset of unloading is S . This figure is based upon a representation presented in [127].

larger value of $\xi = 0.75$ needs to be selected when the effective indenter shape during unloading is (accurately) approximated by a paraboloid of revolution [135]. The projected contact area A_p is determined from the value of h_c as deduced from Equation (5.15), by using the fitting procedure described in [127]. Alternatively, the contact area can be measured directly by imaging of the residual indent [127, 128]. Finally, the value of A_p and S are inserted into Equation (5.10) to obtain the Young's modulus E of the indented solid, while the hardness follows from $H = F_{\max}/A_p$.

5.2.3 Indentation of an elastic, ideally plastic solid

Marsh [106] and Johnson [85, 86] assumed that conical indentation of an elastic, ideally plastic solid by a rigid, conical indenter can be idealised by the expansion of an internally pressurised, hemispherical cavity from a vanishing initial radius to a current radius equal to the contact radius a , see Figure 5.3. The stress state σ inside the void (or “core”) is a uniform pressure, $\sigma = -pI$, where I is the usual second-order identity tensor. The deformation state external to the hemispherical core is taken to be the same as that for an elastic, ideally plastic full space containing a spherical cavity of radius a and subjected to an internal pressure p [76]. The plastic zone extends from the core to an outer elastic-plastic boundary at a radius $r = c$, with $c > a$. At the interface $r = a$ between the core and the plastic zone, the radial stress in the plastic zone equals the hydrostatic stress p in the core. In addition, the radial displacement at the interface is compatible with the volume displaced by the conical indenter, assuming that the material within the core is incompressible. It is also assumed that no pile-up or sink-in occurs during indentation, such that the indentation depth is $h = h_c = a/\tan \alpha$, see Figure 5.3.

Write σ_y as the yield strength of the indented material and $\beta = (90^\circ - \alpha)$ as the inclination of the conical indenter. Then, the mean indentation pressure p_m under the indenter is given by [85, 86]:

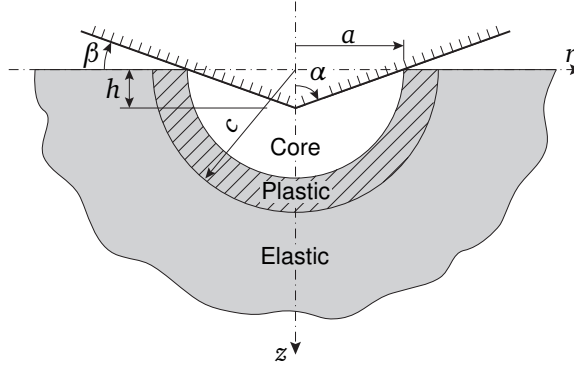


Figure 5.3: Cavity expansion indentation of a homogeneous, elastic, ideally plastic material to a depth h , using an indenter with semi-apex angle α . The indentation produces a hemispherical core of a radius equal to the contact radius a . The stress generated inside the core induces a hemispherical plastic zone with radius c .

$$\frac{p_m}{\sigma_y} = \begin{cases} \frac{p}{\sigma_y} + \frac{2}{3} & \text{for } 2 \leq \frac{E \tan \beta}{\sigma_y} \leq 27, \\ 2.8 & \text{for } \frac{E \tan \beta}{\sigma_y} > 27, \end{cases} \quad (5.16)$$

where

$$\frac{p}{\sigma_y} = \frac{2}{3} \left(1 + \ln \left(\frac{1}{3} \frac{E \tan \beta}{\sigma_y} \right) \right).$$

Equations (5.16)₁ and (5.16)₂ define the elasto-plastic and fully plastic indentation responses, respectively.

Note from Equation (5.16) that the mean indentation pressure p_m is fully determined by the dimensionless parameter $(E \tan \beta)/\sigma_y$, which can be interpreted as the ratio of the representative strain imposed by the indenter, $\tan \beta$, and the yield strain, σ_y/E [85]. The use of alternative headshapes of indenters (spherical, Vickers, Berkovich) somewhat changes the point of first yield and full yielding in Equation (5.16), but preserves the overall form of Equation (5.16) [85]. Although the solution given by Equation (5.16) is based upon the assumption that the indented material is incompressible, the effect of the value of Poisson's ratio upon the elasto-plastic response is minor [85, 86]. The compliance of the indenter is taken into account by replacing the Young's modulus E in Equation (5.16) by the reduced modulus E_r as given by Equation (5.3) [85, 86]. The force F on the conical indenter follows directly from the mean indentation pressure p_m and the projected contact area $A_p = \pi a^2$ such that

$$F = p_m A_p, \quad (5.17)$$

and consequently the constant C_a in the general expression, Equation (5.1)₂, specialises to $C_a = \pi p_m$, with p_m given by Equation (5.16), and the exponent $n = 2$. Further,

from the relation $h = a/\tan\alpha$, the parameters C_h and m in Equation (5.1)₁ follow as $C_h = \pi p_m(\tan\alpha)^2$ and $m = 2$.

Three-dimensional indentation simulations reveal that Johnson's cavity expansion model gives a rather good representation of the nominal hardness of polymers (e.g. paints); an approximately spherical plastic zone develops and no material pile-up occurs next to the indenter [159, 160]. In order to verify the accuracy of Equation (5.16), the results of this model are compared to large deformation Finite Element (FE) simulations of the indentation of an elastic, ideally plastic half space, using the commercial FE package ABAQUS Standard³. The indentation problem is modelled as axisymmetric, with the vertical line of symmetry passing through the centre of the indenter.

The indented solid is discretised using axisymmetric, 4-node, isoparametric elements with a 2×2 Gauss quadrature. The conical indenter is modelled as rigid and frictionless, and is characterised by a semi-apex angle of $\alpha = 70.3^\circ$, corresponding to an inclination $\beta = 19.7^\circ$ of the indenter. The numerical stability of the solution is enhanced by slightly rounding off the indenter tip with a small, finite tip radius. The inclusion of a tip radius also makes the indenter more representative of a practical conical indenter. The indenter is displaced vertically into the solid using an incremental time-marching scheme with an automatic time-step adaptation. The maximum indentation depth is set to $8\ \mu\text{m}$, which is a factor of 6.25 smaller than the radial and vertical dimensions of $50\ \mu\text{m}$ defining the axisymmetric finite element configuration. A so-called node-to-surface contact criterion is adopted in order to rigorously check for new contacts between the indenter and the elements that define the top surface of the solid.

The FE mesh is refined near the indenter tip, and the semi-infinite character of the solid is simulated by placing 4-node infinite elements with an elastic material behaviour along the lateral and lower boundaries of the finite element geometry [177]. The converged FE discretisation deduced from the above mesh refinement study corresponds to a spatial discretisation of 4499 finite elements and 100 infinite elements. The choice of element discretisation is determined from a preliminary mesh refinement study on the initial, elastic indentation response. In the mesh refinement study the elastic response was simulated by selecting an almost incompressible solid with $\nu = 0.499$; the converged numerical results agree with the analytical solution given by Equation (5.2) to within an acceptable inaccuracy of 1%.

In the FE simulations of the indentation of the elastic, ideally plastic solid the mesh density of the converged elastic solution is preserved and the size of the mesh is increased by a factor of 10 in the radial and vertical directions to ensure that the plastic zone generated by the conical indenter does not reach the elastic infinite elements located at the perimeter of the FE model. Consequently, the number of finite elements in this FE model equals 15 557. The number of infinite elements is kept the same as in the mesh convergence study, that is 100. The Poisson's ratio of the solid is $\nu = 0.35$ is representative of various solids, including historical paints [56]. J_2 -flow theory is used for the plastic response, and the Young's modulus E and yield strength σ_y are selected such that the dimensionless parameter $(E \tan\beta)/\sigma_y$ appearing in Equation (5.16) is varied stepwisely from 1 to 100, in correspondence with 100 separate FE simulations.

Figure 5.4 shows a comparison between the results obtained from the FE simulations (grey circles and black solid line) and Johnson's cavity expansion model, Equation (5.16), (dashed line). Each vertical column of data points, designated by the grey circles, corresponds to an increase in indentation depth h for an integer number of contact nodes.

³Dassault Systems Simulia Corp., Providence, RI, USA.

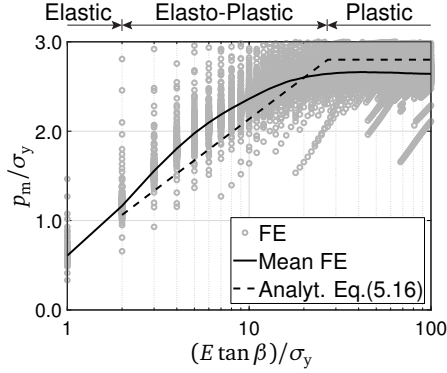


Figure 5.4: Indentation response of an elastic, ideally plastic solid. Mean indentation pressure p_m normalised by the yield strength σ_y as a function of the dimensionless parameter $(E \tan \beta)/\sigma_y$. The figure shows the FE response (grey circles), the mean FE response (solid black line) and the response by the cavity expansion model, Equation (5.16) (dashed line).

The bottom point of each column of data points gives the instant at which a new node comes into contact with the indenter. Thus, the contact radius a remains constant and the mean indentation pressure p_m (plotted along the vertical axis) grows until the next node makes contact. This feature of mesh discretisation repeats itself and a new column of vertical data points is generated, see also [44, 94, 115]. The black solid line depicted in Figure 5.4 captures the mean values of the vertical columns of data points. The cavity expansion model, Equation (5.16), is in reasonable agreement with the response of the FE simulations, with an underprediction in the intermediate elasto-plastic regime and an overprediction in the final, plastic regime. Although not illustrated here, the FE results also show that the ratio of contact depth h_c to indentation depth h in the elasto-plastic regime monotonically increases from $h_c/h = 2/\pi$ to $h_c/h = 1$: the initial, elastic value is in agreement with the expression given by Equation (5.6). When $(E \tan \beta)/\sigma_y$ exceeds 27 the plastic deformation regime is reached, the mean indentation pressure p_m becomes constant, and the contact depth develops with $h_c/h > 1$, indicating that material piles up next to the indenter, as previously discussed [85, 86]. Additional comparisons between the results of the cavity expansion model and those of FE simulations can be found in [86], including a comparison of the subsurface and surface stress fields in Figures 6.15 and 6.16, which shows good agreement.

5.3 Closed-form expression for the effective elastic modulus of a bi-material

The indentation model for a homogeneous solid reviewed in Section 5.2 will be adapted to the case of a bi-material composed of a hemispherical inclusion at the surface of a dissimilar half space, with the indent placed at the centre of the inclusion. As will be demonstrated in Section 5.4, this adaptation will be achieved via an effective elastic modulus of the bi-material, followed by taking this effective modulus as the value of the Young's modulus in an indentation model for a homogeneous solid. In the present section an analytical expression for the effective elastic modulus is derived from the response of a hollow, spherical particle embedded in an infinite medium of dissimilar elastic properties,

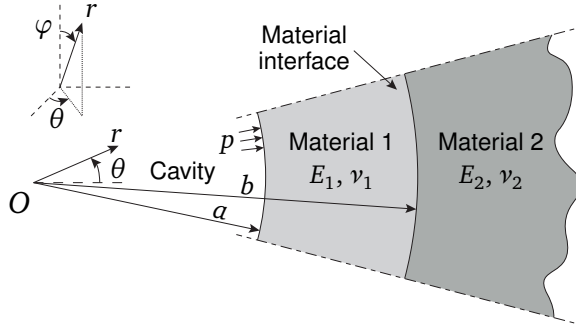


Figure 5.5: A spherical shell of outer radius b (material 1) embedded in an infinite medium (material 2). The spherical cavity of radius a is pressurised by a uniform pressure p . The inset shows the spherical coordinate system (r, θ, φ) , with $r \geq a$ the radial coordinate of a material point, θ the polar angle coordinate, and φ the azimuth angle coordinate.

and subjected to a uniform, internal pressure, see Figure 5.5. The elastic displacement field in the bi-material is derived in Section 5.3.1, and an analytical expression for the effective elastic modulus is obtained in Section 5.3.2.

5.3.1 Elastic displacement field

The geometry depicted in Figure 5.5 is characterised by an elastic spherical shell of outer radius b (material 1) that is embedded in an infinite solid of dissimilar elastic properties (material 2). The spherical cavity of radius a is subjected to an internal uniform pressure p . A spherical coordinate system (r, θ, φ) is adopted, where $r \geq a$ is the radial coordinate, θ the polar angle coordinate, and φ is the azimuth angle coordinate. Upon exploiting the spherical symmetry of the problem, the following equilibrium and kinematic conditions hold:

$$\begin{aligned}
 \sigma_{r\theta} &= \sigma_{r\varphi} = \sigma_{\theta\varphi} = 0, \\
 \sigma_{\theta\theta} &= \sigma_{\varphi\varphi}, \\
 u_{\theta} &= u_{\varphi} = 0, \\
 \varepsilon_{r\theta} &= \varepsilon_{r\varphi} = \varepsilon_{\theta\varphi} = 0, \\
 \varepsilon_{\theta\theta} &= \varepsilon_{\varphi\varphi}.
 \end{aligned} \tag{5.18}$$

Here, σ_{mn} , ε_{mn} , and u_m are the stress, strain and displacement components in the spherical coordinate system. The constitutive relations and the remaining equilibrium and kinematic relations of the solid are

$$\begin{aligned}
 \sigma_{rr} - 2\nu_i\sigma_{\theta\theta} &= E_i\varepsilon_{rr}, \\
 \sigma_{\theta\theta}(1 - \nu_i) - \nu_i\sigma_{rr} &= E_i\varepsilon_{\theta\theta}, \\
 \frac{\partial\sigma_{rr}}{\partial r} + \frac{2}{r}(\sigma_{rr} - \sigma_{\theta\theta}) &= 0, \\
 \varepsilon_{rr} &= \frac{\partial u_r}{\partial r}, \\
 \varepsilon_{\theta\theta} &= \frac{u_r}{r},
 \end{aligned} \tag{5.19}$$

where E_i and ν_i are the Young's modulus and Poisson's ratio of material $i \in \{1, 2\}$. Additionally, the boundary conditions (at $r = a$ and $r \rightarrow \infty$) and interfacial conditions (at

$r = b$) are given by:

$$\begin{aligned} \sigma_{rr}(r = a) &= -p, \\ u_r(r \rightarrow \infty) &= 0, \\ \sigma_{rr,1}(r = b) &= \sigma_{rr,2}(r = b), \\ u_{r,1}(r = b) &= u_{r,2}(r = b), \end{aligned} \quad (5.20)$$

in which the comma and subindices 1 and 2 used in the definition of the interfacial conditions Equation (5.20)_{3,4} refer to materials 1 and 2, respectively. Combining Equations (5.19) and (5.20) leads to the following expression for the radial displacement:

$$u_r(r) = \begin{cases} \frac{a^3 p (2(b^3 - r^3) E_2 (2\nu_1^2 + \nu_1 - 1) - E_1 (b^3 + 2r^3 + (b^3 - 4r^3) \nu_1) (1 + \nu_2))}{2r^2 E_1 (-E_2 (a^3 + 2b^3 + (a^3 - 4b^3) \nu_1) + (a^3 - b^3) E_1 (1 + \nu_2))} & \text{for } a \leq r \leq b, \\ \frac{3a^3 b^3 p (-1 + \nu_1) (1 + \nu_2)}{2r^2 (-E_2 (a^3 + 2b^3 + (a^3 - 4b^3) \nu_1) + (a^3 - b^3) E_1 (1 + \nu_2))} & \text{for } r > b. \end{cases} \quad (5.21)$$

For the specific case of a vanishing material 2 (i.e. $E_2 = 0$, $\nu_2 = 0$), Equation (5.21) reduces to:

$$u_r(r) = \frac{a^3 p (b^3 + 2r^3 + (b^3 - 4r^3) \nu)}{2(b^3 - a^3) r^2 E} \quad \text{with } a \leq r \leq b, \quad (5.22)$$

in which the subscripts of the elastic parameters E_1 and ν_1 have been dropped for the sake of clarity. Equation (5.22) gives the elastic displacement field for a homogeneous spherical shell of finite thickness ($b - a$), with a free outer boundary at $r = b$, and loaded by a uniform pressure p at its inner boundary $r = a$; this expression is in agreement with that given in [76]. For the special case of an internally pressurised spherical cavity in an infinite, homogeneous medium, i.e. $E_1 = E_2 = E$ and $\nu_1 = \nu_2 = \nu$, Equation (5.21) reduces to the classical solution [21]:

$$u_r(r) = \frac{a^3 p (1 + \nu)}{2r^2 E} \quad \text{with } r \geq a. \quad (5.23)$$

5.3.2 Effective elastic modulus of an embedded spherical shell

It follows from Equations (5.19)₄ and (5.23) that, for the case of a homogeneous infinite medium, the radial strain at the boundary $r = a$ of the cavity can be written as

$$\varepsilon_{rr}(r = a) = \frac{-p(1 + \nu)}{E}, \quad (5.24)$$

which, upon rearrangement, expresses the Young's modulus as a function of the radial strain at $r = a$:

$$E = \frac{-p(1 + \nu)}{\varepsilon_{rr}(r = a)}. \quad (5.25)$$

The assumption is made that the embedded spherical shell can be idealised by an equivalent cavity of radius a in a homogeneous full space by introducing an effective modulus \bar{E} for the cavity in a homogeneous full space. The calibration is based on the assumption that the radial strain at the boundary $r = a$ of the cavity is the same for the two cases. Thus, the effective modulus \bar{E} for the cavity in a homogeneous full space is defined by rearrangement of the above equation to read:

$$\bar{E} \equiv \frac{-p(1 + \nu_1)}{\varepsilon_{rr}(r = a)}. \quad (5.26)$$

Here, the value of the radial strain at the boundary $r = a$ is for the embedded spherical shell, and is determined from Equations (5.19)₄ and (5.21)₁ as

$$\varepsilon_{rr}(r = a) = \frac{-p \left((2b^3 + a^3)E_2(2\nu_1^2 + \nu_1 - 1) - E_1(b^3 - a^3 + (b^3 + 2a^3)\nu_1)(1 + \nu_2) \right)}{E_1(-E_2(a^3 + 2b^3 + (a^3 - 4b^3)\nu_1) + (a^3 - b^3)E_1(1 + \nu_2))}. \quad (5.27)$$

Now insert Equation (5.27) into Equation (5.26) to obtain the effective elastic modulus:

$$\bar{E} = \frac{E_1(-E_2(a^3 + 2b^3 + (a^3 - 4b^3)\nu_1) + (a^3 - b^3)E_1(1 + \nu_2))(1 + \nu_1)}{(a^3 + 2b^3)E_2(2\nu_1^2 + \nu_1 - 1) - E_1(-a^3 + b^3 + (2a^3 + b^3)\nu_1)(1 + \nu_2)}. \quad (5.28)$$

This expression reduces to the Young's modulus of a homogeneous material, $\bar{E} = E$, when $E_1 = E_2 = E$ and $\nu_1 = \nu_2 = \nu$, as required. In Section 5.4 the above expression for the effective elastic modulus of the bi-material is combined with the indentation models for homogeneous materials reviewed in Section 5.2 obtain an analytical expression for the indentation response of elastic and elasto-plastic bi-materials.

Note that an alternative expression for the effective modulus of the bi-material can be obtained by suitable matching of the hoop strain of the bi-material problem and the cavity in an effective, homogeneous full space at $r = a$. Combine Equations (5.19)₅ and (5.23) for the cavity in a homogeneous full space, and substitute E by \bar{E} and ν by ν_1 :

$$\bar{E} \equiv \frac{p(1 + \nu_1)}{2\varepsilon_{\theta\theta}(r = a)}. \quad (5.29)$$

Then, assume that the value of $\varepsilon_{\theta\theta}(r = a)$ for the embedded spherical shell equals that for the equivalent effective full space. A comparison study has been performed between the use of hoop and radial strain components to obtain \bar{E} , but is not detailed here. It is found that the effective modulus \bar{E} based on Equation (5.26) provides a more accurate estimate of the elastic indentation response of an embedded hemispherical inclusion than that based on Equation (5.29).

5.4 Indentation of embedded hemispherical particles

The closed-form expression for the effective elastic modulus of the bi-material, Equation (5.28), is now combined with the analytical indentation models for homogeneous materials, as reviewed in Section 5.2. First, the indentation of an *elastic* hemispherical particle embedded in an elastic half space is reported in Section 5.4.1. Second, the indentation of an *elastic, ideally plastic* hemispherical particle embedded in an elastic half space is given in Section 5.4.2. In each section, the accuracy of the analytical models is established by comparing the analytical predictions with detailed finite element simulations.

5.4.1 Indentation of an elastic hemispherical particle embedded in an elastic half space

The elastic indentation of a hemispherical particle embedded in a half space of differing elastic properties is sketched in Figure 5.6. The analytical indentation model makes use of Equation (5.28) in the $F - a$ relation, Equation (5.2)₂. Accordingly, the indentation

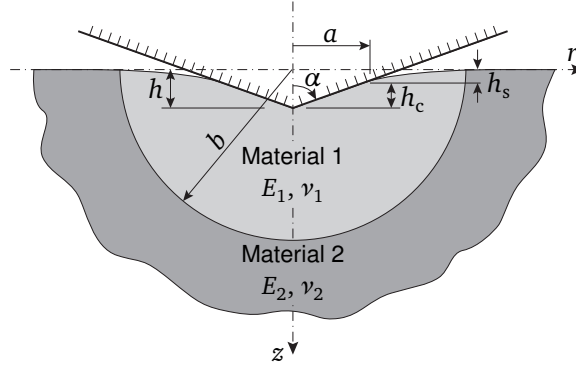


Figure 5.6: Indentation of an elastic hemispherical particle of radius b (material 1) embedded in an elastic half space (material 2), using an indenter with semi-apex angle α . The contact radius a , contact depth h_c , and sink-in depth h_s each depend upon the indentation depth h .

force F on the rigid conical indenter is expressed in terms of the contact radius a of the bi-material as

$$F = \gamma \frac{\pi}{2 \tan \alpha} \frac{\bar{E}}{(1 - \nu_1^2)} a^2, \quad (5.30)$$

in which the Poisson's ratio corresponds to that of the indented material 1. Equation (5.30) has been extended with a factor γ , which corrects for a small, artificial overlap between the geometry of the rigid indenter and the deformed material surface, as characteristic of Sneddon's solution, see also [60]. An analytical expression for the factor γ is obtained by calibrating Equation (5.30) on the FE indentation response of a homogeneous material – here designated as “material 1” – with the Poisson's ratio taking values in the range of 0 to 0.5. The FE mesh used for the axisymmetric indentation models corresponds to that following from the mesh convergence study described in Section 5.2.3. The calibration of the factor γ is performed when the indentation response has converged towards a steady state, as characterised by an almost constant value of the dimensionless indentation force $F/(A_p E_1)$, with $A_p = \pi a^2$ the projected contact area. The value of γ is taken as the average of the values calibrated for a range of contact radii a . Figure 5.7 illustrates that the numerical values for γ are accurately captured by the linear relation

$$\gamma = 1.2 - 0.4 \nu_1. \quad (5.31)$$

Note that $\gamma = 1$ in the limit of an incompressible material, $\nu = 0.5$, which is the case that has been selected for the mesh refinement study discussed Section 5.2.3.

Elastic indentation response

The elastic indentation response of the bi-material configuration sketched in Figure 5.6 is illustrated in Figure 5.8. Specifically, the dimensionless indentation force $F/(A_p E_1)$ is plotted as a function of the dimensionless indentation radius a/b for three values of the stiffness mismatch, $E_2/E_1 = [0.2, 1.0, 5.0]$, and 6 choices of Poisson's ratios, $\nu_1 = \nu_2$ in the range of 0 to 0.5. The black solid line represents the FE response, which develops in a sawtooth fashion due to the fact that the contact condition of the indenter is prescribed in

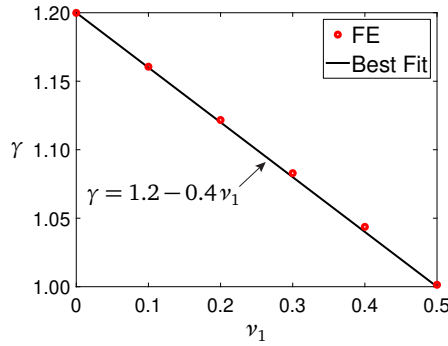


Figure 5.7: Analytical expression for the factor γ (black line) as given by Equation (5.31), which is obtained from calibrating Equation (5.30) on the FE indentation response of a homogeneous, elastic half space (red circles) for selected values of Poisson’s ratio ν_1 .

a spatially discrete manner via the individual finite element nodes, see also Figure 5.4 and the explanation provided in Section 5.2.3. The mean of the FE sawtooth curve is given by the red dotted line. The analytical model, Equation (5.30), with γ and \bar{E} respectively given by Equations (5.31) and (5.28), is represented by the black dashed line. Additionally, for the specific case of $E_2/E_1 = 0.2$, the analytical model with an effective modulus for an *incompressible* bi-material is depicted in Figures 5.8(a)–(f) by the black dotted line; the corresponding expression for the effective modulus follows from inserting $\nu_1 = \nu_2 = 0.5$ into Equation (5.28):

$$\bar{E} = \bar{E}_{\text{inc}} = \frac{E_1(b^3 - a^3) + E_2a^3}{b^3}, \quad (5.32)$$

with the subscript “inc” referring to “incompressible”. This expression correctly reduces to $\bar{E}_{\text{inc}} = E_1$ for a homogeneous material, $E_2/E_1 = 1$. The analytical indentation model, Equation (5.30), that uses the effective modulus of the incompressible material, Equation (5.32), henceforth will be denoted “analytical model for the incompressible bi-material”; the indentation model also describes indented materials with a Poisson’s ratio ν_1 different from 0.5, via the terms $\gamma = 1.2 - 0.4\nu_1$ and $(1 - \nu_1^2)$ in Equation (5.30).

For the case $E_2/E_1 = 0.2$ of a stiff particle embedded in a soft matrix, the mean FE results plotted in Figure 5.8 show that the dimensionless indentation force $F/(A_p E_1)$ monotonically decreases with increasing indentation radius a/b after a relatively short initiation phase⁴. In contrast, for a homogeneous material, $E_2/E_1 = 1.0$, $F/(A_p E_1)$ is independent of a/b , and for the case $E_2/E_1 = 5.0$ of a compliant particle embedded in a stiff matrix $F/(A_p E_1)$ increases monotonically with a/b . Remarkably, the indentation load for the stiff particle configuration, $E_2/E_1 = 0.2$, is almost insensitive to the choice of Poisson’s ratio ν_1 and ν_2 , and is adequately captured by the analytical model for an incompressible bi-material, Equation (5.32). The analytical model with the general stiffness expression, Equation (5.28), overpredicts the FE results for this case, although the discrepancy decreases for a larger value of Poisson’s ratios, and eventually vanishes in the limit of an incompressible bi-material, $\nu_1 = \nu_2 = 0.5$. For a homogeneous material, $E_2/E_1 = 1$, the analytical models with the stiffness expressions given by Equations (5.28)

⁴The FE results shown in Figure 5.8 are characterised by a short initial phase, during which the round indenter tip establishes contact with the material surface and the dimensionless indentation force $F/(A_p E_1)$ increases.

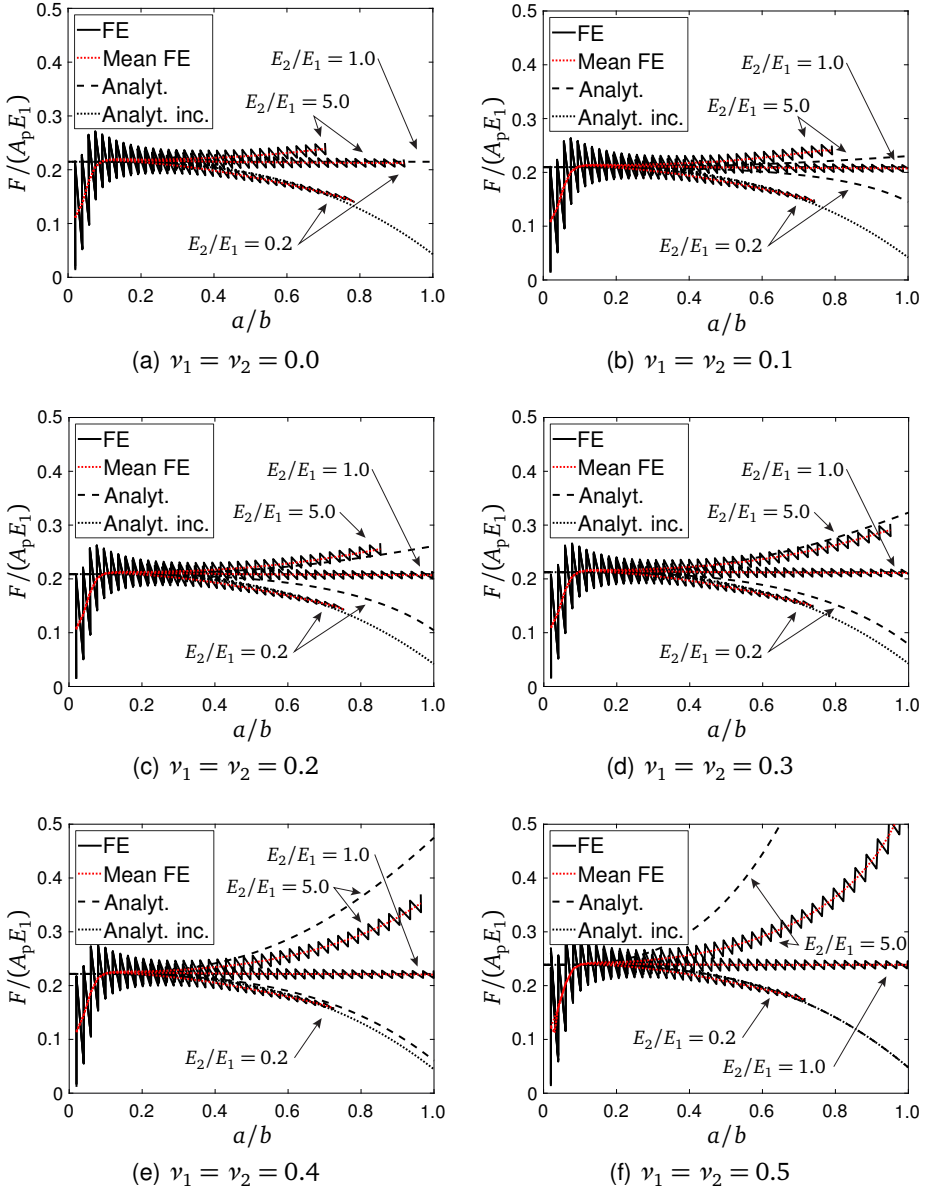


Figure 5.8: Indentation response of an elastic hemispherical particle embedded in an elastic half space. Dimensionless indentation force $F/(A_p E_1)$ versus the dimensionless indentation radius a/b , as calculated by FE simulations (black solid line), the analytical model Equation (5.30) with the general stiffness expression Equation (5.28) (black dashed line), and the analytical model Equation (5.30) with the stiffness expression for an incompressible material Equation (5.32) (black dotted line). The mean FE response is represented by the red dotted line. The results are shown for three different values of the stiffness mismatch, $E_2/E_1 = 0.2, 1.0,$ and 5.0 , for (a) $\nu_1 = \nu_2 = 0.0$, (b) $\nu_1 = \nu_2 = 0.1$, (c) $\nu_1 = \nu_2 = 0.2$, (d) $\nu_1 = \nu_2 = 0.3$, (e) $\nu_1 = \nu_2 = 0.4$, (f) $\nu_1 = \nu_2 = 0.5$.

and (5.32) lead to an identical result, and accurately describe the mean FE response. For the compliant particle configuration, $E_2/E_1 = 5.0$, the analytical model with the general stiffness expression Equation (5.28) gives close agreement with the mean FE results over the full range of dimensionless indentation radii a/b in case of moderate values of the Poisson's ratios, $0.2 \leq \nu_i \leq 0.3$ and $i \in \{1, 2\}$. Since this range includes the Poisson's ratios of many engineering materials, it is concluded that this analytical indentation model is of practical value. For values of Poisson's ratios falling outside this range, Figure 5.8 shows that the analytical model only provides accurate results up to a normalised indentation radius of $a/b \approx 0.3$ to 0.4, and for larger indentation values the model may significantly underpredict (for $\nu_1, \nu_2 < 0.2$) or overpredict (for $\nu_1, \nu_2 > 0.3$) the mean FE response of the compliant particle configuration. Finally, note from Figure 5.8(f) that, for $E_2/E_1 = 5.0$, the analytical model for the incompressible bi-material deviates from the FE results obtained for a Poisson's ratio of 0.5, which is the reason that analytical predictions for an incompressible bi-material with $E_2/E_1 = 5.0$ have been omitted from Figures 5.8(a)–(e).

Effective elastic modulus

The mean FE results indicated by the red dotted line in Figure 5.8 can be used to compute the normalised effective elastic modulus \bar{E}/E_1 of the bi-material from the inverse relation of Equation (5.30), i.e.

$$\frac{\bar{E}}{E_1} = \frac{2 \tan \alpha F(1 - \nu_1^2)}{\gamma A_p E_1}. \quad (5.33)$$

Accordingly, in Figures 5.9(a)–(f) the effective modulus following from the FE simulations is compared to the effective modulus, Equation (5.28), and the effective modulus for the incompressible bi-material, Equation (5.32), by plotting the dimensionless value \bar{E}/E_1 against the dimensionless indentation radius a/b for three values of stiffness mismatches $E_2/E_1 = [0.2, 1.0, 5.0]$ and six values of Poisson's ratio over the range 0 to 0.5. After a minor initiation phase, all curves attain an effective modulus of $\bar{E} = E_1$, which confirms that at small indentation the effective modulus equals the Young's modulus of the hemispherical particle. Under continued indentation, the effective modulus of the stiff particle configuration, $E_2/E_1 = 0.2$, monotonically decreases, for the homogeneous material, $E_2/E_1 = 1.0$, it remains constant and equals $\bar{E} = E_1$, and for the compliant particle configuration, $E_2/E_1 = 5.0$, it monotonically increases. In agreement with the observation made from Figure 5.8, for the stiff particle configuration, $E_2/E_1 = 0.2$, the analytical model for the incompressible bi-material closely matches the effective modulus determined from the FE simulations. For the homogeneous material the general analytical expression, Equation (5.28), and the expression for the incompressible bi-material, Equation (5.32), lead to the same result $\bar{E} = E_1$, which match the FE results. For the compliant particle configuration, $E_2/E_1 = 5.0$, the agreement between the effective modulus expression, Equation (5.28), and the FE results is adequate for Poisson's ratios in the range $0.2 \leq \nu_i \leq 0.3$ where $i \in \{1, 2\}$, and is adequate up to an indentation of $a/b = 0.3$ to 0.4 for Poisson's ratios falling outside this range.

From the above comparison with the FE results (and from similar comparisons with FE results for alternative stiffness mismatches $E_2/E_1 = 0.5$ and 2.0, but omitted here for the sake of brevity), it is concluded that the analytical expressions for the effective elastic modulus \bar{E} of the indented bi-material given by Equations (5.28) and (5.32) are adequate for a broad range of stiffness mismatches, $0.2 \leq E_2/E_1 \leq 5.0$, and Poisson's ratios,

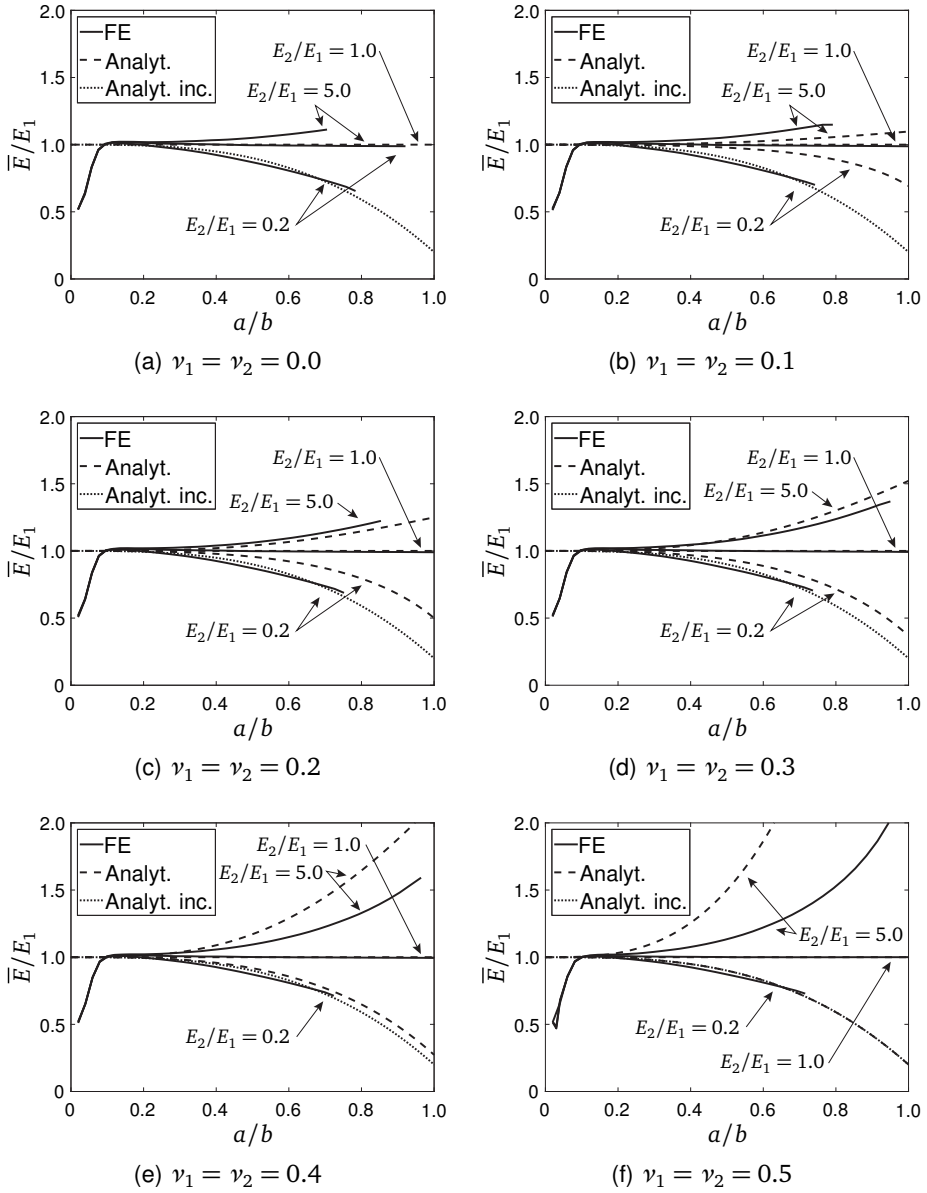


Figure 5.9: Indentation response of an elastic hemispherical particle embedded in an elastic half space. Dimensionless effective elastic modulus \bar{E}/E_1 versus dimensionless indentation radius a/b , as calculated by FE simulations and using Equation (5.33) (black solid line), the analytical model Equation (5.28) (black dashed line), and the analytical model for the incompressible material Equation (5.32) (black dotted line). The results are shown for three values of the stiffness mismatch, $E_2/E_1 = 0.2, 1.0$, and 5.0 , for (a) $\nu_1 = \nu_2 = 0.0$, (b) $\nu_1 = \nu_2 = 0.1$, (c) $\nu_1 = \nu_2 = 0.2$, (d) $\nu_1 = \nu_2 = 0.3$, (e) $\nu_1 = \nu_2 = 0.4$, (f) $\nu_1 = \nu_2 = 0.5$.

$0 \leq \nu_i \leq 0.5$ with $i \in \{1, 2\}$, within the following regimes of the normalised indentation radius a/b :

$$\bar{E} = \left\{ \begin{array}{l} \frac{E_1(-E_2(a^3 + 2b^3 + (a^3 - 4b^3)\nu_1) + (a^3 - b^3)E_1(1 + \nu_2))(1 + \nu_1)}{(a^3 + 2b^3)E_2(2\nu_1^2 + \nu_1 - 1) - E_1(-a^3 + b^3 + (2a^3 + b^3)\nu_1)(1 + \nu_2)}, \\ \text{for } 0 \leq a/b \leq 1 \quad \text{if } 1.0 < E_2/E_1 \leq 5.0 \quad \text{and } 0.2 \leq \nu_i \leq 0.3, \\ \text{for } 0 \leq a/b \leq 0.3 \quad \text{if } 1.0 < E_2/E_1 \leq 5.0 \quad \text{and } 0 \leq \nu_i < 0.2 \\ \text{or } 0.3 < \nu_i \leq 0.5, \\ \text{for } 0 \leq a/b \leq 1 \quad \text{if } 0.5 < E_2/E_1 < 1.0 \quad \text{and } 0.3 \leq \nu_i \leq 0.4, \\ \text{for } 0 \leq a/b \leq 0.5 \quad \text{if } 0.5 < E_2/E_1 < 1.0 \quad \text{and } 0 \leq \nu_i < 0.3 \\ \text{or } 0.4 < \nu_i \leq 0.5, \\ \frac{E_1(b^3 - a^3) + E_2a^3}{b^3}, \\ \text{for } 0 \leq a/b \leq 0.6 \quad \text{if } 0.2 \leq E_2/E_1 \leq 0.5 \quad \text{and } 0 \leq \nu_i \leq 0.5, \\ \text{with } i \in \{1, 2\}. \end{array} \right. \quad (5.34)$$

In the above expressions the various regimes follow each other through the specific ranges selected for the elastic parameters. The homogeneous limit $E_2/E_1 = 1$ is omitted from Equation (5.34), but, as has already been mentioned, the correct limit is obtained from this equation as $\bar{E} = E_1$ for the complete range of Poisson's ratios $0 \leq \nu_i \leq 0.5$. Further, the maximum indentation radius $a/b = 1$ for simplicity has been included in the applicability ranges of Equation (5.34), although for certain combinations of elastic parameters the maximum value of a/b may be somewhat smaller than unity, due to the fact that the indenter prematurely touches the supporting material 2 under a relatively large vertical deformation of material 1, see also Figures 5.8 and 5.9.

5.4.2 Indentation of an elastic, ideally plastic hemispherical particle embedded in an elastic half space

The elastic configuration studied in Section 5.4.1 is now extended to the case of an elastic, ideally plastic hemispherical particle (material 1) embedded in an elastic half space (material 2), see Figure 5.10. The size of the plastic zone generated within the hemispherical particle is denoted by the radius c . The plastic zone can expand until it reaches the material interface between the hemispherical particle and the supporting elastic half space, $c = b$, or until the indenter reaches the material interface, $a = b$. The indentation response of the bi-material configuration is analysed analytically by an adapted version of Johnson's cavity expansion model for a homogeneous material Equation (5.16), and numerically by means of finite element analyses. The adaptation of Johnson's model involves the replacement of the Young's modulus E in Equation (5.16) by the analytical expression for the effective elastic modulus \bar{E} of the bi-material, leading to

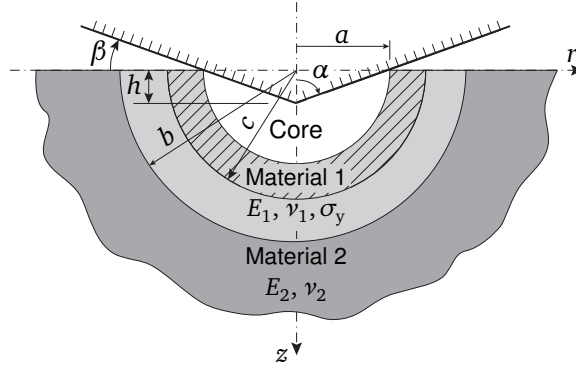


Figure 5.10: Indentation of an elastic, ideally plastic hemispherical particle of radius b (material 1) embedded in an elastic half space (material 2), using an indenter with semi-apex angle α . The indentation produces a hemispherical core of radius equal to the contact radius a , and a hemispherical plastic zone of radius c .

$$\frac{p_m}{\sigma_y} = \begin{cases} \frac{p}{\sigma_y} + \frac{2}{3} & \text{for } 2 \leq \frac{\bar{E} \tan \beta}{\sigma_y} \leq 27, \\ 2.8 & \text{for } \frac{\bar{E} \tan \beta}{\sigma_y} > 27, \end{cases} \quad (5.35)$$

where

$$\frac{p}{\sigma_y} = \frac{2}{3} \left(1 + \ln \left(\frac{1}{3} \frac{\bar{E} \tan \beta}{\sigma_y} \right) \right),$$

with \bar{E} given by Equation (5.28). Instead of Equation (5.28), the refined, more complicated stiffness expression, Equation (5.34), could have been used, but this leads to only minor differences in the elasto-plastic indentation response.

Figure 5.11 illustrates the indentation response from both the FE simulations and the analytical cavity expansion model of the bi-material, Equation (5.35). The Poisson's ratios of the materials 1 and 2 are taken to be $\nu_1 = \nu_2 = 0.35$. Note that the incorporation of the effective elastic modulus \bar{E} of the bi-material in the dimensionless parameter $(\bar{E} \tan \beta)/\sigma_y$ plotted along the horizontal axis is consistent with the analytical expression in Equation (5.35). Consequently, the response plotted for the cavity expansion model includes the role of stiffness mismatch E_2/E_1 . As already discussed in Section 5.2.3, the mean FE response for a homogeneous material, $\bar{E} = E_1 = E_2$, is adequately approximated by the cavity expansion model. The mean FE responses for the bi-material refer to a high stiffness ratio $E_2/E_1 = 10$ (red solid line) and to a low stiffness ratio $E_2/E_1 = 0.1$ (blue solid line). These FE responses are calculated by performing separate analyses for 9 different values of the yield strength σ_y , which start along the horizontal axis at 9 selected values of $(\bar{E} \tan \beta)/\sigma_y$. In correspondence with the range of validity of the cavity expansion model, the FE analyses are continued until the plastic zone reaches the material interface, $c = b$, or the indenter reaches the material interface, $a \approx b$.

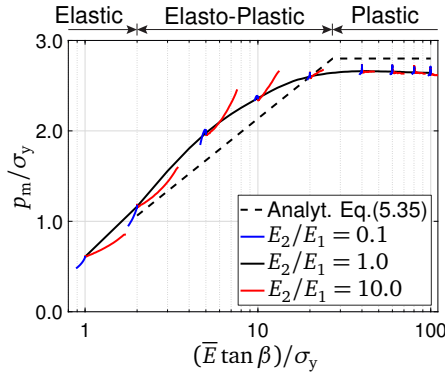


Figure 5.11: Indentation of an elastic, ideally plastic hemispherical particle embedded in an elastic half space. Mean indentation pressure p_m normalised by the yield strength σ_y as a function of the dimensionless parameter $(\bar{E} \tan \beta)/\sigma_y$, with \bar{E} given by Equation (5.28). The FE results are depicted for a homogeneous solid, $E_2/E_1 = 1$ (black solid line), and for bi-materials with stiffness mismatches $E_2/E_1 = 0.1$ (blue solid line) and $E_2/E_1 = 10$ (red solid line), with 9 initial values of $(\bar{E} \tan \beta)/\sigma_y$. The Poisson's ratios are $\nu_1 = \nu_2 = 0.35$. The analytical result for the cavity expansion model of the bi-material Equation (5.35) (black dashed line) holds for arbitrary values of the stiffness mismatch E_2/E_1 via the parameter \bar{E} .

For small indentations the contribution of the supporting material 2 to the overall response is negligible, as a result of which the effective modulus equals that of the hemispherical particle, $\bar{E} = E_1$. Under increasing indentation of the particle embedded in a relatively *compliant* half space, $E_2/E_1 = 0.1$, the values of $(\bar{E} \tan \beta)/\sigma_y$ and p_m/σ_y *decrease* in the initial elastic regime and also in the subsequent elasto-plastic regime. Specifically, the contribution of the compliant half space to the response grows with increasing indentation, so that the values of the mean hydrostatic stress $p_m = F/A_p$ and the effective modulus \bar{E} diminish, as already observed for the elastic responses shown in Figures 5.8 and 5.9, respectively. For the same reason, the elastic and elasto-plastic indentation responses of the particle embedded in a relatively *stiff* half space, $E_2/E_1 = 10$, reveal an *increase* of $(\bar{E} \tan \beta)/\sigma_y$ and p_m/σ_y . Note further that in the final, plastic regime, the mean indentation pressure p_m becomes almost insensitive to the elastic properties of the bi-material, and is essentially set by the yield strength σ_y .

In summary, the elastic, ideally plastic indentation response of a bi-material can be quantified in terms of the effective elastic modulus, Equation (5.28), in the representation in Figure 5.11, with the FE results supporting the analytical cavity expansion model, Equation (5.35). Thus, the cavity expansion model can be used as a practical, analytical tool to estimate the elasto-plastic material properties of embedded samples from indentation tests.

5.5 Case study: use of analytical model to interpret indentation test on embedded paint sample

The practical applicability of the analytical expression for the effective modulus, Equation (5.28), is demonstrated through a case study on indentation tests taken from the literature [48]. Indentation tests were performed on an acrylic, titanium white paint layer

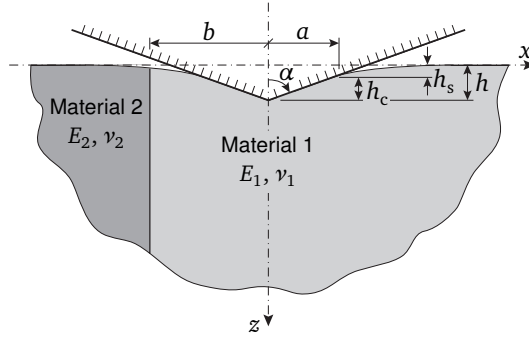


Figure 5.12: Indentation of a semi-infinite elastic bi-material with a straight, vertical material interface. The indentation of material 1 (paint) is performed at a distance b from the interface with material 2 (resin). The indentation depth h relates to a contact radius a , a contact depth h_c , and a sink-in depth h_s . The configuration is representative of the embedded paint sample tested in [48].

of Golden Artist Colors[®] (material 1) that was fully embedded into a resin specified as a Technovit[®] 2000 LC fixing paste (material 2). The width of the paint sample was $210\ \mu\text{m}$ and the thickness in the depth direction was considerably larger, above $1\ \text{mm}$. The reduced modulus measured by indenting the resin with a diamond Berkovich indenter was $E_r \approx 15\ \text{GPa}$ [48]. Assuming a representative value of $\nu_2 = 0.35$ for the Poisson's ratio of the resin, with Equation (5.3) implies that $E_2 \approx E_r(1 - \nu_2^2) = 13.2\ \text{GPa}$. The challenge is to deduce the Young's modulus E_1 of the paint from the measured unloading modulus S of an indentation test on the paint layer.

A sketch of the geometry at the material interface and the characteristics of the indenter is presented in Figure 5.12. The embedded paint sample was subjected to two indentations, performed at distances $b = 12\ \mu\text{m}$ and $b = 72\ \mu\text{m}$ from the vertical interface between the paint and the resin. The indentation tests were carried out using a continuous stiffness measurement (CSM) technique, entailing harmonic loading of amplitude F_0 at a frequency of $20\ \text{Hz}$, superimposed on the quasi-static loading. This allows for the determination of the contact stiffness as a function of indent depth without interrupting the indentation [43, 128]. The amplitude h_0 of the induced dynamic oscillation was on the order of nanometres, much less than that of the quasi-static signal. The unloading contact stiffness S equals $(F_0/h_0) \cos \delta$, where δ is the phase shift between the harmonic load and displacement induced in the embedded viscoelastic paint sample [43, 65, 66, 100].

The contact stiffness S measured at a specific quasi-static loading step F_{\max} and corresponding indentation depth h_{\max} were determined from the raw experimental indentation data⁵, and provide the actual contact depth h_c through Equation (5.15) (using $\xi = 0.75$), which, under the assumption of a perfect Berkovich indenter, subsequently renders the contact area as $A_p = \pi a^2 = \pi(h_c \tan \alpha)^2$ [127], where $\alpha = 68.6^\circ$ for the Berkovich indenter employed in the experiment [48]. From the value of A_p and the corresponding value

⁵The author is grateful to Dr. Naoki Fujisawa and Dr. Michał Łukomski of The Getty Conservation Institute in Los Angeles, U.S.A. for providing the raw experimental indentation data.

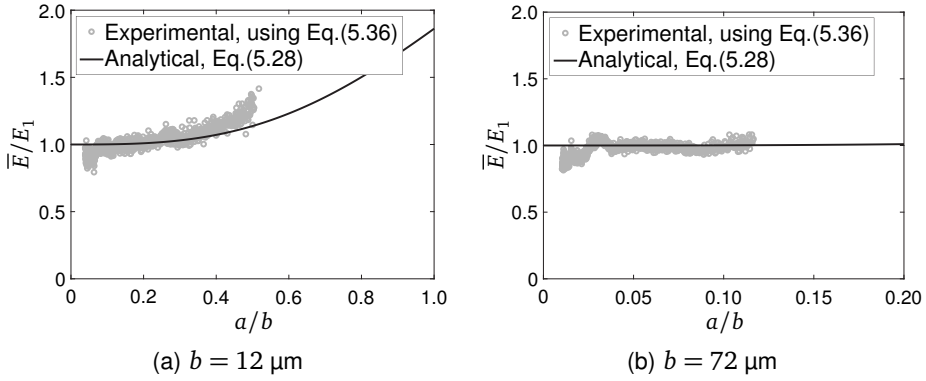


Figure 5.13: Indentation response of a paint sample embedded in a resin. Dimensionless effective elastic modulus \bar{E}/E_1 versus the dimensionless indentation radius a/b , as determined from the experimental data in [48] via Equation (5.36) (grey circles), and from the analytical model, Equation (5.28) (black solid line). The indentations were performed at distances (a) $b = 12 \mu\text{m}$ and (b) $b = 72 \mu\text{m}$ from the material interface between the paint sample and the supporting resin, see Figure 5.12 for the geometrical characteristics at the material interface.

of S , the effective modulus \bar{E} of the bi-material is calculated as

$$\bar{E} = \frac{\pi S(1 - \nu_1^2)}{2 \gamma \sqrt{A_p}}. \quad (5.36)$$


Equation (5.36) is an approximation based on Equation (5.10) for a homogeneous solid, whereby the Young's modulus E is replaced by the effective modulus \bar{E} . Further, the factor γ given by Equation (5.31) has been added to correct for the artificial overlap between the indenter geometry and the deformed material surface, which typifies Sneddon's solution, Equation (5.10). The accuracy of Equation (5.36) for determining the effective modulus of the experimental bi-material configuration sketched in Figure 5.12 has been confirmed in Appendix A via a comparison with the indentation results obtained from a detailed, three-dimensional FE simulation. Since the Berkovich indenter used in the experiment generates a triangular shape indent, the effective modulus computed with Equation (5.36) needs to be multiplied by a correction factor $1/\zeta$, with $\zeta = 1.034$, recall the discussion below Equation (5.10).

Figures 5.13(a) and (b) show the normalised effective modulus, \bar{E}/E_1 , as a function of the normalised contact radius a/b of the indenter, as measured at distances $b = 12 \mu\text{m}$ and $b = 72 \mu\text{m}$ from the material interface, respectively. The grey circles represent the experimental data in the format provided by the approximate stiffness expression, Equation (5.36), and the black solid line reflects the result from the analytical model, Equation (5.28). In both figures the experimental data is accurately matched by the analytical model, whereby it is observed that the indentation response close to the material interface, $b = 12 \mu\text{m}$, reveals a stiffening effect caused by the supporting resin. This stiffening effect increases monotonically with the indentation depth, and remains absent if the indenter is sufficiently far away from the material interface, as can be clearly seen in Figure 5.13(b) for $b = 72 \mu\text{m}$. Upon assuming the Poisson's ratio of the paint to be $\nu_1 = 0.35$ [56], together with the elastic parameters of the resin, $E_2 = 13.2 \text{ GPa}$ and $\nu_2 = 0.35$, the Young's modulus E_1 of the paint material is obtained from Figures 5.13(a) and (b)

by evaluating the calibrated curves for the effective modulus \bar{E} at $a/b = 0$, resulting in $E_1 = 1.8$ GPa for the indentation at $b = 12$ μm , and $E_1 = 1.4$ GPa, for the indentation at $b = 72$ μm . These modulus values are in close correspondence with the values following from the calibration procedure applied in [48], whereby the indentation response was corrected by compensating for the overall structural compliance of the embedded paint sample. The relative difference of 22% in the above two modulus values is likely caused by spatial material heterogeneities in the test sample. With this result, the average stiffness mismatch of the embedded paint sample becomes $E_2/E_1 = 13.2/1.6 = 8.3$.

5.6 Conclusions

An analytical model has been successfully developed to deduce the elastic and plastic properties of embedded samples from indentation measurements. The model makes use of the analytical expressions for the elastic and elasto-plastic indentation responses of homogeneous materials, but adapts them by the introduction of an effective modulus for the embedded sample. The range of validity of the predictions has been established by comparing the analytical results for various bi-material configurations with those from detailed finite element method simulations. The analyses show that, in the elastic and elasto-plastic regimes, the indentation response may be substantially influenced by the modulus of the embedding material. In the fully plastic regime the response is essentially set by the yield strength of the embedded particle. The practical applicability of the indentation model has been demonstrated by deducing the elastic modulus of a paint from indentation measurements on an embedded paint sample as reported in the literature.



Conclusions

Chapter 6

Conclusions and recommendations

6.1 Conclusions

The formation of metal soap in historical oil paintings is threatening museum collections worldwide. Understanding how the formation of metal soap affects the structural integrity of oil paintings might serve as a basis to define guidelines for their preservation. This dissertation has aimed at improving the understanding of the chemo-mechanical behaviour of oil paintings due to metal soap formation, by focusing on: *i)* the numerical modelling of the formation and growth of crystalline metal soap inside paint layers; and *ii)* the development of a practical, analytical model to obtain material properties from historical paint samples via nanoindentation tests. The main conclusions of this work are presented in the following sections.

6.1.1 Chemo-mechanical behaviour of historic oil paintings

The chemo-mechanical behaviour of historical oil paintings due to metal soap formation is investigated via numerical simulations. These simulations are based on a modelling framework that consists of a diffusion-reaction model sequentially coupled to a mechanical model. The growth of the metal soap crystal(s) introduces stresses in the paint layer, which is accounted for in the model through a chemically-induced growth strain. These stresses may lead to the nucleation and propagation of cracks, which is modelled by means of a cohesive zone approach. The mechanical behaviour of the corresponding cohesive interface elements is governed by a traction-separation law, while for the diffusion-reaction model a flux-concentration relationship is defined, which includes a damage-dependent diffusion coefficient. This makes the problem two-way coupled. The coupled model is solved by using a staggered solution scheme.

The computational model summarised above was used to perform different sets of numerical simulations. Initially, a simplified reaction process was assumed by neglecting the formation of amorphous metal soap, i.e. the reaction between metal ions and saturated fatty acids directly forms crystalline metal soap. This preliminary model was used to study the influence of different material properties, chemical and mechanical boundary conditions, and different geometries (i.e. different nucleus shapes and metal soap distributions) on the chemo-mechanical damage process. These simulations showed that the damage in the paint layer is significantly affected by the constraints provided by the

mechanical boundary conditions, the stiffness mismatch between the paint and the metal soap, the fracture length scale, the chemical growth strain, and the chemical reaction rate. However, none of these parameters had a significant influence on the growth characteristics of the metal soap crystal. Unlike the parameters mentioned above, the initial nucleus shape and chemical boundary conditions showed to have some local effect on the shape of the metal soap crystal, which in turn affects the local stress distribution in the paint layer and thus the damage of the paint layer.

The results obtained with the preliminary model are qualitatively in good agreement with *in situ* observations of painting cross-sections. However, the predicted time scale was significantly shorter than what is observed in reality. To improve the quantitative predictions, the diffusion-reaction model was extended to describe both the reversible reaction between saturated fatty acids and metal ions to form amorphous metal soap, and the irreversible reaction to form crystalline metal soap. This enhanced diffusion-reaction model was first calibrated on experiments presented in the literature, which refer to the formation of lead soap in a lead-containing ionomer, thereby mimicking lead soap formation in a paint layer. The calibrated model was subsequently used to analyse two boundary value problems. The first boundary value problem represents a single-layer paint model, in which multiple metal soap crystals can form. This geometry was analysed by both the preliminary and the enhanced model. This revealed that, compared to the preliminary model, the enhanced model formulation leads to a substantial increase in the predicted characteristic time scale. In addition, the reduction in the reaction rate leads to a more homogeneous spatial development of the saturated fatty acid concentration. The second boundary value problem represented a multi-layer paint model in which a single metal soap crystal forms. The crystal was assumed to grow within the ground layer of the model, where the continuous growth caused a significant upward deflection of the paint surface. This upward deflection resulted in a single surface crack in the pictorial layer and was located directly above the crystal. Besides this surface crack, two delamination cracks formed along the interface between the ground and pictorial layers, which might ultimately lead to local paint flaking. It can be concluded that the proposed model realistically predicts the effect of metal soap formation on the chemo-mechanical degradation of historical oil paintings, and shows the contribution of a wide range of parameters on the structural integrity of the paintings.

6.1.2 Mechanical properties of embedded historical oil paints

Obtaining the material properties of historic paint samples is not straightforward, as only micrometre sized samples are available for testing, e.g. via nanoindentation tests. These paint samples are typically embedded in a resin with different material properties, which may affect the measured properties if the (relative) indentation size is substantial. To simplify the process of calibrating the elastic and plastic properties of the embedded sample, an analytical model was proposed. This model is based on analytical expressions for the indentation of a homogeneous material, whereby the homogeneous stiffness modulus is replaced by a representative effective stiffness modulus. The validity of the analytical model has been established by comparing the analytical results to results obtained from dedicated finite element simulations. These comparisons show that for a considerable range of material parameters the analytical model describes the elastic indentation behaviour with acceptable accuracy. Additionally, the elasto-plastic and plastic indentation responses are adequately described by the model, with the plastic indentation essentially being dictated by the yield strength of the embedded material. Finally,

the practical applicability of the indentation model has been demonstrated by calibrating the elastic stiffness of an embedded paint sample from indentation tests reported in the literature.

6.2 Recommendations

The results obtained from the numerical simulations presented in Chapters 2, 3, and 4 provide a better understanding of the coupled chemo-mechanical degradation of historical oil paintings due to metal soap formation. In these simulations, the mechanical properties of the paint were estimated from uniaxial tensile tests reported in literature. These tests, however, were performed on relatively young paint samples and were performed at a larger length scale than that characteristic of the computational models. In addition, the mechanical and diffusive properties of the crystalline metal soap were not available, and, for simplicity, were therefore assumed to be equal to the properties of the paint. To improve the quantitative predictions of the numerical simulations, it is recommended to set up dedicated experiments to accurately determine the different mechanical properties at the relevant length scales. This can be done, for example, by means of nanoindentation tests, for which the model presented in Chapter 5 can be used to analyse the indentation results. To further improve the accuracy of the numerical model, the model formulation could be enhanced by including different relevant physical phenomena, such as, metal ion diffusion, the effect of climate conditions on the material properties and the reaction processes, and the drying and hydrolysis reactions. In addition, it may be of interest to study the interaction between metal soap related degradation and climate induced failure of historical paintings. Finally, validation experiments of historically accurate paint samples may be designed. The results obtained from these experiments can be used to quantitatively validate the computational model, or help to identify the key physical phenomena to be included in the model formulation. These paint samples can also be used to accurately determine the characteristic time and length scales involved in the chemo-mechanical degradation of oil paints.

The proposed analytical model for the indentation of embedded materials currently focuses on extracting the elasto-plastic response of the embedded material. For the chemo-mechanical model presented in this thesis, additional mechanical parameters, such as fracture strength and toughness, are also required; these can be also obtained from indentation tests. It may be, therefore, of interest to incorporate the fracture properties in the modelling of the indentation behaviour of embedded paint samples.

Appendices

Appendix A

Three-dimensional finite element model versus analytical model for a paint indentation problem

The bi-material configuration sketched in Figure 5.12 represents a paint (material 1) embedded in a resin (material 2), which has been subjected to indentation testing as reported in [48], see also Section 5.5. The suitability of the analytical model, Equation (5.28), for determining the effective stiffness \bar{E} of this configuration is assessed by means of a comparison with the results obtained from a detailed 3D FE indentation model. The 3D FE simulation is carried out in a similar fashion as described in Section 5.2.3 for the axisymmetric indentation models. For the tests performed in [48] the sample depth and width are considerably larger than the indentation contact radius a and the distance b between the indenter and the material interface; consequently, the geometry of the embedded sample is treated as semi-infinite. The origin of the (x, y, z) coordinate system shown in Figure 5.12 corresponds to the horizontal centre point of the half space configuration, and is located along the free upper boundary, at a distance b from the vertical interface between the paint (material 1) and the supporting resin (material 2). The dimensions of the FE geometry are $100 \times 100 \times 50 \mu\text{m}^3$. This tetragonal volume is discretised using 8-node isoparametric brick elements with a $2 \times 2 \times 2$ Gaussian quadrature. The model symmetry in the y -direction is exploited by applying appropriate fixed and roller supports along the $x - z$ plane that crosses the origin of the (x, y, z) coordinate system. The semi-infinite character of the half space is simulated by placing 8-node infinite elements along the lateral boundaries and the lower boundary of the FE model. The FE mesh is constructed by employing 606 786 finite elements and 22 594 infinite elements, whereby the mesh density is increased towards the indenter tip for obtaining highly accurate numerical results, as confirmed from a mesh refinement study.

Figure A.1 shows the effective modulus calculated with the FE model and the analytical model, by plotting the dimensionless modulus \bar{E}/E_1 versus the dimensionless indentation radius a/b for a stiffness mismatch of $E_2/E_1 = 5.0$ and Poisson's ratios of $\nu_1 = \nu_2 = 0.35$. The value of the stiffness mismatch is considered as an initial estimate for the embedded paint sample tested in [48]. The effective modulus is deduced from the FE results by applying the stiffness expression Equation (5.36), whereas for the analytical result it directly follows from Equation (5.28). The unloading contact stiffness S in Equation (5.36) is determined from the FE results via the discrete approximation of

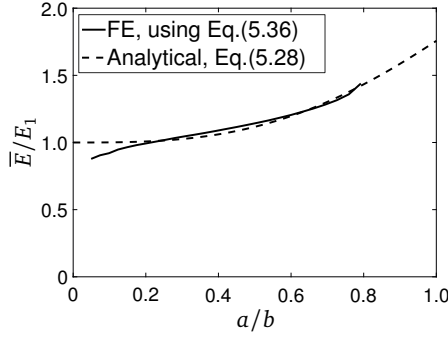


Figure A.1: Indentation response of the semi-infinite elastic bi-material with a straight, vertical material interface as shown in Figure 5.12 (which represents an embedded paint sample). The modulus mismatch equals $E_2/E_1 = 5.0$ and the Poisson's ratios are $\nu_1 = \nu_2 = 0.35$. Dimensionless effective elastic modulus \bar{E}/E_1 versus the dimensionless indentation radius a/b , as determined from applying the stiffness expression Equation (5.36) (solid line) to the FE results, and from the analytical model Equation (5.28) (dashed line).

its definition given in Equation (5.12), i.e. $S \approx \Delta F/\Delta h$, with ΔF and Δh the numerical increments of the applied load and the indentation depth, respectively. The results of the FE simulation are plotted up to the stage at which the indenter reaches the supporting material 2; as indicated in Figure 5.12, the contact radius a is measured in the direction opposite to the material interface, so that the indenter reaches the material interface at a value a/b somewhat smaller than unity, i.e. $a/b = 0.76$. It can be observed in Figure A.1 that the analytical effective modulus matches the numerical effective modulus closely over its full range of indentation radius a/b . Hence, the analytical model, Equation (5.28), can be used for an accurate calibration of the experimental indentation response presented in [48] if the interpretation of the test data is done with the stiffness expression, Equation (5.36).

Although the initially estimated stiffness mismatch of $E_2/E_1 = 5.0$ adopted for generating the results in Figure A.1 is somewhat lower than the stiffness mismatch of $E_2/E_1 = 8.3$ deduced in Section 5.5 from the experimental indentation data, it may be reasonably expected that this does not significantly affect the accuracy of the calibration procedure.

Bibliography

Bibliography

- [1] A. Ahmed and L.J. Sluys. A phantom node formulation for modeling coupled adiabatic-isothermal cracking in FRP composites. *Computer Methods in Applied Mechanics and Engineering*, 278:291–313, 2014.
- [2] T. Alfred. *Fats and Fatty Oils*, pages 1–72. Ullmann’s Encyclopedia of Industrial Chemistry, 2000.
- [3] D.J. Anneken, S. Both, R. Christoph, G. Fieg, U. Steinberner, and A. Westfachtel. *Fatty Acid*, pages 73–116. Ullman’s Encyclopedia of Industrial Chemistry, 2012.
- [4] P. Areias, E. Samaniego, and T. Rabczuk. A staggered approach for the coupling of Cahn-Hilliard type diffusion and finite strain elasticity. *Computational Mechanics*, 57(2):339–351, 2016.
- [5] I.I. Argatov and F.J. Sabina. Small-scale indentation of a hemispherical inhomogeneity in an elastic half-space. *European Journal of Mechanics A/Solids*, 53:151–162, 2015.
- [6] I.I. Argatov and F.J. Sabina. Small-scale indentation of an elastic coated half-space: The effect of compliant substrate. *International Journal of Engineering Science*, 104: 87–96, 2016.
- [7] J.K. Atkinson. Environmental conditions for safeguarding of collections: a background to the current debate on the control of relative humidity and temperature. *Studies in Conservation*, 59(4):205–212, 2014.
- [8] L. Baij, J.J. Hermans, K. Keune, and P.D. Iedema. Time-dependent ATR-FTIR spectroscopic studies on fatty acid diffusion and the formation of metal soaps in oil paint model systems. *Angewandte Chemie International Edition*, 57(25):7351–7354, 6 2018.
- [9] L. Baij, L. Chassouant, J.J. Hermans, K. Keune, and P.D. Iedema. The concentration and origins of carboxylic acid groups in oil paint. *RSC Advances*, 9(61):35559–35564, 2019.
- [10] M. Beerse, K. Keune, P.D. Iedema, S. Woutersen, and J.J. Hermans. Evolution of zinc carboxylate species in oil paint ionomers. *Applied Polymer Materials*, 2(12): 5674–5685, 2020.
- [11] J. Bentley. Organic film formers. In R. Lambourne and T.A. Strivens, editors, *Paint and Surface Coatings - Theory and Practice*, chapter 2, pages 19–90. Woodhead Publishing, second edition, 1999.

- [12] J. Bickersteth. Environmental conditions for safeguarding collections: what should our set points be? *Studies in Conservation*, 59(4):218–224, 2014.
- [13] I. Bonaduce, L. Carlyle, M.P. Colombini, C. Duce, C. Ferrari, E. Ribechini, P. Seleri, and M.R. Tiné. New insights into the ageing of linseed oil paint binder: A qualitative and quantitative analytical study. *PLOS ONE*, 7(11):1–14, 2012.
- [14] I. Bonaduce, C. Duce, A. Lluveras-Tenorio, J. Lee, B. Ormsby, A. Burnstock, and K.J. van den Berg. Conservation issues of modern oil paintings: a molecular model on paint curing. *Accounts of Chemical Research*, 52:3397–3406, 2019.
- [15] J.J. Boon, S. Peulvé, O.F. van den Brink, M.C. Duursma, and D. Rainford. Molecular aspects of mobile and stationary phases in ageing tempera and oil paint films. In T. Bakkenist, R. Hoppenbrouwers, and H. Dubois, editors, *Early Italian Paintings: Techniques and Analysis, Symposium, Maastricht, 09–10 October 1996*, pages 35–56. Limburg Conservation Institute, 1997.
- [16] J.J. Boon, J. van der Weerd, K. Keune, P. Noble, and J. Wadum. Mechanical and chemical changes in Old Master paintings: dissolution, metal soap formation and remineralization processes in lead pigmented ground/intermediate paint layers of 17th century painting. In R. Vontobel, editor, *13th Triennial Meeting of the ICOM Committee for Conservation in Rio De Janeiro*, pages 401–406. James & James, London, 2003.
- [17] E. Bosco, A.S.J. Suiker, and N.A. Fleck. Crack channelling mechanisms in brittle coating systems under moisture or temperature gradients. *International Journal of Fracture*, 225:1–30, 2020.
- [18] E. Bosco, A.S.J. Suiker, and N.A. Fleck. Moisture-induced cracking in a flexural bilayer with application to historical paintings. *Theoretical and Applied Fracture Mechanics*, 112:102779, 2021.
- [19] T.E. Buchheit and T.J. Vogler. Measurement of ceramic powders using instrumented indentation and correlation with their dynamic response. *Mechanics of Materials*, 42(6):599–614, 2010.
- [20] J. Catalano, Y. Yao, A. Murphy, N. Zumbulyadis, S.A. Centeno, and C. Dybowski. Understanding soap formation in paint films by 207 Pb, 119 Sn, and 13 C solid-state NMR. *Materials Science and Technology*, 3:2161–2168, 2014.
- [21] P. Chadwick. The quasi-static expansion of a spherical cavity in metals and ideal soils. *The Quarterly Journal of Mechanics and Applied Mathematics*, 12(1):52–71, 1959.
- [22] X. Chen and J.J. Vlassak. Numerical study on the measurement of thin film mechanical properties by means of nanoindentation. *Journal of Materials Research*, 16(10):2974–2982, 2001.
- [23] Y.K. Chen-Wiegart, J. Catalano, G.J. Williams, A. Murphy, Y. Yao, N. Zumbulyadis, S.A. Centeno, C. Dybowski, and J. Thieme. Elemental and molecular segregation in oil paintings due to lead soap degradation. *Scientific Reports*, 7:11656, 2017.

-
- [24] Y.T. Cheng and C.M. Cheng. Scaling, dimensional analysis, and indentation measurements. *Materials Science and Engineering: R: Reports*, 44(4):91–149, 2004.
- [25] M.V. Cid Alfaro, A.S.J. Suiker, R. de Borst, and J.J.C. Remmers. Analysis of fracture and delamination in laminates using 3D numerical modelling. *Engineering Fracture Mechanics*, 76(6):761–780, 2009.
- [26] M.V. Cid Alfaro, A.S.J. Suiker, and R. de Borst. Transverse failure behavior of fiber-epoxy systems. *Journal of Composite Materials*, 44(12):1493–1516, 2010.
- [27] M.V. Cid Alfaro, A.S.J. Suiker, C.V. Verhoosel, and R. de Borst. Numerical homogenization of cracking processes in thin fibre-epoxy layers. *European Journal of Mechanics, A/Solids*, 29(2):119–131, 2010.
- [28] M. Cotte, E. Checroun, J. Susini, P. Dumas, P. Tchoreloff, M. Besnard, and Ph. Walter. Kinetics of oil saponification by lead salts in ancient preparations of pharmaceutical lead plasters and painting lead mediums. *Talanta*, 70:1136–1142, 2006.
- [29] M. Cotte, E. Checroun, J. Susini, and Ph. Walter. Micro-analytical study of interactions between oil and lead compounds in paintings. *Applied Physics A: Materials Science & Processing*, 89:841–848, 2007.
- [30] M. Cotte, E. Checroun, W. De Nolf, Y. Taniguchi, L. De Viguerie, M. Burghammer, Ph. Walter, C. Rivard, M. Salomé, K. Janssens, and J. Susini. Lead soaps in paintings: Friends or foes? *Studies in Conservation*, 62(1):2–23, 2017.
- [31] N. de Keyser, G. van der Snickt, A. van Loon, S. Legrand, A. Wallert, and K. Janssens. Jan Davidsz. de Heem (1606–1684): a technical examination of fruit and flower still lifes combining MA-XRF scanning, cross-section analysis and technical historical sources. *Heritage Science*, 5(1):38, 2017.
- [32] G. dePolo, M. Walton, K. Keune, and K.R. Shull. After the paint has dried: a review of testing techniques for studying the mechanical properties of artists’ paint. *Heritage Science*, 9:68, 2021.
- [33] M.F. Doerner and W.D. Nix. A method for interpreting the data from depth-sensing indentation instruments. *Journal of Materials Research*, 1(4):601–609, 1986.
- [34] K. Durst, M. Göken, and H. Vehoff. Finite element study for nanoindentation measurements on two-phase materials. *Journal of Materials Research*, 19(1):85–93, 2004.
- [35] K. Durst, M. Göken, and G.M. Pharr. Indentation size effect in spherical and pyramidal indentations. *Journal of Physics D: Applied Physics*, 41(7):074005, 2008.
- [36] D. Erhard, C.S. Tumosa, and M.F. Mecklenburg. Long-term chemical and physical processes in oil paint films. *Studies in Conservation*, 50(2):143–150, 2005.
- [37] G.J.A.M. Eumelen, E. Bosco, A.S.J. Suiker, A. van Loon, and P.D. Iedema. A computational model for chemo-mechanical degradation of historical oil paintings due to metal soap formation. *Journal of the Mechanics and Physics of Solids*, 132:103683, 2019.
-

- [38] G.J.A.M. Eumelen, E. Bosco, A.S.J. Suiker, J.J. Hermans, A. van Loon, K. Keune, and P.D. Iedema. Computational modelling of metal soap formation in historical oil paintings: the influence of fatty acid concentration and nucleus geometry on the induced chemo-mechanical damage. *SN Applied Sciences*, 2:1310, 2020.
- [39] G.J.A.M. Eumelen, E. Bosco, A.S.J. Suiker, J.J. Hermans, A. van Loon, P.D. Iedema, and K. Keune. Numerical modeling of metal soap formation and microcracking in historical oil paintings. In J. Bridgland, editor, *Transcending Boundaries: Integrated Approaches to Conservation*. ICOM-CC 19th Triennial Conference Preprints, Beijing, 17–21 May 2021, International Council of Museums, 2021.
- [40] G.J.A.M. Eumelen, E. Bosco, A.S.J. Suiker, and J.J. Hermans. Chemo-mechanical model for degradation of oil paintings by amorphous and crystalline metal soaps. *Submitted*, 2022.
- [41] G.J.A.M. Eumelen, A.S.J. Suiker, E. Bosco, and N.A. Fleck. Analytical model for elasto-plastic indentation of a hemispherical surface inclusion. *International Journal of Mechanical Sciences*, 224:107267, 2022.
- [42] F.D. Fischer and J. Svoboda. Stress, deformation and diffusion interactions in solids – A simulation study. *Journal of the Mechanics and Physics of Solids*, 78:427–442, 2015.
- [43] A.C. Fischer-Cripps. *Nanoindentation*. Springer, New York, 3rd edition, 2011.
- [44] N.A. Fleck, H. Otoyoy, and A. Needleman. Indentation of porous solids. *International Journal of Solids and Structures*, 29(13):1613–1636, 1992.
- [45] N.A. Fleck, G.M. Muller, M.F. Ashby, and J.W. Hutchinson. Strain gradient plasticity: theory and experiment. *Acta Metallurgica et Materialia*, 42(2):475–487, 1994.
- [46] P.J.J. Forschelen, A.S.J. Suiker, and O. van der Sluis. Effect of residual stress on the delamination response of film-substrate systems under bending. *International Journal of Solids and Structures*, 97–98:284–299, 2016.
- [47] A. Freeman, M. Łukomski, and V. Beltran. Mechanical characterization of a cross-sectional TiO₂ acrylic-based paint by nano-indentation. *Journal of the American Institute for Conservation*, pages 1–13, 2019.
- [48] N. Fujisawa and M. Łukomski. Nanoindentation near the edge of a viscoelastic solid with a rough surface. *Materials & Design*, 184:108174, 2019.
- [49] N. Fujisawa, T.F. Zhang, B.H. Lee, and K.H. Kim. A robust method for extracting the mechanical properties of thin films with rough surfaces by nanoindentation. *Journal of Materials Research*, 31(23):3777–3785, 2016.
- [50] L. Fuster-López, F.C. Izzo, M. Piovesan, D.J. Yusà-Marco, L. Sporni, and E. Zendri. Study of the chemical composition and the mechanical behaviour of 20th century commercial artists’ oil paints containing manganese-based pigments. *Microchemical Journal*, 124:962–973, 2016.
- [51] L. Fuster-López, F.C. Izzo, V. Damato, D.J. Yusà-Marco, and E. Zendri. An insight into the mechanical properties of selected commercial oil and alkyd paint films containing cobalt blue. *Journal of Cultural Heritage*, 35:225–234, 2019.

-
- [52] M. Gagliardi, P. Lenarda, and M. Paggi. A reaction-diffusion formulation to simulate EVA polymer degradation in environmental and accelerated ageing conditions. *Solar Energy Materials and Solar Cells*, 164:93–106, 2017.
- [53] H. Gao, C.H. Chiu, and J. Lee. Elastic contact versus indentation modeling of multi-layered materials. *International Journal of Solids and Structures*, 29(20): 2471–2492, 1992.
- [54] F. Geng and A.S.J. Suiker. An interface damage model for high-cycle fatigue. *Engineering Fracture Mechanics*, 221:106644, 2019.
- [55] E.W.S. Hagan. Thermo-mechanical properties of white oil and acrylic artist paint. *Progress in Organic Coatings*, 104:28–33, 2017.
- [56] E.W.S. Hagan, M.N. Charalambides, C.R.T. Young, T.J.S. Learner, and S. Hackney. Influence of the inorganic phase concentration and geometry on the viscoelastic properties of latex coatings through the glass-transition. *Polymer*, 52(7):1662–1673, 2011.
- [57] J.W. Harding and I.N. Sneddon. The elastic stresses produced by the indentation of the plane surface of a semi-infinite elastic solid by a rigid punch. *Mathematical Proceedings of the Cambridge Philosophical Society*, 41(1):16–26, 1945.
- [58] A. Hattiangadi and T. Siegmund. A numerical study on interface crack growth under heat flux loading. *International Journal of Solids and Structures*, 42(24): 6335–6355, 2005.
- [59] J. Hay and B. Crawford. Measuring substrate-independent modulus of thin films. *Journal of Materials Research*, 26(6):727–738, 2011.
- [60] J.C. Hay, A. Bolshakov, and G.M. Pharr. A critical examination of the fundamental relations used in the analysis of nanoindentation data. *Journal of Materials Research*, 14(6):2296–2305, 1999.
- [61] O.M. Heeres, A.S.J. Suiker, and R. de Borst. A comparison between the Perzyna viscoplastic model and the consistency viscoplastic model. *European Journal of Mechanics - A/Solids*, 21(1):1–12, 2002.
- [62] K. Helwig, J. Poulin, M.-C. Corbeil, E. Moffatt, and D. Duguay. Conservation issues in several twentieth-century Canadian oil paintings: The role of zinc carboxylate reaction products. In K.J. van den Berg, A. Burnstock, M. de Keijzer, J. Krueger, T. Learner, A. de Tagle, and G. Heydenreich, editors, *Issues in contemporary oil paint*, chapter 11, pages 167–184. Springer, 2014.
- [63] E.J. Henderson, K. Helwig, S. Read, and S.M. Rosendahl. Infrared chemical mapping of degradation products in cross-sections from paintings and painted objects. *Heritage Science*, 7(71), 2019.
- [64] E.G. Herbert, G.M. Pharr, W.C. Oliver, B.N. Lucas, and J.L. Hay. On the measurement of stress-strain curves by spherical indentation. *Thin Solid Films*, 398-399: 331–335, 2001.
-

- [65] E.G. Herbert, W.C. Oliver, and G.M. Pharr. Nanoindentation and the dynamic characterization of viscoelastic solids. *Journal of Physics D: Applied Physics*, 41(7): 074021, 2008.
- [66] E.G. Herbert, W.C. Oliver, A. Lumsdaine, and G.M. Pharr. Measuring the constitutive behavior of viscoelastic solids in the time and frequency domain using flat punch nanoindentation. *Journal of Materials Research*, 24(3):626–637, 2009.
- [67] J.J. Hermans. *Metal soaps in oil paint - structure, mechanisms and dynamics*. PhD thesis, University of Amsterdam, 2017.
- [68] J.J. Hermans, K. Keune, A. van Loon, R.W. Corkery, and P.D. Iedema. The molecular structure of three types of long-chain zinc(II) alkanoates for the study of oil paint degradation. *Polyhedron*, 81:335–340, 2014.
- [69] J.J. Hermans, K. Keune, A. van Loon, M.J.N. Stols-Witlox, R.W. Corkery, and P.D. Iedema. The synthesis of new types of lead and zinc soaps: A source of information for the study of oil paint degradation. In J. Bridgland, editor, *ICOM-CC 17th Triennial Conference Preprints, Melbourne, 15-19 September 2014*. International Council of Museums, 2014.
- [70] J.J. Hermans, K. Keune, A. van Loon, and P.D. Iedema. An infrared spectroscopic study of the nature of zinc carboxylates in oil paintings. *Journal of Analytical Atomic Spectrometry*, 30(7):1600–1608, 2015.
- [71] J.J. Hermans, K. Keune, A. van Loon, R.W. Corkery, and P.D. Iedema. Ionomer-like structure in mature oil paint binding media. *RSC Advances*, 6(96):93363–93369, 2016.
- [72] J.J. Hermans, K. Keune, A. van Loon, and P.D. Iedema. The crystallization of metal soaps and fatty acids in oil paint model systems. *Physical Chemistry Chemical Physics*, 18(16):10896–10905, 2016.
- [73] J.J. Hermans, G. Osmond, A. van Loon, P.D. Iedema, R. Chapman, J. Drennan, K. Jack, R. Rasch, G. Morgan, Z. Zhang, M. Monteiro, and K. Keune. Electron microscopy imaging of zinc soaps nucleation in oil paint. *Microscopy and Microanalysis*, 24(3):318–322, 2018.
- [74] J.J. Hermans, L. Zuidgeest, P.D. Iedema, S. Woutersen, and K. Keune. The kinetics of metal soap crystallization in oil polymers. *Physical Chemistry Chemical Physics*, 23:22589–22600, 2021.
- [75] C. Higgitt, M. Spring, and D. Saunders. Pigment-medium interactions in oil paint films containing red lead or lead-tin yellow. *National Gallery Technical Bulletin*, 24: 75–95, 2003.
- [76] R. Hill. *The Mathematical Theory of Plasticity*. Oxford University Press, 1950.
- [77] R. Hill, B. Storåkers, and A.B. Zdunek. A theoretical study of the Brinell hardness test. *Proceedings of the Royal Society of London. Series A: Mathematical, Physical and Engineering Sciences*, 423(1865):301–330, 1989.

-
- [78] T.S. Hille, T.J. Nijdam, A.S.J. Suiker, S. Turteltaub, and W.G. Sloof. Damage growth triggered by interface irregularities in thermal barrier coatings. *Acta Materialia*, 57(9):2624–2630, 2009.
- [79] T.S. Hille, S. Turteltaub, and A.S.J. Suiker. Oxide growth and damage evolution in thermal barrier coatings. *Engineering Fracture Mechanics*, 78(10):2139–2152, 2011.
- [80] J.C. Hubert, R.A.M. Venderbosch, W.J. Muizebelt, R.P. Klaasen, and K.H. Zabel. Mechanistic study of drying of alkyd resins using (Z,Z)- and (E,E)-3,6-nonadiene as model substances. *Progress in Organic Coatings*, 31(4):331–340, 1997.
- [81] A.E. Idiart, C.M. López, and I. Carol. Chemo-mechanical analysis of concrete cracking and degradation due to external sulfate attack: A meso-scale model. *Cement and Concrete Composites*, 33(3):411–423, 2011.
- [82] S. Issa, S. Eliasson, A. Lundberg, M. Wallin, and H. Hallberg. Cohesive zone modeling of crack propagation influenced by martensitic phase transformation. *Materials Science and Engineering: A*, 712:564–573, 2018.
- [83] F.C. Izzo, M. Kratter, A. Nevin, and E. Zendri. A critical review on the analysis of metal soaps in oil paintings. *ChemistryOpen*, 10(9):904–921, 2021.
- [84] J.E. Jakes, C.R. Frihart, J.F. Beecher, R.J. Moon, and D.S. Stone. Experimental method to account for structural compliance in nanoindentation measurements. *Journal of Materials Research*, 23(4):1113–1127, 2008.
- [85] K.L. Johnson. The correlation of indentation experiments. *Journal of the Mechanics and Physics of Solids*, 18(2):115–126, 1970.
- [86] K.L. Johnson. *Contact Mechanics*. Cambridge University Press, 1985.
- [87] K. Keune and J.J. Boon. Analytical imaging studies of cross-sections of paintings affected by lead soap aggregate formation. *Studies in Conservation*, 52(3):161–176, 2007.
- [88] K. Keune, F.G. Hoogland, D. Peggie, C. Higgitt, and J.J. Boon. Comparative study of the effect of traditional pigments on artificially aged oil paint systems using complementary analytical techniques. In J. Bridgland, editor, *15th Triennial Conference, New Delhi*, volume II, pages 833–842. New Delhi: Allied Publishers Pvt.Ltd., 2008.
- [89] K. Keune, A. van Loon, and J.J. Boon. SEM backscattered-electron images of paint cross sections as information source for the presence of the lead white pigment and lead-related degradation and migration phenomena in oil paintings. *Microscopy and Microanalysis*, 17:696–701, 2011.
- [90] K. Keune, R.P. Kramer, Z. Huijbregts, H.L. Schellen, M.H.L. Stappers, and M.H. van Eikema Hommes. Pigment degradation in oil paint induced by indoor climate: Comparison of visual and computational backscattered electron images. *Microscopy and Microanalysis*, 22(2):448–457, 2016.
- [91] J. Kimm, M. Sander, F. Pöhl, and W. Theisen. Micromechanical characterization of hard phases by means of instrumented indentation and scratch testing. *Materials Science and Engineering: A*, 768:138480, 2019.
-

- [92] R.B. King. Elastic analysis of some punch problems for a layered medium. *International Journal of Solids and Structures*, 23(12):1657–1664, 1987.
- [93] J. La Nasa, A. Lluveras-Tenorio, F. Modugno, and I. Bonaduce. Two-step analytical procedure for the characterization and quantification of metal soaps and resinates in paint samples. *Heritage Science*, 6(1):57, 2018.
- [94] T.A. Laursen and J.C. Simo. A study of the mechanics of microindentation using finite elements. *Journal of Materials Research*, 7(3):618–626, 1992.
- [95] M. Lazzari and O. Chiantore. Drying and oxidative degradation of linseed oil. *Polymer Degradation and Stability*, 65(2):303–313, 1999.
- [96] J. Lee, I. Bonaduce, F. Modugno, J. La Nassa, B. Ormsby, and K.J. van den Berg. Scientific investigation into the water sensitivity of twentieth century oil paints. *Microchemical Journal*, 138:282–295, 2018.
- [97] J.H. Lee, Y.F. Gao, K.E. Johanns, and G.M. Pharr. Cohesive interface simulations of indentation cracking as a fracture toughness measurement method for brittle materials. *Acta Materialia*, 60(15):5448–5467, 2012.
- [98] D.R. Lide, editor. *CRC handbook of chemistry and physics, 84th edition*, chapter 4, page 65. CRC Press, 2003.
- [99] T.F. Low, C.L. Pun, and W. Yan. Theoretical study on nanoindentation hardness measurement of a particle embedded in a matrix. *Philosophical Magazine*, 95(14):1573–1586, 2015.
- [100] B.N. Lucas, W.C. Oliver, and J.E. Swindeman. The dynamics of frequency-specific, depth-sensing indentation testing. *MRS Proceedings*, 522:3–14, 1998.
- [101] R.A. Luimes and A.S.J. Suiker. Numerical modelling of climate-induced fracture and deformation in wood: Application to historical museum objects. *International Journal of Solids and Structures*, 210-211:237–254, 2021.
- [102] R.A. Luimes, A.S.J. Suiker, C.V. Verhoosel, A.J.M. Jorissen, and H.L. Schellen. Fracture behaviour of historic and new oak wood. *Wood Science and Technology*, 52(5):1243–1269, 2018.
- [103] M. Łukomski, A. Bridarolli, and N. Fujisawa. Nanoindentation of historic and artists’ paints. *Applied Sciences*, 12:1018, 2022.
- [104] M.G. MacDonald, M.R. Palmer, M.R. Suchomel, and B.H. Berrie. Reaction of Pb(II) and Zn(II) with ethyl linoleate to form structured hybrid inorganic-organic complexes: A model for degradation in historic paint films. *ACS Omega*, 1(3):344–350, 2016.
- [105] C.A. Maines, D. Rogala, S. Lake, and M. Mecklenburg. Deterioration in abstract experssionist paintings: Analysis of zinc oxide paint layers in works from the collection of the Hirshhorn Museum and Sculpture Garden, Smithsonian Institute. *MRS Proceedings, Cambridge University Press*, 1319:275–284, 2011.
- [106] D.M. Marsh. Plastic flow in glass. *Proceedings of the Royal Society of London. Series A: Mathematical, Physical and Engineering Sciences*, 249(1378):420–435, 1964.

-
- [107] E.J. Martínez-Casado, M. Ramos-Riesco, J.A. Rodríguez-Cheda, M.I. Redondo-Yélamos, L. Garrido, A. Fernández-Martínez, J. García-Barriocanal, I. da Silva, M. Durán-Olivencia, and A. Poulain. Lead(II) soaps: crystal structures, polymorphism, and solid and liquid mesophases. *Physical Chemistry Chemical Physics*, 19: 17009, 2017.
- [108] M.R. Maughan, A.A. Leonard, D.D. Stauffer, and D.F. Bahr. The effects of intrinsic properties and defect structures on the indentation size effect in metals. *Philosophical Magazine*, 97(20):1902–1920, 2017.
- [109] M.F. Mecklenburg. Methods and materials and the durability of canvas paintings: a preface to the topical collection failure mechanisms in Picasso’s paintings. *SN Applied Sciences*, 2:2182, 2020.
- [110] M.F. Mecklenburg and C.S. Tumosa. Mechanical behavior of paintings subjected to changes in temperature and relative humidity. In M.F. Mecklenburg, editor, *Art in transit: Studies in the transport of paintings*, pages 173–216. National Gallery of Art, Washington, DC, 1991.
- [111] M.F. Mecklenburg, C.S. Tumosa, and D. Erhardt. The changing mechanical properties of aging oil paints. *MRS Proceedings*, 852:OO3.1, 2004.
- [112] M.F. Mecklenburg, C.S. Tumosa, and D. Erhardt. The influence of pigments and ion migration on the durability of drying oil and alkyd paints. In M.F. Mecklenburg, A.E. Charola, and R.J. Koestler, editors, *New insights into the cleaning of paintings*, pages 59–67. Universidad Politécnica de Valencia, Smithsonian Contributions to Museum Conservation, 2012.
- [113] S.A. Meguid and M.S. Klair. Elasto-plastic co-indentation analysis of a bounded solid using finite element method. *International Journal of Mechanical Sciences*, 27(3):157–168, 1985.
- [114] Z. Mei and J.W. Morris. Analysis of transformation-induced crack closure. *Engineering Fracture Mechanics*, 39(3):569–573, 1991.
- [115] S.Dj. Mesarovic and N.A. Fleck. Spherical indentation of elastic-plastic solids. *Proceedings of the Royal Society of London. Series A: Mathematical, Physical and Engineering Sciences*, 455(1987):2707–2728, 1999.
- [116] C. Miehe, S. Mauthe, and H. Ulmer. Formulation and numerical exploitation of mixed variational principles for coupled problems of Cahn-Hilliard-type and standard diffusion in elastic solids. *International Journal for Numerical Methods in Engineering*, 99(10):737–762, 2014.
- [117] C. Miehe, H. Dal, L.M. Schänzel, and A. Raina. A phase-field model for chemo-mechanical induced fracture in lithium-ion battery electrode particles. *International Journal for Numerical Methods in Engineering*, 106(9):683–711, 2016.
- [118] F. Modugno, F. Di Gianvincenzo, I. Degano, I.D. van der Werf, I. Bonaduce, and K.J. van den Berg. On the influence of relative humidity on the oxidation and hydrolysis of fresh and aged oil paints. *Scientific Reports*, 9:5533, 2019.
-

- [119] W.D. Nix and H. Gau. Indentation size effects in crystalline materials: a law for strain gradient plasticity. *Journal of the Mechanics and Physics of Solids*, 46(3): 411–425, 1998.
- [120] P. Noble. A brief history of metal soaps in paintings from a conservation perspective. In F. Casadio, K. Keune, P. Noble, A. van Loon, E. Hendriks, S.A. Centeno, and G. Osmond, editors, *Metal Soaps in Art: Conservation and Research*, chapter 1, pages 1–22. Springer, 2019.
- [121] P. Noble and J.J. Boon. Metal soap degradation of oil paintings: Aggregates, increased transparency and efflorescence. In H.M. Parkin, editor, *AIC Paintings Specialty Group Postprints: Papers presented at the 34th Annual Meeting of the American Institute for Conservation of Historic & Artistic Works, Providence, Rhode Island*, pages 1–15. Washington, D.C.: AIC, 2007.
- [122] P. Noble, J.J. Boon, and J. Wadum. Dissolution aggregation and protrusion: lead soap formation in 17th century grounds and paint layers. *ArtMatters*, 1:46–61, 2002.
- [123] P. Noble, A. van Loon, and J.J. Boon. Chemical changes in old master paintings II: darkening due to increased transparency as a result of metal soap formation. In I. Verger, editor, *Paintings: Scientific study, conservation and restoration*, volume I, pages 496–503. Preprints of the 14th Triennial Meeting of the ICOM Committee for conservation, London: James & James/Earthscan, 2005.
- [124] P. Noble, A. van Loon, and J.J. Boon. Selective darkening of ground layers associated with the wood grain in 17th-century panel paintings. In J.H. Townsend, T. Doherty, G. Heydenreich, and J. Ridge, editors, *Preparation for painting: The artist's choice and its consequences*, pages 68–78. London: Archetype Publications, 2008.
- [125] P. Noble, E. van Duijn, E. Hermens, K. Keune, A. van Loon, S. Smelt, G. Tauber, and R. Erdmann. An exceptional commission: Conservation history, treatment and painting technique of Rembrandt's Marten and Oopjen. *Rijksmuseum Bulletin*, 66(4):308–345, 2018.
- [126] N. Ogbonna, N.A. Fleck, and A.C.F. Cocks. Transient creep analysis of ball indentation. *International Journal of Mechanical Sciences*, 37(11):1179–1202, 1995.
- [127] W.C. Oliver and G.M. Pharr. An improved technique for determining hardness and elastic modulus using load and displacement sensing indentation experiments. *Journal of Materials Research*, 7(6):1564–1583, 1992.
- [128] W.C. Oliver and G.M. Pharr. Measurement of hardness and elastic modulus by instrumented indentation: Advances in understanding and refinements to methodology. *Journal of Materials Research*, 19(1):3–20, 2004.
- [129] A.S. Ortiz Miranda, D. Kronkright, and M. Walton. The influence of commercial primed canvases in the manifestation of metal soaps protrusions in Georgia O'Keeffe's oil paintings. *Heritage Science*, 8(107), 2020.

-
- [130] G. Osmond, J.J. Boon, L. Puskar, and J. Drennan. Metal stearate distributions in modern artists' oil paints: surface and cross-sectional investigation of reference paint films using conventional and synchrotron infrared microspectroscopy. *Applied Spectroscopy*, 66(10):1136–1144, 2012.
- [131] D.W. Oxtoby, H.P. Gillis, and A. Campion. *Principles of Modern Chemistry*. Thomson, Brooks/Cole, USA, 6th edition, 2008.
- [132] J. Parmigiani and M. Thouless. The roles of toughness and cohesive strength on crack deflection at interfaces. *Journal of the Mechanics and Physics of Solids*, 54(2): 266–287, 2006.
- [133] Y.T. Pei, G.M. Song, W.G. Sloof, and J.Th.M. De Hosson. A methodology to determine anisotropy effects in non-cubic coatings. *Surface and Coatings Technology*, 201(16):6911–6916, 2007.
- [134] P. Perzyna. Fundamental problems in viscoplasticity. *Advances in Applied Mechanics*, 9(2):243–377, 1966.
- [135] G.M. Pharr and A. Bolshakov. Understanding nanoindentation unloading curves. *Journal of Materials Research*, 17(10):2660–2671, 2002.
- [136] G.M. Pharr, E.G. Herbert, and Y. Gao. The indentation size effect: a critical examination of experimental observations and mechanistic interpretations. *Annual Review of Materials Research*, 40:271–292, 2010.
- [137] M.J. Plater, B. De Silva, T. Gelbrich, M.B. Hursthouse, C.L. Higgitt, and D.R. Saunders. The characterisation of lead fatty acid soaps in 'protrusions' in aged traditional oil paint. *Polyhedron*, 22:3171–3179, 2003.
- [138] F. Pöhl, S. Huth, and W. Theisen. Finite element method-assisted acquisition of the matrix influence on the indentation results of an embedded hard phase. *Materials Science and Engineering: A*, 559:822–828, 2013.
- [139] M. Poluektov, A.B. Freidin, and Ł. Figiel. Modelling stress-affected chemical reactions in non-linear viscoelastic solids with application to lithiation reaction in spherical Si particles. *International Journal of Engineering Science*, 128:44–62, 2018.
- [140] L.E. Raven, M. Bisschoff, M. Leeuwestein, M. Geldof, J.J. Hermans, M. Stols-Witlox, and K. Keune. Delamination due to zinc soap formation in an oil painting by Piet Mondrian (1872–1944). In F. Casadio, K. Keune, P. Noble, A. van Loon, E. Hendriks, S.A. Centeno, and G. Osmond, editors, *Metal Soaps in Art: Conservation and Research*, chapter 20, pages 343–358. Springer, 2019.
- [141] A. Roy, editor. *Artists' pigments: A handbook of their history and characteristics*, volume 2. National Gallery of Art, Washington and Archetype Publications, London, 1993.
- [142] R. Saha and W.D. Nix. Effects of the substrate on the determination of thin film mechanical properties by nanoindentation. *Acta Materialia*, 50(1):23–38, 2002.
-

- [143] A. Salvadori, E. Bosco, and D. Grazioli. A computational homogenization approach for Li-ion battery cells: Part 1 - formulation. *Journal of the Mechanics and Physics of Solids*, 65:114–137, 2014.
- [144] J. Salvant, E. Barthel, and M. Menu. Nanoindentation and the micromechanics of Van Gogh oil paints. *Applied Physics A*, 104:509–515, 2011.
- [145] J.C.J. Schellekens and R. de Borst. On the numerical integration of interface elements. *International journal for numerical methods in engineering*, 36(1):43–66, 1993.
- [146] I.C. Schepersboer, A.S.J. Suiker, R.A. Luimes, E. Bosco, and A.J.M. Jorissen. Collapse response of two-dimensional cellular solids by plasticity and cracking – application to wood. *International Journal of Fracture*, 219(2):221–244, 2019.
- [147] I.C. Schepersboer, R.A. Luimes, A.S.J. Suiker, E. Bosco, and F.H.L.R. Clemens. Experimental-numerical study on the structural failure of concrete sewer pipes. *Tunnelling and Underground Space Technology*, 116:104075, 2021.
- [148] Y. Shimadzu, K. Keune, J.J. Boon, J.H. Townsend, and K.J. van den Berg. The effects of lead and zinc white saponification on surface appearance of paints. In J. Bridgland, editor, *Diversity in Heritage Conservation: Tradition, Innovation and Participation*, volume II, pages 626–632. ICOM-CC 15th Triennial Conference Preprints, New Delhi, 22–26 September, 2008, New Delhi: Allied Publishers Pvt. Ltd., 2008.
- [149] I.N. Sneddon. Boussinesq’s problem for a rigid cone. *Mathematical Proceedings of the Cambridge Philosophical Society*, 44(4):492–507, 1948.
- [150] I.N. Sneddon. The relation between load and penetration in the axisymmetric Boussinesq problem for a punch of arbitrary profile. *International Journal of Engineering Science*, 3(1):47–57, 1965.
- [151] Z. Suo, S. Ho, and X. Gong. Notch ductile-to-brittle transition due to localized inelastic band. *Journal of Engineering Materials and Technology*, 115(3):319–326, 1993.
- [152] M. Thoury, A. van Loon, K. Keune, J.J. Hermans, M. Réfrégiers, and B.H. Berrie. Photoluminescence micro-imaging sheds new light on the development of metal soaps in oil paintings. In F. Casadio, K. Keune, P. Noble, A. van Loon, E. Hendriks, S.A. Centeno, and G. Osmond, editors, *Metal Soaps in Art: Conservation and Research*, chapter 12, pages 211–225. Springer, 2019.
- [153] M. Tiennent, E. Paardekam, D. Iannuzzi, and E. Hermens. Mapping the mechanical properties of paintings via nanoindentation: a new approach for cultural heritage studies. *Scientific Reports*, 10:7924, 2020.
- [154] M.G.A. Tijssens, E. van der Giessen, and L.J. Sluys. Simulation of mode I crack growth in polymers by crazing. *International Journal of Solids and Structures*, 37(48-50):7307–7327, 2000.

-
- [155] J.H. Townsend, R. Jones, and K. Stonor. Lead soap aggregates in sixteenth and seventeenth century British paintings. In *AIC Paintings Working Group Meeting 2006 Postprints*, 2007.
- [156] G.J. Tudryn, M.V. O'Reilly, S. Dou, D.R. King, K.I. Winey, J. Runt, and R.H. Colby. Molecular mobility and cation conduction in polyether-ester-sulfonate copolymer ionomers. *Macromolecules*, 45(9):3962–3973, 2012.
- [157] A. Turon, P.P. Camanho, J. Costa, and C.G. Dávila. A damage model for the simulation of delamination in advanced composites under variable-mode loading. *Mechanics of Materials*, 38(11):1072–1089, 2006.
- [158] V. Tvergaard and J.W. Hutchinson. The relation between crack growth resistance and fracture process parameters in elastic-plastic solids. *Journal of the Mechanics and Physics of Solids*, 40(6):1377–1397, 1992.
- [159] V. Tvergaard and A. Needleman. Polymer indentation: Numerical analysis and comparison with a spherical cavity model. *Journal of the Mechanics and Physics of Solids*, 59(9):1669–1684, 2011.
- [160] V. Tvergaard and A. Needleman. Effect of viscoplastic material parameters on polymer indentation. *Modelling and Simulation in Materials Science and Engineering*, 20(6):065002, 2012.
- [161] J.D.J. van den Berg. *Analytical chemical studies on traditional linseed oil paints*. PhD thesis, University of Amsterdam, 2002.
- [162] J.D.J. van den Berg, K.J. van den Berg, and J.J. Boon. Determination of the degree of hydrolysis of oil paint samples using a two-step derivatisation method and on-column GC/MS. *Progress in Organic Coatings*, 41(1):143–155, 2001.
- [163] J. van der Weerd, J.J. Boon, M. Geldof, R.M.A. Heeren, and P. Noble. Chemical changes in old master paintings: dissolution, metal soap formation and remineralisation processes in lead pigmented paint layers of 17th century paintings. *Zeitschrift für Kunsttechnologie und Konservierung*, 16(1):36–51, 2002.
- [164] J. van der Weerd, A. van Loon, and J.J. Boon. FTIR studies of the effects of pigments on the aging of oil. *Studies in Conservation*, 50(1):3–22, 2005.
- [165] R. van Gorkum and E. Bouwman. The oxidative drying of alkyd paint catalysed by metal complexes. *Coordination Chemistry Reviews*, 249:1709–1728, 2005.
- [166] A. van Loon. De korrelige verf in Vermeers Gezicht op Delft. Nieuwe onderzoeksgegevens. *kM Materiaaltechnische informatie over kunst en vormgeving*, 72:10–13, 2009.
- [167] A. van Loon, P. Noble, and A. Burnstock. Ageing and deterioration of traditional oil and tempera paints. In J.H. Stoner and R. Rushfield, editors, *Conservation of Easel Paintings: Principle and Practice*, pages 214–241. Butterworth-Heinemann, 2012.
- [168] B. Vignesh, W.C. Oliver, G. Siva Kumar, and P. Sudharshan Phani. Critical assessment of high speed nanoindentation mapping technique and data deconvolution on thermal barrier coatings. *Materials & Design*, 181:108084, 2019.
-

- [169] A. Villani, E.P. Busso, K. Ammar, S. Forest, and M.G.D. Geers. A fully coupled diffusional-mechanical formulation: numerical implementation, analytical validation, and effects of plasticity on equilibrium. *Archive of Applied Mechanics*, 84(9): 1647–1664, 2014.
- [170] M. Wilsea, K.L. Johnson, and M.F. Ashby. Indentation of foamed plastics. *International Journal of Mechanical Sciences*, 17(7):457–460, 1975.
- [171] X.-P. Xu and A. Needleman. Numerical simulations of fast crack growth in brittle solids. *Journal of the Mechanics and Physics of Solids*, 42(9):1397–1434, 1994.
- [172] W. Yan, C.L. Pun, Z. Wu, and G.P. Simon. Some issues on nanoindentation method to measure the elastic modulus of particles in composites. *Composites Part B: Engineering*, 42(8):2093–2097, 2011.
- [173] H.Y. Yu, S.C. Sanday, and B.B. Rath. The effect of substrate on the elastic properties of films determined by the indentation test – axisymmetric Boussinesq problem. *Journal of the Mechanics and Physics of Solids*, 38(6):745–764, 1990.
- [174] T. Zhang, S. Wang, and W. Wang. A comparative study on uniaxial tensile property calculation models in spherical indentation tests (SITs). *International Journal of Mechanical Sciences*, 155:159–169, 2019.
- [175] M. Zhao, X. Chen, N. Ogasawara, A.C. Razvan, N. Chiba, D. Lee, and Y.X. Gan. New sharp indentation method of measuring the elastic–plastic properties of compliant and soft materials using the substrate effect. *Journal of Materials Research*, 21(12): 3134–3151, 2006.
- [176] Y. Zhao and T.C. Ovaert. Error estimation of nanoindentation mechanical properties near a dissimilar interface via finite element analysis and analytical solution methods. *Journal of Materials Research*, 25(12):2308–2316, 2010.
- [177] O.C. Zienkiewicz, C. Emson, and P. Bettess. A novel boundary infinite element. *International Journal for Numerical Methods in Engineering*, 19(3):393–404, 1983.
- [178] S.S. Zumdahl and S.A. Zumdahl. *Chemistry*. Brooks/Cole Cengage Learning, USA, 9th edition, 2017.

Curriculum Vitae

G.J.A.M. Eumelen

- | | |
|-----------|--|
| 2017–2022 | PhD Researcher,
Department of the Built Environment,
Chair of Applied Mechanics,
Eindhoven University of Technology |
| 2014–2017 | MSc (cum laude), Architecture, Building and Planning –
Structural Engineering and Design,
Eindhoven University of Technology |
| 2010–2014 | BBE, Architecture and Construction Engineering,
Avans University of Applied Sciences, Tilburg |
| 2005–2010 | Hoger Algemeen Voortgezet Onderwijs (HAVO),
Theresialyceum, Tilburg |
| 1993 | Born in Nijmegen, The Netherlands |

Publication List

Journal papers

- G.J.A.M. Eumelen, E. Bosco, A.S.J. Suiker, and J.J. Hermans. Chemo-mechanical model for degradation of oil paintings by amorphous and crystalline metal soaps. *Submitted*, 2022
- G.J.A.M. Eumelen, A.S.J. Suiker, E. Bosco, and N.A. Fleck. Analytical model for elasto-plastic indentation of a hemispherical surface inclusion. *International Journal of Mechanical Sciences*, 224:107267, 2022
- G.J.A.M. Eumelen, E. Bosco, A.S.J. Suiker, J.J. Hermans, A. van Loon, K. Keune, and P.D. Iedema. Computational modelling of metal soap formation in historical oil paintings: the influence of fatty acid concentration and nucleus geometry on the induced chemo-mechanical damage. *SN Applied Sciences*, 2:1310, 2020
- G.J.A.M. Eumelen, E. Bosco, A.S.J. Suiker, A. van Loon, and P.D. Iedema. A computational model for chemo-mechanical degradation of historical oil paintings due to metal soap formation. *Journal of the Mechanics and Physics of Solids*, 132:103683, 2019

Conference papers

- G.J.A.M. Eumelen, E. Bosco, A.S.J. Suiker, J.J. Hermans, A. van Loon, P.D. Iedema, and K. Keune. Numerical modeling of metal soap formation and microcracking in historical oil paintings. In J. Bridgland, editor, *Transcending Boundaries: Integrated Approaches to Conservation*. ICOM-CC 19th Triennial Conference Preprints, Beijing, 17–21 May 2021, International Council of Museums, 2021

Conference contributions

- G.J.A.M. Eumelen, E. Bosco, A.S.J. Suiker, and J.J. Hermans. Oral presentation: Chemo-mechanical model for degradation of oil paintings by amorphous and crystalline metal soap. Netherlands Institute for Conservation, Art and Science (NICAS) Colloquium, Online, 24 February, 2022.
- G.J.A.M. Eumelen, A.S.J. Suiker, E. Bosco, and N.A. Fleck. Poster presentation: Elastic and elastic-plastic indentation of embedded materials. Twenty-fourth Engineering Mechanics Symposium, Arnhem, The Netherlands, 26 October, 2021.

- G.J.A.M. Eumelen, E. Bosco, A.S.J. Suiker, J.J. Hermans, A. van Loon, P.D. Iedema, and K. Keune. Oral presentation: Numerical modeling of metal soap formation and microcracking in historical oil paintings. ICOM-CC 19th Triennial Conference, Online, 17–21 May 2021.
- G.J.A.M. Eumelen, E. Bosco, and A.S.J. Suiker. Oral presentation: Modelling chemo-mechanical damage of historical oil paintings. Netherlands Institute for Conservation, Art and Science (NICAS) Colloquium, Online, 12 November, 2020.
- G.J.A.M. Eumelen, E. Bosco, and A.S.J. Suiker. Oral presentation: Modeling chemo-mechanical damage of historical oil paintings. Twenty-third Engineering Mechanics Symposium, Online, 27–28 October, 2020.
- G.J.A.M. Eumelen, E. Bosco, and A.S.J. Suiker. Poster presentation: A computational model for predicting chemo-mechanical degradation of historical oil paintings. Twenty-second Engineering Mechanics Symposium, Arnhem, The Netherlands, 22–23 October, 2019.
- G.J.A.M. Eumelen, E. Bosco, and A.S.J. Suiker. Oral presentation: Numerical modelling of the chemo-mechanical degradation of historical oil paintings. VIII International Conference on Computational Methods for Coupled Problems in Science and Engineering (COUPLED PROBLEMS 2019), Sitges, Spain, 03–05 June, 2019.
- G.J.A.M. Eumelen, E. Bosco, and A.S.J. Suiker. Poster presentation: Determining the elastic modulus of historic oil paintings. Twenty-first Engineering Mechanics Symposium, Arnhem, The Netherlands, 23–24 October, 2018.
- G.J.A.M. Eumelen, E. Bosco, and A.S.J. Suiker. Oral presentation: Damage formation in historic oil paintings due to metal soap growth. Netherlands Institute for Conservation, Art and Science (NICAS) Match day 2018, Amsterdam, The Netherlands, 05 June, 2018.
- G.J.A.M. Eumelen, A.S.J. Suiker, and E. Bosco. Poster presentation: Saving Masterpieces: A multi-physics model for damage formation in oil paintings. Twentieth Engineering Mechanics Symposium, Arnhem, The Netherlands, 23–25 October, 2017.

Bouwstenen is een publicatiereeks van de Faculteit Bouwkunde, Technische Universiteit Eindhoven. Zij presenteert resultaten van onderzoek en andere activiteiten op het vakgebied der Bouwkunde, uitgevoerd in het kader van deze Faculteit.

Bouwstenen en andere proefschriften van de TU/e zijn online beschikbaar via:
<https://research.tue.nl/>

Reeds verschenen in de serie

Bouwstenen

nr 1

Elan: A Computer Model for Building Energy Design: Theory and Validation

Martin H. de Wit

H.H. Driessen

R.M.M. van der Velden

nr 2

Kwaliteit, Keuzevrijheid en Kosten: Evaluatie van Experiment Klarendal, Arnhem

J. Smeets

C. le Nobel

M. Broos

J. Frenken

A. v.d. Sanden

nr 3

Crooswijk: Van 'Bijzonder' naar 'Gewoon'

Vincent Smit

Kees Noort

nr 4

Staal in de Woningbouw

Edwin J.F. Delsing

nr 5

Mathematical Theory of Stressed Skin Action in Profiled Sheeting with Various Edge Conditions

Andre W.A.M.J. van den Bogaard

nr 6

Hoe Berekenbaar en Betrouwbaar is de Coëfficiënt k in x -ksigma en x -ks?

K.B. Lub

A.J. Bosch

nr 7

Het Typologisch Gereedschap: Een Verkennende Studie Omtrent Typologie en Omtrent de Aanpak van Typologisch Onderzoek

J.H. Luiten

nr 8

Informatievoorziening en Beheerprocessen

A. Nauta

Jos Smeets (red.)

Helga Fassbinder (projectleider)

Adrie Proveniers

J. v.d. Moosdijk

nr 9

Strukturering en Verwerking van Tijdgegevens voor de Uitvoering van Bouwwerken

ir. W.F. Schaefer

P.A. Erkelens

nr 10

Stedebouw en de Vorming van een Speciale Wetenschap

K. Doevendans

nr 11

Informatica en Ondersteuning van Ruimtelijke Besluitvorming

G.G. van der Meulen

nr 12

Staal in de Woningbouw, Korrosie-Bescherming van de Begane Grondvloer

Edwin J.F. Delsing

nr 13

Een Thermisch Model voor de Berekening van Staalplaatbetonvloeren onder Brandomstandigheden

A.F. Hamerlinck

nr 14

De Wijkgedachte in Nederland: Gemeenschapstreven in een Stedebouwkundige Context

K. Doevendans

R. Stolzenburg

nr 15

Diaphragm Effect of Trapezoidally Profiled Steel Sheets: Experimental Research into the Influence of Force Application

Andre W.A.M.J. van den Bogaard

nr 16

Versterken met Spuit-Ferrocement: Het Mechanische Gedrag van met Spuit-Ferrocement Versterkte Gewapend Betonbalken

K.B. Lubir

M.C.G. van Wanroy

nr 17

**De Tractaten van
Jean Nicolas Louis Durand**
G. van Zeyl

nr 18

**Wonen onder een Plat Dak:
Drie Opstellen over Enkele
Vooronderstellingen van de
Stedebouw**
K. Doevendans

nr 19

**Supporting Decision Making Processes:
A Graphical and Interactive Analysis of
Multivariate Data**
W. Adams

nr 20

**Self-Help Building Productivity:
A Method for Improving House Building
by Low-Income Groups Applied to Kenya
1990-2000**
P. A. Erkelens

nr 21

**De Verdeling van Woningen:
Een Kwestie van Onderhandelen**
Vincent Smit

nr 22

**Flexibiliteit en Kosten in het Ontwerpproces:
Een Besluitvormingondersteunend Model**
M. Prins

nr 23

**Spontane Nederzettingen Begeleid:
Voorwaarden en Criteria in Sri Lanka**
Po Hin Thung

nr 24

**Fundamentals of the Design of
Bamboo Structures**
Oscar Arce-Villalobos

nr 25

Concepten van de Bouwkunde
M.F.Th. Bax (red.)
H.M.G.J. Trum (red.)

nr 26

Meaning of the Site
Xiaodong Li

nr 27

**Het Woonmilieu op Begrip Gebracht:
Een Speurtocht naar de Betekenis van het
Begrip 'Woonmilieu'**
Jaap Ketelaar

nr 28

Urban Environment in Developing Countries
editors: Peter A. Erkelens
George G. van der Meulen (red.)

nr 29

**Stategische Plannen voor de Stad:
Onderzoek en Planning in Drie Steden**
prof.dr. H. Fassbinder (red.)
H. Rikhof (red.)

nr 30

Stedebouwkunde en Stadsbestuur
Piet Beekman

nr 31

**De Architectuur van Djenné:
Een Onderzoek naar de Historische Stad**
P.C.M. Maas

nr 32

Conjoint Experiments and Retail Planning
Harmen Oppewal

nr 33

**Strukturformen Indonesischer Bautechnik:
Entwicklung Methodischer Grundlagen
für eine 'Konstruktive Pattern Language'
in Indonesien**
Heinz Frick arch. SIA

nr 34

**Styles of Architectural Designing:
Empirical Research on Working Styles
and Personality Dispositions**
Anton P.M. van Bakel

nr 35

**Conjoint Choice Models for Urban
Tourism Planning and Marketing**
Benedict Dellaert

nr 36

Stedelijke Planvorming als Co-Productie
Helga Fassbinder (red.)

nr 37

Design Research in the Netherlands

editors: R.M. Oxman
M.F.Th. Bax
H.H. Achten

nr 38

Communication in the Building Industry

Bauke de Vries

nr 39

**Optimaal Dimensioneren van
Gelaste Plaatliggers**

J.B.W. Stark
F. van Pelt
L.F.M. van Gorp
B.W.E.M. van Hove

nr 40

Huisvesting en Overwinning van Armoede

P.H. Thung
P. Beekman (red.)

nr 41

**Urban Habitat:
The Environment of Tomorrow**

George G. van der Meulen
Peter A. Erkelens

nr 42

A Typology of Joints

John C.M. Olie

nr 43

**Modeling Constraints-Based Choices
for Leisure Mobility Planning**

Marcus P. Stemerding

nr 44

Activity-Based Travel Demand Modeling

Dick Ettema

nr 45

**Wind-Induced Pressure Fluctuations
on Building Facades**

Chris Geurts

nr 46

Generic Representations

Henri Achten

nr 47

**Johann Santini Aichel:
Architectuur en Ambiguiteit**

Dirk De Meyer

nr 48

**Concrete Behaviour in Multiaxial
Compression**

Erik van Geel

nr 49

Modelling Site Selection

Frank Witlox

nr 50

Ecolemma Model

Ferdinand Beetstra

nr 51

**Conjoint Approaches to Developing
Activity-Based Models**

Donggen Wang

nr 52

On the Effectiveness of Ventilation

Ad Roos

nr 53

**Conjoint Modeling Approaches for
Residential Group preferences**

Eric Molin

nr 54

**Modelling Architectural Design
Information by Features**

Jos van Leeuwen

nr 55

**A Spatial Decision Support System for
the Planning of Retail and Service Facilities**

Theo Arentze

nr 56

Integrated Lighting System Assistant

Ellie de Groot

nr 57

Ontwerpend Leren, Leren Ontwerpen

J.T. Boekholt

nr 58

**Temporal Aspects of Theme Park Choice
Behavior**

Astrid Kemperman

nr 59

**Ontwerp van een Geïndustrialiseerde
Funderingswijze**

Faas Moonen

nr 60

**Merlin: A Decision Support System
for Outdoor Leisure Planning**

Manon van Middelkoop

nr 61

The Aura of Modernity

Jos Bosman

nr 62

Urban Form and Activity-Travel Patterns

Daniëlle Snellen

nr 63

Design Research in the Netherlands 2000

Henri Achten

nr 64

**Computer Aided Dimensional Control in
Building Construction**

Rui Wu

nr 65

Beyond Sustainable Building

editors: Peter A. Erkelens
Sander de Jonge
August A.M. van Vliet

co-editor: Ruth J.G. Verhagen

nr 66

Das Globalrecyclingfähige Haus

Hans Löfflad

nr 67

Cool Schools for Hot Suburbs

René J. Dierckx

nr 68

**A Bamboo Building Design Decision
Support Tool**

Fitri Mardjono

nr 69

Driving Rain on Building Envelopes

Fabien van Mook

nr 70

Heating Monumental Churches

Henk Schellen

nr 71

**Van Woningverhuurder naar
Aanbieder van Woongenot**

Patrick Dogge

nr 72

**Moisture Transfer Properties of
Coated Gypsum**

Emile Goossens

nr 73

Plybamboo Wall-Panels for Housing

Guillermo E. González-Beltrán

nr 74

The Future Site-Proceedings

Ger Maas
Frans van Gassel

nr 75

**Radon transport in
Autoclaved Aerated Concrete**

Michel van der Pal

nr 76

**The Reliability and Validity of Interactive
Virtual Reality Computer Experiments**

Amy Tan

nr 77

**Measuring Housing Preferences Using
Virtual Reality and Belief Networks**

Maciej A. Orzechowski

nr 78

**Computational Representations of Words
and Associations in Architectural Design**

Nicole Segers

nr 79

**Measuring and Predicting Adaptation in
Multidimensional Activity-Travel Patterns**

Chang-Hyeon Joh

nr 80

Strategic Briefing

Fayez Al Hassan

nr 81

Well Being in Hospitals

Simona Di Cicco

nr 82

**Solares Bauen:
Implementierungs- und Umsetzungs-
Aspekte in der Hochschulausbildung
in Österreich**

Gerhard Schuster

nr 83

**Supporting Strategic Design of
Workplace Environments with
Case-Based Reasoning**

Shauna Mallory-Hill

nr 84

**ACCEL: A Tool for Supporting Concept
Generation in the Early Design Phase**

Maxim Ivashkov

nr 85

**Brick-Mortar Interaction in Masonry
under Compression**

Ad Vermeltfoort

nr 86

Zelfredzaam Wonen

Guus van Vliet

nr 87

Een Ensemble met Grootstedelijke Allure

Jos Bosman

Hans Schippers

nr 88

**On the Computation of Well-Structured
Graphic Representations in Architectural
Design**

Henri Achten

nr 89

**De Evolutie van een West-Afrikaanse
Vernaculaire Architectuur**

Wolf Schijns

nr 90

ROMBO Tactiek

Christoph Maria Ravesloot

nr 91

**External Coupling between Building
Energy Simulation and Computational
Fluid Dynamics**

Ery Djunaedy

nr 92

Design Research in the Netherlands 2005

editors: Henri Achten

Kees Dorst

Pieter Jan Stappers

Bauke de Vries

nr 93

Ein Modell zur Baulichen Transformation

Jalil H. Saber Zaimian

nr 94

**Human Lighting Demands:
Healthy Lighting in an Office Environment**

Myriam Aries

nr 95

**A Spatial Decision Support System for
the Provision and Monitoring of Urban
Greenspace**

Claudia Pelizaro

nr 96

Leren Creëren

Adri Proveniers

nr 97

Simlandscape

Rob de Waard

nr 98

Design Team Communication

Ad den Otter

nr 99

**Humaan-Ecologisch
Georiënteerde Woningbouw**

Juri Czabanowski

nr 100

Hambase

Martin de Wit

nr 101

**Sound Transmission through Pipe
Systems and into Building Structures**

Susanne Bron-van der Jagt

nr 102

Het Bouwkundig Contrapunt

Jan Francis Boelen

nr 103

**A Framework for a Multi-Agent
Planning Support System**

Dick Saarloos

nr 104

**Bracing Steel Frames with Calcium
Silicate Element Walls**

Bright Mweene Ng'andu

nr 105

Naar een Nieuwe Houtskeletbouw

F.N.G. De Medts

nr 106 and 107
Niet gepubliceerd

nr 108
Geborgenheid
T.E.L. van Pinxteren

nr 109
Modelling Strategic Behaviour in Anticipation of Congestion
Qi Han

nr 110
Reflecties op het Woondomein
Fred Sanders

nr 111
On Assessment of Wind Comfort by Sand Erosion
Gábor Dezsö

nr 112
Bench Heating in Monumental Churches
Dionne Limpens-Neilen

nr 113
RE. Architecture
Ana Pereira Roders

nr 114
Toward Applicable Green Architecture
Usama El Fiky

nr 115
Knowledge Representation under Inherent Uncertainty in a Multi-Agent System for Land Use Planning
Liying Ma

nr 116
Integrated Heat Air and Moisture Modeling and Simulation
Jos van Schijndel

nr 117
Concrete Behaviour in Multiaxial Compression
J.P.W. Bongers

nr 118
The Image of the Urban Landscape
Ana Moya Pellitero

nr 119
The Self-Organizing City in Vietnam
Stephanie Geertman

nr 120
A Multi-Agent Planning Support System for Assessing Externalities of Urban Form Scenarios
Rachel Katoshevski-Cavari

nr 121
Den Schulbau Neu Denken, Fühlen und Wollen
Urs Christian Maurer-Dietrich

nr 122
Peter Eisenman Theories and Practices
Bernhard Kormoss

nr 123
User Simulation of Space Utilisation
Vincent Tabak

nr 125
In Search of a Complex System Model
Oswald Devisch

nr 126
Lighting at Work: Environmental Study of Direct Effects of Lighting Level and Spectrum on Psycho-Physiological Variables
Grazyna Górnicka

nr 127
Flanking Sound Transmission through Lightweight Framed Double Leaf Walls
Stefan Schoenwald

nr 128
Bounded Rationality and Spatio-Temporal Pedestrian Shopping Behavior
Wei Zhu

nr 129
Travel Information: Impact on Activity Travel Pattern
Zhongwei Sun

nr 130
Co-Simulation for Performance Prediction of Innovative Integrated Mechanical Energy Systems in Buildings
Marija Trčka

nr 131
Niet gepubliceerd

nr 132

Architectural Cue Model in Evacuation Simulation for Underground Space Design
Chengyu Sun

nr 133

Uncertainty and Sensitivity Analysis in Building Performance Simulation for Decision Support and Design Optimization
Christina Hopfe

nr 134

Facilitating Distributed Collaboration in the AEC/FM Sector Using Semantic Web Technologies
Jacob Beetz

nr 135

Circumferentially Adhesive Bonded Glass Panes for Bracing Steel Frame in Façades
Edwin Huveners

nr 136

Influence of Temperature on Concrete Beams Strengthened in Flexure with CFRP
Ernst-Lucas Klamer

nr 137

Sturen op Klantwaarde
Jos Smeets

nr 139

Lateral Behavior of Steel Frames with Discretely Connected Precast Concrete Infill Panels
Paul Teewen

nr 140

Integral Design Method in the Context of Sustainable Building Design
Perica Savanović

nr 141

Household Activity-Travel Behavior: Implementation of Within-Household Interactions
Renni Anggraini

nr 142

Design Research in the Netherlands 2010
Henri Achten

nr 143

Modelling Life Trajectories and Transport Mode Choice Using Bayesian Belief Networks
Marloes Verhoeven

nr 144

Assessing Construction Project Performance in Ghana
William Gyadu-Asiedu

nr 145

Empowering Seniors through Domotic Homes
Masi Mohammadi

nr 146

An Integral Design Concept for Ecological Self-Compacting Concrete
Martin Hunger

nr 147

Governing Multi-Actor Decision Processes in Dutch Industrial Area Redevelopment
Erik Blokhuis

nr 148

A Multifunctional Design Approach for Sustainable Concrete
Götz Hüsken

nr 149

Quality Monitoring in Infrastructural Design-Build Projects
Ruben Favié

nr 150

Assessment Matrix for Conservation of Valuable Timber Structures
Michael Abels

nr 151

Co-simulation of Building Energy Simulation and Computational Fluid Dynamics for Whole-Building Heat, Air and Moisture Engineering
Mohammad Mirsadeghi

nr 152

External Coupling of Building Energy Simulation and Building Element Heat, Air and Moisture Simulation
Daniel Cóstola

nr 153

**Adaptive Decision Making In
Multi-Stakeholder Retail Planning**

Ingrid Janssen

nr 154

Landscape Generator

Kymo Slager

nr 155

Constraint Specification in Architecture

Remco Niemeijer

nr 156

**A Need-Based Approach to
Dynamic Activity Generation**

Linda Nijland

nr 157

**Modeling Office Firm Dynamics in an
Agent-Based Micro Simulation Framework**

Gustavo Garcia Manzato

nr 158

**Lightweight Floor System for
Vibration Comfort**

Sander Zegers

nr 159

Aanpasbaarheid van de Draagstructuur

Roel Gijsbers

nr 160

'Village in the City' in Guangzhou, China

Yanliu Lin

nr 161

Climate Risk Assessment in Museums

Marco Martens

nr 162

Social Activity-Travel Patterns

Pauline van den Berg

nr 163

**Sound Concentration Caused by
Curved Surfaces**

Martijn Vercammen

nr 164

**Design of Environmentally Friendly
Calcium Sulfate-Based Building Materials:
Towards an Improved Indoor Air Quality**

Qingliang Yu

nr 165

**Beyond Uniform Thermal Comfort
on the Effects of Non-Uniformity and
Individual Physiology**

Lisje Schellen

nr 166

Sustainable Residential Districts

Gaby Abdalla

nr 167

**Towards a Performance Assessment
Methodology using Computational
Simulation for Air Distribution System
Designs in Operating Rooms**

Mônica do Amaral Melhado

nr 168

**Strategic Decision Modeling in
Brownfield Redevelopment**

Branco Glumac

nr 169

**Pamela: A Parking Analysis Model
for Predicting Effects in Local Areas**

Peter van der Waerden

nr 170

**A Vision Driven Wayfinding Simulation-System
Based on the Architectural Features Perceived
in the Office Environment**

Qunli Chen

nr 171

**Measuring Mental Representations
Underlying Activity-Travel Choices**

Oliver Horeni

nr 172

**Modelling the Effects of Social Networks
on Activity and Travel Behaviour**

Nicole Ronald

nr 173

**Uncertainty Propagation and Sensitivity
Analysis Techniques in Building Performance
Simulation to Support Conceptual Building
and System Design**

Christian Struck

nr 174

**Numerical Modeling of Micro-Scale
Wind-Induced Pollutant Dispersion
in the Built Environment**

Pierre Gousseau

nr 175

**Modeling Recreation Choices
over the Family Lifecycle**

Anna Beatriz Grigolon

nr 176

**Experimental and Numerical Analysis of
Mixing Ventilation at Laminar, Transitional
and Turbulent Slot Reynolds Numbers**

Twan van Hooff

nr 177

**Collaborative Design Support:
Workshops to Stimulate Interaction and
Knowledge Exchange Between Practitioners**

Emile M.C.J. Quanjel

nr 178

Future-Proof Platforms for Aging-in-Place

Michiel Brink

nr 179

**Motivate:
A Context-Aware Mobile Application for
Physical Activity Promotion**

Yuzhong Lin

nr 180

**Experience the City:
Analysis of Space-Time Behaviour and
Spatial Learning**

Anastasia Moiseeva

nr 181

**Unbonded Post-Tensioned Shear Walls of
Calcium Silicate Element Masonry**

Lex van der Meer

nr 182

**Construction and Demolition Waste
Recycling into Innovative Building Materials
for Sustainable Construction in Tanzania**

Mwita M. Sabai

nr 183

**Durability of Concrete
with Emphasis on Chloride Migration**

Przemysław Spiesz

nr 184

**Computational Modeling of Urban
Wind Flow and Natural Ventilation Potential
of Buildings**

Rubina Ramponi

nr 185

**A Distributed Dynamic Simulation
Mechanism for Buildings Automation
and Control Systems**

Azzedine Yahiaoui

nr 186

**Modeling Cognitive Learning of Urban
Networks in Daily Activity-Travel Behavior**

Şehnaz Cenani Durmazoğlu

nr 187

**Functionality and Adaptability of Design
Solutions for Public Apartment Buildings
in Ghana**

Stephen Agyefi-Mensah

nr 188

**A Construction Waste Generation Model
for Developing Countries**

Lilliana Abarca-Guerrero

nr 189

**Synchronizing Networks:
The Modeling of Supernetworks for
Activity-Travel Behavior**

Feixiong Liao

nr 190

**Time and Money Allocation Decisions
in Out-of-Home Leisure Activity Choices**

Gamze Zeynep Dane

nr 191

**How to Measure Added Value of CRE and
Building Design**

Rianne Appel-Meulenbroek

nr 192

**Secondary Materials in Cement-Based
Products:
Treatment, Modeling and Environmental
Interaction**

Miruna Florea

nr 193

**Concepts for the Robustness Improvement
of Self-Compacting Concrete:
Effects of Admixtures and Mixture**

**Components on the Rheology and Early
Hydration at Varying Temperatures**

Wolfram Schmidt

nr 194

Modelling and Simulation of Virtual Natural Lighting Solutions in Buildings

Rizki A. Mangkuto

nr 195

Nano-Silica Production at Low Temperatures from the Dissolution of Olivine - Synthesis, Tailoring and Modelling

Alberto Lazaro Garcia

nr 196

Building Energy Simulation Based Assessment of Industrial Halls for Design Support

Bruno Lee

nr 197

Computational Performance Prediction of the Potential of Hybrid Adaptable Thermal Storage Concepts for Lightweight Low-Energy Houses

Pieter-Jan Hoes

nr 198

Application of Nano-Silica in Concrete

George Quercia Bianchi

nr 199

Dynamics of Social Networks and Activity Travel Behaviour

Fariya Sharmeen

nr 200

Building Structural Design Generation and Optimisation including Spatial Modification

Juan Manuel Davila Delgado

nr 201

Hydration and Thermal Decomposition of Cement/Calcium-Sulphate Based Materials

Ariën de Korte

nr 202

Republiek van Beelden: De Politieke Werkingen van het Ontwerp in Regionale Planvorming

Bart de Zwart

nr 203

Effects of Energy Price Increases on Individual Activity-Travel Repertoires and Energy Consumption

Dujuan Yang

nr 204

Geometry and Ventilation: Evaluation of the Leeward Sawtooth Roof Potential in the Natural Ventilation of Buildings

Jorge Isaac Perén Montero

nr 205

Computational Modelling of Evaporative Cooling as a Climate Change Adaptation Measure at the Spatial Scale of Buildings and Streets

Hamid Montazeri

nr 206

Local Buckling of Aluminium Beams in Fire Conditions

Ronald van der Meulen

nr 207

Historic Urban Landscapes: Framing the Integration of Urban and Heritage Planning in Multilevel Governance

Loes Veldpaus

nr 208

Sustainable Transformation of the Cities: Urban Design Pragmatics to Achieve a Sustainable City

Ernesto Antonio Zumelzu Scheel

nr 209

Development of Sustainable Protective Ultra-High Performance Fibre Reinforced Concrete (UHPFRC): Design, Assessment and Modeling

Rui Yu

nr 210

Uncertainty in Modeling Activity-Travel Demand in Complex Urban Systems

Soora Rasouli

nr 211

Simulation-based Performance Assessment of Climate Adaptive Greenhouse Shells

Chul-sung Lee

nr 212

Green Cities: Modelling the Spatial Transformation of the Urban Environment using Renewable Energy Technologies

Saleh Mohammadi

nr 213

A Bounded Rationality Model of Short and Long-Term Dynamics of Activity-Travel Behavior

Ifigeneia Psarra

nr 214

Effects of Pricing Strategies on Dynamic Repertoires of Activity-Travel Behaviour

Elaheh Khademi

nr 215

Handstorm Principles for Creative and Collaborative Working

Frans van Gassel

nr 216

Light Conditions in Nursing Homes: Visual Comfort and Visual Functioning of Residents

Marianne M. Sinoo

nr 217

**Woonsporen:
De Sociale en Ruimtelijke Biografie van een Stedelijk Bouwblok in de Amsterdamse Transvaalbuurt**

Hüseyin Hüsnü Yegenoglu

nr 218

Studies on User Control in Ambient Intelligent Systems

Berent Willem Meerbeek

nr 219

Daily Livings in a Smart Home: Users' Living Preference Modeling of Smart Homes

Erfaneh Allameh

nr 220

Smart Home Design: Spatial Preference Modeling of Smart Homes

Mohammadali Heidari Jozam

nr 221

**Wonen:
Discoursen, Praktijken, Perspectieven**

Jos Smeets

nr 222

**Personal Control over Indoor Climate in Offices:
Impact on Comfort, Health and Productivity**

Atze Christiaan Boerstra

nr 223

Personalized Route Finding in Multimodal Transportation Networks

Jianwe Zhang

nr 224

The Design of an Adaptive Healing Room for Stroke Patients

Elke Daemen

nr 225

Experimental and Numerical Analysis of Climate Change Induced Risks to Historic Buildings and Collections

Zara Huijbregts

nr 226

Wind Flow Modeling in Urban Areas Through Experimental and Numerical Techniques

Alessio Ricci

nr 227

Clever Climate Control for Culture: Energy Efficient Indoor Climate Control Strategies for Museums Respecting Collection Preservation and Thermal Comfort of Visitors

Rick Kramer

nr 228

Fatigue Life Estimation of Metal Structures Based on Damage Modeling

Sarmediran Silitonga

nr 229

A multi-agents and occupancy based strategy for energy management and process control on the room-level

Timilehin Moses Labeodan

nr 230

Environmental assessment of Building Integrated Photovoltaics: Numerical and Experimental Carrying Capacity Based Approach

Michiel Ritzen

nr 231

Performance of Admixture and Secondary Minerals in Alkali Activated Concrete: Sustaining a Concrete Future

Arno Keulen

nr 232

World Heritage Cities and Sustainable Urban Development: Bridging Global and Local Levels in Monitoring the Sustainable Urban Development of World Heritage Cities

Paloma C. Guzman Molina

nr 233

Stage Acoustics and Sound Exposure in Performance and Rehearsal Spaces for Orchestras:

Methods for Physical Measurements

Remy Wenmaekers

nr 234

Municipal Solid Waste Incineration (MSWI) Bottom Ash:

From Waste to Value Characterization, Treatments and Application

Pei Tang

nr 235

Large Eddy Simulations Applied to Wind Loading and Pollutant Dispersion

Mattia Ricci

nr 236

Alkali Activated Slag-Fly Ash Binders: Design, Modeling and Application

Xu Gao

nr 237

Sodium Carbonate Activated Slag: Reaction Analysis, Microstructural Modification & Engineering Application

Bo Yuan

nr 238

Shopping Behavior in Malls

Widiyani

nr 239

Smart Grid-Building Energy Interactions: Demand Side Power Flexibility in Office Buildings

Kennedy Otieno Aduda

nr 240

Modeling Taxis Dynamic Behavior in Uncertain Urban Environments

Zheng Zhong

nr 241

Gap-Theoretical Analyses of Residential Satisfaction and Intention to Move

Wen Jiang

nr 242

Travel Satisfaction and Subjective Well-Being: A Behavioral Modeling Perspective

Yanan Gao

nr 243

Building Energy Modelling to Support the Commissioning of Holistic Data Centre Operation

Vojtech Zavrel

nr 244

Regret-Based Travel Behavior Modeling: An Extended Framework

Sunghoon Jang

nr 245

Towards Robust Low-Energy Houses: A Computational Approach for Performance Robustness Assessment using Scenario Analysis

Rajesh Reddy Kotireddy

nr 246

Development of sustainable and functionalized inorganic binder-biofiber composites

Guillaume Doudart de la Grée

nr 247

A Multiscale Analysis of the Urban Heat Island Effect: From City Averaged Temperatures to the Energy Demand of Individual Buildings

Yasin Toparlar

nr 248

Design Method for Adaptive Daylight Systems for buildings covered by large (span) roofs

Florian Heinzelmann

nr 249

Hardening, high-temperature resistance and acid resistance of one-part geopolymers

Patrick Sturm

nr 250

Effects of the built environment on dynamic repertoires of activity-travel behaviour

Aida Pontes de Aquino

nr 251

Modeling for auralization of urban environments: Incorporation of directivity in sound propagation and analysis of a framework for auralizing a car pass-by

Fotis Georgiou

nr 252

Wind Loads on Heliostats and Photovoltaic Trackers

Andreas Pfahl

nr 253

Approaches for computational performance optimization of innovative adaptive façade concepts

Roel Loonen

nr 254

Multi-scale FEM-DEM Model for Granular Materials: Micro-scale boundary conditions, Statics, and Dynamics

Jiadun Liu

nr 255

Bending Moment - Shear Force Interaction of Rolled I-Shaped Steel Sections

Rianne Willie Adriana Dekker

nr 256

Paralympic tandem cycling and hand-cycling: Computational and wind tunnel analysis of aerodynamic performance

Paul Fionn Mannion

nr 257

Experimental characterization and numerical modelling of 3D printed concrete: Controlling structural behaviour in the fresh and hardened state

Robert Johannes Maria Wolfs

nr 258

Requirement checking in the building industry: Enabling modularized and extensible requirement checking systems based on semantic web technologies

Chi Zhang

nr 259

A Sustainable Industrial Site Redevelopment Planning Support System

Tong Wang

nr 260

Efficient storage and retrieval of detailed building models: Multi-disciplinary and long-term use of geometric and semantic construction information

Thomas Ferdinand Krijnen

nr 261

The users' value of business center concepts for knowledge sharing and networking behavior within and between organizations

Minou Weijs-Perrée

nr 262

Characterization and improvement of aerodynamic performance of vertical axis wind turbines using computational fluid dynamics (CFD)

Abdolrahim Rezaeiha

nr 263

In-situ characterization of the acoustic impedance of vegetated roofs

Chang Liu

nr 264

Occupancy-based lighting control: Developing an energy saving strategy that ensures office workers' comfort

Christel de Bakker

nr 265

Stakeholders-Oriented Spatial Decision Support System

Cahyono Susetyo

nr 266

Climate-induced damage in oak museum objects

Rianne Aleida Luimes

nr 267

Towards individual thermal comfort: Model predictive personalized control of heating systems

Katarina Katic

nr 268

Modelling and Measuring Quality of Urban Life: Housing, Neighborhood, Transport and Job

Lida Aminian

nr 269

Optimization of an aquifer thermal energy storage system through integrated modelling of aquifer, HVAC systems and building

Basar Bozkaya

nr 270

Numerical modeling for urban sound propagation: developments in wave-based and energy-based methods

Raúl Pagán Muñoz

nr 271

Lighting in multi-user office environments: improving employee wellbeing through personal control

Sanae van der Vleuten-Chraibi

nr 272

A strategy for fit-for-purpose occupant behavior modelling in building energy and comfort performance simulation

Isabella I. Gaetani dell'Aquila d'Aragona

nr 273

Een architectuurhistorische waardestelling van naoorlogse woonwijken in Nederland: Het voorbeeld van de Westelijke Tuinsteden in Amsterdam

Eleonore Henriette Marie Mens

nr 274

Job-Housing Co-Dependent Mobility Decisions in Life Trajectories

Jia Guo

nr 275

A user-oriented focus to create healthcare facilities: decision making on strategic values

Emilia Rosalia Catharina Maria Huisman

nr 276

Dynamics of plane impinging jets at moderate Reynolds numbers – with applications to air curtains

Adelya Khayrullina

nr 277

Valorization of Municipal Solid Waste Incineration Bottom Ash - Chemical Nature, Leachability and Treatments of Hazardous Elements

Qadeer Alam

nr 278

Treatments and valorization of MSWI bottom ash - application in cement-based materials

Veronica Caprai

nr 279

Personal lighting conditions of office workers - input for intelligent systems to optimize subjective alertness

Juliëtte van Duijnhoven

nr 280

Social influence effects in tourism travel: air trip itinerary and destination choices

Xiaofeng Pan

nr 281

Advancing Post-War Housing: Integrating Heritage Impact, Environmental Impact, Hygrothermal Risk and Costs in Renovation Design Decisions

Lisanne Claartje Havinga

nr 282

Impact resistant ultra-high performance fibre reinforced concrete: materials, components and properties

Peipeng Li

nr 283

Demand-driven Science Parks: The Perceived Benefits and Trade-offs of Tenant Firms with regard to Science Park Attributes

Wei Keat Benny Ng

nr 284

Raise the lantern; how light can help to maintain a healthy and safe hospital environment focusing on nurses

Maria Petronella Johanna Aarts

nr 285

Modelling Learning and Dynamic Route and Parking Choice Behaviour under Uncertainty

Elaine Cristina Schneider de Carvalho

nr 286

Identifying indoor local microclimates for safekeeping of cultural heritage

Karin Kompatscher

nr 287

Probabilistic modeling of fatigue resistance for welded and riveted bridge details. Resistance models and estimation of uncertainty.

Davide Leonetti

nr 288

Performance of Layered UHPFRC under Static and Dynamic Loads: Effects of steel fibers, coarse aggregates and layered structures

Yangyueye Cao

nr 289

Photocatalytic abatement of the nitrogen oxide pollution: synthesis, application and long-term evaluation of titania-silica composites

Yuri Hendrix

nr 290

Assessing knowledge adoption in post-disaster reconstruction: Understanding the impact of hazard-resistant construction knowledge on reconstruction processes of self-recovering communities in Nepal and the Philippines

Eefje Hendriks

nr 291

Locating electric vehicle charging stations: A multi-agent based dynamic simulation

Seheon Kim

nr 292

De invloed van Lean Management op de beheersing van het bouwproces

Wim van den Bouwhuisen

nr 293

Neighborhood Environment and Physical Activity of Older Adults

Zhengying Liu

nr 294

Practical and continuous luminance distribution measurements for lighting quality

Thijs Willem Krusselbrink

nr 295

Auditory Distraction in Open-Plan Study Environments in Higher Education

Pieterella Elizabeth Braat-Eggen

nr 296

Exploring the effect of the sound environment on nurses' task performance: an applied approach focusing on prospective memory

Jikke Reinten

nr 297

Design and performance of water resistant cementitious materials– Mechanisms, evaluation and applications

Zhengyao Qu

nr 298

Design Optimization of Seasonal Thermal Energy Storage Integrated District Heating and Cooling System: A Modeling and Simulation Approach

Luyi Xu

nr 299

Land use and transport: Integrated approaches for planning and management

Zhongqi Wang

nr 300

Multi-disciplinary optimization of building spatial designs: co-evolutionary design process simulations, evolutionary algorithms, hybrid approaches

Sjonnie Boonstra

nr 301

Modeling the spatial and temporal relation between urban land use, temperature, and energy demand

Hung-Chu Chen

nr 302

Seismic retrofitting of masonry walls with flexible deep mounted CFRP strips

Ömer Serhat Türkmen

nr 303

Coupled Aerostructural Shape and Topology Optimization of Horizontal-Axis Wind Turbine Rotor Blades

Zhijun Wang

nr 304

Valorization of Recycled Waste Glass and Converter Steel Slag as Ingredients for Building Materials: Hydration and Carbonation Studies

Gang Liu

nr 305

Low-Carbon City Development based on Land Use Planning

Gengzhe Wang

nr 306

Sustainable energy transition scenario analysis for buildings and neighborhoods - Data driven optimization

Shalika Saubhagya Wickramarachchi Walker

nr 307

In-between living and manufactured: an exploratory study on biobuilding components for building design

Berrak Kirbas Akyurek

nr 308

Development of alternative cementitious binders and functionalized materials: design, performance and durability

Anna Monika Kaja

nr 309

Development a morphological approach for interactive kinetic façade design: Improving multiple occupants' visual comfort

Seyed Morteza Hosseini

nr 310

PV in urban context: modeling and simulation strategies for analyzing the performance of shaded PV systems

Ádám Bognár

nr 311

Life Trajectory, Household Car Ownership Dynamics and Home Renewable Energy Equipment Adoption

Gaofeng Gu

nr 312

Impact of Street-Scale Built Environment on Walking/Cycling around Metro Stations

Yanan Liu

nr 313

Advances in Urban Traffic Network Equilibrium Models and Algorithms

Dong Wang

nr 314

Development of an uncertainty analysis framework for model-based consequential life cycle assessment: application to activity-based modelling and life cycle assessment of multimodal mobility

Paul Martin Baustert

nr 315

Variable stiffness and damping structural joints for semi-active vibration control

Qinyu Wang

nr 316

Understanding Carsharing-Facilitating Neighborhood Preferences

Juan Wang

nr 317

Dynamic alignment of Corporate Real Estate to business strategies: An empirical analysis using historical data and in-depth modelling of decision making

Howard Cooke

nr 318

Local People Matter: Towards participatory governance of cultural heritage in China

Ji Li

nr 319

Walkability and Walkable Healthy Neighborhoods

Bojing Liao

nr 320

Light directionality in design of healthy offices: exploration of two methods

Parisa Khademagha

nr 321

Room acoustic modeling with the time-domain discontinuous Galerkin method

Huiqing Wang

nr 322

Sustainable insulating lightweight materials for enhancing indoor building performance: miscanthus, aerogel and nano-silica

Yuxuan Chen

nr 323

Computational analysis of the impact of façade geometrical details on wind flow and pollutant dispersion

Xing Zheng

nr 332

Comfort in Urban Public Spaces

You Peng

nr 324

Analysis of urban wind energy potential around high-rise buildings in close proximity using computational fluid dynamics

Yu-Hsuan Jang

nr 325

A new approach to automated energy performance and fault detection and diagnosis of HVAC systems: Development of the 4S3F method

Arie Taal

nr 326

Innovative Admixtures for Modifying Viscosity and Volume Change of Cement Composites

Hossein Karimi

nr 327

Towards houses with low grid dependency: A simulation-based design optimization approach

Zahra Mohammadi

nr 328

Activation of demand flexibility for heating systems in buildings: Real-life demonstration of optimal control for power-to-heat and thermal energy storage

Christian Finck

nr 329

A computational framework for analysis and optimisation of automated solar shading systems

Samuel B. de Vries

nr 330

Challenges and potential solutions for cultural heritage adaptive reuse: a comparative study employing the Historic Urban Landscape approach

Nadia Pintossi

nr 331

Shared control in office lighting systems

Tatiana Aleksandrovna Lashina